



HAL
open science

State estimation in fluid-structure interaction from 4D-flow MRI data

Mocia Agbalessi

► **To cite this version:**

Mocia Agbalessi. State estimation in fluid-structure interaction from 4D-flow MRI data. Numerical Analysis [math.NA]. Sorbonne Université, 2023. English. NNT: . tel-04072648v1

HAL Id: tel-04072648

<https://inria.hal.science/tel-04072648v1>

Submitted on 18 Apr 2023 (v1), last revised 5 Jul 2023 (v2)

HAL is a multi-disciplinary open access archive for the deposit and dissemination of scientific research documents, whether they are published or not. The documents may come from teaching and research institutions in France or abroad, or from public or private research centers.

L'archive ouverte pluridisciplinaire **HAL**, est destinée au dépôt et à la diffusion de documents scientifiques de niveau recherche, publiés ou non, émanant des établissements d'enseignement et de recherche français ou étrangers, des laboratoires publics ou privés.



State estimation in fluid-structure interaction from 4D-flow MRI data

THÈSE DE DOCTORAT

Présentée par

Mocia AGBALESSI

pour obtenir le grade de

DOCTEUR DE
Sorbonne Université

Spécialité : MATHÉMATIQUES APPLIQUÉES

Soutenue publiquement le 3 avril 2023 devant le jury composé de :

Miguel A. FERNÁNDEZ	Directeur de thèse
Damiano LOMBARDI	Codirecteur de thèse
Jean-Joseph CHRISTOPHE	Encadrant industriel
Stéphanie SALMON	Rapporteur
Christian VERGARA	Rapporteur
Frédéric NATAF	Président
Marcela SZOPOS	Examinatrice
Elie MOUSSEaux	Examineur

Après avis favorables des rapporteurs: Stéphanie SALMON et Christian VERGARA

Thèse préparée au sein de l'équipe-projet Commedia
Centre de Recherche Inria de Paris
et **Laboratoire Jacques-Louis Lions**

Abstract

This thesis is devoted to the development of FSI state estimation algorithms using the 4D Flow MRI data. It is motivated by the increasing demand for patient-specific blood flow simulations for the assessment of predictive Wall Shear Stress (WSS) related biomarkers. However patient-specific simulations raise major technical concerns such as the imposition of inflow/outflow boundary conditions, the way to use efficiently the medical data available.

In the first chapter we leverage the richness of the 4D Flow data to develop a method that extracts the time-resolved wall displacement and velocity from 4D MRI, using a Kalman filter approach. The Kalman filter corrects a simplified dynamical model prediction with observed configurations generated by a position observation operator. The position observation operator first finds the configuration that maximizes the image intensity gradient around a previously estimated configuration, using a nearest neighbor search on the voxel grid. Pixelated mesh that is obtained is then regularized. The estimation of the wall displacement and velocity from 4D MRI with the tracking is tested for the reconstruction of the motion of an immersed vesicle with synthetic 4D Flow MRI data. An application to the tracking of the aorta wall of a patient is presented as a response to the need for non-static semi-automatic segmentation of the aortic wall using 4D MRI.

The second and third chapters tackle the FSI state estimation on the academic FSI setting of a pressure wave propagating in a 3D tube. We propose novel approach for FSI state estimation in which no inflow and outflow boundary conditions are imposed.

In the second chapter, small vibrations of the solid are assumed and with suitable kinematic assumptions, the FSI problem is simplified for a FSI fixed-domain problem, in which the solid state is expressed in terms of the fluid state. A first fluid-structure interaction state estimation algorithm is proposed based on unique continuation using fluid velocity measurements. The FSI state estimation algorithm is formulated as a PDE-constraint optimization problem in a L^2 distance between simulation and measured data is minimized. Without specifying inflow and outflow boundary conditions, the problem is ill-posed and the solvability is ensured at the discrete level by weakly consistent stabilization terms. It results in the resolution of a system in the primal variables and associated dual variables. Another FSI state algorithm is proposed in which non-parametric inflow and outflow boundary conditions are estimated using a unique continuation, and imposed on a Luenberger state observer with fluid velocity measurements. Numerical studies illustrate the

performance of the two FSI algorithm for fixed domain FSI state estimation. In the third chapter, the FSI state estimation combining unique continuation with Luenberger observer for the fluid sub-problem is extended to moving domain FSI. We no longer consider a monolithic formulation of the FSI problem but a partitioned resolution. The fluid sub-problem and the solid sub-problem are solved independently and the FSI coupling is ensured by interface coupling conditions. A fourth algorithm is proposed to leverage displacements and velocity in the solid, by adding data feedback terms in the solid sub-problem in the form of a Luenberger state observer. A series of numerical tests are performed to illustrate the two algorithms.

Keywords: Fluid structure-interaction, 4D Flow MRI, Kalman filter, semi-automatic segmentation, Luenberger observers, unique continuation.

Contents

I	Introduction	1
1	Introduction	3
1.1	Clinical context - the AORYSK Project	3
1.1.1	The research goal	3
1.1.2	The research goal of the PhD	5
1.2	Data assimilation for blood flow simulations	6
1.3	Summary of the contribution	8
II	Contribution	9
2	Tracking of blood vessels motion from 4D Flow MRI data	11
2.1	Introduction	11
2.2	Continuous problem and discretization	13
2.2.1	State estimation	14
2.2.2	The position observation operator from grayscale images	15
2.2.3	Fully discrete formulation	18
2.2.3.1	Spatial and temporal discretization	18
2.2.3.2	Discrete observation operator	19
2.2.3.3	Discrete estimation problem	20
2.3	State estimation via Kalman filter	21
2.3.1	Kalman filter	21
2.3.2	Proposed estimation algorithm	22
2.4	Numerical experiments	24
2.4.1	Tracking of a vesicle immersed in a lid-driven cavity flow	25
2.4.1.1	Data generation	26
2.4.1.2	Sensitivity to data quality	29
2.4.1.3	Sensitivity to regularization parameters	35
2.4.2	Aorta tracking from 4D-flow MRI data	37
2.4.2.1	Data generation	37
2.4.2.2	Description of the test	39
2.4.2.3	Results	42
2.5	Conclusion	44
3	FSI fixed domain	47
3.1	FSI Model	48
3.1.1	Setting of the problem	48

3.1.2	Variational formulation and monolithic formulation of the FSI problem	50
3.1.3	Discretization	51
3.1.3.1	Time discretization	51
3.1.3.2	Space discretization with finite element method with fitted meshes	52
3.2	The FSI state estimation algorithm based on a unique continuation approach	53
3.2.1	Notions of unique continuation	53
3.2.2	Unique continuation for FSI state estimation - fixed fluid domain	55
3.2.3	Numerical results	57
3.2.3.1	Data generation (forward problem)	57
3.2.3.2	Pressure estimation	58
3.3	FSI State estimation by combining unique continuation and a Luenberger state estimator	64
3.3.1	FSI state estimation algorithm	64
3.3.2	Numerical results	66
3.4	Conclusion	67
4	State estimation in fluid-structure interaction from 4D Flow MRI data: moving fluid domain	71
4.1	Introduction	71
4.2	The FSI (forward) problem	72
4.2.1	General setting and equations	72
4.2.2	Numerical Resolution and Robin-Neumann coupling scheme	74
4.2.2.1	Continuous variational formulation	75
4.2.2.2	Time discretization and FSI coupling scheme	76
4.2.2.3	Space discretization using fitted meshes	78
4.3	UcL-Fluid state estimator (moving domain)	80
4.3.1	Presentation of the method	81
4.3.2	Numerical results	84
4.3.2.1	Synthetic data generation	84
4.3.2.2	FSI State estimation with UcL-Fluid	90
4.3.3	Intermediate conclusion	97
4.4	UcL-FSI estate estimator	98
4.4.1	Presentation of the algorithm	99
4.4.2	Pole placement analysis	100
4.4.2.1	FSI state estimation coupled with position observation operator (4D Flow MRI)	107
4.4.3	Numerical results	108
4.4.3.1	Coupling between the solid Luenberger and the position observation operator	108

4.4.3.2	Correction of the solid geometrical error in the FSI state estimation UCL-FSI	110
III	Conclusion	115
IV	Appendix	121
A	Unique continuation for FSI	123
A.1	Unique continuation on fixed fluid domain	123
A.2	Unique continuation for moving domain	125

List of Figures

2.1	Illustration of the transport of $\Gamma(t)$ through the velocity field \mathbf{u} .	14
2.2	The surface $\Gamma(t)$ is transported by \mathbf{u} within the domain Ω . $\Gamma(t)$ is sufficiently detectable on the image sequences F_M and \mathbf{u}_M is a measurement of the velocity field \mathbf{u} .	14
2.3	The position observer. On the image at $t \in [0, T]$, the maximization of the norm of the image gradient would result in the mapping ψ with high local curvature. Among all those maps, the regularizing constraint selects ψ_M . Having the trust region around $\tilde{\phi}$ enforces a selection of a specific extremal area.	17
2.4	Two-dimensional illustration of optimization step parameters in the position observation operator ($\Delta N = 2$). The landmark (mesh point) i is in $\tilde{\mathbf{q}}_i(t)$ in the prior mesh (yellow). It is inside the voxel $\Omega_{\pi(\tilde{\mathbf{q}}_i)}$ (in red) which defines the local window search $B(\pi(\tilde{\mathbf{q}}_i(t)), \Delta N)$ for the optimum. The functional $J_t(\tilde{\mathbf{q}}_i; \cdot)$ will be evaluated in the voxel centers c_k for all $k \in B(\pi(\tilde{\mathbf{q}}_i(t)), \Delta N)$.	20
2.5	The parameters of the Kalman filter and the state observation.	25
2.6	Geometrical configuration.	26
2.7	Data generation - Motion of the immersed vesicle, from FSI simulations.	27
2.8	Data generation - The mesh of the cavity, with the initial geometrical configuration of the real vesicle.	28
2.9	Initial configuration. In red, the initial position of the real vesicle. In blue, the initial mesh given to the filter for reconstruction.	29
2.10	Noisy images with $\sigma = 2.0, 6.0$.	30
2.11	Gradient magnitude images with $\sigma = 2.0, 6.0$.	30
2.12	The velocity field around the vesicle, images with $\sigma = 2.0$ and $\sigma_v = 0.003, 0.030, 0.075, 0.105$.	31
2.13	Dice evolution, averaged over 100 runs. $\gamma = 100, \kappa = 10, \kappa_{\text{obs}}\delta = 0.1$.	33
2.14	Simulation for $\sigma = 2.0, \sigma_v = 0.003, \sigma_q = 1.5$. Red : real vesicle. Blue : estimation by the method. $\kappa = 10, \kappa_{\text{obs}}\delta = 0.1$.	33
2.15	Simulation for $\sigma = 2.0, \sigma_v = 0.105, \sigma_q = 1.5$. Red : real vesicle. Blue : estimation by the method. $\kappa = 10, \kappa_{\text{obs}}\delta = 0.1$.	34
2.16	Simulation with $\sigma = 6.0, \sigma_v = 0.003, \sigma_q = 2.5$. Red : real vesicle. Blue : estimation by the method. $\kappa = 10, \kappa_{\text{obs}}\delta = 0.1$.	34

2.17	Simulation with $\sigma = 6.0$, $\sigma_v = 0.105$, $\sigma_q = 2.5$. Red : real vesicle. Blue : estimation by the method. $\kappa_{\text{obs}}\delta = 0.1$	34
2.18	Marginal effect. $\gamma = 100$, $\sigma = 6.0$, $\sigma_v = 0.075$	36
2.19	Effects of κ and $\kappa_{\text{obs}}\delta$. $\gamma = 100$, $\sigma = 6.0$, $\sigma_v = 0.075$	36
2.20	Vesicle configuration (blue) at $t_n, n = 1, 69, 199$ against the solution (red). Right hand side : trajectory of a point in the estimation (blue) compared to the one of the presumed tracked point in the real vesicle (red) at final iteration. Parameters : $\kappa = 0.0, \kappa_{\text{obs}}\delta = 0.1, \sigma = 6.0, \sigma_v = 0.075$	37
2.21	Vesicle configuration (blue) at $t_n, n = 1, 69, 199$ against the solution (red). Right hand side : trajectory of a point in the estimation (blue) compared to the one of the presumed tracked point in the real vesicle (red) at final iteration. Parameters : $\kappa = 10, \kappa_{\text{obs}}\delta = 0.0, \sigma = 6.0, \sigma_v = 0.075$	37
2.22	Vesicle configuration (blue) at $t_n, n = 1, 69, 199$ against the solution (red). Right hand side : trajectory of a point in the estimation (blue) compared to the one of the presumed tracked point in the real vesicle (red) at final iteration. Parameters : $\kappa = 10, \kappa_{\text{obs}}\delta = 0.1, \sigma = 6.0, \sigma_v = 0.075$	38
2.23	Slice of magnitude series and MRA series. The view is oblique sagittal. The slices are taken in the middle of the respective volume of acquisitions.	39
2.24	Input data for the proposed method.	40
2.25	Snapshots of the 4DFLow MRI velocity field data at peak systolic phase.	40
2.26	Slice view of the initial configuration against the magnitude images of the 4D MRI series, at time iteration t_0 (A.), t_4 (B.) and t_7 (C.).	41
2.27	Flow rate at the inlet of the initial configuration. Time iteration $t_k = k \cdot \Delta T$	41
2.28	Definition of the ROI and the slice plane location for the computation of the Dice coefficient. A: the aorta from manual segmentation at t_3 (green). B: the reconstruction at t_3 (red). C: The region of interest for the calculation of the Dice in blue.	43
2.29	Dice on the region of interest	43

2.30 Visualization of the contours obtained by cutting the geometries at 5 planes locations : AAO_P0 = inlet of the geometry, AAO_P1, AAO_P2 = ascending aorta, DAO_P3, DAO_P4 = descending aorta. On the left, the position of the 5 planes. At the right, 10 slices cut views. For each plane, on the left side (with asterix (*)), the contour with the best Dice configuration and the manual segmentation with low opacity for better image visualization, and on the right side, the 4 contours corresponding to the worse Dice configuration (red), one of the average Dice configurations (yellow), the best Dice configuration (green), the manual segmentation (black), see Table 2.4 for more detail on the parameters. 45

2.31 Slice cut view, at the inlet of the geometry. On the left, the position of the plane for slice visualization. On the right, the slice cut at 3 time iterations : A) t_3 , B) t_9 is the end of the systolic phase, C) t_{20} during the diastolic phase. The best Dice reconstruction is in green, one of the 3 average Dice reconstruction in yellow, and the worst Dice case is in red. . . 46

2.32 Slice cut view, at the level of the ascending aorta. On the left, the position of the plane for slice visualization. On the right, the slice cut at 3 time iterations : A) t_3 , B) t_9 is the end of the systolic phase, C) t_{20} during the diastolic phase. The best Dice reconstruction is in green, one of the 3 average Dice reconstruction in yellow, and the worst Dice case is in red. . . 46

3.1 Sketch of the domain Ω . Arrow represents stream lines directions. 49

3.2 Geometrical configuration - FSI on fixed domain, small vibrations 49

3.3 Ground truth solution. 58

3.4 The data at t_{50} . From top to bottom: ground truth without noise, $\delta_{\text{noise}} = 1\%$, and $\delta_{\text{noise}} = 15\%$ 59

3.5 Relative error for the pressure with noise-free measurements . 59

3.6 Relative error for the pressure with 1% noise in the velocity measurements 60

3.7 Relative error for the pressure with 5% noise in the velocity measurements 60

3.8 Estimated inflow pressure profiles with noise-free data 61

3.9 Estimated inflow pressure profiles with 1% noise in the measurements 62

3.10 Estimated inflow pressure profiles with 5% noise in the measurements 62

3.11 Estimated pressure at t_{50} . $\gamma_M = 10^3$, for 1% noise (middle), 5% noise (bottom). The reference solution is given on top. . . 63

3.12 Vertical velocity at the interface, with noise-free data 63

3.13	Relative error of velocity and the pressure for $\gamma_M = 10^3$, noise-free data.	67
3.14	Relative error of velocity and the pressure for $\gamma_M = 10^4$, noise-free data.	67
3.15	Relative error of velocity and the pressure for $\gamma_M = 10^5$, noise-free data.	68
3.16	Relative error for the velocity and the pressure estimations, for $\gamma_M = 10^3$ with noisy data, δ_{noise} parametrizes the percentage of noise.	69
4.1	Geometric configuration.	72
4.2	Reference geometric configuration. (A) View of the 3D cylinder, colored by surface label ($\hat{\Gamma}_{\text{in}}$ in green, $\hat{\Sigma}$ in red. (B) Plane cut visualization with tetrahedra ($y = 0$). (C) Mesh of the circular basis.	86
4.3	Snapshots of the velocity magnitude (reference solution) at $t_{30}, t_{50}, t_{70}, t_{100}, t_{120}$ and t_{140}	86
4.4	Snapshots of the pressure (reference solution) at $t_{30}, t_{50}, t_{70}, t_{100}, t_{120}$ and t_{140}	86
4.5	Snapshots of the wall displacement (reference solution) at $t_{30}, t_{50}, t_{70}, t_{100}, t_{120}$ and t_{140}	87
4.6	Parametrized measurements: transport of the velocity data from Ω^n to $\tilde{\Omega}^n$	88
4.7	Geometric configuration: $\hat{\Omega}_2$, surrounding the cylinder.	89
4.8	2D sketch of the Eulerian velocity data generation. (A) Reference domains in dashed lines. (B) Extension to $\Omega_2^n := \mathcal{V} \setminus \Omega^n$. (C) Interpolation on the hexahedral grid.	90
4.9	Eulerian velocity data (noise-free, grid resolution 0.1cm) at $t_{30}, t_{50}, t_{70}, t_{100}, t_{120}$ and t_{140}	90
4.10	Snapshots of the pressure estimated with Algorithm 6, $\gamma_M = 10^4, \gamma_f = 10^4$	91
4.11	Relative errors of the estimation with Algorithm 6 using parametrized data. (a) Velocity. (b) Pressure. (c) Fluid domain displacement.	92
4.12	Relative errors of the estimation with Algorithm 6 using Eulerian measurements. (a) Velocity. (b) Pressure. (c) Fluid domain displacement.	92
4.13	Inflow boundary data from the unique continuation. (a) Inflow rate. (b) Inflow pressure.	92
4.14	Wall displacement norm at different time instants.	93
4.15	Snapshots of the pressure estimation for the two types of boundary conditions, $\gamma_M = 10^4, \gamma_f = 10^4$, (Eulerian velocity data). (a) Inflow Dirichlet/Outflow Neumann. (b) Inflow Neumann/Outflow Neumann.	93

4.16	Comparison of the relative errors for two types of boundary conditions, $\gamma_M = 10^4$, $\gamma_f = 10^4$ (Eulerian velocity data). (a) Velocity. (b) Pressure. (c) Fluid domain displacement.	93
4.17	Noisy velocity data (5%), at $t_{100} = 0.01$. Note that the left figure has been rescaled.	94
4.18	Relative errors of the estimation with Algorithm 6 using parametrized noisy data (5%). (a) Velocity. (b) Pressure. (c) Fluid domain displacement.	94
4.19	Relative errors of the estimation with Algorithm 6 using noisy Eulerian data (5%). (a) Velocity. (b) Pressure. (c) Fluid domain displacement.	95
4.20	FSI state estimation using Algorithm 6 with (parametrized) noisy data (5%) at $t_{30}, t_{50}, t_{70}, t_{100}, t_{120}$ and t_{140}	96
4.21	FSI state estimation using Algorithm 6 with (Eulerian) noisy data (5%) at $t_{30}, t_{50}, t_{70}, t_{100}, t_{120}$ and t_{140}	97
4.22	Snapshots of the estimated velocity, with initial conditions at $t_{30}, t_{50}, t_{70}, t_{100}, t_{120}$ and t_{140}	98
4.23	Snapshots of the estimated pressure, with initial conditions at $t_{30}, t_{50}, t_{70}, t_{100}, t_{120}$ and t_{140}	98
4.24	Snapshots of the estimated wall displacement, with initial conditions.	98
4.25	Relative errors of the estimated pressure, velocity and pressure.	99
4.26	Example of placement.	104
4.27	$\max_{n=1,2}\{\text{Re}(\omega_{k,n})\}$, for $\gamma_f = 100$, $R = 0.5$, $L = 5$	105
4.28	$\max_{n=1,2}\{\text{Re}(\omega_{k,n})\}$, for $\gamma_f = 100$, $R = 0.5$, $L = 5$, different view.	105
4.29	$\max_{n=1,2}\{\text{Re}(\omega_{k,n})\}$, for $\gamma_f = 100$, $R = 0.5$, $L = 5$, different view.	106
4.30	UcL-FSI using 4D MRI data	108
4.31	Decay of the displacement L^2 -norm	110
4.32	Decay of the displacement (amplified by a factor 2).	110
4.33	Estimated pressure with Algorithm 8 for $\gamma_M = 10^5$, $\gamma_f = 50$, $\gamma_{\text{sdf}} = 2000$ and $\gamma_{\text{dvf}} = 200$, at $t_0, t_{30}, t_{50}, t_{70}, t_{100}, t_{120}$ and t_{140} . The displacement has not been amplified	111
4.34	Relative error in the velocity, the pressure and the (fluid domain) displacement for $\gamma_M = 10^5$, $\gamma_f = 50$, $\gamma_{\text{sdf}} = 2000$ and $\gamma_{\text{dvf}} = 200$	112

List of Tables

2.1	Parameters for the first synthetic test case.	29
2.2	Parameters for the second synthetic test case.	35
2.3	Parameters used in Algorithm 2 for the reconstruction of the aorta.	42
2.4	Parameters of best,average and worse dice configurations, with Dice on the ROI at t_3	44

Part I

Introduction

CHAPTER 1

Introduction

The PhD is in the continuity of an international research effort to improve the prediction of aortic aneurysm. The AORYSK includes a consortium composed of the Institute of Fluid Science (IFS), Dijon University Hospital, the project-team COMMEDIA of INRIA, and the company CASIS SA – CArdiac Simulation & Imaging Software. Its different axes of research are presented in Section 1.1. Among those, enriching the modeling framework for medical data assimilation is a key point to improve the computation of predictive biomarkers. We focus on fluid-structure interaction with data assimilation in view of designing patient-specific blood flow simulations. In Section 1.2, the main difficulties of FSI data assimilation are synthetically reviewed.

1.1 Clinical context - the AORYSK Project

1.1.1 The research goal

The PhD research is part of the AORYSK international project to improve the prediction of aortic aneurysm.

Bicuspid Aortic Valve (BAV) is a congenital heart disease affecting 0.5 to 1.4% of the population [GTdM13]. Statistics suggest that BAV is related to higher risk of aortic stenosis and coarctation, since 50% of the adults with an aortic stenosis and 50 to 80% of the patients with a coarctation of the aorta have BAV[WSC⁺12]. Efficient diagnosis and predictive treatment of aortic affections for the patients with BAS is consequently a clinical concern. However, the prediction of the risk of rupture of thoracic aorta is a challenging problem. Currently the criteria to predict rupture are aneurysm diameter and growth rates. However, different studies has shown the limitation of such morphological criteria. For instance, the American College of Cardiology recommend a replacement of the aortic root or the ascending aorta in patient with BAV when the aortic diameter exceeds 5.5 cm [AB15] though it has been reported that aortic dissection can often occur in case of an aortic diameter lesser than 5.5cm [AB15, YSFJ16]. Studies even show higher occurrence of aortic dissection for aortic diameters between 40 and 49mm in comparaiso to diameters between 55 and 64 mm [YSFJ16]. It has been suggested to rely more on an aortic size index (aortic diameter / Body Surface Area), but still no study has demonstrated the relevancy of this index [AB15]. For patients with BAV, the risk of rupture is permanent without any significant dilatation of the aorta. In the recent years, physicians and scientists have been investigating the potential of hemodynamics to improve the diagnosis, using the medical imaging techniques with functional analysis of the blood flow. Among them, MRI is an imaging technique of choice in the study of the aortic function, and in particular morphological and kinetic studies from MRI already provide reliable data. It enables to calculate parameters such as the aortic diameter, the aortic compliance and, and also extract blood flow data. Albeit relevant, those data are not sufficient by themselves to provide a robust and reliable predictive model for pathologies such as aortic aneurysm. With the last

decade, 4D flow MRI has become very attractive for blood flow quantification in view of parametric studies. Yet, few research has been held on the matter of aortic aneurysm prediction based on 4D flow MRI. A study carried out by REO (former name of COMMEDIA) Inria's project-team in collaboration with CASIS aimed at highlighting the ability for some parameters related to the Wall Shear Stress (WSS) to predict the risk of occurrence of a thoracic aneurysm. It was based on the hypothesis that a high WSS might trigger biological and morphological responses leading to a thinning of the aortic wall, hence the presumed relation between WSS-related parameters and the formation of aneurysm, or aortic dilatation.[YSFJ16]. Due to the limited temporal and spatial resolution of 4D Flow MRI and also the noise in the data, the calculation of biomarkers of interest directly with 4D Flow MRI may lack of accuracy. Assessing those predictive parameters from a time-resolved 3D model including blood flow behavior has grown interest in the cardiovascular field. In this context, blood flow simulations have already proven good efficiency as predictive models to assess the location of area where aneurysm is more likely to develop for cerebral arteries[SII⁺09]. The first studies of blood flow in the thoracic aorta based on MRI started already more than 15 years ago [CL13]. The main interest of performing blood flow simulations for clinical application is for parametric studies. Those parametric studies consist in the assessment of well-chosen bio-markers for a cohort of patients to identify their abilities to segregate the population in level of risks for a pathology. It requires to identify, or elaborate, proper parameters (or bio-markers) usually related to the Wall Shear Stress (WSS) for the prediction of aortic aneurysm. Such recent studies have been conducted in the case of a BAV[SMY15], highlighting some parameters of interest (the viscous shear stress, the effective orifice area. . .). Unfortunately, the use of theoretical models of the boundary conditions (BC) does not allow clinical applications as such. A possible option is to develop a fluid-structure interaction computational model to account for the coupled effect of the vessel wall compliance on the blood flow. In the context of the AORYSK project, this has been done progressively. In a first step, fluid-structure interaction has been ignored to develop an efficient Computational Fluid Dynamic (CFD) model of the thoracic aorta. The main topic of this proposed work is to use the 4D flow MRI to enrich the models of the boundary conditions in the CFD model (at the level of the BAV, of the descending aorta and at the level of the brachiocephalic arteries), and the whole process must be adapted to each patient in a very straightforward fashion. As a first step to overcome this technical challenge, effort has focused on blood flow simulation, ignoring the fluid-structure interactions at the inlet. The wall motion has been integrated by retrieving wall shape at different time step from 4D PC-MRI as it has been done previously for the left ventricle by Prof. HAYASE's laboratory[YHMF18], or for the thoracic aorta by other teams[KPG⁺16]. Our model has then been improved using a mix of 4D PC-MRI, angiography, and 2D CINE MRI, as tried by other teams[BvOP⁺16]. The predictability of a set of chosen parameters using the latter model has been assessed on a patient-specific geometry after (artificial) removal of the aneurysm. Several studies pointed out effects of BAV on blood flow[MBS⁺15, HKK⁺16], and in particular the effect of the opening orifice area and leaflet orientation[MdSJK⁺16] A possible next step is to take into account the effect of the aortic valve phenotype on the blood flow characteristics and its impact on predictive parameters such as the Wall Shear Stress. It has been reported that the aortic valve can be included in CFD study using PC MRI[WSC⁺12]. Several options exist to include fluid-structure interaction, such as

linearized kinematics, coupled momentum method, immersed boundary method, and the Arbitrarily Lagrangian Eulerian formulation[CL13] for the valve. PC-MRI data could even be used to retrieve positions of the valve at different time-step as for the wall. A model of FSI at the aortic valve has been already been explored formerly by the REO team[AGPT09]. An intrinsic limitation of MRI is the low spatial and temporal resolution. To overcome this, the IFS laboratory proposed a Magnetic Resonance Measurement-Integrated (MR-MI) method based on the CFD model, neglecting the aortic wall deformation. Hence the main goals of the AORYSK project in terms of modeling could be summarized in two main directions:

1. Enriching the existing patient-specific model, especially for FSI simulations,
2. Modeling the valve morphology and variability in a fully FSI model,

in view of running a deep parameters study with well-chosen biomarkers on at least three to five patient cases, and ultimately compare them with phantom studies. One could also think of including the effect of the heart motion, With formerly chosen parameters, running a deep parameters study on at least three to five patient cases.

1.1.2 The research goal of the PhD

In the context of the PhD, the highlight is made on the enrichment of patient-specific FSI simulations using 4D MRI data to circumvent the use of Windkessel model of the outflow boundary conditions on the one hand, and estimate the FSI state (blood flow + vessel wall deformation) of the aorta, on another hand. Windkessel model have been intensively used in blood flow model, however the estimation of the model parameters are required to patient-specific blood flow simulation. More discussion will be provided in Section 1.2

The aortic artery being a large vessel, non-Newtonian effects are neglected and the blood flow is assumed incompressible and Newtonian[IGOY98, Thi08]. In fact, at the microscopic level, the blood is a complex medium composed of billions of living cells (erythrocytes, leukocytes, platelets, ...) transported in a liquid called the plasma, which represents around 55% of the blood volume. The plasma is made of water (>90%) and other substances (proteins, etc). In large blood vessels (diameter of the lumen between 1 and 25, possibly more), the ratio between the vessel bore and the size of blood cells is sufficiently large to consider that the blood is a homogeneous continuum medium. The macroscopic behavior of the blood flow (newtonian or not) results from the microscopic interaction between the erythrocytes (red blood cells) and the molecules inside the plasma. In fact, erythrocytes which are predominant over the other cells are responsible for the shear-thinning in micro-circulation, resulting in a decrease of the blood viscosity with the rate of deformation. This shear-thinning effect can be explained by the aggregation of red blood cells in low shear areas. The shear-thinning effect is associated to non-Newtonian behavior of the blood flow and is mostly observed in small size vessels. In large vessel however, stagnant blood flow areas can also results in non-newtonian behavior. Unsteady flow is considered. The governing equations are given by the Navier-Stokes equations. Large-sized vessels such as the aorta undergo deformation up to 15% of their diameter. Even though fixed-wall assumption is sufficient to obtain the main flow pattern, accurate computation of shear stresses requires the interaction between the vessel wall and the blood flow to be taken into account. Despite the fact that the aortic wall is non homogeneous

three-layered media, reduced models such as the shell kinematics are sufficient since the focus is not to model inner-walled stresses. The fluid-structure is ensured by interface coupling conditions. The boundary conditions (BC) at the aortic valve (or inlet), at the descending thoracic aorta outlet and at the brachiocephalic arteries should be cautiously chosen and, in our work, based on 4D MR blood flow data. This last point is one of the innovative aspect of this research project. For instance, we would like to replace the Windkessel 0D model by non parametrized boundary conditions. At the inlet, we could take into consideration the impact of cardiac motion, by tracking the displacement of the aortic root. Considering the low spatial and temporal resolution of 4D flow MRI data, 4D flow MRI data would allow to reconstruct each patient inlet flow as well.

In order to assimilate data to calibrate the wall displacement with 4D flow MRI data, the reconstruction of the aortic configuration for each patient is necessary. This is the main goal of Chapter 2. The FSI simulation will be conducted with FELiScE-NS and FELiScE libraries developed by INRIA based on the Finite Element Method (FEM). FEM has the capability to incorporate the displacement of the biological tissue (aortic wall) in a medical simulation problem (such as the aortic flow simulation) more accurately than other methods[KKB⁺15].

1.2 Data assimilation for blood flow simulations

During the last decades, data assimilation for cardiovascular simulations has been intensively investigated as a promising support for clinical diagnosis and treatment of aortic aneurysms. In particular, one seeks to estimate hemodynamic quantities of interest such as pressure-gradient, wall-shear stress related parameters in a more robust and accurate fashion.

Pressure-gradient estimation using medical imaging data such as 2D-PC MRI and Doppler Ultrasound has already become a common practice for clinicians[BSN⁺99]. The velocity measurements obtained with the functional images are replaced in the Bernoulli or the Navier-Stokes equations[BNG⁺17] to provide a direct calculation of the pressure-gradient. This class of methods are limited by the resolution of the medical images and the level of noise. An alternative is to estimate hemodynamic quantities through patient-specific blood flow simulations. Personalized blood flow simulations enable accurate calculation of non-invasive biomarkers with desired space resolution. However, a systematic personalization to each patient using medical data must be performed for clinical relevance of those diagnosis biomarkers. The design of new methods for data assimilation has benefited from the increasing amount of medical imaging data with anatomic description and functional analysis of vessel blood flows, such as 3D PC MRI or Doppler Ultrasonography. A first to integrate medical data in blood simulation to estimate the pressure field has been performed in[FH13]. The blood flow is assumed governed by Navier-Stokes equations with rigid vessel wall, which restricts the validity of the approach to region that are far from the vessel wall.

Data assimilation applied to fluid-structure interaction models of vessel blood flow seeks to combine theoretical dynamical models with observations to estimate the fluid velocity \mathbf{u} , the pressure p and the vessel wall displacement \mathbf{d} (FSI state). Techniques can be divided into two main families: variational approaches and sequential approaches. Variational approaches minimize the distance between all the state observations and the model prediction, with additional terms to incorporate

some a priori knowledge on the solution. In [PVV11] for instance, synthetic measurements data are assimilated using a variational approach to estimate the solid mechanical parameters and the aFSI state. Besides the cost of implementation of variational approaches, the state of the system at all time iterations needs to be calculated and stored, which might be costly in terms of memory. On the contrary, sequential approaches also called filtering approaches improve the model prediction sequentially with state observations, by adding a correction based on the discrepancy between the predicted state and the observation. For linear dynamical system and linear observations, Kalman filter provide an optimal state estimation. Extension of Kalman filter have been designed for non-linear problem and/or non-linear observations. Even though the optimality can no longer be stated, those filters yield satisfactory estimations in the practice. Among them, the Reduced-order Unscented Kalman Filter(ROUKF)[MC11] has been designed to estimate the FSI state and the parameters of the Windkessel outflow boundary conditions using 2D PC-MRI (time-resolved through-plane velocity at pre-defined plane locations) in [AXM+20]. Since the FSI state depends on the boundary conditions in a nonlinear fashion, the distribution of the state around a given set of Windkessel parameters is calculated using particles (state associated to a given parameter). A perturbation of the Windkessel parameters demands a computation of the backward state history. A least square approach is consequently added to relax the dependency of the particles on their history. The use of parametrized boundary conditions such as Windkessel lumped models demands sophisticated joint parameter-state estimation. Another class of sequential approaches are the Luenberger observers, with consist in adding data feedback terms to correct the original dynamical equations. The implementation implies few modifications of the dynamical equations and the state estimation is solved with the same complexity as the forward problem. A starting point for the PhD has been the work of C. Bertoglio[BCF+13, Ber12] where Luenberger observers with measurements of displacements or velocity in the solid are used to estimate the FSI state of vessel blood flow. Measurements in the fluid are not considered to reduce the uncertainty in the initial conditions. As 4D Flow MRI provides rich measurements in the fluid and the solid, we propose to leverage 4D Flow MRI using Luenberger observers.

The use of Luenberger observers requires to apply appropriate boundary conditions at inflow and outflow vessel boundaries. With Windkessel model for the outflow boundary conditions, the parameters have to be calibrated with respect to the data[MBX+12] at the same time as the FSI state. Recent work has proposed alternatives to provide non-parametric boundary conditions. One notable contribution[TGS17] comes up with inflow Dirichlet velocity profiles estimated using a boundary control approach, for stationary Navier-Stokes equations with rigid wall assumption. In[BBFV20], data assimilation using velocity measurements in the fluid is applied to linearized Navier-Stokes equations without knowledge of the inflow/outflow boundary conditions. The data assimilation problems is formulated as the minimization of the distance between the estimated velocity and the measurements, constrained by the discrete weak formulation of the dynamical equations. Consistent regularization is added at the discrete level to address the ill-posedness of the problem. The originality of the approach is that the regularization vanishes with the refinement of the mesh size and ensures a convergence toward the discrete formulation.

1.3 Summary of the contribution

In this thesis, we first propose a tracking algorithm to estimate the solid deformation and velocity using 4D Flow MRI. This first step aims at providing a segmentation tool to extract measurements in the solid for FSI state estimation. The tracking approach makes use of Kalman filter to regularize solid observations coming from a home-designed position observation operator. It thus translates the eulerian information available with 4D Flow MRI into a Lagrangian estimation of the wall displacement and velocity. In the continuity of the FSI data assimilation, we propose non-parametric estimation of the fluid boundary conditions for FSI problem using velocity measurements, combined with Luenberger estimators using fluid and solid measurements to estimate the FSI state. The algorithm is validated on synthetic data which mimics 4D Flow MRI data. The document is organized as follows. In Chapter 2, an estimation of the Lagrangian displacement and velocity at the vessel wall using 4D Flow MRI is proposed in the form of a tracking. The content of this chapter is an article[ALB⁺22], that has been submitted for publication. Chapter 3 introduces two FSI state estimations applied on fixed-domain FSI case. The first one in Section 3.2 is mostly based on unique continuation and the second one presented in Section 3.2.2 combines unique continuation with a Luenberger observer using the velocity measurements. Finally in Chapter 4, we extend the second estimator to moving domain FSI in Section 4.3, and build up on the latter, to provide a new FSI state estimator with velocity measurements in the fluid and the solid. In Part III, the main conclusions are drawn with perspectives.

Part II

Contribution

Tracking of blood vessels motion from 4D Flow MRI data

2.1 Introduction

Among cardiovascular diseases, arterial aneurysms (i.e., abnormal enlargement of arteries), depict a high risk of mortality [DGC⁺02, KET⁺17]. To prevent complications, surgery is proposed in current clinical practice, consisting in the removal of the aneurysm and the replacement of the aortic section by a synthetic tube in Dacron. The surgical decision follows guidelines [CDE⁺18, mEA⁺14, RMP⁺17] which are solely based on the diameter of the aneurysm [CDE⁺18, mEA⁺14]. Nevertheless, recent studies [PTI⁺07] showed that dissection and rupture can appear even when the aortic diameter is lower than current thresholds, in case of ascending aorta aneurysms and for patients without any specific medical history. Consequently, there is a strong clinical demand for more robust predictive parameters of aortic aneurysm risk. Biomarkers derived from mechanistic parameters such as wall stiffness, wall shear stress (WSS), inlet flow jet angle, etc. are being increasingly investigated to assess the risk of rupture of aneurysm. In *Hope et. al* [HSW⁺14], a correlation has been established between high growth rate of aortic aneurysm and abnormal flow displacement for patients with bicuspid aortic valve (BAV).

The most convenient way to obtain those parameters is based on Phase Contrast Magnetic Resonance Imaging (PC-MRI) [SAG⁺14], a medical imaging modality developed in recent decades with the aim of visualizing and quantifying the blood flow in the vasculature. In the literature, this imaging technique is also called 4D PC-MRI or 4D-flow MRI, because it includes time-resolved slice images covering a volume of acquisition, with flow encoding. It provides both anatomical (magnitude images) and functional (phase images) information that enables the non invasive analysis of blood vessel hemodynamics, and consequently the assessment of flow driven parameters of interest. *Hope et. al* [HSW⁺14] demonstrate a good reproducibility of biomarkers computed through 4D-flow MRI. However, 4D-flow analysis requires extensive pre-processing. In particular, the extraction of the aortic geometry at each time step of the cardiac cycle may be needed. The manual contouring of the aortic lumen takes 20-30 minutes for each time step¹ and cannot be considered as viable part in any clinical routine. It is thus necessary to develop automatic or at least semi-automatic segmentation algorithms of the aortic wall.

We distinguish segmentation from reconstruction, the first aims at enhancing in the images (for example with a binary mask or contours) pixels belonging to an organ of interest (aorta), whereas with the latter, the geometrical configurations of this organ are extracted. In the practice, 4D-flow MRI visualization and quantification require a 3D reconstruction of the geometry. Single 3D reconstruction can be achieved by segmented a MRA sequence acquired separately or some MRA sequence calculated the time-resolved cine MRI data. The purpose of using a MRA sequence

¹There is no standard time, but it depends on the expert.

is to benefit from a better image quality (contrast and/or spatial resolution) than 4D Flow MRI. Using this sequence, different techniques adapted to 2D image segmentation can be applied on the stack images of the MRA sequences, such as model based approaches, tracking techniques [LL15] or supervised/unsupervised image contour segmentations as referred in the review [MRM⁺20]. The common practice is thus to extract one 3D patient specific aortic reconstruction from 4D Flow derived image sequences, and all biomarkers are evaluated based on that single configuration. However, more advanced parameters such as time-averaged WSS are often computed through numerical simulation, due to the limited spatial and temporal resolution of 4D MRI. WSS related biomarkers are increasingly investigated first to quantify the effect of abnormal flows near the aortic wall, and then to predict the location of dissection or rupture. Ideally, one would like to evaluate the biomarkers from patient specific fluid-structure interaction simulations of the aorta. This would require to reconstruct different aortic wall configurations from 4D-flow MRI. Furthermore, the extraction of Lagrangian information (i.e., point-to-point match between configurations) from 4D-flow MRI would also facilitate this calibration. Robust and accurate techniques have been proposed for the time coherent segmentation of 4D MRI image sequences (anatomic series) of the aorta with minimal human intervention [ZZW⁺06]. The surface of the aorta can be reconstructed afterwards from 4D segmentation resulting in a series of mesh representing different time configurations. Point-to-point correspondence is not generally required in these meshes. Notable results have been achieved in the reconstruction of time configurations with point-to-point matching, specifically for the left ventricle [LSY⁺14]. 2D contours lines are pre-segmented from time series of grayscale 3D images prior to applying the reconstruction. A patient specific template is reconstructed and deformed to fit the segmented contours, using a tree-based structure. The point-to-point matching is obtained by relying on geometrical assumptions. Note that the twist of the ventricle is not captured. Another alternative is to use 4D Tagged MRI data. The local deformation of the left ventricle endocardium is integrated in the reconstruction in terms of Lagrangian tracking [WMQ⁺12]. Tagged MRI is however limited to organs with sufficient thickness, so that assessing the local deformation of the aortic wall from Tagged MRI might be delicate.

In this work, we address the tracking of the aortic wall motion from 4D-flow MRI sequences. The velocity data serves as a kinematical a priori for the estimation of the Lagrangian wall deformation. Several corrections are proposed in the literature to the near-wall velocity, due to the so-called partial volume effect [Seu, Pui19]. In the proposed method, we model this effect as an additive noise in the 4D-flow velocity field and the subsequent uncertainty is treated via Kalman filtering estimator. This provides both an estimate of the state of the system and of the quality of the estimation. A position observation operator is introduced to extract geometrical information from the grayscale images. It mimics active contours approaches [KWT88, Act09], which minimize the sum of an internal energy (the deformation energy which ensures surface regularity) and of an external energy (often built from the gradient of image intensity). Since the image gradient can be noisy or have some irregularities, additional features are added to smooth the image gradient as in [XP98], where the external energy is expressed with a generalized gradient vector flow.

In the literature, active contour approaches have been combined with Kalman

filtering in order to achieve robust edge detection in 3D CTA segmentation, by tracking 2D contours from slice to slice [LL15]. Kalman filter has also been combined with active contours to perform 4D reconstruction of vessels from ultrasound [PYG⁺12], by tracking the centerline of the vessel at specific time steps. In the present Chapter, Kalman filtering is considered with a model-based prediction and correction from both time resolved anatomic images and flow series. Alternative algorithms that address the time reconstruction of moving parts of the heart from time-resolved image sequences can be found in [LCV⁺18, WMQ⁺12, LSY⁺14]. They mainly rely on pre-processed or pre-segmented images, and do not exploit the flow information (eulerian velocity field) provided by 4D MRI. The mesh point tracking, when considered, is performed through morphological hypotheses, image intensity or velocity approximations from complementary images with enhanced temporal resolution.

The rest of this Chapter is organized as follows. In the next section, the tracking problem is presented in both the continuous and the discrete settings. The position observation operator is presented in Section 2.2.3.2. After a brief presentation of Kalman filter, the proposed tracking algorithm is detailed in Section 2.3.2. Section 2.4 provides a numerical assessment of the proposed approach using synthetic and clinical data. Finally, a summary of the results and some conclusion with perspectives are drawn in Section 2.5.

2.2 Continuous problem and discretization

At the continuous level, we assume that the Lagrangian tracking of the aorta can be approximated by the tracking of the local deformation of an elastic surface Γ , which is transported by some regular velocity field \mathbf{u} . The deformation of Γ is parametrized by means of a mapping $\phi: \Gamma_R \times [0, T] \rightarrow \mathbb{R}^d$, for a given final time instant $T > 0$, Γ_R being a reference configuration. The transport equation is given by :

$$\begin{cases} \partial_t \phi(\boldsymbol{\xi}, t) &= \mathbf{u}(\phi(\boldsymbol{\xi}, t), t), & (\boldsymbol{\xi}, t) \in \Gamma_R \times]0, T], \\ \phi(\boldsymbol{\xi}, 0) &= \phi_0(\boldsymbol{\xi}), & \boldsymbol{\xi} \in \Gamma_R, \end{cases} \quad (2.1)$$

where $\phi_0: \Gamma_R \rightarrow \mathbb{R}^d$ stands for initial configuration of the surface (see Figure 2.1).

The problem considered in this Chapter consists in estimating the motion ϕ from the following information (see Figure 2.2):

- the time-resolved grayscale image sequence described in terms of the scalar function $F_M: \Omega \times [0, T] \rightarrow \mathbb{R}$;
- the measurement $\mathbf{u}_M: \Omega \times [0, T] \rightarrow \mathbb{R}^d$ of the Eulerian velocity field \mathbf{u} in Ω . The measured field \mathbf{u}_M is presumably less regular than \mathbf{u} ;
- a prior mapping $\tilde{\phi}: \Gamma_R \times [0, T] \rightarrow \mathbb{R}^d$ such that the surface $\tilde{\phi}(\Gamma_R, \cdot)$ has a similar topology and close geometrical position as $\phi(\Gamma_R, \cdot)$.

The first two points correspond to the data traditionally provided by 4D-flow MRI image sequences [WSW96, MFK⁺12].

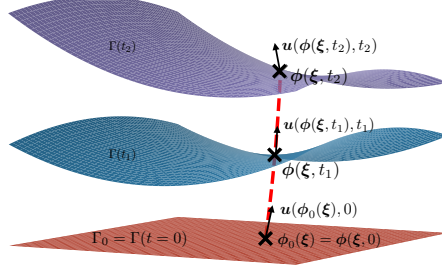


Figure 2.1: Illustration of the transport of $\Gamma(t)$ through the velocity field \mathbf{u} .

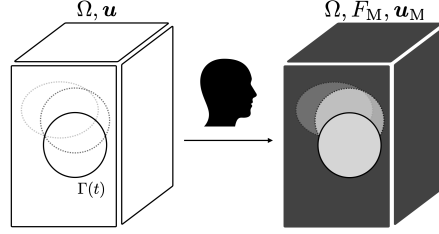


Figure 2.2: The surface $\Gamma(t)$ is transported by \mathbf{u} within the domain Ω . $\Gamma(t)$ is sufficiently detectable on the image sequences F_M and \mathbf{u}_M is a measurement of the velocity field \mathbf{u} .

2.2.1 State estimation

We first introduce a variational formulation of state estimation problem as follows: Find

- a mapping $\hat{\phi}: \Gamma_{\mathbb{R}} \times [0, T] \rightarrow \mathbb{R}^d$
- a velocity field $\hat{\mathbf{v}}: \Gamma_{\mathbb{R}} \times [0, T] \rightarrow \mathbb{R}^d$

which minimizes the misfit functional

$$(\varphi, \mathbf{v}) \mapsto \frac{1}{2} \int_0^T \int_{\Gamma_{\mathbb{R}}} \left(\|\psi_M - \varphi\|_{\mathbf{B}_{\text{pos}}}^2 + \|\mathbf{u}_M(\psi_M) - \mathbf{v}\|_{\mathbf{B}_{\text{vel}}}^2 \right) d\xi, \quad (2.2)$$

where the mapping $\psi_M: \Gamma_{\mathbb{R}} \times [0, T] \rightarrow \mathbb{R}^d$ is an observation of the mapping unknown mapping ϕ and the two norms $\|\cdot\|_{\mathbf{B}_{\text{pos}}}$ and $\|\cdot\|_{\mathbf{B}_{\text{vel}}}$ are equivalent to the L2-norm, respectively weighted by the positive-definite matrices \mathbf{B}_{pos} and \mathbf{B}_{vel} . For the moment let assume that ψ_M is given and depends on both the time-dependent images F_M^n and the prior $\tilde{\phi}$. The procedure to compute this term will be described in the next section. The matrices $\mathbf{B}_{\text{pos}}, \mathbf{B}_{\text{vel}} \in \mathcal{S}_3(\mathbb{R})$ have two purposes. On the one hand, they ensure dimensionless comparison between the misfit to the position observation and the misfit to the velocity observation. On another hand, \mathbf{B}_{pos} and \mathbf{B}_{vel} quantify

the confidence in the observed mapping ψ_M and in the observed velocity $\mathbf{u}_M(\psi_M)$, respectively. An additional constraint on the local velocity derivate will be added to the transport equation (2.1) to impose some regularity on the solution $(\hat{\phi}, \hat{\nu})$. It aims at filtering local high-frequency surface deformations with some elastic properties. For this purpose, we make use of the surface laplacian Δ_{ξ} , for the sake of simplicity, while introducing a user-defined parameter $\kappa > 0$ for finer parameterization. We thus chose the following system of equations :

$$\begin{cases} \partial_t \varphi(\xi, t) = \mathbf{v}(\xi, t), & (\xi, t) \in \Gamma_R \times]0, T], \\ \partial_t \mathbf{v}(\xi, t) = \kappa \Delta_{\xi}(\varphi(\xi, t, t) - \tilde{\phi}_0(\xi)), & (\xi, t) \in \Gamma_R \times]0, T], \\ \varphi(\xi, 0) = \tilde{\phi}_0(\xi), \quad \mathbf{v}(\xi, 0) = \tilde{\mathbf{v}}_0(\xi), & \xi \in \Gamma_R, \end{cases} \quad (2.3)$$

where $\tilde{\phi}_0: \Gamma_R \rightarrow \mathbb{R}^d$ and $\tilde{\mathbf{v}}_0: \Gamma_R \rightarrow \mathbb{R}^d$ denote the initial conditions and play the role of a control on the φ and \mathbf{v} , in order to reach the optimum in (2.2). The misfit functional (2.2) could be written as a function of the initial condition $(\tilde{\phi}_0, \tilde{\mathbf{v}}_0)$ through (2.3). Hence, the optimization problem:

$$\min_{\tilde{\phi}_0, \tilde{\mathbf{v}}_0} \frac{1}{2} \int_0^T \int_{\Gamma_R} \left(\|\psi_M - \varphi\|_{\mathbb{B}_{\text{pos}}}^2 + \|\mathbf{u}_M(\psi_M) - \nu\|_{\mathbb{B}_{\text{vel}}}^2 \right) d\xi dt, \quad (2.4)$$

such that

$$\begin{cases} \partial_t \varphi = \nu, \\ \partial_t \nu = \mathcal{F}(\varphi), \\ \varphi(\cdot, 0) = \tilde{\phi}_0(\cdot) \quad \nu(\cdot, 0) = \mathbf{v}_0(\cdot), \end{cases} \quad (2.5)$$

and with $\mathcal{F}(\varphi) := \kappa \Delta_{\xi}(\varphi - \tilde{\phi}_0)$.

The state estimation is presented as a space and time continuous optimization problem controlled by the initial condition. We propose a method to solve the space and time discretized problem in the following sections.

2.2.2 The position observation operator from grayscale images

In this section, we describe the observation operator of the unknown mapping ϕ from the images F_M . It corresponds to the mapping ψ_M introduced in the minimization problems (2.2) and (2.4). Grayscale intensity images of the domain Ω provide geometrical information on the location of the surface $\Gamma(t)$. In fact, moving objects on images are usually visible and trackable to the naked eyes, at least in cases in which there is sufficient intensity contrast, and provided that there is reasonable prior information on the position and the shape. As shown on Figure 2.2, the mapping describing the motion of the surface is unknown, but we can see the surface moving due to the contrast of the image. The ability to track the surface motion is a consequence of the fact that the contour, which identifies $\Gamma(t)$, is associated with a *local* extremal value of the norm of the gradient of the image intensity. This mere property is widely used in basic edge detection techniques. Different image filters have been developed in order to quantify the gradient of the image intensity [Sob14, Pre70] and thus facilitate contour segmentation. Among them, the Canny edge detection [Can86] proposes contour identification, since it selects candidate contours given ribbons of extremal gradient. This filter can be limited by the image

contrast, and also local inhomogeneities of image intensity inside a coherent region due to image noise, or simply the imaging technique itself. It might thus result in artefacts in the segmentation and non-smooth geometry reconstruction. This shows that maximizing the gradient of the image intensity does not guarantee the regularity of the boundary, even if the boundary of the real object is smooth. For this reason, a regularizing constraint is also added in the surface position operator that will be presented.

In what follows, the norm $\|\cdot\|$ is induced by the canonical euclidian scalar product $\langle \cdot, \cdot \rangle$. If the space of positive-definite symmetric matrices of dimension $d \times d$ is referred as $\mathcal{S}_d(\mathbb{R})$, then for each element $B \in \mathcal{S}_d(\mathbb{R})$ we can define the scalar product $\langle \mathbf{x}, \mathbf{x} \rangle_B = \mathbf{x}^T B^{-1} \mathbf{y}, \forall \mathbf{x}, \mathbf{y} \in \mathbb{R}^d$, and the induced norm $\|\cdot\|_B$. At a given $t \in (0, T)$, the proposed position observation operator involves the minimization of the following functional \mathcal{J}_t , defined for sufficiently regular deformation mapping $\psi: \Gamma_{\mathbb{R}} \rightarrow \mathbb{R}^d$:

$$\begin{aligned} \mathcal{J}_t(\psi) = \frac{1}{2} \int_{\Gamma_{\mathbb{R}}} \left(- \|\nabla_{\mathbf{x}} F_M(\psi(\xi), t)\|_{\mathbf{B}_{\text{img}}}^2 + \|\psi(\xi) - \tilde{\phi}(\xi, t)\|_{\mathbf{B}_{\text{prior}}}^2 \right. \\ \left. + \delta \|\nabla_{\xi}(\psi - \tilde{\phi}_0)(\xi)\|^2 \right) d\xi. \end{aligned} \quad (2.6)$$

Here, the symbols $\nabla_{\mathbf{x}}, \nabla_{\xi}$ denote the gradient with respect to the cartesian and the curvilinear coordinates, respectively. The mapping $\tilde{\phi}$ represents a prior on the unknown mapping ϕ , so that the second term can be interpreted as a trust region. The matrices \mathbf{B}_{img} and $\mathbf{B}_{\text{prior}}$, both in $\mathcal{S}_d(\mathbb{R})$, balance the confidence in the image gradient term, and the confidence in the geometrical prior, respectively. In practice, we have

$$\mathbf{B}_{\text{img}} := \frac{\gamma}{\|\nabla_{\mathbf{x}} F_M(\cdot, t)\|_{\infty}^2} \mathbf{I}_d,$$

with \mathbf{I}_d the identity matrix in dimension d , $\gamma > 0$ a dimensionless user-defined parameter. $\mathbf{B}_{\text{prior}}$ is a diagonal matrix whose coefficients are given by the spacings of the image in its three spatial directions. The larger γ , the more confidence is given to the image gradient maximization. The third term of (2.6) is a regularization term penalizing the norm of the derivatives of the mapping $\psi - \tilde{\phi}_0$. The position observation is thus defined as $\psi_M: \Gamma_{\mathbb{R}} \times [0, T] \rightarrow \mathbb{R}^d$ such that

$$\psi_M(\cdot, t) := \arg \inf_{\psi} \mathcal{J}_t(\psi(\cdot)) \quad (2.7)$$

for all $t \in]0, T]$. Minimizing \mathcal{J}_t is equivalent to selecting a smooth surface among all possible surfaces resulting from the local maximization of the image gradient around $\tilde{\phi}$, see Figure 2.3.

The Euler-Lagrange equations yield the following necessary condition satisfied by ψ_M :

$$-\nabla_{\mathbf{x}\mathbf{x}} F_M(\psi_M) \mathbf{B}_{\text{img}}^{-1} \nabla_{\mathbf{x}} F_M(\psi_M) + \mathbf{B}_{\text{prior}}^{-1} (\psi_M - \tilde{\phi}) - \delta \Delta_{\xi} (\psi_M - \tilde{\phi}_0) = \mathbf{0}, \quad (2.8)$$

where the symbol $\nabla_{\mathbf{x}\mathbf{x}} F_M$ denotes the Hessian matrix of F_M .

Remark 1

As stated, the position observation operator behaves like an active contour method. The functional \mathcal{J}_t can be decomposed into an image-based energy, given by the two first terms, and an internal energy with the norm of the surface gradient. \square

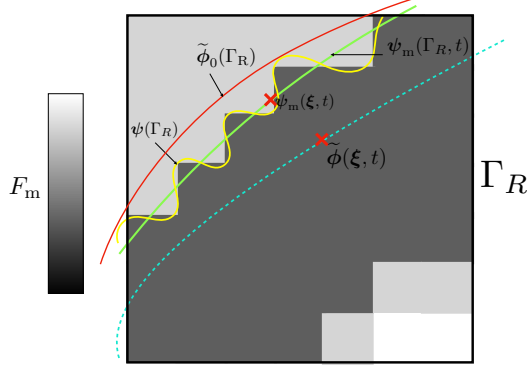


Figure 2.3: The position observer. On the image at $t \in [0, T]$, the maximization of the norm of the image gradient would result in the mapping ψ with high local curvature. Among all those maps, the regularizing constraint selects ψ_M . Having the trust region around $\tilde{\phi}$ enforces a selection of a specific extremal area.

Obtaining the observed mapping ψ_M directly from (2.8) would require to treat the non-linearity induced by the image gradient and Hessian term. In what follows, we propose a splitting procedure which mitigates the difficulties encountered either in a direct minimization of \mathcal{J}_t or in the resolution of the Euler-Lagrange equations. Note that the two first terms of \mathcal{J}_t in (2.6) treat independently points on $\psi(\Gamma_R)$ while the third couples nearby points on the surface. The proposed two-step approach reads as follows:

1. Minimization of a simplified cost functional $\tilde{\mathcal{J}}_t$ to generate an intermediate observation $\tilde{\psi}_M$:

$$\tilde{\psi}_M(\cdot, t) := \arg \inf_{\psi} \tilde{\mathcal{J}}_t(\psi(\cdot)), \quad (2.9)$$

with

$$\tilde{\mathcal{J}}_t: \psi \rightarrow \frac{1}{2} \int_{\Gamma_R} \left(-\|\nabla_{\mathbf{x}} F_M(\psi(\boldsymbol{\xi}), t)\|_{\text{B}_{\text{img}}}^2 + \|\psi(\boldsymbol{\xi}) - \tilde{\phi}(\boldsymbol{\xi}, t)\|_{\text{B}_{\text{prior}}}^2 \right) d\boldsymbol{\xi}. \quad (2.10)$$

2. Surface regularization that provides the end-of-step position observation ψ_M :

$$\psi_M - \tilde{\psi}_M - \delta \Delta_{\boldsymbol{\xi}}(\psi_M - \tilde{\phi}_0) = \mathbf{0}. \quad (2.11)$$

Some remarks are in order to motivate the above splitting approach as an alternative to (2.7).

We have $\mathcal{J}_t = \tilde{\mathcal{J}}_t + \mathcal{G}$, with

$$\mathcal{G}: \psi \rightarrow \frac{1}{2} \int_{\Gamma_R} \delta \|\nabla_{\boldsymbol{\xi}}(\psi - \tilde{\phi}_0)(\boldsymbol{\xi})\|^2 d\boldsymbol{\xi}.$$

The intermediate position observation $\tilde{\psi}_M$ returned by (2.9) does not satisfy *a priori* the optimality condition for \mathcal{J}_t , that is, $\partial_{\psi} \mathcal{J}_t(\tilde{\psi}_M) \neq \mathbf{0}$. Consequently, a descent

gradient method would suggest to move in the opposite direction of the gradient of \mathcal{J}_t , namely, $-\delta(\partial_\psi \tilde{\mathcal{J}}_t(\tilde{\psi}_M) + \partial_\psi \mathcal{G}(\tilde{\psi}_M)) = -\partial_\psi \mathcal{G}(\tilde{\psi}_M)$. The second step (2.11) performs such a gradient descent step from $\tilde{\psi}_M$, but with an implicit treatment of ψ_M in the Fréchet derivative term $\partial_\psi \mathcal{G}$.

2.2.3 Fully discrete formulation

In this section, we present the fully discrete counterpart of the continuous estimation problem introduced in the previous section, after temporal and spatial discretization.

2.2.3.1 Spatial and temporal discretization

The surface $\Gamma(t)$ is discretized in space by means of a triangular mesh with N_P points. The mesh points are uniquely identified by their indices $i \in \{0, \dots, N_P - 1\}$ and the motion of the surface $\Gamma(t)$ is assessed through the time-dependent positions $\{\mathbf{q}_i: [0, T] \rightarrow \mathbb{R}^d\}_{i=0, \dots, N_P-1}$ of its points. Let introduce the position $\mathbf{Q}(t) = (\mathbf{q}_0(t)^T \ \dots \ \mathbf{q}_{N_P-1}(t)^T) \in \mathbb{R}^{dN_P}$ and velocity $\mathbf{U}(t) = (\mathbf{u}_0(t)^T \ \dots \ \mathbf{u}_{N_P-1}(t)^T) \in \mathbb{R}^{dN_P}$ vectors. After discretization in space, the dynamics (2.5) yield the following linear ODE system:

$$\begin{cases} \dot{\mathbf{Q}} = \mathbf{U} & \text{in } [0, T], \\ \dot{\mathbf{U}} = \kappa \mathbf{K} (\mathbf{Q} - \tilde{\mathbf{Q}}^0) & \text{in } [0, T], \\ \mathbf{Q}(0) = \tilde{\mathbf{Q}}^0, \\ \mathbf{U}(0) = \tilde{\mathbf{U}}^0. \end{cases} \quad (2.12)$$

where $\kappa > 0$ is a user-defined parameter, $\tilde{\mathbf{Q}}^0, \tilde{\mathbf{U}}^0 \in \mathbb{R}^{dN_P}$ stands for the (unknown) initial location and velocity of the surface points and \mathbf{K} denotes the stiffness matrix of the surface Laplacian (which can be derived from a finite element approximation, or using spring-mass models [Mon99]). By introducing the full state of the system $\mathbf{X} := (\mathbf{Q}^T \ \mathbf{U}^T) \in \mathbb{R}^{2dN_P}$, system (2.12) can be recast into the general form

$$\dot{\mathbf{X}}(t) = \mathbf{A}\mathbf{X}(t) + \mathbf{R} \quad \text{in } [0, T], \quad (2.13)$$

with the notations

$$\mathbf{A} := \begin{pmatrix} 0 & I_{dN_P} \\ -\mathbf{K}(\kappa) & 0 \end{pmatrix}, \quad \tilde{\mathbf{X}}^0 := \begin{pmatrix} \tilde{\mathbf{Q}}^0 \\ \tilde{\mathbf{U}}^0 \end{pmatrix}, \quad \mathbf{R} := \begin{pmatrix} \mathbf{0} \\ \kappa \mathbf{K} \tilde{\mathbf{Q}}^0 \end{pmatrix}.$$

In the present work, we consider one-step time discretizations of (2.13) by means of implicit methods (Backward Euler or Crank-Nicolson), which yield the following time-marching scheme:

$$\begin{cases} \mathbf{X}^n = \mathbf{D}_{n|n-1} \mathbf{X}^{n-1} + \mathbf{R}^n, & 1 \leq n \leq N_T, \\ \mathbf{X}^0 = \tilde{\mathbf{X}}^0, \end{cases} \quad (2.14)$$

where, for instance, in the case of the Backward Euler scheme we have

$$\mathbf{D}_{n|n-1} = (\mathbf{I} - \Delta T \mathbf{A})^{-1}, \quad \mathbf{R}^n = (\mathbf{I} - \Delta T \mathbf{A})^{-1} \mathbf{R}.$$

Here, $\Delta T := T/N_T$ denotes the time-step length, with $N_T + 1$ the number of data samples available.

2.2.3.2 Discrete observation operator

The continuous position operator (2.9) and (2.11) is also discretized, so as to provide the observation of the mesh points location. For $n = 0, \dots, N_T$, the 4D MRI data is given in terms of the image sequences F_M^n and the Eulerian measured velocity \mathbf{u}_M^n as piecewise constant (scalar and vector, respectively) fields on a voxel grid of size $N_1 \times \dots \times N_d$. In what follows, the voxels are denoted by Ω_α and are uniquely identified by the multi-index $\alpha = (\alpha_1, \dots, \alpha_d) \in [1, N_1] \times \dots \times [1, N_d]$, as in the blue annotations of Figure 2.4 ($d = 2$). The gradient of F_M^n , noted $\nabla_{\mathbf{x}} F_M^n$, is approximated voxel-wise by means of a centered finite differences scheme. Both F_M^n and $\nabla_{\mathbf{x}} F_M^n$ are taken constant per voxel. The voxel values of \mathbf{u}_M^n are assigned to voxel centers, they are defined on a generic point of Ω via trilinear interpolation.

The position observations are evaluated by means of the two-step approach, as in Section 2.2.2:

1. The discrete image-gradient based cost functional counterpart of (2.10), noted $J_n(\tilde{\mathbf{q}}_i^n; \cdot)$ is minimized for voxel centers within a local window search for size $2L+1$ for each mesh point i to generate an intermediate observed position $\mathbf{q}_{i,M}^{n-}$. Note that the mesh points can be treated independently. The voxel window search for the minimization is introduced through the compact notation

$$B(\mathbf{k}, L) = \{\alpha = (\alpha_1, \dots, \alpha_d), \text{ s.t. } |k_j - \alpha_j| \leq L, \forall j\}, \quad (2.15)$$

with $L < \min_{k_d} \{(N_{k_d} - 1)/2\}$, and represents the set of voxel indices within the box centered in the voxel $\Omega_{\mathbf{k}}$, of size $(2L+1)$ in each direction. Let denote $\pi : \Omega \rightarrow [1, N_1] \times \dots \times [1, N_d]$ the function which associates to each point $\mathbf{x} \in \Omega$, the multi-index \mathbf{k}' of the voxel strictly containing \mathbf{x} . The minimization is performed by evaluating the cost functional on the centers \mathbf{c}_α of the voxels Ω_α . Hence, the intermediate observed position is $\mathbf{q}_{i,M}^{n-}(t) = \mathbf{c}_{\mathbf{k}^*}$ with

$$\mathbf{k}^* := \arg \min_{\mathbf{k} \in B(\pi(\tilde{\mathbf{q}}_i^n), \Delta N)} J_n(\tilde{\mathbf{q}}_i^n; \mathbf{c}_{\mathbf{k}}), \quad (2.16)$$

and

$$J_n(\tilde{\mathbf{q}}_i^n; \cdot) : \Omega \rightarrow \mathbb{R} \\ \mathbf{x} \mapsto -\gamma \frac{\|\nabla_{\mathbf{x}} F_M^n(\mathbf{x})\|^2}{\|\nabla_{\mathbf{x}} F_M^n\|_\infty^2} + \|\mathbf{x} - \tilde{\mathbf{q}}_i^n\|_{\mathbb{B}_{\text{prior}}}^2. \quad (2.17)$$

$\mathbb{B}_{\text{prior}} \in \mathcal{S}_d(\mathbb{R})$ is the same as in the space continuous problem, see Section 2.2.2. (2.10) does not explicitly couple the position of points on the surface.

2. The end-of-step observation $\mathbf{q}_{i,M}^n$ is computed by applying the discrete regularization:

$$\mathbf{Q}_M^n - \mathbf{Q}_M^{n-} = -\delta \mathbf{K}_{\text{obs}} \cdot (\mathbf{Q}_M^n - \tilde{\mathbf{Q}}^0), \quad (2.18)$$

with $\mathbf{Q}_M^n = ((\mathbf{q}_{0,M}^n)^T \dots (\mathbf{q}_{N_P-1,M}^n)^T) \in \mathbb{R}^{dN_P}$, $\mathbf{Q}_M^{n-} = ((\mathbf{q}_{0,M}^{n-})^T \dots (\mathbf{q}_{N_P-1,M}^{n-})^T) \in \mathbb{R}^{dN_P}$ and $\mathbf{K}_{\text{obs}} := \kappa_{\text{obs}} \mathbf{K} \in \mathbb{R}^{dN_P \times dN_P}$. The diffusion step (2.18) is performed with the same discretization as introduced in Section 2.2.3.1.

The complete state observation $\mathbf{Z}^n \in \mathbb{R}^{2dN_P}$ is thus given by

$$\mathbf{Z}^n = \begin{pmatrix} \mathbf{Q}_M^n \\ \mathbf{U}_M^n \end{pmatrix},$$

with $\mathbf{U}_M^n = (\mathbf{u}_M^n(\mathbf{q}_{0,M}^n)^T \dots \mathbf{u}_M^n(\mathbf{q}_{N_P-1,M}^n)^T) \in \mathbb{R}^{dN_P}$.

Problem (2.19)-(2.20) can be solved using either variational or sequential approaches (see, e.g., [Moi18]). On the one hand, variational methods (and more specifically 4D-VAR approaches) search for the optimal control (initial condition) such that the resulting estimation best fits all the observations. To this purpose, one may solve the associated Euler-Lagrange equations, or apply an optimization algorithm to find the saddle point of the associated Lagrangian. On the another hand, sequential estimation techniques such as the Kalman filter improve the current state estimation as observations are provided. In case where the model and the observations are both linear, the estimation returned at a certain time by a (linear) Kalman filter is the best linear estimation given the observations provided up to that time. All observations are thus integrated in the estimation only at the final time for Kalman filter. Linear Kalman filter and 4D-VAR approaches return the same state estimation, only at final time [Moi08b].

2.3 State estimation via Kalman filter

In this section, we briefly review the main features of the Kalman filter [Kál60, KB61] then we build on it to formulate the sequential estimation counterpart of (2.19)-(2.20).

2.3.1 Kalman filter

When the model describing the evolution of the state is linear, as Eq.(2.20), and the observations \mathbf{Z}^n are linear in the state, the Kalman filter provides an optimal estimation of the state.

Algorithm 1 (Simplified) Linear Kalman Filter

Require: $(\hat{\mathbf{X}}^0; \mathbf{P}_0)$, $(\mathbf{D}_{n|n-1}, \mathbf{R}_{n=0, \dots, N_T}; \mathbf{W}_{\text{model}})$, $(\mathbf{Z}^n; \mathbf{W}_{\text{obs}})$
for $n = 1, \dots, N_T$ **do**
 Prediction: $(\hat{\mathbf{X}}^{n-1}, \mathbf{P}_{n-1}) \rightarrow (\hat{\mathbf{X}}^{n-}, \mathbf{P}_{n-})$
 $\hat{\mathbf{X}}^{n-} \leftarrow \mathbf{D}_{n|n-1} \hat{\mathbf{X}}^{n-1} + \mathbf{R}^n$
 $\mathbf{P}_{n-} \leftarrow \mathbf{D}_{n|n-1} \mathbf{P}_{n-1} \mathbf{D}_{n|n-1}^T + \mathbf{W}_{\text{model}}$
 Correction: $(\mathbf{Z}^n, \mathbf{W}_{\text{obs}}, \hat{\mathbf{X}}^{n-}, \mathbf{P}_{n-}) \rightarrow (\hat{\mathbf{X}}^n, \mathbf{P}_n)$
 $\mathbf{S}_n \leftarrow \mathbf{P}_{n-} + \mathbb{W}_{\text{obs}}$
 \mathbf{K}_n^T is solution of $\mathbf{S}_n^T \chi = \mathbf{P}_{n-}^T$, χ being the unknown.
 $\hat{\mathbf{X}}^n \leftarrow \hat{\mathbf{X}}^{n-} + \mathbf{K}_n (\mathbf{Z}^n - \hat{\mathbf{X}}^{n-})$
 $\mathbf{P}_n \leftarrow (\mathbf{I} - \mathbf{K}_n) \mathbf{P}_{n-}$
end for
return $(\hat{\mathbf{X}}^n, \mathbf{P}_n)$, $n = 1, \dots, N_T$

The Kalman filter presented in Algorithm 1, and whose main steps are described below, will be directly applied to our specific case.

Initialization To initialise the method, we need to provide an initial prior state $\hat{\mathbf{X}}^0 = ((\hat{\mathbf{Q}}^0)^T \quad (\hat{\mathbf{U}}^0)^T)^T \in \mathbb{R}^{2dN_P}$ and its associated covariance matrix $\mathbf{P}_0 \in$

$\mathbb{R}^{2dN_p \times 2dN_p}$. Its interpretation is the following: the prior can be written as $\mathbf{X}^0 + \eta^0$, where $\mathbf{X}^0 = \mathbf{X}(0)$ is the real (unknown) initial state and η^0 is a random variable such that $\mathbb{E}[\eta^0] = \mathbf{0}$ and of $\mathbb{E}[(\eta^0)^T(\eta^0)] = \mathbf{P}_0$. In the present context, $\hat{\mathbf{Q}}^0$ defines the prior on the initial position the mesh points and $\hat{\mathbf{U}}^0$ their associated initial velocity.

Prediction At time t_n , given the best state estimation at previous time as well as its associated covariance, $\hat{\mathbf{X}}^{n-1} = ((\hat{\mathbf{Q}}^{n-1})^T \ (\hat{\mathbf{U}}^{n-1})^T)^T$, we compute a prediction, denoted by $\hat{\mathbf{X}}^{n-}$ and the so called *a priori* covariance matrix \mathbf{P}_n^- by exploiting the model:

$$\begin{cases} \hat{\mathbf{X}}^{n-} &= \mathbf{D}_{n|n-1} \hat{\mathbf{X}}^{n-1} + \mathbf{R}^n, \\ \mathbf{P}_n^- &= \mathbf{D}_{n|n-1} \mathbf{P}_{n-1} \mathbf{D}_{n|n-1}^T + \mathbf{W}_{\text{model}}, \end{cases}$$

where the symbol $\mathbf{W}_{\text{model}} \in \mathbb{R}^{2dN_p \times 2dN_p}$ stands for the model error covariance matrix.

Correction In its classical formulation, we write the estimation of the state at time instant t_n , denoted by $\hat{\mathbf{X}}^n$, as a correction of the prediction provided by the model, $\hat{\mathbf{X}}^{n-}$. The correction term depends upon the discrepancy, namely $(\mathbf{Z}^n - \hat{\mathbf{X}}^{n-})$. The correction step takes the form:

$$\hat{\mathbf{X}}^n = \hat{\mathbf{X}}^{n-} + \mathbf{K}_n (\mathbf{Z}^n - \hat{\mathbf{X}}^{n-}), \quad (2.22)$$

where \mathbf{K}_n is called the Kalman filter gain. Note that the general formulation of the linear Kalman filter considers the observation $\mathbf{Z} = \mathbf{H}\mathbf{X} + \eta$ as a linear function of the state \mathbf{X} , with \mathbf{H} usually a rectangular matrix and η a white noise. Here, \mathbf{H} is the identity. The covariance matrix $\mathbf{W}_{\text{obs}} \in \mathbb{R}^{2dN_p \times 2dN_p}$ quantifies the uncertainty in the observation. Its expression is derived from the precision of the position observer, and the noise in the measured velocity. The most expensive part of the correction step is the calculation of \mathbf{K}_n in Algorithm 1. In a vast majority of applications, \mathbf{K}_n is of smaller size since the observation is of lower dimension than the state. Here, calculating \mathbf{K}_n might require a significant amount of memory and computational time, depending on the size of the state vector.

2.3.2 Proposed estimation algorithm

Implicit-Explicit model prediction. In the present work we discretised in time the model equations Eq.(2.13) by means of implicit schemes (Backward Euler or Crank-Nicolson). In the case of the Backward Euler scheme this would lead to a prediction step of the form:

$$\begin{aligned} \mathbf{D}_{n|n-1} &= (\mathbf{I} - \Delta T \mathbf{A})^{-1}, \\ \mathbf{R}^n &= (\mathbf{I} - \Delta T \mathbf{A})^{-1} \mathbf{R}, \\ \hat{\mathbf{X}}^{n-} &= \mathbf{D}_{n|n-1} \hat{\mathbf{X}}^{n-1} + \mathbf{R}^n. \end{aligned} \quad (2.23)$$

From a practical point of view, computing the update of the state just involves the resolution of a sparse linear system, which can be performed efficiently. The covariance update, however, will be computationally very expensive, as it would involve the resolution of $4d \cdot N_p$ linear systems. This is the reason why, in the present

work, we propose to update the covariance by means of an explicit scheme. We will refer to this approximation as *implicit-explicit prediction*.

In particular, let $D_{n|n-1}^{(exp)} = I + \Delta T A$, the update of the covariance matrix reads:

$$P_{n-} = D_{n|n-1}^{(exp)} P_{n-1} [D_{n|n-1}^{(exp)}]^\top + W_{\text{model}} \quad (2.24)$$

The covariance matrix of the model error W_{model} is calculated from the assumption that the model error results from a white noise in acceleration whose covariance matrix is $\sigma_a^2 I_{dN_p}$. Consequently we propose an approximation² of model error covariance matrix, given by:

$$W_{\text{model}} = \sigma_a^2 \begin{pmatrix} \frac{\Delta T^4}{4} I_{dN_p} & \frac{\Delta T^3}{2} I_{dN_p} \\ \frac{\Delta T^3}{2} I_{dN_p} & \Delta T^2 I_{dN_p} \end{pmatrix}. \quad (2.25)$$

Remark 2

We propose a reasonable order of magnitude for σ_a from the expression of $W_{\text{model}}(\sigma_a)$. In fact, the noise in acceleration induces an error on the position $\Delta T^2 \sigma_a / 2$ which could be of the order of some voxels spacing $N \sqrt{h_1^2 + \dots + h_d^2}$. In such a case, it would have a significant effect on the reconstruction compared to the observation error introduced by (2.16). This yields to the approximation

$$\sigma_a \sim 2N \sqrt{h_1^2 + \dots + h_d^2} / \Delta T^2. \quad (2.26)$$

This heuristics provides a first evaluation of the order of magnitude, which has proven to work for the synthetic test case and the application to real data in Section 2.4.

Generating the prior \tilde{Q}^n As explained previously, the observation at iteration n depends on \tilde{Q}^n which is yet to be determined. Since \tilde{Q}^n is a prior value for the state at iteration n , a reasonable guess could come from the model prediction. Given \hat{X}^{n-1} the prior for the local maximization of the image gradient is set to $B_{n|n-1}^{-1} (\hat{X}^{n-1} + R^n)$ or equivalently $B_{n|n-1} \tilde{Q}^n = \hat{X}^{n-1} + R^n$. Consequently, the observation is given by

$$Z^n = \mathcal{F}_{\text{obs}} \left(F_M^n, u_M^n, B_{n|n-1}^{-1} (\hat{X}^{n-1} + R^n), \gamma, \Delta N, \delta, \kappa_{\text{obs}} \right),$$

taking up the notation introduced in Section 2.2.3.1. Note that $B_{n|n-1}$ is not actually inverted, we solve the associated linear system instead.

The Kalman filter requires the user to specify the following parameters:

- For the model: $\sigma_a > 0$, directly associated to the norm of W_{model} from (2.25). Through (2.26), an order of magnitude of the σ_a is provided.
- For the observation: $\sigma_q > 0$ and $\sigma_p > 0$, parameters for the covariance matrix $W_{\text{obs}} \in \mathbb{R}^{2dN_p \times 2dN_p}$:

$$W_{\text{obs}} = W_{\text{obs}}(\sigma_q, \sigma_p) = \begin{pmatrix} (\sigma_q D_{N_p})^2 & 0 \\ 0 & \sigma_p^2 I_{dN_p} \end{pmatrix}.$$

²This approximation results from the propagation of a noise in acceleration for a zero-acceleration dynamical equation, that is to say $\ddot{q} = a$, with a a white noise.

Algorithm 2 Full algorithm

Require: $(\hat{\mathbf{X}}^0; \mathbf{P}_0)$, $(\mathbf{A}_{n|n-1}, \mathbf{R}_{n=0, \dots, N_T}; \mathbf{W}_{\text{model}})$, \mathbf{W}_{obs}
for $n = 1, \dots, N_T$ **do**
 Generate observation $\mathbf{Z}^n = \mathcal{F}_{\text{obs}} \left(F_{\text{M}}^n, \mathbf{B}_{n|n-1}^{-1} \left(\hat{\mathbf{X}}^{n-1} + \mathbf{R}^n \right), \gamma, \Delta N, \delta, \kappa_{\text{obs}} \right)$
 Apply Prediction: $(\hat{\mathbf{X}}^{n-1}, \mathbf{P}_{n-1}) \rightarrow (\hat{\mathbf{X}}^{n-}, \mathbf{P}_{n-})$ from Algorithm 1
 Apply Correction: $(\mathbf{Z}^n, \mathbf{W}_{\text{obs}}, \hat{\mathbf{X}}^{n-}, \mathbf{P}_{n-}) \rightarrow (\hat{\mathbf{X}}^n, \mathbf{P}_n)$ from Algorithm 1
end for
return $(\hat{\mathbf{X}}^n, \mathbf{P}_n)$, $n = 1, \dots, N_T$

$\mathbf{D}_{N_{\text{p}}} = \text{diag}(\mathbf{D}, \dots, \mathbf{D}) \in \mathbb{R}^{dN_{\text{p}} \times dN_{\text{p}}}$ denotes the block diagonal matrix defined with the spacing matrix of the image data, $\mathbf{D} = \text{diag}(\delta_0, \dots, \delta_{d-1}) \in \mathbb{R}^{d \times d}$. For $i = 0, \dots, d-1$, δ_i is the image spacing along the i -th axis.

- For the initial configuration: $\sigma_{P_0,q} > 0$ and $\sigma_{P_0,p} > 0$, parameters of the covariance matrix $\mathbf{P}_0 \in \mathbb{R}^{2dN_{\text{p}} \times 2dN_{\text{p}}}$:

$$\mathbf{P}_0 = \mathbf{P}_0(\sigma_{P_0,q}, \sigma_{P_0,p}) = \begin{pmatrix} (\sigma_{P_0,q} \mathbf{D}_{N_{\text{p}}})^2 & 0 \\ 0 & \sigma_{P_0,p}^2 \mathbf{I}_{dN_{\text{p}}} \end{pmatrix}.$$

Unlike σ_p and $\sigma_{P_0,p}$, the user-defined parameters σ_q and $\sigma_{P_0,q}$ are dimensionless and their values represent pixel radius of trust regions. In addition to the Kalman filter parameters, specific parameters must be specified:

- For the model (prediction): the elasticity parameter $\kappa \geq 0$.
- For the observation: $\gamma > 0$, $\Delta N \in \mathbb{N}^*$ the size of the local search window. Those parameters will be fixed. Intuitively the values prescribed should depend on the quality of the image. For the elasticity equation: the parameters $\kappa_{\text{obs}} \geq 0$, or rather the product $\kappa_{\text{obs}} \delta \geq 0$.

One can refer to Figure 2.5 for an overview of the parameters.

Some of the parameters depends on the data quality.

2.4 Numerical experiments

The purpose of this section is to illustrate the capabilities of Algorithm 2 by means of numerical experiments. The proposed test cases also aim to assess the sensitivity of the method to free parameters (see Tables 2.1 and 2.2) and noisy data. We consider two test cases. The first one (Section 2.4.1) is based on synthetic data and the second (Section 2.4.2) uses real data from 4D-flow MRI exam of a human aorta.

The precision of the surface segmentation is evaluated through the Dice coefficient, a metric used in image segmentation to compare the level of similarity of two segmentations. For \mathcal{X} the ground truth segmentation, and \mathcal{X}' another segmentation, both represented by collections of voxels, the Dice coefficient is given by the relation

$$\text{Dice}(\mathcal{X}, \mathcal{X}') := \frac{\text{card}(\mathcal{X} \cap \mathcal{X}')}{\text{card}(\mathcal{X}) + \text{card}(\mathcal{X}')},$$

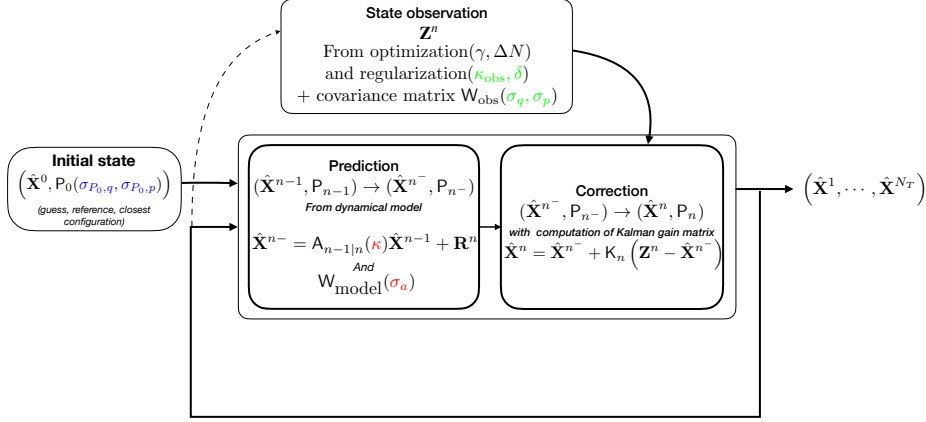


Figure 2.5: The parameters of the Kalman filter and the state observation.

where card stands for the cardinality of a set. In the synthetic test case, another complementary approach is proposed to account for the quality of the point-to-point tracking. It is essential to note that a good surface reconstruction (Dice coefficient close to 1) does not necessarily mean a good point tracking. If we consider the example of a circle rotating on itself, mesh points with a very fine resolution have a rotating motion while the surface would be apparently motionless on images. Standard surface reconstruction methods are not able to detect the motion of the circle on itself, unless additional kinematic information is processed. The tracking that we propose does not only perform a surface reconstruction, but it also provides the local displacement of the surface. Algorithm 2 has been implemented using the standard C++ libraries, and the Eigen library for linear algebra operations [GJ⁺10]. The VTK library has also been intensively used for handling images and geometrical objects [SML06].

2.4.1 Tracking of a vesicle immersed in a lid-driven cavity flow

In this example, we consider the tracking of the motion of an elastic vesicle immersed in a lid-driven cavity flow (see Figure 2.6). The bi-dimensional motion of the vesicle is more complex than the deformation of the aorta under the pulsatile blood flow. Synthetic image data are generated from numerical simulations of the corresponding dynamical system. In particular, the simulated Eulerian velocity field is extracted so as to mimic 4D MRI flow series. Algorithm 2 is then used to retrieve the motion of the vesicle from the generated synthetic data. We investigate the sensitivity of the reconstruction considering the data quality (image, velocity measurements) and the regularization parameters.

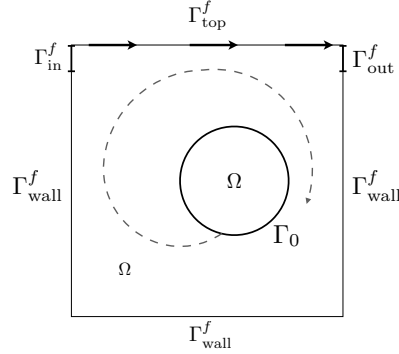


Figure 2.6: Geometrical configuration.

2.4.1.1 Data generation

The considered dynamical system can be modelled by a non-linear fluid-structure interaction model (see, e.g., [BKFG19] for the details). The fluid is initially at rest and occupies the domain $\Omega := [0, 1] \times [0, 1]$. The vesicle is also initially at rest and has the shape of a circle centered at $(0.6, 0.5)$ with radius 0.2. All the units are given in the CGS unit system. The fluid is described by the incompressible Navier-Stokes equations, while a non-linear Reissner-Mindlin beam model in Lagrangian formalism is considered for the vesicle. The physical parameters for the fluid are: $\rho^f = 100$, $\nu = 10$, and for the solid equation $\rho^s = 100$, the Young Modulus $E = 5.6 \times 10^3$ and the Poisson's ratio $\nu = 0.4$. The boundary conditions on $\partial\Omega := \Gamma_{\text{wall}}^f \cup \Gamma_{\text{in}}^f \cup \Gamma_{\text{out}}^f \cup \Gamma_{\text{top}}^f$ (see Figure 2.6) are the following: no-slip boundary conditions on $\Gamma_{\text{top}}^f \cup \Gamma_{\text{wall}}^f$, zero traction on $\Gamma_{\text{in}}^f \cup \Gamma_{\text{out}}^f$, constant velocity equal to 1 on Γ_{top}^f . Synthetic data has been generated by simulating 4000 time steps, of length $\Delta T_0 = 5.0 \times 10^{-3}$, using the numerical method proposed in [BKFG19] with a fluid mesh made of 12800 triangular elements and 19360 edges, and a solid mesh made of 160 edges.

Some snapshots of the fluid velocity magnitude and solid deformation are given in Figure 2.7. The vesicle deforms and rotates within the fluid cavity.

From the solid displacement, the grayscale image frames $\{F_{\text{M}}^n\}_{n=0, \dots, N_T-1}$ of the vesicle in motion are generated, with a sampling time length $\Delta T = 20 \times \Delta T_0$, which represents the temporal resolution of the images. It results in $N_T = 200$ image frames. The pixel grid dimension is 80×80 with an isotropic spacing $h_1 = h_2 = 0.0125$. In fact, two adjacent triangles in the mesh of the cavity combine into one square, defining a pixel, as shown in Figure 2.8. This sets the image resolution. In order to generate the grayscale image at a time-step $n \in \{0, \dots, N_T - 1\}$, we first assign one value among $\{0, 200\}$ to each pixel depending on its location with respect to the vesicle Γ^n . Pixels that cut the vesicle are considered inside the vesicle. Pixels located inside the vesicle are assigned the maximum value 200, and those strictly outside have a value 0. The resulting binary image $F_{\text{M},0}^n$ at the time step n thus

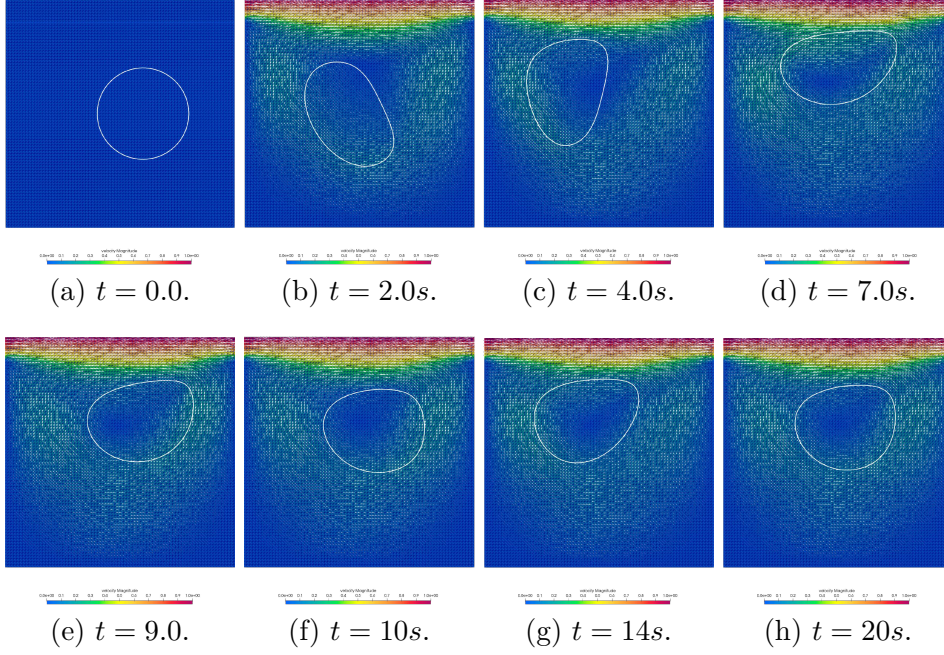


Figure 2.7: Data generation - Motion of the immersed vesicle, from FSI simulations.

writes

$$F_{M,0}^n: \{\Omega_{\alpha=(\alpha_1,\alpha_2)} \text{ s.t. } (\alpha_1, \alpha_2) \in [1, 80] \times [1, 80]\} \longrightarrow \{0, 200\}$$

$$(\Omega_{\alpha}, t) \longmapsto \begin{cases} 200, & \text{if } c_{\alpha} \text{ is inside } \Gamma^n \\ 0 & \text{otherwise,} \end{cases} \quad (2.27)$$

where $\{\Omega_{\alpha}, \alpha \in [1, 80] \times [1, 80]\}$ is the voxel grid covering Ω , c_{α} the center of a voxel Ω_{α} .

$F_{M,0}^n$ is then blurred to generate a grayscale image $F_{M,1}^n$ using a Gaussian filter implemented in the VTK library `vtkImageGaussianSmooth`³. The filter consists in a convolution with a 2D gaussian kernel⁴ as follows:

$$K_{2D}(i,j) := \frac{1}{2\pi\sigma_1\sigma_2} \exp \left[- \left(\frac{i^2}{2\sigma_1^2} + \frac{j^2}{2\sigma_2^2} \right) \right]$$

$$= \underbrace{\frac{1}{\sqrt{2\pi}\sigma_1} \exp \left(- \frac{i^2}{2\sigma_1^2} \right)}_{:=K_{1D}^{(1)}(i)} \underbrace{\frac{1}{\sqrt{2\pi}\sigma_2} \exp \left(- \frac{j^2}{2\sigma_2^2} \right)}_{K_{1D}^{(2)}(j)},$$

for $i \in \{-R_1, -R_1 + 1, \dots, R_1\}$ and $j \in \{-R_2, -R_2 + 1, \dots, R_2\}$, $R_1, R_2 \in \mathbb{N}^*$. For a voxel labelled $\alpha = (\alpha_1, \alpha_2)$, the evaluation of $F_{M,1}^n$ is given by :

³Detailed implementation on <https://github.com/Kitware/VTK/blob/master/Imaging/General/vtkImageGaussianSmooth.cxx>

⁴see `vtkImageGaussianSmooth`

$$\begin{aligned}
F_{M,1}^n(\alpha_1, \alpha_2) &= [F_{M,0}^n * K_{2D}](\alpha_1, \alpha_2) \\
&= \sum_{i=-R_1}^{R_1} \sum_{j=-R_2}^{R_2} F_{M,0}^n(\alpha_1 - i, \alpha_2 - j) K_{2D}(i, j) \\
&= \sum_{i=-R_1}^{R_1} [F_{M,0}^n * K_{1D}^{(2)}](\alpha_1 - i, \alpha_2) K_{1D}^{(1)}(i) \\
&= \sum_{i=-R_2}^{R_2} [F_{M,0}^n * K_{1D}^{(1)}](\alpha_1, \alpha_2 - j) K_{1D}^{(2)}(j),
\end{aligned} \tag{2.28}$$

where $*$ denotes the convolution product. Note the abuse of notation for $F_{M,0}^n, F_{M,1}^n$, since the voxel label is assimilated to the voxel itself. VTK adds a normalization to the gaussian kernel. The kernel size parameters $R_k, k = 1, 2$ depend on the parameters σ_k with the relation $R_k = 2\lceil\sigma_k R'\rceil + 1$, R' being a radius factor. The gaussian blur is performed with $\sigma_1 = \sigma_2 = \sigma$ and $R' = 1$. The standard deviation σ is expressed in pixel units. The main purpose of the gaussian kernel is to reduce the gradient gap across the contours, hence artificially degrading the performance of the image gradient maximization. The larger σ , the more challenging an accurate contour detection might be. Gradient artefacts are finally added to $F_{M,1}^n$, as it may occur with 4DMRI, using a gaussian noise with null-expected value and a standard deviation of 5% of 200, providing the image F_M^n .

The eulerian velocity field \mathbf{u}_M is composed of the exact velocity inside the cavity Ω , with an additive gaussian noise $\boldsymbol{\eta}$ with $\mathbf{0}$ -mean and $\sigma_v^2 \mathbf{I}_2$ covariance matrix. The evaluation of \mathbf{u}_M at any point inside the cavity is approximated by linear interpolation before adding the gaussian noise.

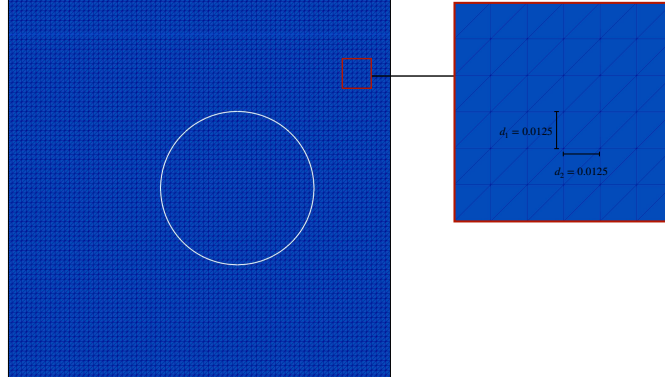


Figure 2.8: Data generation - The mesh of the cavity, with the initial geometrical configuration of the real vesicle.

Initial configuration. The initial configuration for the tracking is given by a mesh composed of $N_P = 16$ equally distributed points $\{\hat{\mathbf{q}}_i^0\}_{i=0, \dots, N_P}$ along an ellipse centered at $(0.65, 0.42)$ of semi-major axis 0.22 and semi-minor axis 0.2, see Figure 2.9. The center of the ellipse has been translated by a vector $(0.05, -0.08)$ with respect to the center of the real initial configuration, such that the Dice coefficient

at the initialization is 0.72. The time resolution is $\Delta T = 0.1$, $N_T = 200$. A finer time integration is used for the model (2.23), namely 0.001, as mentioned in Section 2.3.2.

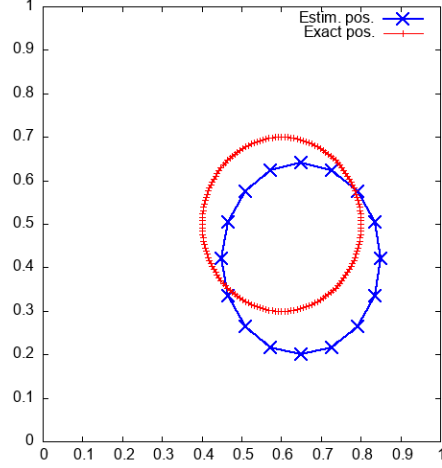


Figure 2.9: Initial configuration. In red, the initial position of the real vesicle. In blue, the initial mesh given to the filter for reconstruction.

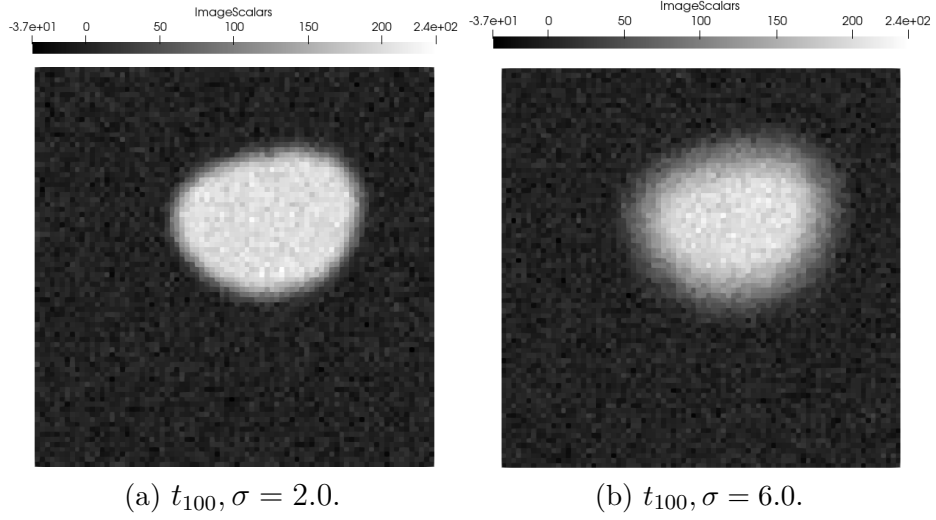
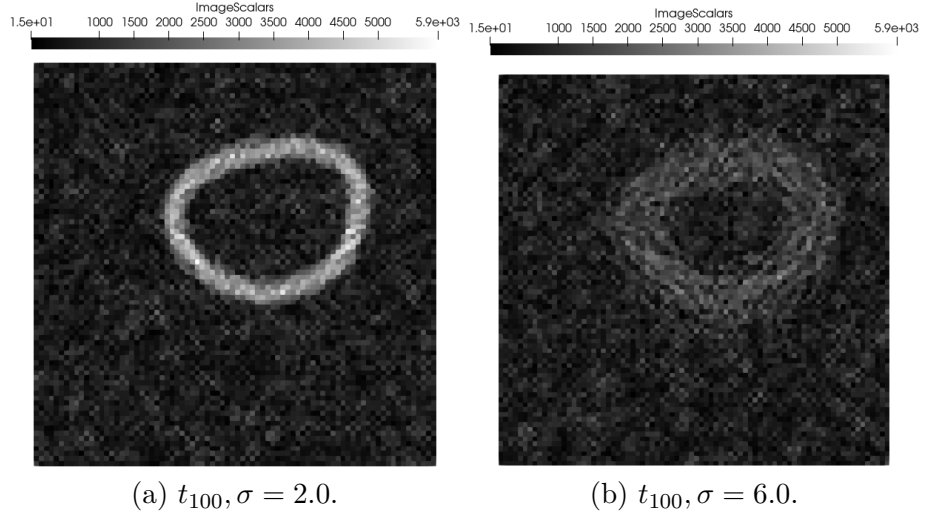
2.4.1.2 Sensitivity to data quality

The sensitivity of the filter with respect of the level of blur σ in the images is investigated for different values of the velocity noise σ_v . The blur parameter σ controls the diffusion of the gradient extremal values, so that large values of σ makes the observation of the surface position more challenging. The data quality thus depends on σ and σ_v . The parameters of the simulations are given in Table 2.1.

Data quality		Intialization		Model		Observation				
σ	σ_v	$\sigma_{P_{0,q}}$	$\sigma_{P_{0,p}}$	κ	σ_a	γ	ΔN	$\kappa_{\text{obs}}\delta$	σ_q	σ_p
{2.0, 6.0}	{0.003, 0.03, 0.075, 0.105}	$10h_x$	0.1	10	5.0	100	30	0.1	{1.5, 2.5, 3.0}	σ_v

Table 2.1: Parameters for the first synthetic test case.

The simulations are performed with $\sigma = 2.0, 6.0$ (see Figures 2.10 and 2.11) and $\sigma_v = 0.003, 0.03, 0.075, 0.105$. The values of σ_v simulate respectively 1%, 10%, 25% and 35% of the half range of variation of the highest component of \mathbf{u}_M^n in an area around the vesicle, for all time steps. Here, that half range corresponds to 0.30. Those percentages deem as an appreciation of the estimated level of noise in the flow series, see Figures 2.12. Depending on the level of blur, the precision σ_q of the position observation operator is adapted accordingly. For $\sigma = 2.0, 6.0, 8.0$, we respectively set $\sigma_q = 1.5, 2.5, 3.0$. Since running two simulations with a same set of parameters $(\sigma, \sigma_q, \sigma_v)$ would provide slightly different estimates due to the noisy data, the instantaneous Dice coefficients are averaged over 100 simulations

Figure 2.10: Noisy images with $\sigma = 2.0, 6.0$.Figure 2.11: Gradient magnitude images with $\sigma = 2.0, 6.0$.

to provide representative indices. In addition to measuring the accuracy of the surface segmentation with the evolution of the dice coefficient, we also check the point-to-point tracking on single simulations. For $n \geq 1$, the exact position of the tracked surface Γ^n is discretized in terms of a set of points $\{\mathbf{q}_j^n\}_{j=0, \dots, N_E}$, and $\{\hat{\mathbf{q}}_i^n\}_{i=0, \dots, N_P}$ denote the estimation provided by Algorithm 2. The quality of the point-to-point tracking of Γ^n by $\{\hat{\mathbf{q}}_i^n\}_{i=0, \dots, N_P}$ is measured by comparing the trajectories of two points whose labels $i_{\min}, i_{\max} \in \{0, \dots, N_P\}$ respectively to the trajectories of $j_{\min}, j_{\max} \in \{0, \dots, N_E\}$. i_{\min}, i_{\max} are defined as follows:

$$i_{\min} := \arg \min_{i \in \{0, \dots, N_P\}} d(\hat{\mathbf{q}}_i^{N_T}, \Gamma^{N_T}), \quad i_{\max} := \arg \max_{i \in \{0, \dots, N_P\}} d(\hat{\mathbf{q}}_i^{N_T}, \Gamma^{N_T}),$$

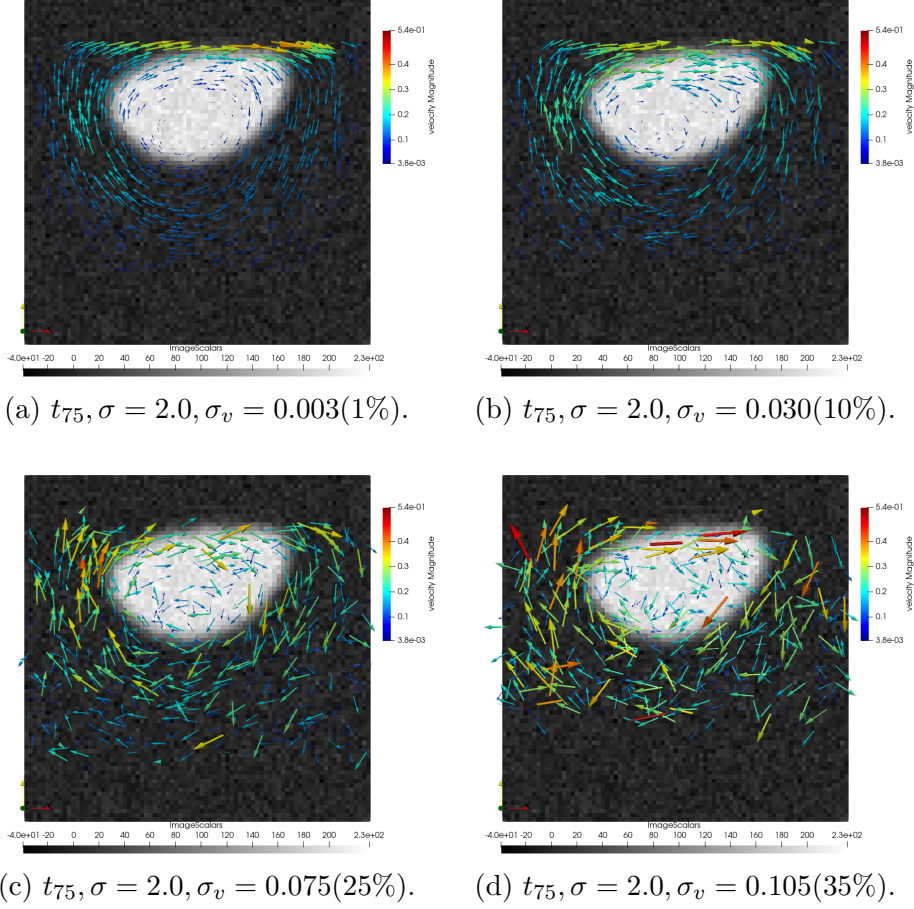


Figure 2.12: The velocity field around the vesicle, images with $\sigma = 2.0$ and $\sigma_v = 0.003, 0.030, 0.075, 0.105$.

where the symbol $d(\mathbf{q}, S)$ indicates the distance between the surface S and the point \mathbf{q} . j_{\min} and j_{\max} are the labels of the closed-point projections on Γ^{N_T} of the points $\hat{\mathbf{q}}_{i_{\min}}^{N_T}$, respectively $\hat{\mathbf{q}}_{i_{\max}}^{N_T}$. Note that, the discrete trajectories $\{\hat{\mathbf{q}}_{i_{\min}}^n\}_{n=1, \dots, N_T}$ and $\{\hat{\mathbf{q}}_{i_{\max}}^n\}_{n=1, \dots, N_T}$ respectively represent the best and worst choice for error quantification. When using Kalman filter, the presumably tracked point on Γ^{N_T} by $\{\hat{\mathbf{q}}_i^n\}_{i=0, \dots, N_p}$ can only be assessed at the final iteration. In fact, the linear Kalman filter estimation improves as observations are provided, which makes it the most accurate at final iteration. In the result section, the plots of the discrete trajectories $\{\hat{\mathbf{q}}_{i_{\min}}^n\}_{n=1, \dots, N_T}$ compared to $\{\mathbf{q}_{j_{\min}}^n\}_{n=1, \dots, N_T}$ is referred as "min" trajectories, and $\{\hat{\mathbf{q}}_{i_{\max}}^n\}_{n=1, \dots, N_T}$ compared to $\{\mathbf{q}_{j_{\max}}^n\}_{n=1, \dots, N_T}$ as "max" trajectories.

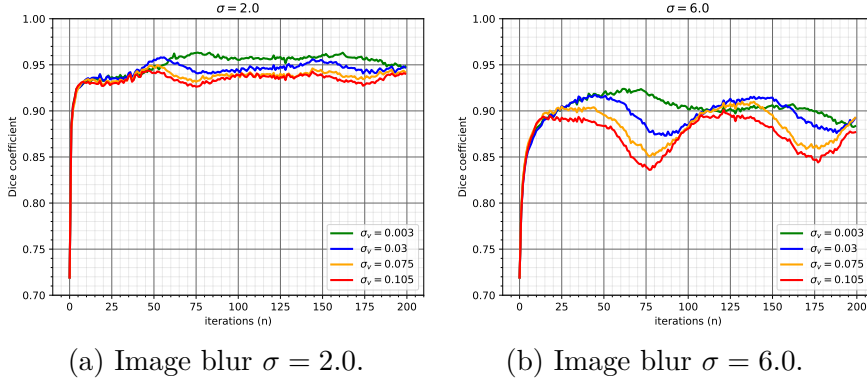
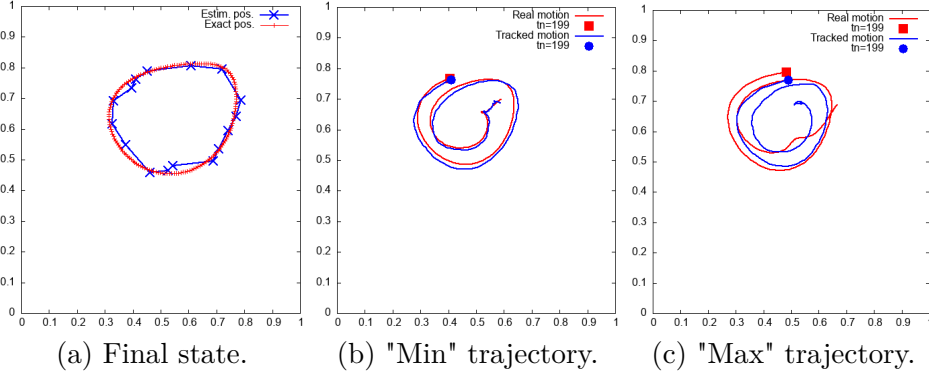
Choice of the free parameters The parameters σ and σ_v are used in this test case to control the data quality. However the user-defined parameter σ_p is given to the Kalman filter as an expected level of noise in the velocity data. We assume that at each time, the noise in each velocity component is gaussian with a standard

deviation σ_p . Here due to the specific synthetic case, we already have $\sigma_p = \sigma_v$, but in real application, this parameter has to be calculated by the user. Even if the noise of the velocity has a very complex origin and structure, a reasonable value for σ_p can be proposed by calculating the standard deviation of the velocity field in a region of the image known to be a white noise area. The parameters to quantify the level of confidence that we have in the initialization are $\sigma_{P_0,q}$ and $\sigma_{P_0,p}$. $\sigma_{P_0,q}$ is expressed in voxel/pixel units. Depending on the origin of the initial configuration, it can be taken more or less close to 1. In the vesicle test case, it is taken quite large, because we force a bias of the initial configuration compared to the real one. When it comes to the aorta, we recommend a value between 1-3 depending whether the initial configuration has been segmented from one time instant in 4D-flow MRI sequences, or from a derived image MRA sequence. This value can be coarsely by evaluating (half of) the error of positioning on the initial configuration provided by the user, compared to the real initial position of the aorta observed on the 4D MRI sequence at time t_0 . $\sigma_{P_0,q}$ has to be taken very high, because the default initial value for the velocity of the aortic wall is null. We have no reasonable estimation of the initial velocity of the aortic wall. The critical parameters of the method are the model parameters. The parameter κ models the vessel elasticity in a simplified way and contributes to regularize the prediction of the wall motion. σ_a is proportional to the norm of the model error covariance matrix W_{model} and ponders the confidence in the model prediction compared to the confidence in the observation. The larger κ is, the more rigid the predicted surface will be. Ultimately, compared to standard semi-automatic segmentation method, few parameters have an incidence on the quality of the tracking, and even for those parameters, it is possible to find through numerical experiments stable range of variable which results in equivalent quality of the reconstruction.

Results We present the results of the numerical tests on the method in this section. For every couple of parameters (σ, σ_v) , 100 simulations are performed and the Dice coefficient is systematically averaged per time iteration, given all the results of the simulations. The evolution of the averaged Dice coefficient from the initial iteration to the final iteration is plotted for $\sigma = 2.0, 6.0$ with different levels of velocity noise, see Figure 2.13.

For $\sigma = 2.0$, the averaged Dice coefficient shows a satisfactory surface reconstruction. The Dice coefficient goes from 0.72 (initial value) to 0.92 within 5 iterations, see Figure 2.13(a). It reaches a narrow range of variation, after only 5-10 iterations. After 60 iterations over 200, the level of similarity is preserved throughout the iterations. The final averaged Dice coefficient is between 0.94 and 0.95. The same trend is observed for the different levels of velocity noise. Note that the lower the level of noise is, the higher the Dice coefficient is in average. For $\sigma = 2$, the gradient magnitude profile is preserved despite the blur and the noise, see Figure 2.10(a). The contours are actually easily detectable to naked eyes. The observation operator finds the position of the surface, hence the fast convergence towards a large Dice coefficient. Regarding the Dice coefficients, the method shows equivalent level of precision for different levels of noise, going from a low velocity noise $\sigma_v = 0.003$ to more severe noise $\sigma_v = 0.105$, as shown in Figure 2.13(a). However the point trajectory plots are more sensitive to the velocity noise, as shown by Figures 2.14 and 2.15, in terms of regularity.

For $\sigma = 6$, an accurate contour detection becomes more challenging, as shown

(a) Image blur $\sigma = 2.0$.(b) Image blur $\sigma = 6.0$.Figure 2.13: Dice evolution, averaged over 100 runs. $\gamma = 100$, $\kappa = 10$, $\kappa_{\text{obs}}\delta = 0.1$.

(a) Final state.

(b) "Min" trajectory.

(c) "Max" trajectory.

Figure 2.14: Simulation for $\sigma = 2.0$, $\sigma_v = 0.003$, $\sigma_q = 1.5$. Red : real vesicle. Blue : estimation by the method. $\kappa = 10$, $\kappa_{\text{obs}}\delta = 0.1$.

by Figures 2.10(b) and 2.11(b) because of the blur in the image. The Dice coefficient requires 10-15 iterations to reach a lower level compared to $\sigma = 6$, namely a value of 0.9. The final Dice coefficient is between 0.85 and 0.90, see Figure 2.13(b). The method is globally less accurate in terms of surface reconstruction and point-to-point trajectory tracking, as shown by Figure 2.16, due to a more diffused image gradient. The behavior of the method differentiates with the noise in the velocity, at least between $\sigma_v = 0.003$ and $\sigma_v > 0.003$. For $\sigma = 6$ large oscillations are observed as the noise in the velocity increases. Those oscillations will be better explained in the second test case. The point-to-point tracking is more erratic for high velocity noise, see Figure 2.17.

The quality of the segmentation is assessed through the Dice coefficient which characterizes a global similarity. However a large Dice coefficient could hide variable local irregularities in the mesh such as point collapsing, edge twists. The predictive model (spring-mass model (2.12)) is designed to avoid point collapse, for instance. In fact large values of κ tends to penalize deformation from the zero-energy configuration (the circular shape here). Despite this model regularization, point collapse can occur

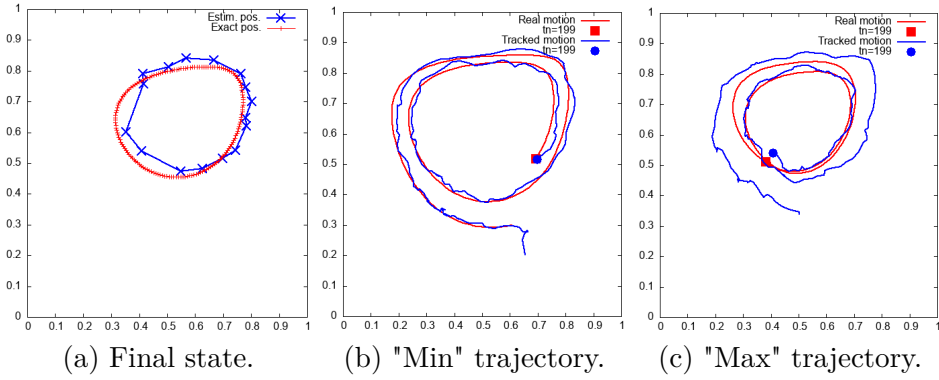


Figure 2.15: Simulation for $\sigma = 2.0$, $\sigma_v = 0.105$, $\sigma_q = 1.5$. Red : real vesicle. Blue : estimation by the method. $\kappa = 10$, $\kappa_{\text{obs}}\delta = 0.1$.

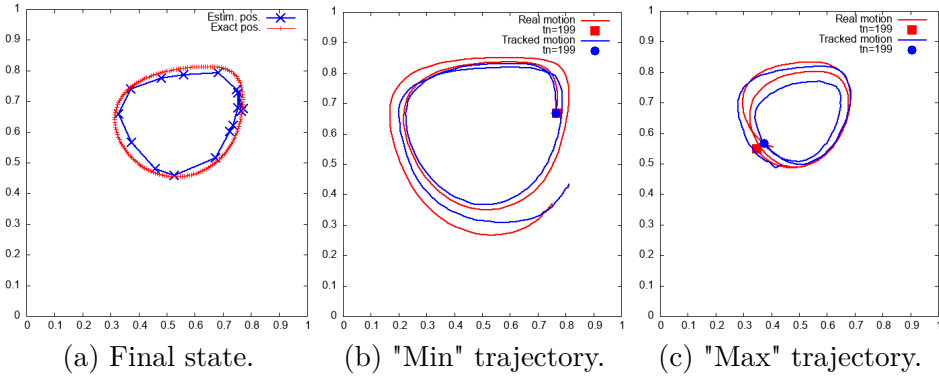


Figure 2.16: Simulation with $\sigma = 6.0$, $\sigma_v = 0.003$, $\sigma_q = 2.5$. Red : real vesicle. Blue : estimation by the method. $\kappa = 10$, $\kappa_{\text{obs}}\delta = 0.1$.

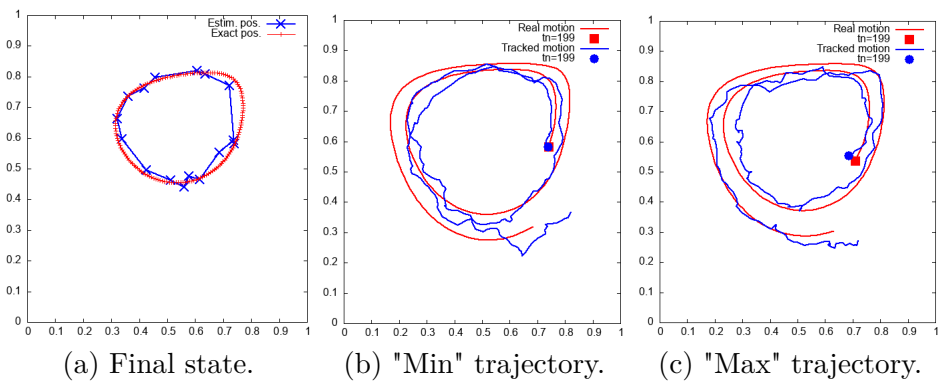


Figure 2.17: Simulation with $\sigma = 6.0$, $\sigma_v = 0.105$, $\sigma_q = 2.5$. Red : real vesicle. Blue : estimation by the method. $\kappa_{\text{obs}}\delta = 0.1$

in the vesicle test case because the vesicle deforms with large amplitudes with respect to the zero-energy configuration. The model prevents vertices from collapsing by penalizing locally high elastic energy, with the assumption of small deformations around the circular shape. A more suitable predictive model adapted to the vesicle deformation might require to take into account the local curvature of the surface in the discrete equation (2.12).

2.4.1.3 Sensitivity to regularization parameters

The isolated and joint effects of the model parameter κ and the observation parameter $\kappa_{\text{obs}}\delta$ on the accuracy of the estimation are investigated in this section.

The data quality is fixed by $\sigma = 6.0$, $\sigma_v = 0.075$, which corresponds to considerably lowered data quality. This test would conjointly serve to exhibit a range of stability of the method, if it exists. The parameters are in the CGS unit system.

Data quality		Initialization		Model		Observation				
σ	σ_v	$\sigma_{P_0,q}$	$\sigma_{P_0,p}$	κ	σ_a	γ	ΔN	$\kappa_{\text{obs}}\delta$	σ_q	σ_p
6.0	0.075	$10h_1$	0.1	{0.0,1.0, 5.0, 10, 30, 50}	5.0	100	30	{0.0, 0.1, 0.5, 0.7, 1.0}	1.5	σ_v

Table 2.2: Parameters for the second synthetic test case.

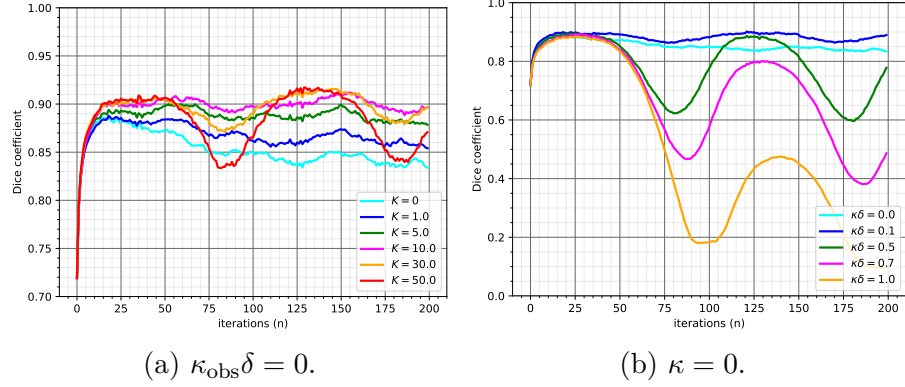
We investigate the following values for the parameters: $\kappa = 0, 1.0, 5.0, 10, 30, 50$ and $\kappa_{\text{obs}}\delta = 0.0, 0.1, 0.5, 0.7, 1.0$. The unchanged parameters are specified in Table 2.2.

For this second test, we appreciate the robustness of the method, regarding the regularization parameters by considering a fixed point labeled $i^* = 12 \in \{0, \dots, N_P\}$. The discrete trajectory $\{\hat{\mathbf{q}}_{i^*}^n\}_{n=0, \dots, N_T}$ of i^* is compared to the trajectory $\{\mathbf{q}_{j^*}^n\}_{n=0, \dots, N_T}$ of a material point j^* such that $\mathbf{q}_{j^*}^{N_T}$ is the closest point projection of $\hat{\mathbf{q}}_{i^*}^{N_T}$ on Γ^{N_T} . If the method is robust, then $\mathbf{q}_{j^*}^{N_T}$ should remain in a same vicinity for the values of parameters improving the regularity of the point trajectories.

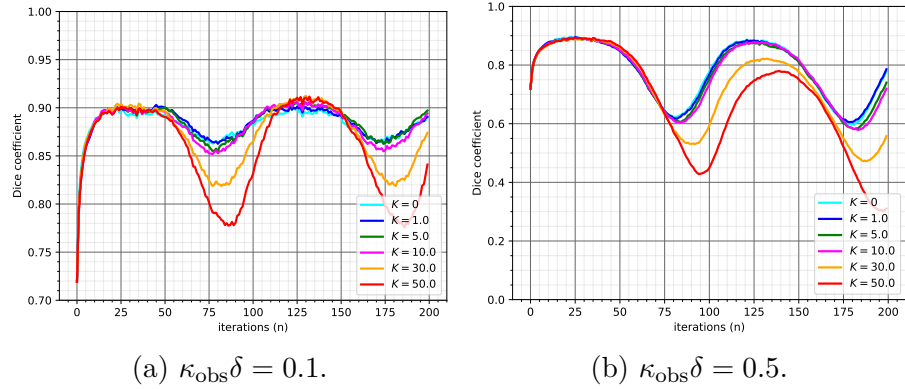
Results We present the results of the sensitivity analysis with respect to the regularization parameters. The image blur is set to $\sigma = 6$ and the noise in the velocity $\sigma_v = 0.075$.

When $\kappa_{\text{obs}}\delta = 0$, the effect of the model regularization κ on the surface reconstruction is evaluated. Increasing κ improves the surface reconstruction within a limited interval, as shown by Figure 2.18(a). From $\kappa = 0$ to $\kappa = 10$, the final averaged Dice coefficient gains more than 5.0. For larger values of κ , $\kappa > 30$, considerable oscillations of the Dice coefficient are observed during the reconstruction. It corresponds to alternative shrinking behavior, as the vesicle deforms and rotates. The vesicle actually alternates between circular and ellipsoidal configurations during its motion, as visible on Figure 2.7. Large values of κ tend to shrink the capsule to a circle, since the zero-energy state of the model is the initial shape which is circular.

When $\kappa = 0$, the effect of the observation regularization is analyzed. Note that having $\kappa = 0$ inhibits the model regularization, and more specifically the velocity regularization. Consequently, the noise in the velocity might amplify and propagate with the model integration. For $\kappa = 0.0$, $\kappa_{\text{obs}}\delta = 0.1$ and $\kappa = 10.0$, $\kappa_{\text{obs}}\delta = 0.0$,

Figure 2.18: Marginal effect. $\gamma = 100$, $\sigma = 6.0$, $\sigma_v = 0.075$.

the reconstruction provides equivalent results, see Figure 2.20, and Figure 2.21. For $\kappa_{\text{obs}}\delta > 0.1$, alternative oscillations of very large amplitude are systematically observed, see Figure 2.18(b). They account for shrinkage behavior and also degraded surface reconstruction. The stable range of variation of $\kappa_{\text{obs}}\delta$ is limited of 0.0 – 0.1. For larger values of $\kappa_{\text{obs}}\delta$, the numerical resolution with the algorithm provides uncontrolled results.

Figure 2.19: Effects of κ and $\kappa_{\text{obs}}\delta$. $\gamma = 100$, $\sigma = 6.0$, $\sigma_v = 0.075$.

Concerning the combined effect of the model and the position observation regularization, oscillation of the Dice coefficient are systematically observed for $\kappa_{\text{obs}}\delta = 0.1$. In fact, the observation generates an additional recall force to the circular initial shape when $\kappa_{\text{obs}}\delta$ is large. The algorithm is unable to properly track ellipsoidal deformation of the surface. The vesicle remains mostly circular and the Dice coefficient is bounded from below by the initial Dice coefficient, which ensures some robustness. As shown through Figure 2.19, $\kappa_{\text{obs}}\delta = 0.1$ is an upper bound in this case. The parameter $\kappa_{\text{obs}}\delta$ seems to be a very critical parameter with dramatic effect on the reconstruction. Note that large values of $\kappa_{\text{obs}}\delta$ are actually very small, which prevents the user to set $\kappa_{\text{obs}}\delta$ arbitrary.

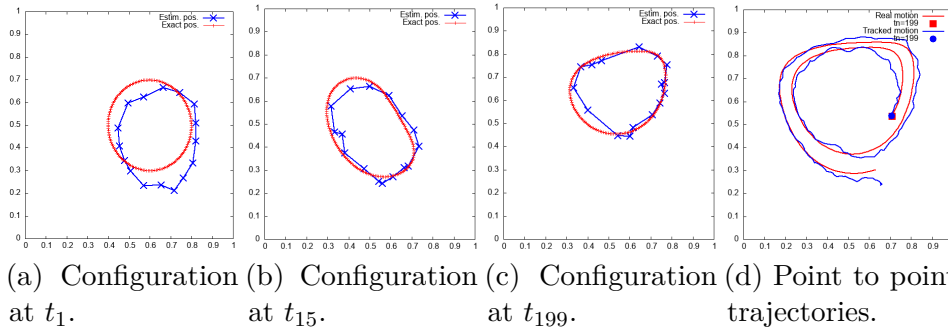


Figure 2.20: Vesicle configuration (blue) at $t_n, n = 1, 69, 199$ against the solution (red). Right hand side : trajectory of a point in the estimation (blue) compared to the one of the presumed tracked point in the real vesicle (red) at final iteration. Parameters : $\kappa = 0.0, \kappa_{\text{obs}}\delta = 0.1, \sigma = 6.0, \sigma_v = 0.075$.

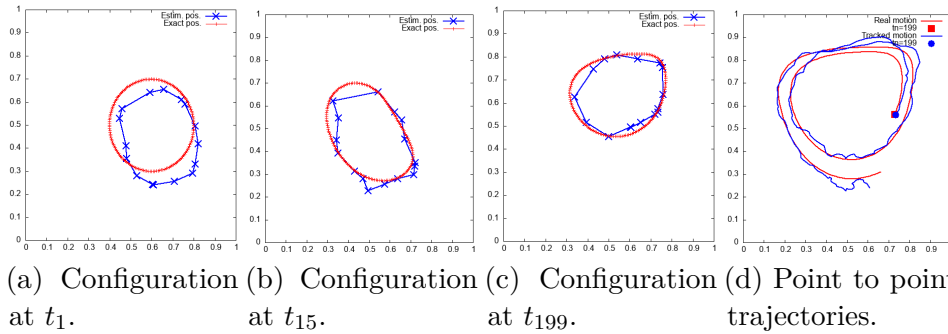


Figure 2.21: Vesicle configuration (blue) at $t_n, n = 1, 69, 199$ against the solution (red). Right hand side : trajectory of a point in the estimation (blue) compared to the one of the presumed tracked point in the real vesicle (red) at final iteration. Parameters : $\kappa = 10, \kappa_{\text{obs}}\delta = 0.0, \sigma = 6.0, \sigma_v = 0.075$.

2.4.2 Aorta tracking from 4D-flow MRI data

In the section, we apply Algorithm 2 to the dynamical reconstruction of the aorta from a real 4D-MRI exam, provided by Dijon University Hospital.

2.4.2.1 Data generation

The 4D-flow MRI acquisition was performed with complete volumetric coverage of the thoracic aorta, on a patient with a dilatation of the ascending aorta. The MRI System of acquisition was a 3T Skyra Siemens. The data were provided and anonymized by Dijon University Hospital. The considered patient was part of a research protocol⁵ which has been approved by the local ethics committee. The 4D-flow MRI data include:

⁵See clinicalTrials.gov with protocol code NCT03817008.

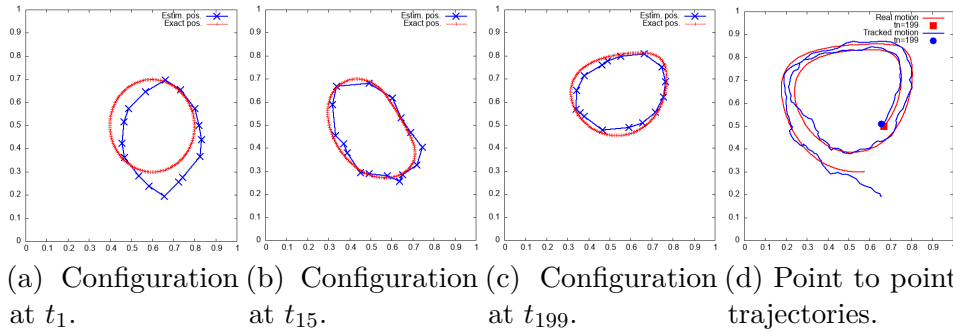


Figure 2.22: Vesicle configuration (blue) at $t_n, n = 1, 69, 199$ against the solution (red). Right hand side : trajectory of a point in the estimation (blue) compared to the one of the presumed tracked point in the real vesicle (red) at final iteration. Parameters : $\kappa = 10, \kappa_{\text{obs}}\delta = 0.1, \sigma = 6.0, \sigma_v = 0.075$

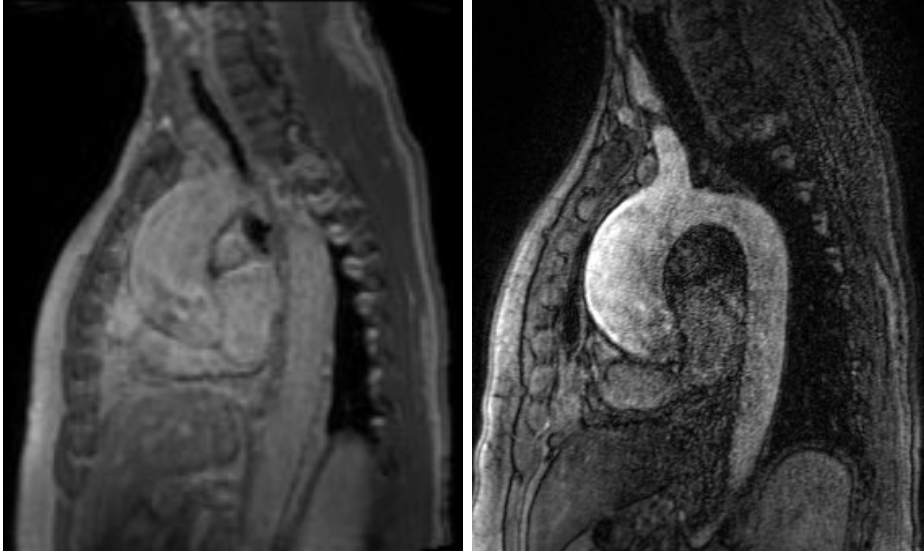
- Time-resolved magnitude images of the volume of acquisition;
- Three series of time resolved images encoding the three directions of the velocity. The velocity encoding (VENC) is $2500 \text{ mm} \cdot \text{s}^{-1}$, which ensures proper representation of velocities in the range $\pm 2500 \text{ mm} \cdot \text{s}^{-1}$.

The image parameters are the following:

- Temporal resolution: $\Delta T = 43.319 \text{ ms}$, with $N_T = 25$ frames;
- Spatial resolution (spacing): $1.988 \times 1.988 \times 2.0 \text{ mm}^3$.

In addition to those images, a contrast enhanced MR angiography (MRA), representing an averaged image of the volume of acquisition, obtained with breath hold was also provided, for the same patient. The spatial resolution of the MRA is $1.0 \times 1.0 \times 1.0 \text{ mm}^3$. The image quality of MRA is more suitable for both vessel visualization and segmentation than 4D Flow MRI, due to the contrast as visible on Figure 2.23. The angiographic series has been in fact acquired right after the injection of contrast agent. Note that a direct segmentation of an aortic configuration directly from 4D anatomic series (Figure 2.23(a)) at any time of the cardiac cycle is challenging, if only based on images, because of the low image quality.

Parsing, reading and extraction of images from the Dicom files were performed using QIR 4D, a 4D MRI post-processing software developed by the CASIS company. The magnitude series and the flow series were exported as VTI files and handled with the VTK Library. No image filter (gaussian, median, etc.) has been applied to the magnitude series. The MRA exam was segmented and reconstructed with the Mimics/Materialise software, and smoothed with Autodesk Meshmixer's tools. The inlet and outlets of the aortic mesh have then been cut by perpendicular planes to the centerlines at the level of the inlet (ascending aorta) and the four outlets (three carotid vessels on the aortic arch and descending aorta). Semi-automatic rigid registration to the first magnitude image has been performed on the resulting geometry to serve as initial configuration for Algorithm 2, Figure 2.24 summarizes the corresponding input data in the present example:

(a) 4D-MRI magnitude image at t_3 .

(b) MRA images.

Figure 2.23: Slice of magnitude series and MRA series. The view is oblique sagittal. The slices are taken in the middle of the respective volume of acquisitions.

1. The mesh point positions $\{\hat{\mathbf{q}}_i^0\}_{i=1,\dots,N_P}$ of the initial configuration obtained after MRA segmentation, reconstruction and registration;
2. Time-dependent grayscale image $\{F_M^n\}_{n=0,\dots,N_T}$ provided by the raw magnitude series;
3. Measured velocity field $\{\mathbf{u}_M^n\}_{n=0,\dots,N_T}$ from the three time-dependent flow series.

One can refer to Figure 2.25 for a three dimensional visualization of the (noisy) velocity field provided by 4D Flow MRI.

2.4.2.2 Description of the test

As indicated above, the initial mesh of the aorta comes from MRA data. As shown on Figure 2.26(A.), the initial mesh is a reasonable guess for the initial state of the tracking. There is in fact a good match between the slice cut of the initial mesh and the position of the aortic wall on the anatomic series at time t_0 .

Note that the largest deformations of the aortic wall during the cardiac cycle are observed close to the inlet (see Figures 2.26(A.-C.)), with a maximum displacement at peak systolic phase. The systolic phase goes approximatively from time iteration t_1 to t_{10} , with the peak systolic at t_4 , as assessed by the flow rate calculation at the inlet (see Figure 2.27).

The inlet motion observed in the grayscale images requires a proper tracking, which is the purpose of Algorithm 2. As shown on Figure 2.25(a), the velocity field

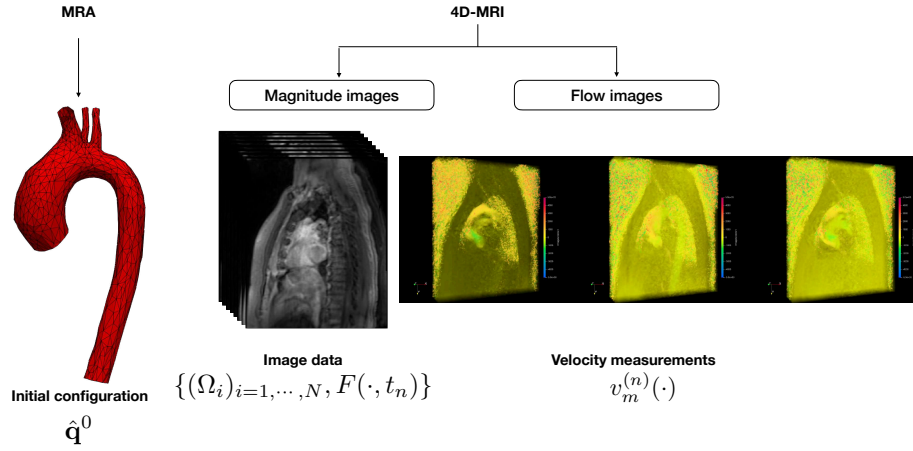
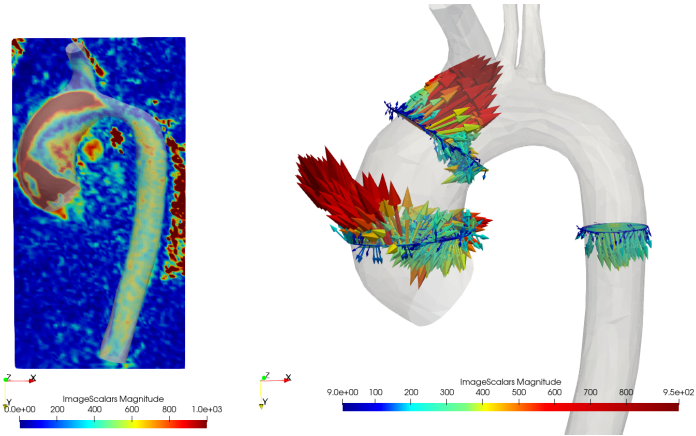


Figure 2.24: Input data for the proposed method.



(a) Slice view of the velocity magnitude. (b) velocity field visualization at 3 slice cuts.

Figure 2.25: Snapshots of the 4DFlow MRI velocity field data at peak systolic phase.

is noisy, especially around the aorta. The mesh consists of $N_p = 793$ points and 1582 triangles. The state estimation $\hat{\mathbf{X}}$ is of size $6N_p = 4758$.

Compared to the reconstruction of the motion of the immersed vesicle example (Section 2.4.1), the tracking of the aorta has some specificities. The aorta is surrounded by other vessels and cavities, whose voxel intensities are also sensitive to blood flow over time (the principle of MRI). Consequently the local window search, introduced to avoid undesired segmentation of neighboring vessels, has to be limited to 1 or 2 voxels. Additionally, the gradient will be normalized by the maximum

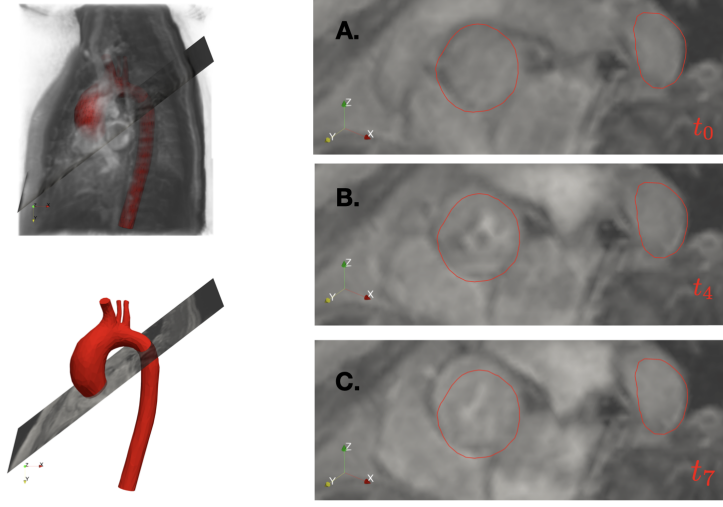


Figure 2.26: Slice view of the initial configuration against the magnitude images of the 4D MRI series, at time iteration t_0 (A.), t_4 (B.) and t_7 (C.).

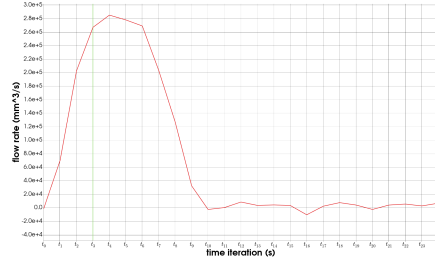


Figure 2.27: Flow rate at the inlet of the initial configuration. Time iteration $t_k = k \cdot \Delta T$.

value inside the local window search instead of the maximum value of the volume of acquisition in the position observation operator (2.16) of Algorithm 2. The purpose is to reduce the sensitivity of the position observation to distant and high image intensity variations. Except those specificities, the parameters that will be tested are almost the same as in the immersed vesicle example:

- κ , which represents the stiffness of the aorta, modeled as spring-mass network. After some preliminary tests, we found appropriate range of variation for κ , namely between $5.0 \cdot 10^3$ and $5.0 \cdot 10^4$;
- σ_a , which indirectly quantifies the level of the confidence in the observation compared to the predictive model. The formula (2.26) provides a reasonable order of magnitude for σ_a , namely $\sigma_a \sim 10^4$, $N=2$. It assumes that the uncertainty induced by the model is comparable to N -voxel size. We have performed a few tests around 10^4 and we propose $1.0 \cdot 10^3 < \sigma_a < 1.0 \cdot 10^4$.
- γ , κ_{obs} , the first one weights the gradient compared to the distance to the

prior in the local maximization of the gradient (2.17), the second parametrizes the regularity of the position observation outcome (2.18).

- σ_p , the global level of noise in the velocity data. The order of magnitude of level noise σ_p for the velocity is assessed by estimating the standard deviation of each component of the velocity field in a region of interest in the middle in the descending aorta at the end the diastolic phase. We found approximately 50 mm/s. The values obtained are possibly underestimated since they do not take into account the noise around the aorta, which is much higher, see Figure 2.25(a).

The parameters of the filter are given in the Table 2.3 (length in mm and time in s).

Initialization		Model		Observation				
$\sigma_{P_0,q}$	$\sigma_{P_0,p}$	κ	σ_a	γ	ΔN	$\kappa_{\text{obs}}\delta$	σ_q	σ_p
2.0	500	$5.0 \cdot 10^3$	$1.0 \cdot 10^3$	20	1	5.0	1.0	75
(voxels)	(mm/s)	$1.0 \cdot 10^4$	$1.0 \cdot 10^4$	40	(voxels)	20		100
		$5.0 \cdot 10^4$	mm/s ²	80		40		(mm/s)

Table 2.3: Parameters used in Algorithm 2 for the reconstruction of the aorta.

Remark 3

For the 4D MRI exam provided, note that the observation of the carotid vessels on the aortic arch from the magnitude images is very challenging, due to the limited contrast and the spacial resolution. This can be inferred from Figure 2.23, by comparing the magnitude of the 4D Flow exam with the angiographic series.

2.4.2.3 Results

The purpose of this section is to show the behavior of the tracking algorithm and to provide insight on the sensitivity of the reconstruction with respect to the user-defined parameters. Algorithm 2 returns a sequence of time-dependent point-to-point displacements from the initial configuration, with the associated velocity field. For each set of parameters, the quality of the reconstruction is assessed by computing the Dice coefficient at time t_3 . To this purpose, we have performed a manual segmentation of the aorta (at time t_3) as ground-truth. This manual segmentation is partial (see Figure 2.28(A)), since one carotid on the aortic arch is not visible due to the quality of the 4D MRI magnitude series. The Dice coefficient is evaluated within a region of interest (ROI) which contains the ascending aorta, the aortic cross, and the beginning of the descending aorta (see Figure 2.28(C)).

Figure 2.29 reports the values of the Dice obtained over all the reconstructions performed with the parameters specified in Table 2.3. The average Dice on the ROI is 0.929 ± 0.00367 , with as maximum Dice 0.935 for $\kappa = 5.0 \cdot 10^3 \text{s}^{-2}$, $\gamma = 80$, $\kappa_{\text{obs}}\delta = 10$, $\sigma_a = 1.0 \cdot 10^4 \text{mm} \cdot \text{s}^{-2}$, $\sigma_p = 100 \text{mm} \cdot \text{s}^{-1}$, and a minimum Dice 0.920 for $\kappa = 1.0 \cdot 10^4 \text{s}^{-2}$, $\gamma = 20$, $\kappa_{\text{obs}}\delta = 20$, $\sigma_a = 1.0 \cdot 10^3 \text{mm} \cdot \text{s}^{-2}$, $\sigma_p = 75 \text{mm} \cdot \text{s}^{-1}$. As a reference the Dice of the initial configuration (registered MRA segmentation) is 0.915.

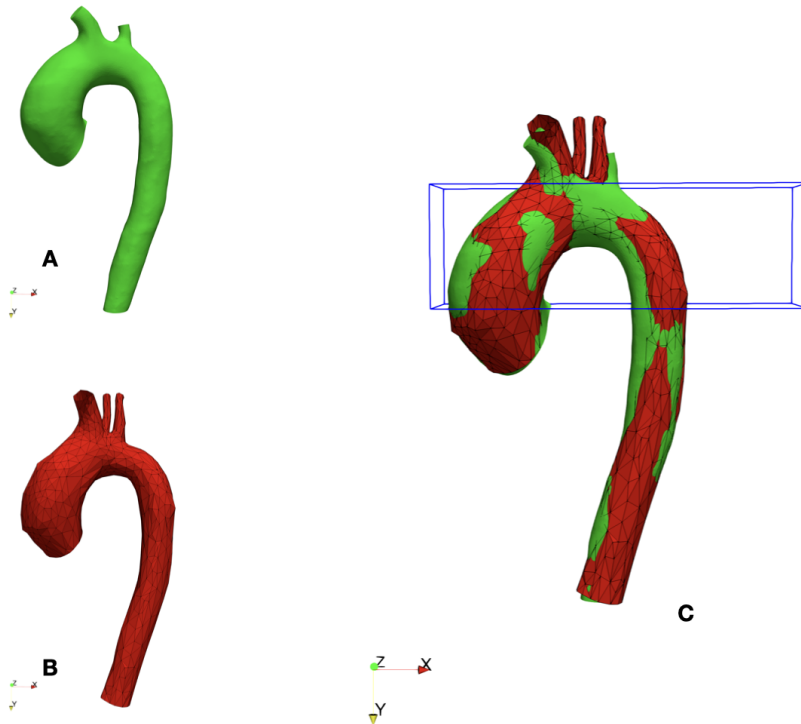


Figure 2.28: Definition of the ROI and the slice plane location for the computation of the Dice coefficient. A: the aorta from manual segmentation at t_3 (green). B: the reconstruction at t_3 (red). C: The region of interest for the calculation of the Dice in blue.

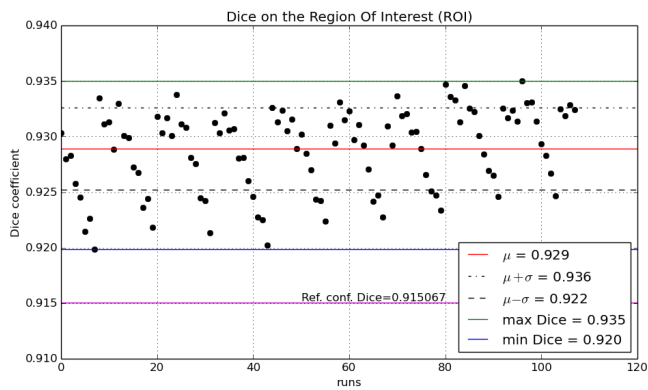


Figure 2.29: Dice on the region of interest

The reconstruction is performed with acceptable accuracy ($\text{Dice} > 0.920$) inside the region of interest at time iteration t_3 . For the range of parameters specified in Table 2.3, the reconstructions are equivalent with a Dice between 0.920 and 0.935

as shown by Figure 2.29 and the slice cut views in Figure 2.30. The best and worst configurations are defined as the ones that realize the maximum, and minimum respectively Dice values, and an average Dice coefficient has a Dice equal to the average Dice of all simulations, namely 0.929, with a tolerance of 10^{-4} . Table 2.4 summarizes the values of the best, average and worse Dice configurations with the parameters that generated them. The significant discrepancy with the manual segmentation especially at the level of the descending aorta (DAO_P3, DAO_P4, Figure 2.30) can be mainly explained by the low variations of the image gradient intensity around the descending aorta.

Configuration	Dice coefficient	κ	α	$\kappa_{\text{obs}}\delta$	σ_a	σ_p
Worse Dice	0.920	$1.0 \cdot 10^4$	20	20	$1.0 \cdot 10^3$	75
Average Dice	0.929	$5.0 \cdot 10^4$	40	10	$1.0 \cdot 10^4$	75
Best Dice	0.935	$5.0 \cdot 10^3$	80	10	$1.0 \cdot 10^4$	100

Table 2.4: Parameters of best, average and worse dice configurations, with Dice on the ROI at t_3 .

Note that, compared to the vesicle test case, the Dice of the initial configuration is much higher (0.72 compared to 0.915), because a MRA exam was available, which is not always the case. Otherwise, a MRA-type image could be generated using the whole time sequences of the 4D MRI exam (see [BGCE17]) to perform segmentation, without need for further registration.

Considering the whole cardiac cycle, the tracking is qualitatively satisfying, at the level of the inlet, the beginning of the descending aorta (Figure 2.31) and the mid-ascending aorta (Figure 2.32). The slice views of the reconstruction show that the filter properly tracks the position of the surface (also observed in the vesicle example of Section 2.4.1). A more notable discrepancy with the image slice contour is however observed at the inlet, especially during the systolic phase (see Figure 2.31(B)).

2.5 Conclusion

We introduced a novel approach to track the aortic wall motion from medical imaging data. Geometrical configuration and Lagrangian deformation of the wall are estimated from one patient specific reconstruction and the complete 4D MRI data set (magnitude and flow series). The magnitude image sequences are interpreted as geometrical information and the flow series as kinematical prior. The reconstruction does not require any pre-processing on the image sequences (smoothing, segmentation, contouring, etc.). The tracking is based on Kalman filter with ad hoc position observation operator which converts grayscale image sequences into a geometrical position given a patient specific prior. The Kalman filter provides a quantification of the uncertainty on the reconstruction. The method was extensively investigated on a 2D synthetic example to track the deformation of a vesicle immersed in an incompressible flow. To this purpose, synthetic data have been generated to mimic 4D-flow (image sequences and volumetric velocity). The results showed that the method achieves proper tracking of the surface of the vesicle and pointed out the

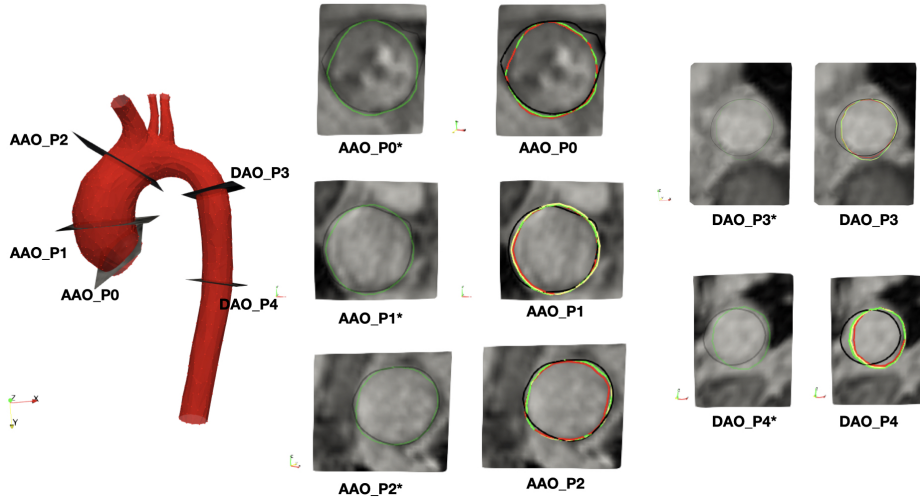


Figure 2.30: Visualization of the contours obtained by cutting the geometries at 5 planes locations : AAO_P0 = inlet of the geometry, AAO_P1, AAO_P2 = ascending aorta, DAO_P3, DAO_P4 = descending aorta. On the left, the position of the 5 planes. At the right, 10 slices cut views. For each plane, on the left side (with asterisk (*)), the contour with the best Dice configuration and the manual segmentation with low opacity for better image visualization, and on the right side, the 4 contours corresponding to the worse Dice configuration (red), one of the average Dice configurations (yellow), the best Dice configuration (green), the manual segmentation (black), see Table 2.4 for more detail on the parameters.

dependence of the parameters on the data quality (image and velocity). A promising tracking of the aorta has been obtained from real 4D-flow MRI and a patient-specific initial configuration. The quality of the tracking has been assessed by comparing with one manual reconstruction. It is important to point out that the lagrangian reconstruction of the aortic wall returned by the tracking algorithm using Kalman filter represents an average outcome. The Kalman filter provides also a covariance matrix of the error associated to the state estimation. Assessing the quality of the local (point-to-point trajectory) tracking would be more challenging, since the literature lacks of validated point-to-point 3D reconstruction of the aorta. The proposed algorithm is currently being tested on a cohort of patients exams acquired with the same MR machine. The method is not limited to the tracking of the aorta, and might be used to reconstruct the motion of other cardiovascular parts (cardiac wall, pulmonary artery, etc.), as long as 4D MRI acquisition is available with a patient specific initial configuration. The initial configuration could be generated from different approaches (MRA, reconstructed MRA, one time reconstruction, etc.). A forthcoming extension of this work will address state estimation in fluid-structure simulations of the aorta from 4D MRI data, by exploiting the complete dynamical information obtained with the present tracking approach.

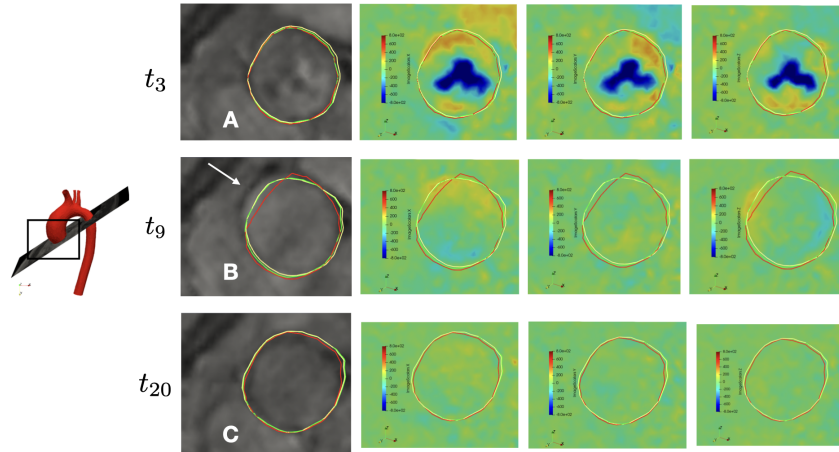


Figure 2.31: Slice cut view, at the inlet of the geometry. On the left, the position of the plane for slice visualization. On the right, the slice cut at 3 time iterations : A) t_3 , B) t_9 is the end of the systolic phase, C) t_{20} during the diastolic phase. The best Dice reconstruction is in green, one of the 3 average Dice reconstruction in yellow, and the worst Dice case is in red.

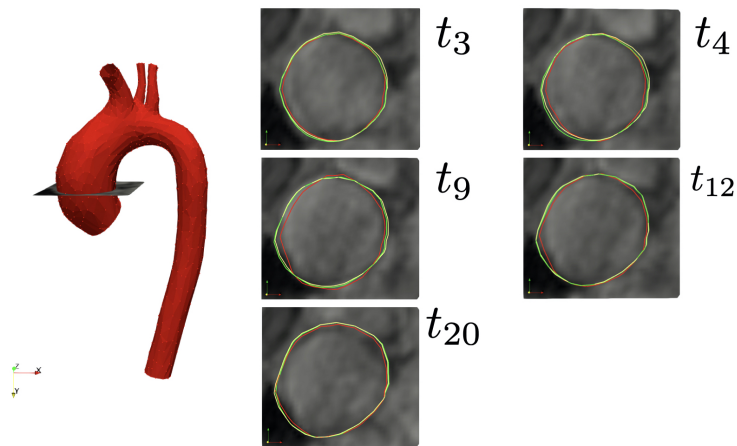


Figure 2.32: Slice cut view, at the level of the ascending aorta. On the left, the position of the plane for slice visualization. On the right, the slice cut at 3 time iterations : A) t_3 , B) t_9 is the end of the systolic phase, C) t_{20} during the diastolic phase. The best Dice reconstruction is in green, one of the 3 average Dice reconstruction in yellow, and the worst Dice case is in red.

State estimation in fluid-structure interaction from fluid velocity measurements: fixed fluid domain

Introduction

One of the most challenging problems in blood flow simulations is (absolute) pressure estimation in vessel using fluid velocity data (e.g., from 4D-flow MRI acquisitions). To the best of our knowledge, most of the existing approaches generally focus on relative pressure estimators in which the noisy velocity data is inserted in the considered state equations (Navier-Stokes) as reported in [BNG⁺17, MRB⁺19]. The main reason is that the Navier-Stokes equations with Dirichlet boundary conditions or without boundary conditions are invariant to additive pressure constants. In fluid-structure interaction (FSI), this invariance is removed by the interface dynamical coupling (balance of forces between the fluid and the solid), which acts as a Neumann boundary condition for the fluid. In this work, we propose to investigate the pressure estimation problem in fluid-structure interaction from fluid velocity measurements. As a first attempt, the problem is tackled in a simplified FSI setting, where a thin-walled solid undergoes infinitesimal displacements (vibrations) in such a way that the fluid domain can be assumed fixed. In this simplified case, the FSI problem can be collapsed in a single fluid problem with generalized Robin boundary conditions (see [NV08]). A first FSI state estimation algorithm is proposed in the spirit of unique continuation using only fluid velocity measurements. The principle of unique continuation consists in extending to a larger domain the solution of a differential equation which is only known on a subdomain. The FSI state estimation problem is formulated as a PDE-constraint optimization problem in which discrepancy between simulation and measured data are minimized. One of the main features of unique continuation is that boundary data is not available in the whole boundary (which is very appealing from the practical point of view). The price to pay is that these types of problems are ill-posed, and hence their corresponding numerical approximation is much more delicate than for traditional well-posed problems. We propose a numerical approach which builds on the work reported in [BBFV20] (without FSI). It relies on a discretize-then-regularize strategy, with appropriate weakly consistent stabilizations to regularize and stabilize the problem (see also [Bur13]). The optimality conditions are formulated in terms of a linear system involving the primal fluid-pressure unknowns and their corresponding dual variables.

Estimating the FSI state with the absolute pressure paves the way for in-flow/outflow boundary conditions assessment from the data. In the literature, a widespread technique to provide realistic boundary conditions for blood flow simulation consists in modeling the effect of the whole cardiovascular system with an analogy of closed hydraulic (or electrical) system. It results in the so-called Windkessel models. This approach leads to a system of ordinary differential equations at the outflow boundaries, to compute the average pressure of a vessel of

interest (the aorta, e.g.) as in [MBX⁺12, CCM⁺17]. In a data assimilation context, the parameters involved in such lumped models could also require state-parameter estimation with patient data [KFL⁺10, BMG12]. The use of lumped models for the outflow pressure conditions requires the personalization of up to 12 parameters. In addition to the value of the averaged pressure, the spatial distribution on the outflow boundary could raise some interest.

When it comes to the inflow boundary conditions, a most common practice consists in imposing an idealized inflow velocity profile (flat, linear, parabolic, cubic, etc.) with respect to a measured inflow flow rate. Recent work [TGS17] has achieved non-parametric boundary conditions estimation using unknown inflow velocity profile as a control for an optimization strategy after discretizing the Navier-Stokes equations. The problem is assumed stationary and the interaction with the solid wall is neglected. It has been applied to realistic geometries with patient data and achieves a satisfying accuracy. A major drawback is still the computational cost of the estimation and the limitation to Navier-Stokes equations on fixed domain. Through the FSI state estimation, one could also provide non-parametric inflow and outflow boundary conditions in velocity or (absolute) pressure using fluid velocity measurements.

With velocity and pressure boundary conditions estimated by means of the first FSI estimation algorithm, another alternative for FSI state estimation could be proposed, in the spirit of Luenberger state observers. Unique continuation would serve as a boundary conditions estimation step, upstream of a Luenberger fluid solver. The Luenberger fluid observer formulated by adding a nudging terms in the momentum equations. The design of this algorithm, especially the continuation step, has been performed in collaboration with Mihai Nechita based on the paper [BBFV20]. We will present that second FSI state estimation algorithm on the fixed domain setting in view of the application to moving domain.

3.1 FSI Model

In this section, the FSI setting is presented and the FSI forward problem used for the FSI state estimation is derived. Most of the useful notations are introduced in this section.

3.1.1 Setting of the problem

The FSI problem is a simplification of the propagation of a pressure wave in bi-dimensional cylinder fluid domain surrounded by an elastic thin wall. We assume that the thickness ϵ of the tube (reference configuration) is small compared to its length L and its height H . The wall structure is assumed to comply with the theory of linear elasticity with membranes deformations. The horizontal deformations of the wall are neglected and only small vertical vibrations are assumed. Under the assumption of symmetric flow, the problem can be solved in half of the domain. The configurations with the successive geometrical approximations are sketched in Figure 3.1.

Hence, let consider a domain fluid domain $\Omega = [0, L] \times [0, H]$, having one interface Σ with a thin elastic wall, an inflow boundary Γ_{in} , an outflow boundary Γ_{out} and a bottom Γ_{bot} , see Figure 4.1.

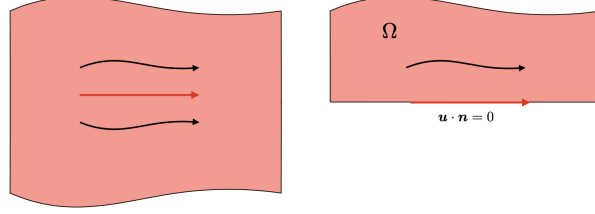
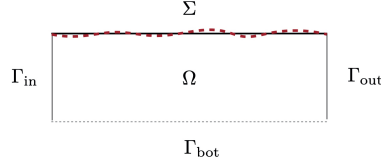
Figure 3.1: Sketch of the domain Ω . Arrow represents stream lines directions.

Figure 3.2: Geometrical configuration - FSI on fixed domain, small vibrations

The inflow and outflow boundary conditions are assumed unknown, but we dispose of possibly noisy velocity measurements \mathbf{u}_M in an open bounded subset $\omega \subset \Omega$.

Let \mathbf{n} and $\boldsymbol{\tau}$ denote the outgoing unit normal and the tangential unit vector at the boundary of the fluid domain, respectively. The fluid flow is assumed newtonian, and the velocity $\mathbf{u}: \Omega \times (0, T) \rightarrow \mathbb{R}^2$ and the pressure $p: \Omega \times (0, T) \rightarrow \mathbb{R}$ satisfy the instationary Stokes equations given by:

$$\left\{ \begin{array}{l} \text{Find } \mathbf{u}: \Omega \times (0, T) \rightarrow \mathbb{R}^2, p: \Omega \times (0, T) \rightarrow \mathbb{R}, \text{ such that} \\ \rho^f \partial_t \mathbf{u} - \operatorname{div} \boldsymbol{\sigma}(\mathbf{u}, p) = 0 \quad \text{in } \Omega \times (0, T), \\ \operatorname{div} \mathbf{u} = 0 \quad \text{in } \Omega \times (0, T), \end{array} \right. \quad (3.1)$$

where ρ^f is the fluid density, $\boldsymbol{\sigma}(\mathbf{u}, p)$ the Cauchy stress tensor which is given by

$$\boldsymbol{\sigma}(\mathbf{u}, p) = -p\mathbf{I} + 2\mu\boldsymbol{\varepsilon}(\mathbf{u}), \quad \boldsymbol{\varepsilon}(\mathbf{u}) := \frac{1}{2}(\nabla \mathbf{u} + \nabla \mathbf{u}^T),$$

and μ the fluid dynamic viscosity. The body forces of the fluid are neglected. The equations have to be complemented with boundary conditions on $\partial\Omega$ and initial conditions. A symmetric boundary condition is imposed on the bottom Γ_{bot} . Without any loss of generality, we assume that the inlet and outlet boundary conditions consist in unknown space and time dependent pressures P_{in} , and P_{out} :

$$\left\{ \begin{array}{ll} \mathbf{u} \cdot \mathbf{n} = 0 \text{ and } \boldsymbol{\sigma}(\mathbf{u}, p) \mathbf{n} \cdot \boldsymbol{\tau} = 0 & \text{on } \Gamma_{\text{bot}} \times (0, T), \\ \boldsymbol{\sigma}(\mathbf{u}, p) \mathbf{n} = -P_{\text{in}} \mathbf{n} & \text{on } \Gamma_{\text{in}} \times (0, T), \\ \boldsymbol{\sigma}(\mathbf{u}, p) \mathbf{n} = -P_{\text{out}} \mathbf{n} & \text{on } \Gamma_{\text{out}} \times (0, T). \end{array} \right. \quad (3.2)$$

The initial conditions are given by $\mathbf{u}(t=0) = \mathbf{u}_0$. At the fluid-structure interface Σ , the outgoing unit normal is $\mathbf{n} = (0,1)^T$ and the tangent vector is $\boldsymbol{\tau} = (1,0)^T$. The tangent displacement of the solid interface is neglected, so that the solid unknown is the normal displacement problem $d = \mathbf{d} \cdot \mathbf{n}$. The solid sub-problem writes: Find the displacement $d: \Sigma \times (0,T) \rightarrow \mathbb{R}$ such that:

$$\begin{cases} d = \mathbf{d} \cdot \mathbf{n}, \mathbf{d} \cdot \boldsymbol{\tau} = 0 & \text{on } \Sigma \times (0,T), \\ \rho^s \epsilon \partial_t \dot{d} + \mathcal{L}d = f_\Sigma & \text{on } \Sigma \times (0,T), \\ \dot{d} = \partial_t d & \text{on } \Sigma \times (0,T), \\ d = 0 & \text{on } \partial\Sigma \times (0,T), \end{cases} \quad (3.3)$$

with $\epsilon > 0$ the thickness of the solid interface. For the kinematic model to be valid, ϵ is assumed small compared to the other dimensions of the vessel wall. The elastic linear differential operator \mathcal{L} is given by

$$\mathcal{L}d := -c_1 \partial_{xx} d + c_0 d,$$

where $c_1 = \frac{E\epsilon}{2(1+\nu)}$, $c_0 = \frac{E\epsilon}{R^2(1-\nu^2)}$, for E being the Young modulus and ν the Poisson ration. The initial condition of the solid problem is given by $d(t=0) = d_0$.

The sub-systems (3.1) and (3.3) are coupled through the fluid-structure interface conditions which ensure ensure kinematic and dynamical coupling:

$$\begin{cases} \dot{d} = \mathbf{u} \cdot \mathbf{n} & \text{on } \Sigma \times (0,T), \\ f_\Sigma = -\boldsymbol{\sigma}(\mathbf{u},p) \mathbf{n} \cdot \mathbf{n} & \text{on } \Sigma \times (0,T), \end{cases} \quad (3.4)$$

The body forces of the solid are neglected, and the external pressure of the solid is assumed null. Consequently f_Σ embodies the forces exerted by the fluid on the solid interface. If the external pressure remains in the equations, then the interface conditions (3.4)₂ becomes

$$f_\Sigma = -(\boldsymbol{\sigma}(\mathbf{u},p) - \sigma_{\text{ext}}) \mathbf{n} \cdot \mathbf{n} \text{ on } \Sigma \times (0,T),$$

with σ_{ext} the tensor resulting from external forces exerted on the wall. Without specifying σ_{ext} , we cannot compute the absolute pressure.

3.1.2 Variational formulation and monolithic formulation of the FSI problem

We first introduce the functional spaces V, Q and W defined by:

$$\begin{aligned} \mathbf{V} &:= \{ \mathbf{v} \in [H^1(\Omega)]^2 : \mathbf{v}|_\Sigma \in [H_0^1(\Sigma)]^2, \mathbf{v} \cdot \boldsymbol{\tau}|_\Sigma = 0, \mathbf{v} \cdot \mathbf{n}|_{\Gamma_{\text{bot}}} = 0 \}, \\ Q &:= L^2(\Omega), \end{aligned}$$

We denote by $(\cdot, \cdot)_\Omega$ and $\langle \cdot, \cdot \rangle_\Gamma, \Gamma \subset \partial\Omega$ the standard L^2 inner scalar product respectively defined in $L^2(\Omega)$ and $L^2(\Gamma)$, respectively. After multiplying the fluid momentum equation in (3.1) by $\mathbf{v} \in \mathbf{V}$, we integrate by part, and we multiply the continuity equation by $q \in Q$. After combining the momentum and the continuity equations, It yields

$$(\rho^f \partial_t \mathbf{u}, \mathbf{v})_\Omega + a^f((\mathbf{u}, p), (\mathbf{v}, q)) + \langle \boldsymbol{\sigma}(\mathbf{u}, p) \mathbf{n}, \mathbf{v} \rangle_{\partial\Omega} = 0 \quad (3.5)$$

where the bilinear form a^f is given by:

$$a^f((\mathbf{u}, p), (\mathbf{v}, q)) := 2\mu(\boldsymbol{\varepsilon}(\mathbf{u}), \boldsymbol{\varepsilon}(\mathbf{v}))_\Omega - (p, \operatorname{div}(\mathbf{v}))_\Omega + (q, \operatorname{div}(\mathbf{u}))_\Omega,$$

for all (\mathbf{u}, p) and (\mathbf{v}, q) in $\mathbf{V} \times Q$. J'ai volontairement évité d'écrire $\forall((\mathbf{u}, p), (\mathbf{v}, q)) \in \mathbf{V} \times Q$ parce que c'est assez lourd.

The boundary integral $\langle \sigma(\mathbf{u}, p)\mathbf{n}, \mathbf{v} \rangle_{\partial\Omega}$ can be simplified using the definition of \mathbf{V} and the boundary conditions on \mathbf{u} . Since $\mathbf{v} \cdot \mathbf{n} = 0$ on Γ_{bot} , $\langle \sigma(\mathbf{u}, p)\mathbf{n}, \mathbf{v} \rangle_{\Gamma_{\text{bot}}} = \sigma(\mathbf{u}, p)\mathbf{n} \cdot \boldsymbol{\tau} = 0$, owing to the boundary condition on Γ_{bot} . For Γ_{in} and Γ_{out} , we can replace with the inlet and outlet pressure boundary conditions, as specified in (3.2). Given (3.3) and (3.4), we can replace the boundary term on Σ using the solid dynamical equation:

$$\begin{aligned} \langle \sigma(\mathbf{u}, p)\mathbf{n}, \mathbf{v} \rangle_\Sigma &= \langle \sigma(\mathbf{u}, p)\mathbf{n} \cdot \mathbf{n}, \mathbf{v} \cdot \mathbf{n} \rangle_\Sigma \\ &= -\langle \rho^s \epsilon \partial_t \dot{d} + \mathcal{L}d, \mathbf{v} \cdot \mathbf{n} \rangle_\Sigma \\ &= -\langle \rho^s \epsilon \partial_t \mathbf{u} \cdot \mathbf{n}, \mathbf{v} \cdot \mathbf{n} \rangle_\Sigma - a^s(d, v), \end{aligned} \quad (3.6)$$

with

$$a^s(d, v) := \langle \mathcal{L}d, \mathbf{v} \cdot \mathbf{n} \rangle_\Sigma = c_1 \langle \partial_x d, \partial_x(v) \rangle_\Sigma + c_0 \langle d, v \rangle_\Sigma,$$

$v := \mathbf{v} \cdot \mathbf{n}$, for $\mathbf{v} \in \mathbf{V}$.

In the present configuration, we are able to combine the fluid and solid sub-problem into a single variational formulation (monolithic formulation): For $t > 0$, find $\mathbf{u}(t) \in \mathbf{V}$, $p(t) \in Q$ such that for all $(\mathbf{v}, q) \in \mathbf{V} \times Q$:

$$\left\{ \begin{aligned} &(\rho^f \partial_t \mathbf{u}, \mathbf{v})_\Omega + a^f((\mathbf{u}, p), (\mathbf{v}, q)) \\ &+ \underbrace{\langle \rho^s \epsilon \partial_t \mathbf{u}, v \rangle_\Sigma}_{\text{wall inertia}} + \underbrace{a^s(d(t'), v) + a^s\left(\int_{t'}^t u|_\Sigma(s) ds, v\right)}_{\text{solid elasticity}} \\ &= -\langle P_{\text{in}}, \mathbf{v} \cdot \mathbf{n} \rangle_{\Gamma_{\text{in}}} - \langle P_{\text{out}}, \mathbf{v} \cdot \mathbf{n} \rangle_{\Gamma_{\text{out}}}, \\ &d(t) = d(t') + \int_{t'}^t u(s)|_\Sigma ds, \end{aligned} \right. \quad (3.7)$$

with $t' < t$. Note that compared to the standard weak formulation of the Stokes equation, the solid inertia and the solid elastic terms appears in the fluid equations as a generalized Robin boundary condition (see [NV08]).

3.1.3 Discretization

3.1.3.1 Time discretization

The time interval $(0, T)$ is discretized by N subintervals (t_{n-1}, t_n) with $t_n = n\tau$, $n = 0, \dots, N-1$ and $\tau = T/(N-1)$. We denote by f^n the value of a function f at time t_n , or any approximation of it. The time derivative is discretized by the first-order backward finite difference

$$\partial_\tau f^n := \frac{1}{\tau}(f^n - f^{n-1}),$$

for $n \geq 1$. For the time discretization of the variational formulation (3.7), we use an implicit time scheme. The discretization of (3.7) yields the relation

$$d^n = d^{n-1} + \tau \partial_\tau d^n = d^{n-1} + \tau \mathbf{u}^n.$$

We introduce the bilinear form a^{fsi} on $\mathbf{V} \times Q$ and the linear form l^n on \mathbf{V} , respectively defined by

$$a^{\text{fsi}}((\mathbf{u}, p), (\mathbf{v}, q)) := \underbrace{\frac{\rho^f}{\tau} (\mathbf{u}, \mathbf{v})_\Omega + a^f((\mathbf{u}^n, p), (\mathbf{v}^n, q))}_{\text{fluid contribution}} + \underbrace{\frac{\rho^s \epsilon}{\tau} \langle u, v \rangle_\Sigma + \tau a^s(u, v)}_{\text{solid wall contribution}},$$

$$l^n(\mathbf{v}) := \frac{\rho^f}{\tau} (\mathbf{u}^{n-1}, \mathbf{v})_\Omega + \frac{\rho^s \epsilon}{\tau} \langle u^{n-1}, v \rangle_\Sigma - a^s(d^{n-1}, v) - \langle P_{\text{in}}^n, \mathbf{v} \cdot \mathbf{n} \rangle_{\Gamma_{\text{in}}} - \langle P_{\text{out}}^n, \mathbf{v} \cdot \mathbf{n} \rangle_{\Gamma_{\text{out}}},$$

for $(\mathbf{u}, p), (\mathbf{v}, q) \in \mathbf{V} \times Q$. The time-discrete variational of the monolithic formulations reads: Find $\mathbf{u}^n \in \mathbf{V}$, $p^n \in Q$ such that for all $\mathbf{v} \in \mathbf{V}$, $q \in Q$

$$\begin{cases} a^{\text{fsi}}((\mathbf{u}^n, p^n), (\mathbf{v}, q)) = l^n(\mathbf{v}) \\ d^n = d^{n-1} + \tau u^n, \end{cases} \quad (3.8)$$

Note that even if we are solving an FSI problem, the weak formulation is ultimately written with the fluid unknown.

3.1.3.2 Space discretization with finite element method with fitted meshes

The problem is discretized using a standard Galerkin method. Let consider a quasi-uniform triangulation \mathcal{T}_h of the domain Ω and a partition \mathcal{I}_h of Σ made of intervals, conforming with \mathcal{T}_h on Σ . The subscript h parametrizes the level of refinement of the triangulation, typically the maximum element diameter in the triangulation. For the numerical resolution of the time-discrete variational formulation, the infinite dimensional spaces V and L are approximated by finite dimensional spaces $\mathbf{V}_h \subset V$ and $Q_h \subset Q$, respectively. The finite element interpolation spaces \mathbf{V}_h and Q_h , for the velocity and the pressure, respectively, are built on the triangulation using

$$X_h^1 := \{\mathbf{V}_h \in C^0(\bar{\Omega}), \mathbf{v}_h|_K \in \mathbb{P}^1, \forall K \in \mathcal{T}_h\},$$

the space of piecewise linear functions on the triangulation. The space \mathbf{V}_h and Q_h are thus given by

$$\begin{aligned} \mathbf{V}_h &:= [X_h^1]^2 \cap V, \\ Q_h &:= X_h^1. \end{aligned}$$

The finite dimensional space approximation the velocity and the pressure do not satisfy the inf-sup condition. To retrieve stability for the forward problem, one can make use of the standard Brezzi-Pitkäranta stabilization [BP84] form

$$\begin{aligned} s_{\text{BP}}: X_h^1 \times X_h^1 &\rightarrow \mathbb{R} \\ (p, q) &\mapsto \mu \int_{\Omega} h^2 \nabla p \cdot \nabla q \, dx, \end{aligned}$$

The fully discrete method reads: Find $\mathbf{u}^n \in \mathbf{V}_h$, $p^n \in Q_h$, such that for all $\mathbf{v}_h \in \mathbf{V}_h$, $q_h \in Q_h$:

$$\begin{cases} a_*^{\text{fsi}}((\mathbf{u}^n, p^n), (\mathbf{v}, q)) = l^n(\mathbf{v}) \\ d^n = d^{n-1} + \tau u^n \end{cases} \quad (3.9)$$

where $a_*^{\text{fsi}} := a^{\text{fsi}}((\mathbf{u}^n, p^n), (\mathbf{v}, q)) + s_{\text{BP}}(p^n, q)$ for $(\mathbf{u}, p), (\mathbf{v}, q) \in \mathbf{V}_h \times Q_h$.

Remark 4

The inflow and outflow boundary conditions could be replaced by an inflow velocity profile, with an outlet pressure profile, which is much more common than 2 pressure boundary conditions in hemodynamic simulations.

3.2 The FSI state estimation algorithm based on a unique continuation approach

If the inflow and outflow boundary conditions are known, problem (3.9) can be solved. However in this section, the inflow and outflow boundary conditions are assumed to be unknown but (possibly noisy) velocity data are provided as a time-dependent field $\mathbf{u}_M : \Omega \times (0, T) \rightarrow \mathbb{R}^2$. The objective is to estimate the velocity and the pressure (and also the solid displacement) such that a certain distance to the velocity data is minimized with respect to the FSI equations (3.9).

3.2.1 Notions of unique continuation

Unique continuation is a class of inverse problems which consists in extending the solution of the PDE known in an open bounded subset to the whole domain of definition. We give in this section a summary of the major problematic of unique continuation. The purpose here is to present the logic of unique continuation in view of application in realistic data assimilation context.

Let consider a bounded domain $\omega \subset \Omega \subset \mathbb{R}^d$, a second order elliptic operator \mathcal{L} (to fix the ideas, $\mathcal{L} := -\Delta$). The general unique continuation problem can be formulated as: Find $u \in H^1(\Omega)$ such that

$$\begin{cases} \mathcal{L}u = f & \text{in } \Omega, \\ u = u_\omega & \text{in } \omega, \end{cases} \quad (3.10)$$

where $f \in H^{-1}(\Omega)$, $u_\omega \in H^1(\omega)$ are compatible data, meaning that $\mathcal{L}u_\omega = f$ in ω . Such a problem is ill-posed, in the sense that the solution does not depend continuously on the data. This means that one cannot find a constant C , such that for any $\mathbf{u} \in H^1(\Omega)$,

$$\|u\|_{H^1(\Omega)} \leq C (\|\mathcal{L}u\|_{H^{-1}(\Omega)} + \|u_\omega\|_{H^1(\omega)}).$$

In fact the unique continuation operator $u \in H^1(\Omega) \rightarrow (\mathcal{L}u, u|_\omega) \in H^{-1}(\Omega) \times H^1(\omega)$ does not have a closed range and its generalized inverse is not continuous. Even if stability cannot be stated, Hölder conditional stability results hold (see, e.g., [BHL18]).

The unique continuation problem (3.10) can be turned into an equivalent optimization problem with a PDE constraint. For instance, $u \in H^1(\Omega)$ solution of (3.10) is also solution of

$$\min_{\substack{u \in H^1(\Omega) \\ \mathcal{L}u = f \text{ in } \Omega}} \frac{1}{2} \|u - u_\omega\|_{L^2(\omega)}^2. \quad (3.11)$$

We can introduce the Lagrangian L associated to (3.11) such that the solution of the problem (3.10) is provided by the saddle points of L . For this purpose, let

consider the weak formulation of $\mathcal{L}u = f$ for test functions in $z \in H_0^1(\Omega)$

$$a(u, z) = l(z),$$

where a is a bilinear form in $H^1(\Omega) \times H_0^1(\Omega)$, and l a linear form on $H_0^1(\Omega)$. The PDE constraint is considered by means of the weak formulation tested with the Lagrange multiplier in $H_0^1(\Omega)$ as follow

$$L(u, z) := \frac{1}{2} \|u - u_\omega\|_{L^2(\omega)}^2 + a(u, z) - l(z).$$

The optimality conditions verified by the saddle points $(\bar{u}, \bar{z}) \in H^1(\Omega) \times H_0^1(\Omega)$ of L are given by

$$\begin{cases} (\bar{u}, v)_{L^2(\omega)} + a(v, \bar{z}) = (u_\omega, v)_{L^2(\omega)}, \\ a(\bar{u}, w) = l(w) \end{cases} \quad (3.12)$$

for all $(v, w) \in H^1(\Omega) \times H_0^1(\Omega)$. Note that the optimality conditions for the Lagrangian L yield a system of two equations, where the unknown and its dual variable must be solved simultaneously. The ill-posedness is commonly address either by regularizing-then-discretizing or discretizing-and-then-regularizing. The regularize-then-discretize strategy consists in regularizing the problem at a continuous level, and then apply the finite element discretization [EHN96]. The discretize-then regularize strategy adds regularizing terms after finite element discretization to ensure well-posedness (see [Bur16]). The discretize-then-regularize strategy is adopted in the present work.

Let $V_h \subset H^1(\Omega)$ denote the finite element space of continuous piecewise linear functions used to approximate the solution, and $V_h^0 := V_h \cap H_0^1(\Omega)$ the discrete space of test functions. The discrete regularized Lagrangian $L_h: V_h \times V_h^0 \rightarrow \mathbb{R}$ is given by:

$$L_h(u, z) := \frac{1}{2} \|u - u_\omega\|_{L^2(\omega)}^2 + \frac{1}{2} s_h(u, u) - \frac{1}{2} s_h^*(z, z) + a(u, z) - l(z),$$

where the bilinear forms

$$s_h: V_h \times V_h \rightarrow \mathbb{R}, \quad s_h^*: V_h^0 \times V_h^0 \rightarrow \mathbb{R},$$

stand for (weakly) consistent symmetric stabilization operators whose purpose is respectively to regularize the discrete problem and to stabilize the Lagrange multiplier associated to the PDE constraint. These stabilization operators are often similar to those used in traditional stabilized finite element methods (e.g., for fluid dynamics), such as the CIP stabilization (see, e.g., [Bur16]):

$$s_h^{\text{CIP}}(u, v) := \gamma \sum_{F \in \mathcal{F}_{int}} \int_F h \llbracket \nabla u \rrbracket_F \cdot \llbracket \nabla v \rrbracket_F ds, \gamma > 0, \quad (3.13)$$

where for a given interior face $F \in \mathcal{F}_{int}$ the symbol denotes $\llbracket \cdot \rrbracket_F$ the jump across the face.

The discrete saddle points $(\bar{u}, \bar{z}) \in V_h \times V_h^0$ are solutions of

$$\begin{cases} (\bar{u}, v)_{L^2(\omega)} + s_h(\bar{u}, v) + a_h(v, \bar{z}) = (u_\omega, v)_{L^2(\omega)}, \\ a(\bar{u}, w) - s_h^*(\bar{z}, w) = l(w) \end{cases} \quad (3.14)$$

3.2. THE FSI STATE ESTIMATION ALGORITHM BASED ON A UNIQUE CONTINUATION APPROX.

for all $(v, w) \in V_h \times V_h^0$. For $s_h = s_h^* = s_h^{\text{CIP}}$ it can be shown that problem (3.14) is well-posed and that the error estimate $\|u - \bar{u}\|_{L^2(\omega_T)} = \mathcal{O}(h^\delta)$ holds for subdomains $\omega_T \subsetneq \Omega$ and where $\delta \in (0,1)$ corresponds to the coefficient of the continuous conditional stability estimate (see, e.g., [BHL18, BBFV20]).

3.2.2 Unique continuation for FSI state estimation - fixed fluid domain

In this section, we want to estimate the FSI state in the fixed domain setting as introduced in (3.1)-(3.3)-(3.4), when no inflow or outflow boundary conditions are available, but only fluid velocity measurements $\mathbf{u}_M : \Omega \rightarrow \mathbb{R}^d$. Taking up the notation of Section 3.1, let introduce the test function space \mathbf{V}^0 defined by:

$$\mathbf{V}^0 = \{\mathbf{v} \in \mathbf{V}, \mathbf{v}|_{\Gamma_{\text{in}} \cup \Gamma_{\text{out}}} = \mathbf{0}\}.$$

We formulate an instantaneous unique continuation problem using the weak formulation (3.7) that reads: find $\bar{\mathbf{u}}(t) \in \mathbf{V}$, $\bar{p}(t) \in Q$, $\bar{d}(t) \in H_0^1(\Sigma)$, which minimizes

$$\frac{\gamma_M}{2} \|\bar{\mathbf{u}}(t) - \mathbf{u}_M(t)\|_{L^2(\Omega)}^2,$$

with respect to (3.7) for $\mathbf{v} \in \mathbf{V}^0$, $q \in Q$. The above problem is ill-posed. As explained in the general presentation of unique continuation Section 3.2.1, consistent regularization at the discrete level can ensure the uniqueness of the problem. In [Bur13, BNO19, BFO20], unique continuation has been considered for stationary problems (no time derivative). In [BBFV20], an extension to transient linearized Navier-Stokes equations is proposed after replacing the discrete time derivative $\partial_\tau \bar{\mathbf{u}}^n$ by $(\mathbf{u}_M^n - \mathbf{u}_M^{n-1})/\tau$. With this trick, instantaneous unique continuation is solved at each time iteration with a time-dependent right-hand side. This provides good results, but replacing the time derivative by the finite difference of the measurements is not recommended, especially when the measurements are noisy. Consequently we propose to approximate the discrete time derivative using the time previous estimation: $\partial_\tau \bar{\mathbf{u}}^n = (\bar{\mathbf{u}}^n - \bar{\mathbf{u}}^{n-1})/\tau$. Let us introduce the discrete test functions space:

$$\mathbf{V}_h^0 := [X_h^1]^d \cap \mathbf{V}^0,$$

the discrete regularized Lagrangian L_h writes:

$$\begin{aligned} L_h[(\mathbf{u}, p), (\mathbf{z}, y)] &:= \frac{\gamma_M}{2} \|\mathbf{u} - \mathbf{u}_M^n\|_\Omega^2 \\ &\quad + a^{\text{fsi}}[(\mathbf{u}, p), (\mathbf{z}, y)] - l^{n-1}(\mathbf{z}) \\ &\quad + \frac{1}{2} s_h[(\mathbf{u}, p), (\mathbf{u}, p)] - \frac{1}{2} s_h^*[(\mathbf{z}, y), (\mathbf{z}, y)]. \end{aligned}$$

for $(\mathbf{u}, p) \in \mathbf{V}_h \times Q_h$ and $(\mathbf{z}, y) \in \mathbf{V}_h^0 \times Q_h$, with $\gamma_M > 0$ a free parameter to quantify the confidence in the data. The bilinear form s_h and s_h^* denotes the stabilization of the primal unknown and their associated dual variables, respectively.

Stabilization terms Let denote by \mathcal{F}_{int} the set of interior element faces. The jump $[[\nabla \mathbf{v}]]_F$ of the normal derivative of a vector function \mathbf{v} across an interior face $F \in \mathcal{F}_{\text{int}}$ is given by the vector

$$[[\nabla \mathbf{v}]]_F := \nabla \mathbf{v} \cdot \mathbf{n}_1|_{K_1} + \nabla \mathbf{v} \cdot \mathbf{n}_2|_{K_2},$$

with $K_1, K_2 \in \mathcal{T}_h$ being two elements such that $K_1 \cap K_2 = F$, and \mathbf{n}_j the outward normal of $K_j, j = 1, 2$.

We introduce the following bilinear forms:

- $s_u(\mathbf{u}, \mathbf{v}) := \gamma_u \sum_{F \in \mathcal{F}_{int}} \int_F h \llbracket \nabla \mathbf{u} \rrbracket_F \cdot \llbracket \nabla \mathbf{v} \rrbracket_F \, ds + \gamma_{div} \int_{\Omega} (\operatorname{div} \mathbf{u})(\operatorname{div} \mathbf{v}) \, dx,$
- $s_p(p, q) := \gamma_p \int_{\Omega} h^2 \nabla p \cdot \nabla q \, dx,$
- $s_u^*(\mathbf{z}, \mathbf{w}) := \gamma_u^* \int_{\Omega} \nabla \mathbf{z} : \nabla \mathbf{w} \, dx,$
- $s_p^*(y, x) := \gamma_p^* \int_{\Omega} yx \, dx,$

for $(\mathbf{u}, p), (\mathbf{v}, q) \in \mathbf{V}_h \times Q_h, (\mathbf{z}, y), (\mathbf{w}, x) \in \mathbf{V}_h^0 \times Q_h^0$, and non-negative free parameters $\gamma_u, \gamma_p, \gamma_u^*, \gamma_p^*, \gamma_{div}$. The stabilization on the primal unknown is given by:

$$s_h[(\mathbf{u}, p), (\mathbf{v}, q)] = s_u(\mathbf{u}, \mathbf{v}) + s_p(p, q) \quad (3.15)$$

and the stabilization on the associated dual variable

$$s_h^*[(\mathbf{z}, y), (\mathbf{w}, x)] = s_u^*(\mathbf{z}, \mathbf{w}) + s_p^*(y, x). \quad (3.16)$$

The velocity is regularized in s_u by two terms. The first term is similar to a continuous interior penalization (CIP), see [Dou76]. It ensures smoothness of the solution by preventing internal fluctuations with a penalization of the jumps of the normal gradient across interior faces. The second term is a control on the incompressibility condition. The term $s_p(p, q)$ is close to the standard H^1 -Tikhonov regularization. Note that the stabilization of the direct unknown is only defined on a discrete level, and for the exact solution, the stabilization terms vanish when the level of refinement goes to zero. As the exact solution of the adjoint state is zero, the stabilizations of the adjoint variables is consistent with the exact solution. The numerical values of $\gamma_u, \gamma_p, \gamma_u^*, \gamma_p^*, \gamma_{div} > 0$ do not have an effect on the well-posedness, the stability or the convergence of the method over series of refined meshes, however they could parametrize the conditionnement of the numerical resolution [Nec20].

Optimality conditions for the regularized Lagrangian The saddle points $((\bar{\mathbf{u}}^n, \bar{p}^n), (\mathbf{z}, y)) \in \mathbf{V}_h \times Q_h \times \mathbf{V}_h^0 \times Q_h^0$ of the regularized Lagrangian L_h satisfy the following optimality conditions

$$\begin{cases} \gamma_M(\bar{\mathbf{u}}^n, \mathbf{v})_{\Omega} + s_h((\bar{\mathbf{u}}^n, \bar{p}^n), (\mathbf{v}, q)) + a^{\text{fsi}}((\mathbf{v}, q), (\mathbf{z}, y)) = \gamma_M(\mathbf{u}_M^n, \mathbf{v})_{\Omega}, \\ a^{\text{fsi}}((\bar{\mathbf{u}}^n, \bar{p}^n), (\mathbf{w}, x)) - s_h^*((\mathbf{z}, y), (\mathbf{w}, x)) = l^n(\mathbf{w}), \end{cases} \quad (3.17)$$

for all $(\mathbf{v}, q) \in \mathbf{V}_h \times Q_h$ and $(\mathbf{w}, x) \in \mathbf{V}_h^0 \times Q_h^0$.

The linear system associated to the numerical resolution of (3.17) writes as follows with block-matrix representation:

$$\left[\begin{array}{cc|cc} M_m + S_u & 0 & & A_{\text{fsi}}^T \\ 0 & S_p & & \\ \hline & & -S_u^* & 0 \\ A_{\text{fsi}} & & 0 & -S_p^* \end{array} \right] \begin{bmatrix} U \\ P \\ Z \\ Y \end{bmatrix} = \begin{bmatrix} U_m \\ 0 \\ L \\ 0 \end{bmatrix}. \quad (3.18)$$

The wall displacement \bar{d}^n is updated with the relation: $\bar{d}^n = \bar{d}^{n-1} + \tau \bar{\mathbf{u}}^n \cdot \mathbf{n}|_{\Sigma}$ in (3.9)₃.

The state estimation method is summarized in Algorithm 3

3.2. THE FSI STATE ESTIMATION ALGORITHM BASED ON A UNIQUE CONTINUATION APPRO.

Algorithm 3 Unique Continuation for FSI state estimation on fixed domain

Require: Initial conditions :

$$\begin{cases} \bar{\mathbf{u}}^0 = \mathbf{u}_0, p^0 = p_0 \text{ on } \Omega & \bar{d}^0 = d_0 \text{ on } \hat{\Sigma} \\ \gamma_M > 0 \\ \gamma_u, \gamma_p, \gamma_u^*, \gamma_p^*, \gamma_{div} > 0 \end{cases} \quad (3.19)$$

for $n = 1, \dots, N_T$ **do**

1) Find $((\bar{\mathbf{u}}^n, \bar{p}^n), (\mathbf{z}, y)) \in \mathbf{V}_h \times Q_h \times \mathbf{V}_h^0 \times Q_h$ solution of

$$\begin{cases} \gamma_M(\bar{\mathbf{u}}^n, \mathbf{v})_\Omega + s_h((\bar{\mathbf{u}}^n, \bar{p}^n), (\mathbf{v}, q)) + a^{\text{fsi}}((\mathbf{v}, q), (\mathbf{z}, y)) = \gamma_M(\mathbf{u}_M^n, \mathbf{v})_\Omega, \\ a^{\text{fsi}}((\bar{\mathbf{u}}^n, \bar{p}^n), (\mathbf{w}, x)) - s_h^*((\mathbf{z}, y), (\mathbf{w}, x)) = l^n(\mathbf{w}), \end{cases} \quad (3.20)$$

for all $(\mathbf{v}, q) \in \mathbf{V}_h \times Q_h$ and $(\mathbf{w}, x) \in \mathbf{V}_h^0 \times Q_h$, with s_h, s_h^* defined in (3.15) and (3.16), respectively.

2) Update the wall displacement $\bar{d}^n = \bar{d}^{n-1} + \tau \bar{\mathbf{u}}^n \cdot \mathbf{n}|_\Sigma$.

end for

3.2.3 Numerical results

In this section, we illustrate the FSI estimation method in Algorithm 3 on the synthetic test case of the pressure wave propagation in a compliant tube, inspired from hemodynamics. We also provide numerical results with noisy data.

3.2.3.1 Data generation (forward problem)

In order to validate the continuation (Section 3.2.2), the measurements are generated by solving the problem (3.9), with

$$T = 1.5 \cdot 10^{-2} \text{s}$$

$$\rho^f = 1.0 \text{g/cm}^3, \quad \mu = 0.035 \text{P}$$

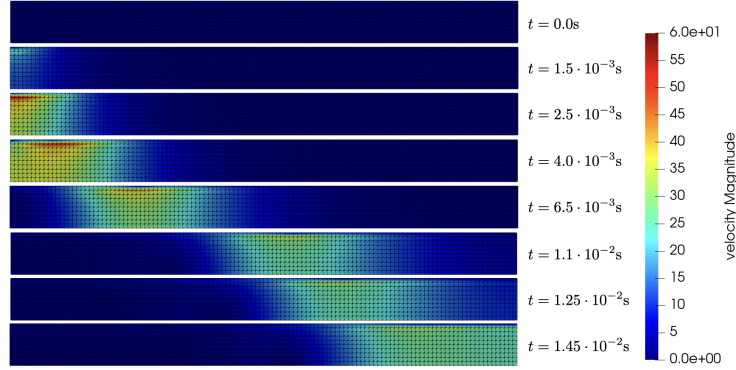
$$\rho^s = 1.1 \text{g/cm}^3, \quad \epsilon = 0.1 \text{cm}, \quad E = 0.75 \cdot 10^6 \text{Ba (barye)}, \quad \nu = 0.5$$

Physical parameters and time are given in the CGS unit system. The fluid domain is a rectangle $[0, 6] \times [0, 0.5]$, $R = 0.5 \text{cm}$, $L = 6 \text{cm}$. A pressure profile is imposed in the inlet Γ_{in} :

$$\forall t \in (0, T), \forall \boldsymbol{\xi} \in \Gamma_{\text{in}}, P_{\text{in}}(\boldsymbol{\xi}, t) = \begin{cases} -\frac{P_{\text{max}}}{2} (1 - \cos(\frac{2\pi t}{T^*})) & \text{if } t < T^* \\ 0 & \text{otherwise} \end{cases}$$

with $P_{\text{max}} = 2.0e4 \text{ dyne/cm}^2$, $T^* = 5.0e - 3 \text{s}$.

An homogeneous Neumann condition is imposed on the outflow boundary Γ_{out} ($P_{\text{out}} = 0$). The mesh of the fluid domain is composed of 2400 regular triangles. It is composed of 1331 vertices, 260 edges and 2400 triangles. The characteristic mesh size is $h \approx 0.05 \text{cm}$ (10 edges along y). The parameters of the time step of discretization is $\tau = 1.0 \cdot 10^{-4} \text{s}$. As initial conditions, we use $\mathbf{u}^0 \equiv 0$ and $\mathbf{d}^0 \equiv 0$.



(a) Velocity (cm/s)

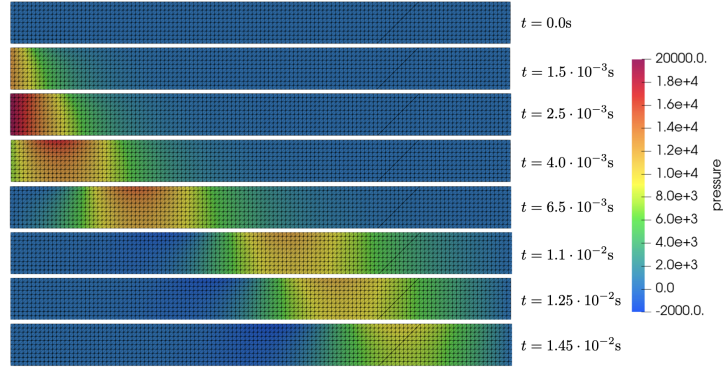
(b) Pressure (dyne/cm²)

Figure 3.3: Ground truth solution.

The discrete solution of the forward problem (the synthetic data) will be referred as \mathbf{u}_M^n and is reported in Figure 3.3.

Noisy data are also generated by adding a gaussian noisy proportional to the maximum velocity component-wise at the nodal values of \mathbf{u}_M^n , as follows:

$$\mathbf{u}_M^n(\mathbf{x}_h^j) = \begin{pmatrix} \mathbf{u}_M^n(\mathbf{x}_h^j) \cdot \mathbf{e}_x \\ \mathbf{u}_M^n(\mathbf{x}_h^j) \cdot \mathbf{e}_y \end{pmatrix} \rightarrow \begin{pmatrix} \mathbf{u}_M^n(\mathbf{x}_h^j) \cdot \mathbf{e}_x + \delta_{j,x} \mathbf{u}^n \\ \mathbf{u}_M^n(\mathbf{x}_h^j) \cdot \mathbf{e}_y + \delta_{j,y} \mathbf{u}^n \end{pmatrix} \quad (3.21)$$

with for each component $d = x, y$, $\delta_{j,d} \mathbf{u}^n := \delta_{\text{noise}} k_j \|\mathbf{u}_M^n \cdot \mathbf{e}_d\|_\infty$, $0 \leq \delta_{\text{noise}} \leq 1$ being the level of noise, k_j a realization of a random variable with a unit normal distribution. In Figure 3.4, a visualization of the velocity is provided at one time step, for $\delta_{\text{noise}} = 1\%, 5\%$.

3.2.3.2 Pressure estimation

In this section, the FSI state estimation on fixed domain is applied for the absolute pressure estimation, when the inlet pressure is unknown P_{in} , with $P_{\text{out}} = 0$. The values of the parameters $\gamma_u, \gamma_p, \gamma_u^*, \gamma_p^*, \gamma_{\text{div}}$ are set once for all simulations, and

3.2. THE FSI STATE ESTIMATION ALGORITHM BASED ON A UNIQUE CONTINUATION APPRO.



Figure 3.4: The data at t_{50} . From top to bottom: ground truth without noise, $\delta_{\text{noise}} = 1\%$, and $\delta_{\text{noise}} = 15\%$

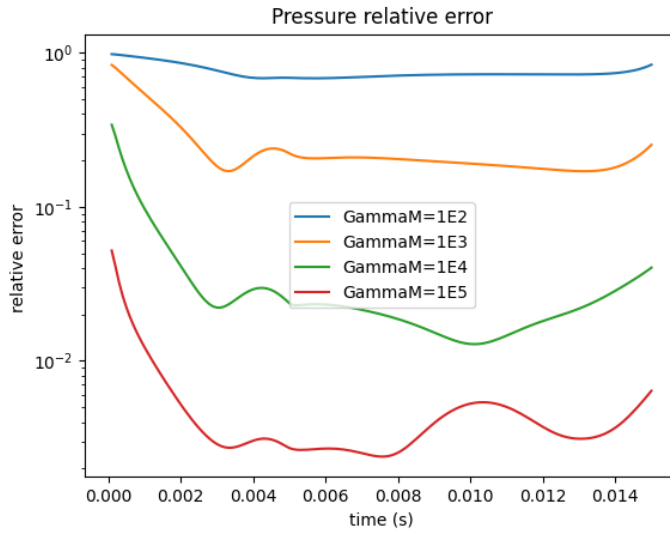


Figure 3.5: Relative error for the pressure with noise-free measurements

we consider different level of confidence in the data, by testing different values of γ_M .

$$\gamma_u = 0.1(1.0, \text{ for noisy data}), \quad \gamma_p = 0.01, \quad \gamma_u^* = 0.1, \quad \gamma_p^* = 0.1, \quad \gamma_{div} = 0.1$$

Firstly, the data are assumed to be noise-free. Then noisy data are assimilated for $\delta_{\text{noise}}, \delta_{\text{noise}} = 1\%, 5\%$. The computations are performed on **FELiSCE** and the linear system (3.18) is solved at each iteration using a ASM pre-conditioned GMRES solver. The comparisons with the reference solution are quantified in terms of the

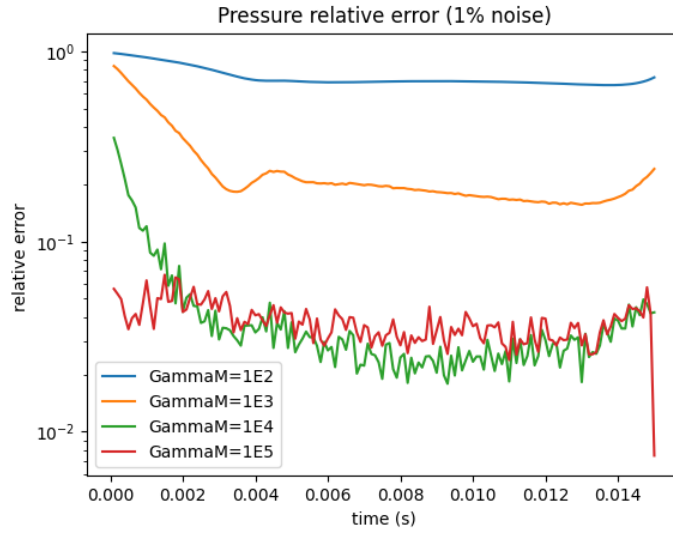


Figure 3.6: Relative error for the pressure with 1% noise in the velocity measurements

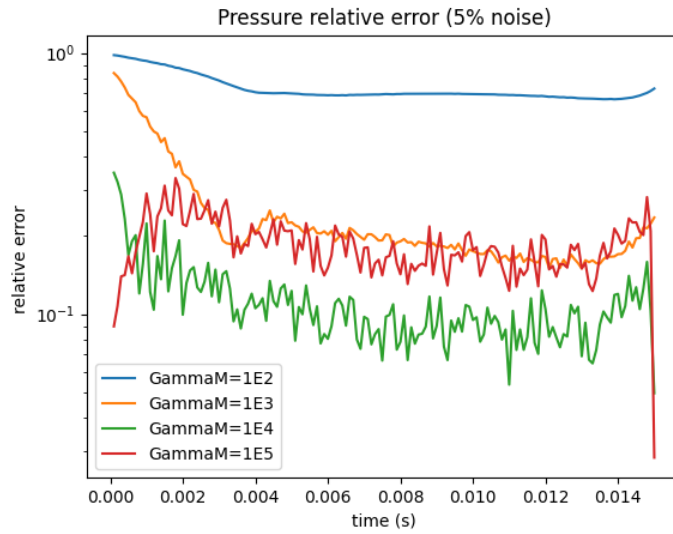


Figure 3.7: Relative error for the pressure with 5% noise in the velocity measurements

relative error defined by:

$$\text{Err}_{L^2(\Omega)}(q) := \frac{\|q - q_{ref}\|_{L^2(\Omega)}}{\|q_{ref}\|_{L^2(\Omega)}},$$

3.2. THE FSI STATE ESTIMATION ALGORITHM BASED ON A UNIQUE CONTINUATION APPRO.

where $q \in L^2(\Omega)$ and q_{ref} are the estimated quantities and the reference solution (obtained numerically), respectively.

The Algorithm 3 provides a reasonable approximation of the pressure with noise-free measurements. For $\gamma_M > 10^4$, the relative error is below 5%, after 20 time iterations as reported in Figure 3.5. The larger the parameter γ_M , the more accurate the state estimation algorithm is, as shown by Figure 3.5. As suggested by Figure 3.9 and 3.10, small values of γ_M filter the noise in the measurements and yield state estimation with very low sensitivity to the level of noise. In fact for $\gamma_M = 10^2, 10^3$ the relative error of the pressure is equivalent from $\delta_{noise} = 0$ to 5%. In Figure 3.11, a snapshot of the estimated (absolute) pressure at t_{50} for $\gamma_M = 10^3$ with 0 to 5% noise in the measurements confirms this statement, qualitatively. Increasing γ_M decreases the relative error while adding up noise in the estimation progressively, see Figure 3.6, 3.7. For $\gamma_M = 10^4, 10^5$, the pressure estimation is provided with a relative error lower than 1%. The fluctuation in the pressure estimation due to the noisy measurements are of small amplitude. Large γ_M could even deteriorate the pressure estimation for higher level of noise.

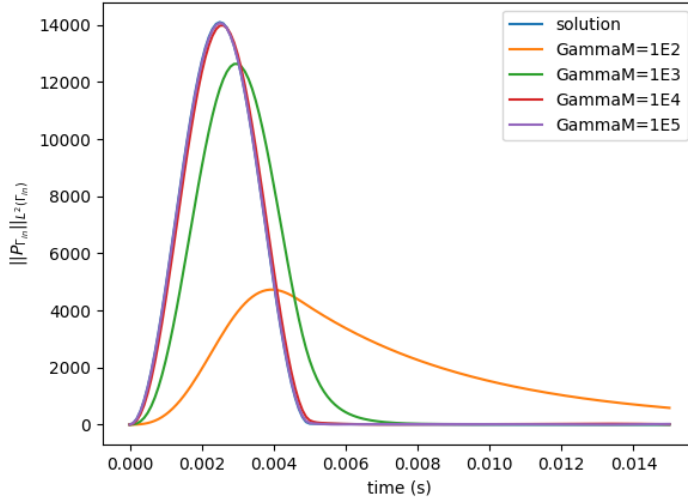


Figure 3.8: Estimated inflow pressure profiles with noise-free data

We now investigate the quality of the inflow pressure estimation $\int_{\Gamma_{in}} \bar{p}^n d\gamma$. With sufficiently large values of γ_M , a satisfactory estimation of the inflow pressure profile is returned, as reported in Figures 3.9 and 3.8. Having $\gamma_M = 10^3$ seems to be a fair compromise between accuracy of inflow profile and its smoothness, when the data are noisy.

We finally look at the velocity at the fluid structure interface. Since the forward problem and the FSI estimation have the same initial condition for the displacement at the interface $\bar{d}^0 = d^0 = 0$, a good approximation of the velocity at the interface is equivalent to a good approximation of the displacement. The velocity at the interface is provided in Figure 3.12 at the time $t_n, n = 10, 50, 100, 150$. The displacement is well approximated with $\gamma_M > 10^4$, however in case of noise, such a large value would

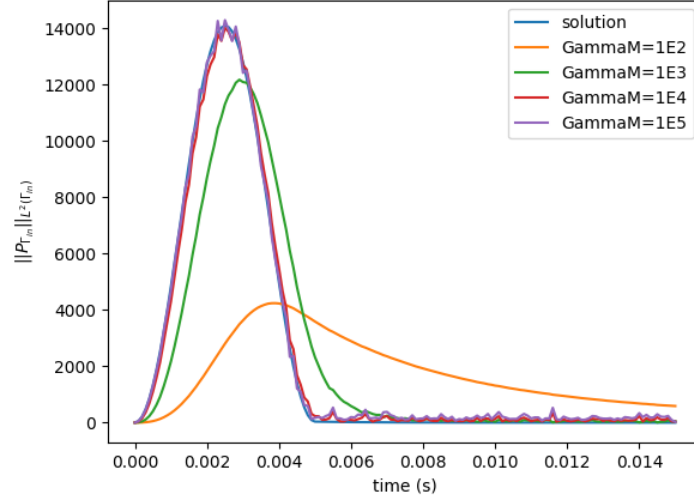


Figure 3.9: Estimated inflow pressure profiles with 1% noise in the measurements

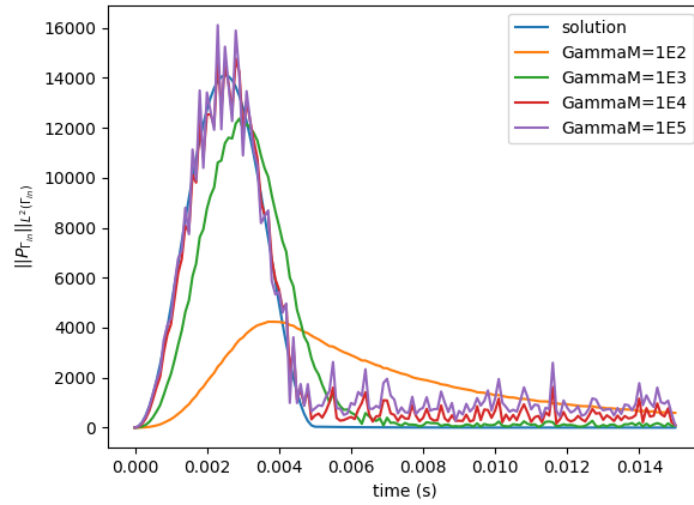


Figure 3.10: Estimated inflow pressure profiles with 5% noise in the measurements

not be reasonable. For $\gamma_M = 10^3$ the displacement at the interface estimated by the continuation has relevant order of magnitude and profile, even if it lacks accuracy.

The method has shown good estimation of the FSI state, and especially at the boundary of the domain where the inflow boundary condition is unknown. A major

3.2. THE FSI STATE ESTIMATION ALGORITHM BASED ON A UNIQUE CONTINUATION APPROX.



Figure 3.11: Estimated pressure at t_{50} . $\gamma_M = 10^3$, for 1% noise (middle), 5% noise (bottom). The reference solution is given on top.

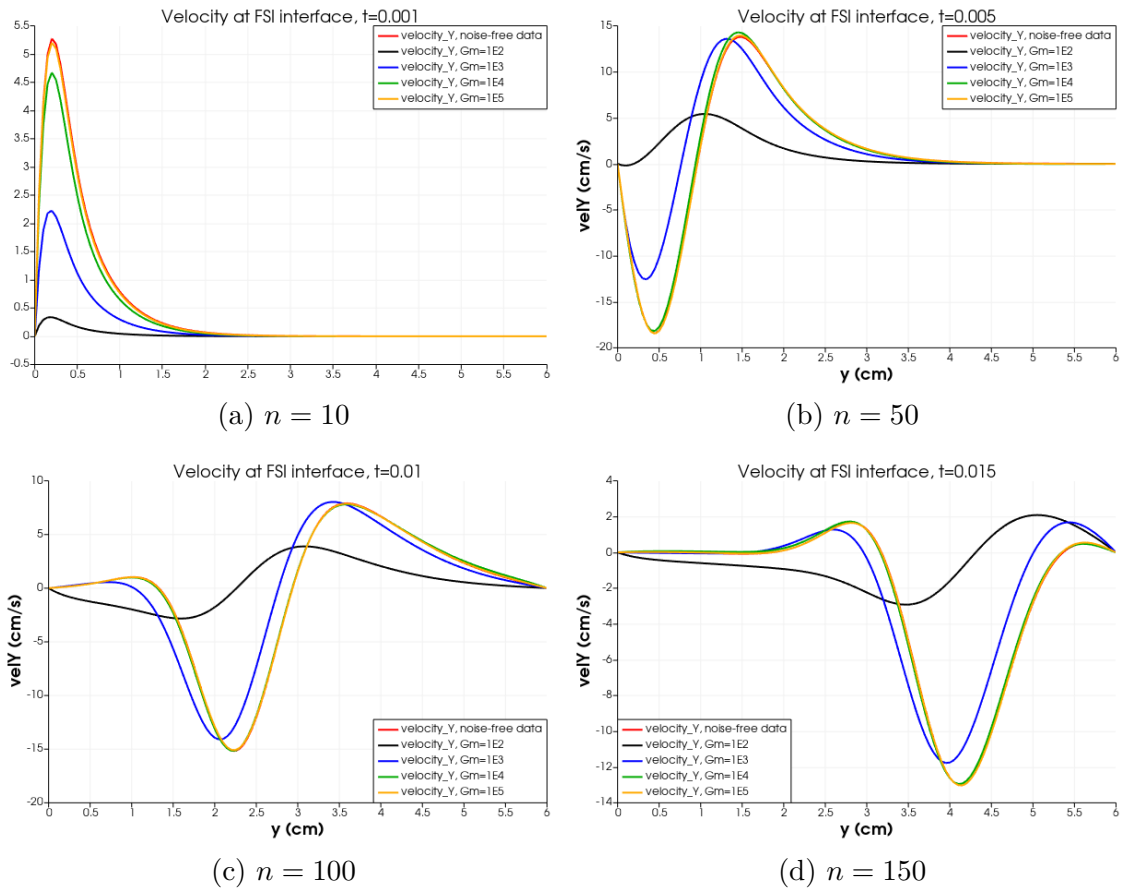


Figure 3.12: Vertical velocity at the interface, with noise-free data

limitation of those results is in the FSI setting is that the FSI state (fluid and solid) has been reduced to the fluid state variables with few manipulations, and no moving domain is considered. In a more realistic FSI setting the motion of the fluid domain has to be taken into account in the equations, and the solid variable cannot be

eliminated in the form of fluid unknowns. In this case, partitioned solvers are often preferred. Instead of designing a continuation applied to a partitioned resolution of non-linear FSI, which additional unknowns, we propose to investigate an approach which combines a Luenberger estimator with continuation based estimation of the boundary conditions.

3.3 FSI State estimation by combining unique continuation and a Luenberger state estimator

In this section, we keep the same FSI setting with the monolithic formulation. Next chapter will tackle partitioned resolution of FSI equations with moving domain. As shown previously, the unique condition approach provide pressure estimation via the integration of the FSI coupling. It is also possible to get reasonable boundary information. Hence we will formulate an FSI state estimation based on the combinaison of unique continuation and a filter on the fluid equations (Stokes). The filter on the Stokes equations will be designed as a Luenberger state observer on the fluid velocity. Luenberger state observers dissipate the error due to perturbed initial condition, but it requires suitable boundary conditions. Those will be provided using unique continuation on the fluid equations with FSI coupling at the interface. In view of a partitioned resolution, this combination of unique continuation and Luenberger observer is used on the fluid solver, with appropriate interface boundary conditions. We propose a formulation of the monolithic FSI case, as a preliminary step toward the FSI estimations state for partitioned fluid-solid computation.

3.3.1 FSI state estimation algorithm

We consider a state estimation approach based Luenberger observer for the velocity. However to solve the fluid equations, boundary conditions have to be specified, especially inflow and outflow boundary conditions. We assume that velocity measurements are provided $\mathbf{u}_M^n, n = 1, \dots, N_T$, at equally distributed time intervals. We denote by $(\tilde{\mathbf{u}}^n, \tilde{p}^n, \tilde{\mathbf{d}}^n)$ the FSI state estimation at time $t = t_n$, with $\tilde{\mathbf{u}}^n$ the estimated fluid velocity, \tilde{p}^n the estimated pressure and $\tilde{\mathbf{d}}^n$ the estimated interface displacement. Since it is a sequential state estimation, at $t = t_n$, we dispose of $(\tilde{\mathbf{u}}^{n-1}, \tilde{p}^{n-1}, \tilde{\mathbf{d}}^{n-1})$, with the measurement \mathbf{u}_M^n .

Boundary conditions estimation using unique continuation To provide boundary conditions for the Luenberger observer, an intermediate fluid state is obtained by solving the unique continuation problem at the discrete level: Find $(\bar{\mathbf{u}}^n, \bar{p}^n) \in \mathbf{V}_h \times Q_h, (\mathbf{z}, y) \in \mathbf{V}_h^0 \times Q_h$ solution of

$$\begin{cases} \gamma_M(\bar{\mathbf{u}}^n, \mathbf{v})_\Omega + s_h((\bar{\mathbf{u}}^n, \bar{p}^n), (\mathbf{v}, q)) + a^{\text{fsi}}((\mathbf{v}, q), (\mathbf{z}, y)) = \gamma_M(\mathbf{u}_M^n, \mathbf{v})_\Omega, \\ a^{\text{fsi}}((\bar{\mathbf{u}}^n, \bar{p}^n), (\mathbf{w}, x)) - s_h^*((\mathbf{z}, y), (\mathbf{w}, x)) = \tilde{l}^n(\mathbf{w}), \end{cases} \quad (3.25)$$

for all $(\mathbf{v}, q) \in \mathbf{V}_h \times Q_h$ and $(\mathbf{w}, x) \in \mathbf{V}_h^0 \times Q_h$. $\gamma_M > 0$ a free parameter and the linear form $\tilde{l}_h^{n-1} : \mathbf{V}_h^0 \rightarrow \mathbb{R}$ is given by

$$\tilde{l}_h^{n-1}(\mathbf{z}) = \frac{\rho^f}{\tau}(\tilde{\mathbf{u}}^{n-1}, \mathbf{z})_\Omega + \frac{\rho^s \epsilon}{\tau}(\tilde{u}^{n-1}, z)_\Sigma - a^s(\tilde{\mathbf{d}}^{n-1}, z), \quad (3.26)$$

3.3. FSI STATE ESTIMATION BY COMBINING UNIQUE CONTINUATION AND A LUENBERGER OBSERVER

Algorithm 4 FSI state estimation with Luenberger observer in fluid velocity and continuation-based boundary conditions - fixed fluid domain

Require: Initial conditions :

$$\begin{cases} \bar{\mathbf{u}}^0 = \mathbf{u}_0, p^0 = p_0 \text{ on } \Omega & \bar{d}^0 = d_0 \text{ on } \hat{\Sigma} \\ \gamma_M > 0, \gamma_L > 0 \\ \gamma_u, \gamma_p, \gamma_u^*, \gamma_p^*, \gamma_{div} > 0 \end{cases} \quad (3.22)$$

for $n = 1, \dots, N_T$ **do**

1) Find $((\bar{\mathbf{u}}^n, \bar{p}^n), (\mathbf{z}, y)) \in \mathbf{V}_h \times Q_h \times \mathbf{V}_h^0 \times Q_h$ solution of

$$\begin{cases} \gamma_M(\bar{\mathbf{u}}^n, \mathbf{v})_\Omega + s_h((\bar{\mathbf{u}}^n, \bar{p}^n), (\mathbf{v}, q)) + a^{\text{fsi}}((\mathbf{v}, q), (\mathbf{z}, y)) = \gamma_M(\mathbf{u}_M^n, \mathbf{v})_\Omega, \\ a^{\text{fsi}}((\bar{\mathbf{u}}^n, \bar{p}^n), (\mathbf{w}, x)) - s_h^*((\mathbf{z}, y), (\mathbf{w}, x)) = \tilde{l}^n(\mathbf{w}), \end{cases} \quad (3.23)$$

for all $(\mathbf{v}, q) \in \mathbf{V}_h \times Q_h$ and $(\mathbf{w}, x) \in \mathbf{V}_h^0 \times Q_h$, with s_h, s_h^* defined in (3.15) and (3.16), respectively.

2) Find the fluid state estimation $(\tilde{\mathbf{u}}_h^n, \tilde{p}_h^n) \in \mathbf{V}_h \times Q_h$, solution of

$$\begin{cases} a^{\text{fsi}}((\tilde{\mathbf{u}}^n, \tilde{p}^n), (\mathbf{v}, q)) + s_{\text{BP}}(\tilde{p}^n, q) + \gamma_L(\tilde{\mathbf{u}}^n - \mathbf{u}_M^n, \mathbf{v})_\Omega \\ = \tilde{l}^n(\mathbf{v}) - \langle \tilde{p}^n |_{\Gamma_{\text{in}}}, \mathbf{v} \cdot \mathbf{n} \rangle_{\Gamma_{\text{in}}} - \langle \tilde{p}^n |_{\Gamma_{\text{out}}}, \mathbf{v} \cdot \mathbf{n} \rangle_{\Gamma_{\text{out}}} \end{cases} \quad (3.24)$$

3) Update the wall displacement $\tilde{d}^n = \tilde{d}^{n-1} + \tau \tilde{\mathbf{u}}^n \cdot \mathbf{n}|_\Sigma$.

end for

for $\mathbf{z} \in \mathbf{V}_h^0$, $z := \mathbf{z} \cdot \mathbf{n}$ on Σ .

This is equivalent to solving the constrained minimization problem:

$$\begin{aligned} \min_{\mathbf{u} \in \mathbf{V}_h} \quad & \frac{1}{2} \|\mathbf{u} - \mathbf{u}_M^n\|_{L^2(\Omega)}^2 \\ a^{\text{fsi}}((\mathbf{u}, p), (\mathbf{v}, q)) &= l^n(\mathbf{v}) \\ \forall (\mathbf{v}, q) \in \mathbf{V}_h^0 \times Q_h \end{aligned} \quad (3.27)$$

with the instantaneous discrete time derivative approximated by $(\bar{\mathbf{u}}^n - \tilde{\mathbf{u}}^{n-1})/\tau$.

Luenberger state observer for the fluid equations The current state estimation is obtained from the following problem: Find $(\tilde{\mathbf{u}}_h^n, \tilde{p}_h^n) \in \mathbf{V}_h \times Q_h$, such that $\forall (\mathbf{v}_h, q_h) \in \mathbf{V}_h \times Q_h$,

$$\begin{cases} a^{\text{fsi}}((\tilde{\mathbf{u}}^n, \tilde{p}^n), (\mathbf{v}, q)) + s_{\text{BP}}(\tilde{p}^n, q) + \gamma_L(\tilde{\mathbf{u}}^n - \mathbf{u}_M^n, \mathbf{v})_\Omega \\ = \tilde{l}^n(\mathbf{v}) - \langle \tilde{p}^n |_{\Gamma_{\text{in}}}, \mathbf{v} \cdot \mathbf{n} \rangle_{\Gamma_{\text{in}}} - \langle \tilde{p}^n |_{\Gamma_{\text{out}}}, \mathbf{v} \cdot \mathbf{n} \rangle_{\Gamma_{\text{out}}} \\ \tilde{d}^n = \tilde{d}^{n-1} + \tau \tilde{\mathbf{u}}^n \cdot \mathbf{n}|_\Sigma \end{cases} \quad (3.28)$$

with $\gamma_L > 0$ a free-parameter which quantifies the confidence in the data. Compared to the forward problem in (3.1), we are just solving on a discrete level the momentum equation for the fluid equation which reads

$$\rho^f \partial_t \mathbf{u} - \text{div } \boldsymbol{\sigma}(\mathbf{u}, p) + \gamma_L(\tilde{\mathbf{u}} - \mathbf{u}_M) = 0 \quad \text{in } \Omega \times (0, T),$$

and the boundary conditions are imposed at the discrete level from the solution of (3.25). Here Neumann inflow and outflow boundary conditions but we could consider Dirichlet inflow and Neumann outflow boundary conditions.

The FSI State estimation combining unique continuation and a Luenberger state estimator is summarized in Algorithm 4.

3.3.2 Numerical results

In this section, we provide some numerical results of application of the FSI state estimation algorithm 4, based on the two-stepped approach. The velocity measurements are generated as in Section 3.2.3, with the same physical parameters.

Numerical results with the new approach are provided with the following parameters:

$$\gamma_u = 0.1, \quad \gamma_p = 0.01, \quad \gamma_u^* = 0.1, \quad \gamma_p^* = 0.1, \quad \gamma_{div} = 0.1.$$

With noise-free data, we assess the accuracy of the estimation for $\gamma_M \in \{10^3, 10^4, 10^5\}$ and $\gamma_L \in \{10^2, 10^3, 10^4, 10^5\}$. We use the unique continuation solution to impose inflow and outflow pressure for the fluid equations. The results are reported in Figure 3.13, 3.14 and 3.15. The continuation is solved using a *GMRES – ASM* solver. Note that for $\gamma_M = 10^5$, we run the simulations with $\gamma_u = 10, \gamma_p = 0.1$, to improve the conditionnement of the unique continuation linear system.

The relative error for the pressure and the velocity are computed respectively as follows:

$$\text{ErrU}_{L^2(\Omega)} := \frac{\|\tilde{\mathbf{u}} - \mathbf{u}_{ref}\|_{L^2(\Omega)}}{\|\mathbf{u}\|_{L^2(\Omega)}}, \quad \text{ErrP}_{L^2(\Omega)} := \frac{\|\tilde{p} - p_{ref}\|_{L^2(\Omega)}}{\|p\|_{L^2(\Omega)}},$$

for $\mathbf{u}_{ref}, p_{ref}$ the reference solution, obtained by solving the forward problem. The relative errors are reported in Figure 3.13 to 3.15, when noise-free velocity measurements are used.

Velocity-pressure estimation for noise-free data For a same value of γ_M , increasing γ_L reduces the relative error for the fluid velocity estimation, see Figures 3.13(a), 3.14(a) and 3.15(a). Concerning the absolute pressure estimation, one would expect the same behavior for the (absolute) pressure estimation, as for the unique continuation based FSI estimation, see Figure 3.5. For γ_M going from 10^3 to 10^4 , there is significant improvement of the accuracy of the estimated pressure. The relative error of the estimated pressure is under 20% after 30 iterations (Figures 3.13(b)) for $\gamma_M = 10^3$ and strictly under 9% for $\gamma_M = 10^4, 10^5$ (Figures 3.14(b), 3.15(b)) after only 5 iterations. Nevertheless, for $\gamma_L > 10^3$, the relative error for the pressure seems similar for all γ_M . For the same γ_L , increasing γ_M slightly improves the overall accuracy of the fluid state estimation.

Velocity-pressure estimation with noisy data We also provide some results when dealing with noisy data. We still get reasonable relative error. For $\gamma_M = 10^3, \gamma_L = 10^3$ and 5% of noise, the relative error is mostly under 20% for the velocity and the pressure estimation. However for $\gamma_L > 10^4$, the noisy in the data starts to severely affect the regularity of the solution in space and time, as reported in Figure 3.16.

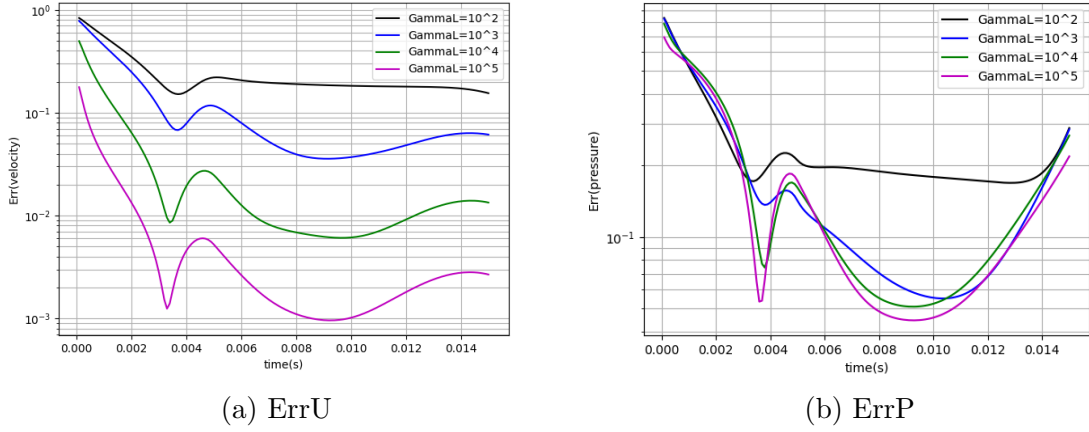


Figure 3.13: Relative error of velocity and the pressure for $\gamma_M = 10^3$, noise-free data.

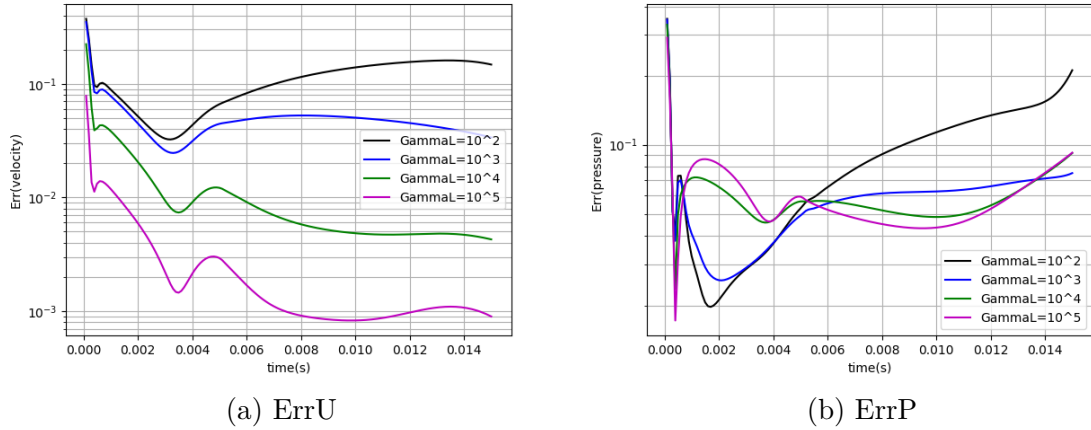


Figure 3.14: Relative error of velocity and the pressure for $\gamma_M = 10^4$, noise-free data.

3.4 Conclusion

In this chapter, we provide two FSI state estimation algorithms 3 and 4 to estimate the FSI state pressure with velocity measurements. The algorithms have been formulated based on a monolithic FSI equations on a fixed domain, where the solid unknowns can be substituted to the fluid unknown. The first FSI state estimation algorithm is based on a unique continuation approach, written as a PDE constraint minimization of the distance to the velocity measurements. The ill-posedness of such problem is resolved at the discrete level with suitable consistent stabilizations. Without any knowledge of the inflow and outflow boundary conditions,

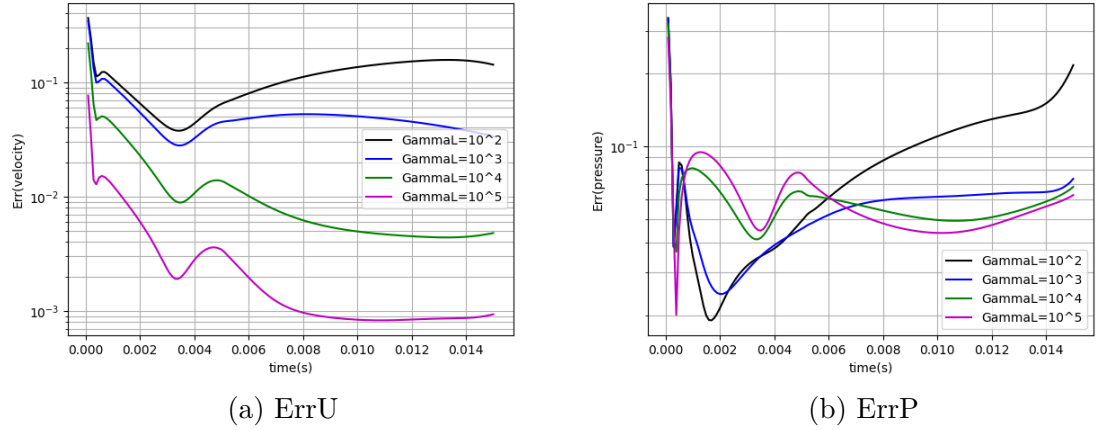
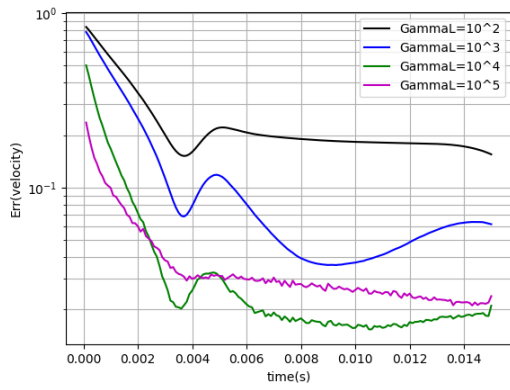
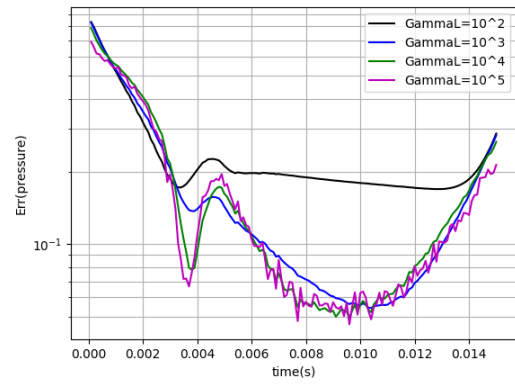


Figure 3.15: Relative error of velocity and the pressure for $\gamma_M = 10^5$, noise-free data.

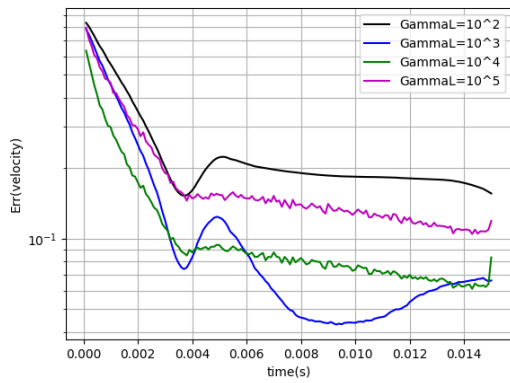
we are thus able to provide an estimated pressure with reasonable accuracy. The second FSI State estimation starts with a unique continuation as the previous algorithm, but only to provide boundary conditions for a fluid solver with a data feedback terms. The utility of such approach is that it can be adapted to FSI partitioned solvers with low computation effort, as it will be detailed in the next chapter. The second FSI algorithm provides similar accuracy as the first algorithm.



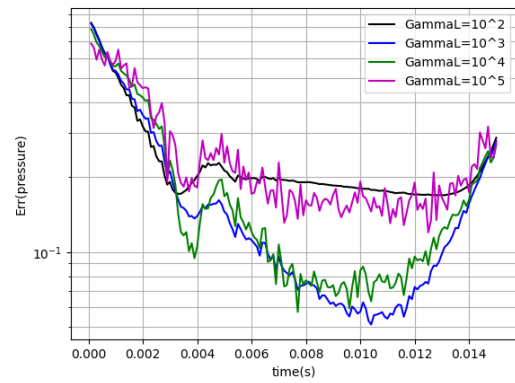
(a) ErrU, $\delta_{\text{noise}} = 1\%$



(b) ErrP, $\delta_{\text{noise}} = 5\%$



(c) ErrU, $\delta_{\text{noise}} = 5\%$



(d) ErrP, $\delta_{\text{noise}} = 5\%$

Figure 3.16: Relative error for the velocity and the pressure estimations, for $\gamma_M = 10^3$ with noisy data, δ_{noise} parametrizes the percentage of noise.

State estimation in fluid-structure interaction from 4D Flow MRI data: moving fluid domain

4.1 Introduction

In this chapter, the fluid-structure interaction (FSI) state estimation is addressed in the case in which the fluid domain motion cannot be neglected (e.g., for moderate or large interfacial deflections). In the previous chapter, the linear FSI setting assumed small solid displacements in the framework of the propagation of a pressure wave within an elastic two-dimensional channel. The fluid was governed by the Stokes equations, whereas the elastic thin wall was restricted to membrane deformations, sufficiently small to consider a fixed-domain problem. In this chapter, we propose an extension of the combined unique continuation / Luenberger FSI state estimation (see Algorithm 4) named UCL-Fluid to the case of moving fluid domains. In contrast to Chapter 3, the FSI system is here solved using a partitioned resolution procedure. The fluid and solid solvers are hence completely independent and are coupled by exchanging appropriate interfacial data (velocity and stresses). More precisely, the fluid and the solid solver are coupled by means of explicit Robin-Neumann scheme, as reported in [FMV13, LVCF17]. This loosely coupled scheme is unconditionally stable and delivers first-order accuracy in time (see [FMV13, LVCF17]). Moreover, it (only) involves the solid inertia contribution within the fluid equations in the form of a standard Robin condition on the fluid-structure interface, much simpler than in Chapter 3 (generalized Robin condition).

For UCL-Fluid, the fluid solver is formulated as the two-stepped approach introduced in Section 3.3.1 with: (i) unique continuation to provide physically filtered and non-parametric boundary conditions using the velocity data and some information at the interface; (ii) a Luenberger state observer for the fluid equations to estimate the whole fluid state. Note that, in the present moving fluid domain framework, it may be useful to introduce also a correction in the solid, since perturbations in the fluid state estimation can lead to perturbations in the solid and, subsequently, to errors in the fluid domain configuration. As a result, Eulerian velocity data could be taken from locations outside the (target) fluid domain. In order to circumvent this issue, a second FSI state estimation algorithm is proposed in which the solid solver involves two state observers, the *Direct Velocity Feedback* (DVF) and *Schur Displacement Feedback* (SDF), using solid displacements and velocity measurements, as reported in [MCLT08, MCLT09, BCF⁺13]. This second approach will be termed UCL-FSI. The reconstruction of the wall displacement and velocity proposed in Chapter 2 could be (partly) used as measured data for UCL-FSI.

The rest of this chapter is organized as follows. After introducing the forward problem, the algorithm UCL-Fluid for moving domain is presented (without solid feedback). Numerical investigations are reported on an academic example modeling the propagation of the pressure wave in a three-dimensional elastic tube. The

need for solid feedback is also discussed and motivated. Then, the new UcL-FSI state estimator is introduced. The optimal choice of the free feedback parameters is discussed through spectral analysis, in a simplified but physically relevant FSI model. Finally, numerical results are reported in the moving fluid domain setting, with an arbitrary solid initial state, in order to show the capabilities of the second FSI state estimator.

4.2 The FSI (forward) problem

In this section, the forward FSI problem is presented after introducing the kinematical assumptions and the useful notions.

4.2.1 General setting and equations

Let consider the reference configuration of a fluid domain $\hat{\Omega} \subset \mathbb{R}^d$ and a partition of its boundary $\partial\hat{\Omega} = \hat{\Gamma}_{\text{in}} \cup \hat{\Gamma}_{\text{out}} \cup \hat{\Gamma}_{\text{wall}}$, $\hat{\Gamma}_{\text{wall}}$ being the fluid-structure interface, sometimes referred as the wall. The fluid is described by the Navier-Stokes equations written in the Arbitrary Eulerian Lagrangian (ALE) formalism, to account for the deformation of the fluid domain. We assume that the solid is thin-walled and, hence, its mechanical behavior can be described by a simplified model (shell in 3D or beam in 2D) written on the reference mid-surface $\hat{\Sigma}$ (total Lagrangian formulation). The effect of the thickness of the solid in the fluid-structure coupling is neglected, which is a common simplifying assumption, so that $\hat{\Gamma}_{\text{wall}} = \hat{\Sigma}$.

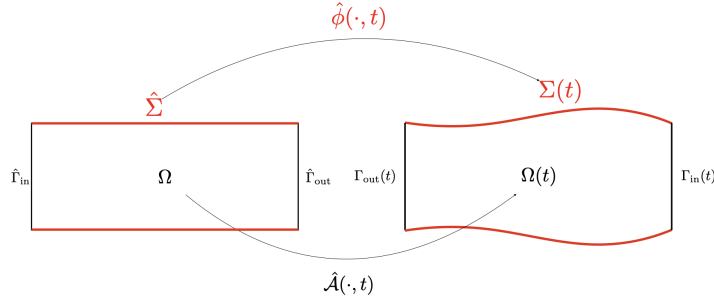


Figure 4.1: Geometric configuration.

The fluid sub-problem. We briefly introduce some notations for the ALE mapping of the fluid domain. The main purpose for using such a parametrization is to facilitate the discretization of the Eulerian time derivative in the context of a moving fluid domain (moving meshes after spatial discretization). Let the Arbitrary Eulerian Lagrangian (ALE) map be given by

$$\begin{aligned} \hat{\mathcal{A}}: \hat{\Omega} \times (0, T) &\rightarrow \mathbb{R}^d \\ (\hat{\boldsymbol{x}}, t) &\mapsto \boldsymbol{x} := \hat{\mathcal{A}}(\hat{\boldsymbol{\xi}}, t), \end{aligned}$$

with $T > 0$ the time horizon and d the dimension of the problem. To lighten the notations, $\hat{\mathcal{A}}(\cdot, t)$ will be also denoted by $\hat{\mathcal{A}}_t(\cdot)$. For $t \in (0, T)$, the current fluid domain is denoted $\Omega(t) := \hat{\mathcal{A}}_t(\hat{\Omega})$. The ALE velocity $\hat{\mathbf{w}}$ is given by

$$\hat{\mathbf{w}}(\hat{\mathbf{x}}, t) := \frac{\partial \hat{\mathcal{A}}}{\partial t}(\hat{\mathbf{x}}, t),$$

such that for a given quantity $q: \Omega(t) \rightarrow \mathbb{R}^d$, the ALE derivative $\partial_t q|_{\hat{\mathcal{A}}}$ is defined by

$$\partial_t q|_{\hat{\mathcal{A}}}(\mathbf{x}, t) := \frac{d}{dt} q(\hat{\mathcal{A}}_t(\hat{\mathbf{x}}), t) = \lim_{\tau \rightarrow 0} \frac{q(\hat{\mathcal{A}}(\hat{\mathbf{x}}, t + \tau), t + \tau) - q(\hat{\mathcal{A}}(\hat{\mathbf{x}}, t), t)}{\tau}, \quad \hat{\mathbf{x}} = \hat{\mathcal{A}}_t^{-1}(\mathbf{x}, t).$$

Using the chain rule, we hence get the classical relation

$$\partial_t q|_{\hat{\mathcal{A}}} = \mathbf{w} \cdot \nabla q + \partial_t q. \quad (4.1)$$

In order to write integrals with the ALE formalism, one needs to remember the Reynolds transport formula. For a function q defined on a subdomain $V = \hat{\mathcal{A}}_t(\hat{V})$, with $\hat{V} \subset \hat{\Omega}$:

$$\frac{d}{dt} \int_V q d\mathbf{x} = \int_V (\partial_t q|_{\hat{\mathcal{A}}} + q \operatorname{div} \mathbf{w}) \quad (4.2)$$

The displacement of the fluid computational domain $\mathbf{d}_f: \hat{\Omega} \times (0, T) \rightarrow \mathbb{R}^d$ is given by the relation $\mathbf{d}_f(\hat{\Omega}, t) := (\hat{\mathcal{A}}_t - I)(\hat{\Omega})$.

Let \mathbf{n} be the unit outward normal to the boundary $\partial\Omega_t$. For $t \in (0, T)$, let $\mathbf{u}(t): \Omega(t) \rightarrow \mathbb{R}^d$ be the fluid velocity, $p(t): \Omega(t) \rightarrow \mathbb{R}$ the fluid pressure. Using (4.1), the incompressible Navier-Stokes equations governing the fluid flow dynamics in a moving domain write as follows:

$$\left\{ \begin{array}{ll} \rho^f (\partial_t \mathbf{u}|_{\hat{\mathcal{A}}} + (\mathbf{u} - \mathbf{w}) \cdot \nabla \mathbf{u}) - \operatorname{div} \boldsymbol{\sigma}(\mathbf{u}, p) = 0 & \text{in } \Omega(t), \\ \operatorname{div} \mathbf{u} = 0 & \text{in } \Omega(t), \\ \boldsymbol{\sigma}(\mathbf{u}, p) \mathbf{n} = -P_{\text{in}} \mathbf{n} & \text{on } \Gamma_{\text{in}}(t), \\ \boldsymbol{\sigma}(\mathbf{u}, p) \mathbf{n} = -P_{\text{out}} \mathbf{n} & \text{on } \Gamma_{\text{out}}(t), \end{array} \right. \quad (4.3)$$

with ρ^f the fluid density, $\mathbf{w} = \hat{\mathbf{w}} \circ \hat{\mathcal{A}}_t^{-1}$ the ALE velocity in the current configuration, with the relation $\partial_t \mathbf{d}_f = \hat{\mathbf{w}}$. The stress tensor is given by

$$\boldsymbol{\sigma}(\mathbf{u}, p) := -p\mathbf{I} + 2\mu\boldsymbol{\varepsilon}(\mathbf{u}), \quad \boldsymbol{\varepsilon}(\mathbf{u}) := \frac{1}{2}(\nabla \mathbf{u} + \nabla \mathbf{u}^T),$$

where μ denotes the fluid dynamic viscosity. The inflow and outflow boundary conditions are provided through prescribed pressure profiles on $\Gamma_{\text{in}}(t) = \hat{\mathcal{A}}_t(\hat{\Gamma}_{\text{in}})$ and $\Gamma_{\text{out}}(t) = \hat{\mathcal{A}}_t(\hat{\Gamma}_{\text{out}})$.

We also introduce the deformation gradient $\mathbf{F}: \hat{\Omega} \times (0, T) \rightarrow \mathbb{R}^{d \times d}$ defined by

$$\mathbf{F}(\hat{\mathbf{x}}, t) = \nabla_{\hat{\mathbf{x}}} \hat{\mathcal{A}}(\hat{\mathbf{x}}, t),$$

and its determinant $J: \hat{\Omega} \times (0, T) \rightarrow \mathbb{R}$, $J = \det \mathbf{F}$. With those notations, let introduce the Piola-Kirchhoff transformation. The Piola transformation of a second order tensor $\sigma: \Omega(t) \rightarrow \mathbb{R}^{d \times d}$ defined in the current configuration $\Omega(t)$ is given by a second order tensor $\boldsymbol{\Pi} \cdot \sigma: \hat{\Omega}^f \rightarrow \mathbb{R}^{d \times d}$ defined by

$$\boldsymbol{\Pi} \cdot \sigma(\hat{\mathbf{x}}) := J(\hat{\mathbf{x}}) \sigma(\hat{\mathcal{A}}(\hat{\mathbf{x}}, t)) \mathbf{F}^{-T}(\hat{\mathbf{x}}). \quad (4.4)$$

The Piola transformation enables to write stress from the current configuration to the reference configuration (see, e.g., [LF19]):

$$\int_{\partial\hat{V}} \mathbf{\Pi} \cdot \sigma \hat{\mathbf{n}} \, d\hat{\gamma} = \int_{\partial V} \sigma \mathbf{n} \, d\gamma \quad (4.5)$$

for any sub-domain $\hat{V} \subset \hat{\Omega}$, $V = \hat{\mathcal{A}}_t(\hat{V})$, where $\hat{\mathbf{n}}$ stands for the unit outward normal to the boundary $\partial\hat{V}$ and \mathbf{n} for the unit outward normal to the boundary ∂V in the current configuration. Moreover, the following relations also hold:

$$\mathbf{n} = \frac{\mathbf{F}^{-T} \hat{\mathbf{n}}}{\|\mathbf{F}^{-T} \hat{\mathbf{n}}\|}, \quad d\gamma = J \|\mathbf{F}^{-T} \hat{\mathbf{n}}\| \, d\hat{\gamma}.$$

The solid sub-problem. The solid structure is governed by a non-linear elastic shell (or beam). In general abstract form, the problem is formulated as follows: Find the displacement field of the mid-surface $\mathbf{d} : \hat{\Sigma} \times (0, T) \rightarrow \mathbb{R}^d$ and the velocity $\dot{\mathbf{d}} : \hat{\Sigma} \times (0, T) \rightarrow \mathbb{R}^d$ such that

$$\begin{cases} \rho^s \epsilon \partial_t \dot{\mathbf{d}} + \mathcal{L}^e(\mathbf{d}) = \mathbf{f}_\Sigma & \text{on } \hat{\Sigma}, \\ \partial_t \mathbf{d} = \dot{\mathbf{d}}, & \text{on } \hat{\Sigma}, \\ \mathbf{d} = \mathbf{0} & \text{on } \partial\hat{\Sigma}, \end{cases} \quad (4.6)$$

with ρ^s being the density and ϵ the thickness. The equations are complemented by the initial conditions $\mathbf{d}(0) = \mathbf{d}_0$ and $\dot{\mathbf{d}}(0) = \dot{\mathbf{d}}_0$. The surface operators $\mathcal{L}^e(\mathbf{d})$ account for the (non-linear) elastic shell behavior of the vessel wall.

Interface coupling conditions The fluid sub-problem (4.3) and the solid sub-problem (4.6) are coupled by the following relations:

$$\begin{cases} \mathbf{d}_f = \text{Ext}(\mathbf{d}), \quad \mathbf{w} = \partial_t \mathbf{d}_f, \quad \hat{\mathcal{A}} = \mathbf{I} + \mathbf{d}_f, \quad \Omega(t) = \hat{\mathcal{A}}_t(\hat{\Omega}), \\ \mathbf{f}_\Sigma = (p_{\text{ext}} \mathbf{I} - \mathbf{\Pi} \cdot \sigma) \hat{\mathbf{n}} = J(\sigma_{\text{ext}} - \sigma(\mathbf{u}, p)) \mathbf{F}^{-T} \hat{\mathbf{n}} & \text{on } \hat{\Sigma}, \\ \dot{\mathbf{d}} = \mathbf{u} \circ \hat{\mathcal{A}} & \text{on } \hat{\Sigma}, \end{cases} \quad (4.7)$$

with $\text{Ext}(\mathbf{d})$ a given smooth lifting of the solid displacement at the interface inside the reference fluid domain. p_{ext} represents the external forces exerted on the wall, whereas $\mathbf{\Pi} \cdot \sigma$ is the Piola transformations of the Cauchy stress tensor σ of the fluid which models the forces exerted by the fluid on the wall. If p_{ext} is not provided, the fluid pressure p cannot be considered as an absolute pressure. For the sake of simplicity, we shall assume that $\sigma_{\text{ext}} \equiv 0$.

Remark 5

The choice of the lifting Ext is arbitrary. In practice, one often uses harmonic or elastic based lifting operators.

4.2.2 Numerical Resolution and Robin-Neumann coupling scheme

To approximate the FSI problem (4.3), (4.6), (4.7), we first derive the variational formulation by multiplying the fluid and solid equations by appropriate test functions.

For the time discretization, the fluid and solid problems are discretized using a backward Euler scheme in the bulk terms and an explicit Robin-Neumann treatment of the interface conditions.

4.2.2.1 Continuous variational formulation

We introduce the fluid spaces of tests functions in the reference configuration

$$\begin{aligned} \mathbf{V} &:= \{ \hat{\mathbf{v}} \in [H^1(\hat{\Omega})]^d, \quad \hat{\mathbf{v}}|_{\hat{\Sigma}} \in [H^1(\hat{\Sigma})]^d \}, \\ Q &:= L^2(\hat{\Omega}). \end{aligned}$$

Tests functions in the current configuration will be defined via transport back through the ALE map, that is,

$$\mathbf{v} = \hat{\mathbf{v}} \circ \hat{\mathcal{A}}_t^{-1}, \quad q = \hat{q} \circ \hat{\mathcal{A}}_t^{-1}.$$

Any of these tests functions satisfies the relation $\partial_t \mathbf{v}|_{\hat{\mathcal{A}}} = \mathbf{0}$, which basically states that their dependence on time comes exclusively from the motion of the fluid domain, through the (unknown) ALE map $\hat{\mathcal{A}}$.

We multiply (4.3)₁ by $\mathbf{v} = \hat{\mathbf{v}} \circ \hat{\mathcal{A}}_t^{-1}$ with $\hat{\mathbf{v}} \in \mathbf{V}$, integrate by parts, and replace the boundary terms with the boundary conditions. Then, the relation (4.3)₂ is multiplied by a test function $q \in Q(t)$. After combining the two variational expressions, we get:

$$\begin{aligned} (\rho^f \partial_t \mathbf{u}|_{\hat{\mathcal{A}}}, \mathbf{v})_{\Omega(t)} + (\rho^f (\mathbf{u} - \mathbf{w}) \nabla \mathbf{u}, \mathbf{v})_{\Omega(t)} - (p, \operatorname{div} \mathbf{v})_{\Omega(t)} + (q, \operatorname{div} \mathbf{u})_{\Omega(t)} \\ + 2\mu(\varepsilon(\mathbf{u}), \varepsilon(\mathbf{v}))_{\Omega(t)} - \langle \sigma(\mathbf{u}, p) \mathbf{n}, \mathbf{v} \rangle_{\partial\Omega(t)} = 0. \end{aligned} \quad (4.8)$$

The ALE time-derivative term can be rewritten as follows:

$$(\rho^f \partial_t \mathbf{u}|_{\hat{\mathcal{A}}}, \mathbf{v})_{\Omega(t)} = \frac{d}{dt} (\rho^f \mathbf{u}, \mathbf{v})_{\Omega(t)} - (\rho^f \operatorname{div} \mathbf{w} \mathbf{u}, \mathbf{v})_{\Omega(t)}, \quad (4.9)$$

using a change of variable from the current configuration to the reference configuration with (4.2), since ρ^f is constant and, by construction, $\hat{\mathbf{v}} = \mathbf{v} \circ \hat{\mathcal{A}}_t$ is independent of t . It yields

$$\begin{aligned} \frac{d}{dt} (\rho^f \mathbf{u}, \mathbf{v})_{\Omega(t)} - (\rho^f \operatorname{div} \mathbf{w} \mathbf{u}, \mathbf{v})_{\Omega(t)} + (\rho^f (\mathbf{u} - \mathbf{w}) \cdot \nabla \mathbf{u}, \mathbf{v})_{\Omega(t)} \\ - (p, \operatorname{div} \mathbf{v})_{\Omega(t)} + (q, \operatorname{div} \mathbf{u})_{\Omega(t)} + 2\mu(\varepsilon(\mathbf{u}), \varepsilon(\mathbf{v}))_{\Omega(t)} \\ - \langle \sigma(\mathbf{u}, p) \mathbf{n}, \mathbf{v} \rangle_{\partial\Omega(t)} = 0 \end{aligned} \quad (4.10)$$

After inserting the Neumann boundary conditions, the stress on $\partial\Omega(t)$, we have that the fluid velocity $\mathbf{u}(t)$ and the pressure $p(t)$ satisfy

$$\begin{aligned} \frac{d}{dt} (\rho^f \mathbf{u}, \mathbf{v})_{\Omega(t)} + a^f[(\mathbf{w}, \mathbf{u}); (\mathbf{u}, p), (\hat{\mathbf{v}}, \hat{q})] - \langle \sigma(\mathbf{u}, p) \mathbf{n}, \mathbf{v} \rangle_{\Sigma(t)} \\ = - \langle P_{\text{in}} \mathbf{n}, \mathbf{v} \rangle_{\Gamma_{\text{in}}(t)} - \langle P_{\text{out}} \mathbf{n}, \mathbf{v} \rangle_{\Gamma_{\text{out}}(t)} \end{aligned} \quad (4.11)$$

for all $\hat{\mathbf{v}} \in \mathbf{V}$ and $\hat{q} \in Q$, where

$$\begin{aligned} a^f[(\mathbf{w}, \mathbf{z}); (\mathbf{u}, p), (\hat{\mathbf{v}}, \hat{q})] &:= -(\rho^f \operatorname{div}(\mathbf{w}) \mathbf{u}, \mathbf{v})_{\Omega(t)} + (\rho^f (\mathbf{z} - \mathbf{w}) \nabla \mathbf{u}, \mathbf{v})_{\Omega(t)} + 2\mu(\varepsilon(\mathbf{u}), \varepsilon(\mathbf{v}))_{\Omega(t)} \\ &\quad - (p, \operatorname{div} \mathbf{v})_{\Omega(t)} + (q, \operatorname{div} \mathbf{u})_{\Omega(t)} \end{aligned} \quad (4.12)$$

for $\mathbf{u} \in [H^1(\Omega(t))]^d$, $p \in L^2(\Omega(t))$, $\hat{\mathbf{v}} \in \mathbf{V}$, $\hat{q} \in Q$.

Solid variational formulation. We introduce the spaces

$$\hat{\mathbf{W}} := [H^1(\hat{\Sigma})]^d, \quad \hat{\mathbf{W}}_0 := [H_0^1(\hat{\Sigma})]^d.$$

Using the FSI coupling conditions (4.7)₁ and (4.7)₂, the weak formulation of the solid problem is given by: Find $\mathbf{d}(t) \in \hat{\mathbf{W}}_0$, such that

$$\begin{cases} (\rho^s \epsilon \partial_t \dot{\mathbf{d}}, \hat{\mathbf{w}})_{\hat{\Sigma}} + \mathbf{a}^s(\mathbf{d}, \hat{\mathbf{w}}) = (-\sigma(\mathbf{u}, p) \mathbf{n}, \mathbf{w})_{\Sigma(t)}, \\ \partial_t \mathbf{d} = \dot{\mathbf{d}}, \end{cases} \quad (4.13)$$

for all $\hat{\mathbf{w}} \in \hat{\mathbf{W}}_0$, and with $\mathbf{w} := \hat{\mathbf{w}} \circ \hat{\mathcal{A}}_t^{-1}$, $\mathbf{a}^s(\mathbf{d}, \hat{\mathbf{w}}) := (\mathcal{L}^e(\mathbf{d}), \hat{\mathbf{w}})_{\hat{\Sigma}}$.

Fluid variational formulation. Since the dynamic coupling condition (4.7)₂ has already been integrated into the variational solid problem above, it remains:

$$\begin{cases} \mathbf{d}_f = \text{Ext}(\mathbf{d}), \quad \mathbf{w} = \partial_t \mathbf{d}_f, \quad \hat{\mathcal{A}}_t = I + \mathbf{d}_f, \quad \Omega(t) = \hat{\mathcal{A}}_t(\hat{\Omega}), \\ \dot{\mathbf{d}} = \mathbf{u} \circ \hat{\mathcal{A}}_t \text{ on } \hat{\Sigma}, \end{cases} \quad (4.14)$$

The interface kinematic condition (4.14)₂ is naturally integrated in the fluid variational expression (4.11) as a Dirichlet boundary condition by taking $\hat{\mathbf{v}} = \mathbf{0}$ on $\partial \hat{\Sigma}$, which yields the variational problem: Find $\mathbf{u}(t) \in [H^1(\Omega(t))]^d$ and $p(t) \in L^2(\Omega(t))$ with $\mathbf{u} \circ \hat{\mathcal{A}}_t = \dot{\mathbf{d}}$ on $\hat{\Sigma}$, such that

$$\begin{aligned} \frac{d}{dt} (\rho^f \mathbf{u}, \mathbf{v})_{\Omega(t)} + a^f[(\mathbf{w}, \mathbf{u}); (\mathbf{u}, p), (\mathbf{v}, q)] \\ = -\langle P_{\text{in}} \mathbf{n}, \mathbf{v} \rangle_{\Gamma_{\text{in}}(t)} - \langle P_{\text{out}} \mathbf{n}, \mathbf{v} \rangle_{\Gamma_{\text{out}}(t)} \end{aligned} \quad (4.15)$$

for all $\hat{\mathbf{v}} \in \mathbf{V}$ and $\hat{q} \in Q$ with $\hat{\mathbf{v}} = \mathbf{0}$ on $\partial \hat{\Sigma}$.

Finally, in what follows the symbol Ext denotes the harmonic extension, which associates to solid interfacial displacement $\mathbf{d}_{\hat{\Sigma}} \in [H^1(\hat{\Sigma})]^d$ the bulk fluid domain displacement $\mathbf{d}_{\hat{\Omega}} \in [H^1(\hat{\Omega})]^d$, solution of

$$\begin{cases} -\Delta \mathbf{d}_{\hat{\Omega}} = 0 \text{ in } \hat{\Omega}, \\ \mathbf{d}_{\hat{\Omega}} = \mathbf{d}_{\hat{\Sigma}} \text{ on } \hat{\Sigma}, \\ \mathbf{d}_{\hat{\Omega}} = 0 \text{ on } \hat{\Gamma}_{\text{in}} \cup \hat{\Gamma}_{\text{out}}. \end{cases} \quad (4.16)$$

A consequence of the boundary conditions (4.16)₃ is that $\hat{\Gamma}_{\text{in}}$ and $\hat{\Gamma}_{\text{out}}$ are invariant. (4.16)₃ have been set for compatibility with the Dirichlet boundary conditions for the displacement on $\partial \hat{\Sigma}$ in (4.6).

4.2.2.2 Time discretization and FSI coupling scheme

We discretize the time interval $(0, T)$ by N subintervals (t_{n-1}, t_n) such that $t_n = n\tau$, where $n = 0, \dots, N-1$ and $\tau = T/(N-1)$ is the time-step. We denote by f^n the approximation of a time-dependent function f at time t_n . The time derivative is discretized by means of first-order backward finite difference

$$\partial_\tau f^n := \frac{1}{\tau} (f^n - f^{n-1}),$$

for $n \geq 1$.

Fluid domain update. At every discrete time level n , the fluid domain Ω^n is updated in an explicit fashion as follows:

$$\begin{cases} \mathbf{d}_f^n = \text{Ext}(\mathbf{d}^{n-1}) \\ \mathbf{w}^n = \partial_\tau \mathbf{d}_f^n, \\ \hat{\mathcal{A}}^n = I + \mathbf{d}_f^n \text{ in } \hat{\Omega}, \quad \Omega^n = \hat{\mathcal{A}}^n(\hat{\Omega}) \end{cases} \quad (4.17)$$

with Ext the harmonic extension explicitly defined in (4.16). Note that the geometric compatibility between the fluid and the solid domains (4.7)₁ is treated explicitly.

Solid problem. The relation between $\dot{\mathbf{d}}$ and \mathbf{d} is discretized in time as specified in (4.13)₃ to write the second derivative of the displacement

$$\begin{aligned} \dot{\mathbf{d}}^n &= \partial_\tau \mathbf{d}^n = \frac{1}{\tau}(\mathbf{d}^n - \mathbf{d}^{n-1}), \\ \partial_\tau \dot{\mathbf{d}}^n &= \frac{1}{\tau}(\dot{\mathbf{d}}^n - \dot{\mathbf{d}}^{n-1}) = \frac{1}{\tau^2} \mathbf{d}^n - \frac{1}{\tau^2} \mathbf{d}^{n-1} - \frac{1}{\tau} \dot{\mathbf{d}}^{n-1}. \end{aligned}$$

The solid problem writes in a time semi-discrete formulation: find $\mathbf{d}^n \in \hat{\mathbf{W}}_0$, such that for all $\hat{\boldsymbol{\xi}} \in \hat{\mathbf{W}}_0$, with $\boldsymbol{\xi} := \hat{\boldsymbol{\xi}} \circ (\hat{\mathcal{A}}^n)^{-1}$:

$$\begin{cases} \left(\frac{\rho^s \epsilon}{\tau^2} \mathbf{d}^n, \hat{\boldsymbol{\xi}} \right)_{\hat{\Sigma}} + \mathbf{a}^s(\mathbf{d}^n, \hat{\boldsymbol{\xi}}) = b_n^s(\hat{\boldsymbol{\xi}}) - (\sigma(\mathbf{u}^n, p^n) \mathbf{n}, \boldsymbol{\xi})_{\Sigma^n} \\ \dot{\mathbf{d}}^n = \frac{1}{\tau}(\mathbf{d}^n - \mathbf{d}^{n-1}), \end{cases} \quad \text{on } \hat{\Sigma}, \quad (4.18)$$

with b_n^s the linear form on $\hat{\mathbf{W}}_0$ defined by $b_n^s(\hat{\boldsymbol{\xi}}) := \left(\frac{\rho^s \epsilon}{\tau} \dot{\mathbf{d}}^{n-1}, \hat{\boldsymbol{\xi}} \right)_{\hat{\Sigma}} + \left(\frac{\rho^s \epsilon}{\tau^2} \mathbf{d}^{n-1}, \hat{\boldsymbol{\xi}} \right)_{\hat{\Sigma}}$, for $\hat{\boldsymbol{\xi}} \in \hat{\mathbf{W}}_0$.

Fluid problem. The ALE time-derivative $\frac{d}{dt}(\rho^f \mathbf{u}, \mathbf{v})_{\Omega(t)}$ is discretized in time using the first-order backward finite difference:

$$\frac{1}{\tau} \left((\rho^f \mathbf{u}^n, \mathbf{v})_{\Omega^n} - (\rho^f \mathbf{u}^{n-1}, \mathbf{v})_{\Omega^{n-1}} \right).$$

Note that there is a little abuse of notation in this expression, since we have to respectively understand $\mathbf{v} = \hat{\mathbf{v}} \circ (\hat{\mathcal{A}}^n)^{-1}$ and $\mathbf{v} = \hat{\mathbf{v}} \circ (\hat{\mathcal{A}}^{n-1})^{-1}$ in the two terms, since the test function is linked to the same reference test function $\hat{\mathbf{v}} \in \mathbf{V}$ in the reference configuration, this is why we simply write \mathbf{v} .

The non-linearities due the convective terms are treated explicitly, and we add the Temam's stabilization term

$$s_T^n(\mathbf{u}^n, \mathbf{v}) := \frac{\rho^f}{2} (\text{div } \mathbf{u}^{n-1} \mathbf{u}^n, \mathbf{v})_{\Omega^n},$$

to ensure energy stability at the fully discrete level (see, e.g., [Tem68]). The proposed time semi-discrete counterpart of (4.11) is hence the following

$$\begin{aligned} & \frac{1}{\tau} (\rho^f \mathbf{u}^n, \mathbf{v})_{\Omega^n} + a_n^f[(\mathbf{u}^n, p^n), (\mathbf{v}, q)] - \langle \sigma(\mathbf{u}^n, p^n) \mathbf{n}, \mathbf{v}^n \rangle_{\Sigma^n} \\ &= \frac{1}{\tau} (\rho^f \mathbf{u}^{n-1}, \mathbf{v})_{\Omega^{n-1}} - \langle P_{\text{in}}^n \mathbf{n}, \mathbf{v} \rangle_{\Gamma_{\text{in}}^n} - \langle P_{\text{out}}^n \mathbf{n}, \mathbf{v} \rangle_{\Gamma_{\text{out}}^n}, \end{aligned} \quad (4.19)$$

where the bilinear form $a_n^f[\cdot, \cdot]$ is defined by

$$\begin{aligned} a_n^f[(\mathbf{u}, p), (\mathbf{v}, q)] &:= -(\rho^f \text{div } \mathbf{w}^n \mathbf{u}, \mathbf{v})_{\Omega^n} + (\rho^f (\mathbf{u}^{n-1} - \mathbf{w}^n) \cdot \nabla \mathbf{u}, \mathbf{v})_{\Omega^n} + 2\mu(\varepsilon(\mathbf{u}), \varepsilon(\mathbf{v}))_{\Omega^n} \\ &+ s_T^n(\mathbf{u}^n, \mathbf{v}) - (p, \text{div } \mathbf{v})_{\Omega^n} + (q, \text{div } \mathbf{u})_{\Omega^n}. \end{aligned}$$

Interface fluid Robin condition. In order to avoid the traditional instabilities of Dirichlet-Neumann based loosely coupled schemes, instead of discretizing directly (4.15) in time, we propose to follow [FMV13, Fer13] where the Dirichlet condition for the fluid is replaced by a Robin condition which treats implicitly the solid inertia contributions within fluid (hence ensuring stability). By considering (4.13) as a boundary condition for the fluid we can write the time discretization equivalent to (4.18)₁:

$$-(\sigma(\mathbf{u}^n, p^n) \mathbf{n}, \mathbf{v})_{\Sigma^n} = \frac{\rho^s \epsilon}{\tau} (\mathbf{d}^n - \mathbf{d}^{n-1}, \hat{\boldsymbol{\xi}})_{\hat{\Sigma}} + \mathbf{a}^s(\mathbf{d}^n, \hat{\boldsymbol{\xi}}),$$

the idea is to treat implicitly the solid inertia in the fluid and explicitly the remaining contributions, via the following Robin condition for the fluid

$$-\langle \sigma(\mathbf{u}^n, p^n) \mathbf{n}, \mathbf{v} \rangle_{\Sigma^n} = \frac{\rho^s \epsilon}{\tau} (\hat{\mathbf{u}}^n - \mathbf{d}^{n-1}, \hat{\mathbf{v}})_{\hat{\Sigma}} + \mathbf{a}^s(\mathbf{d}^{n-1}, \hat{\mathbf{v}})_{\hat{\Sigma}},$$

with $\hat{\mathbf{u}}^n|_{\Sigma^n} := \mathbf{u}^n \circ (\hat{\mathcal{A}}^n)^{-1}|_{\Sigma^n}$ using the kinematic and the geometric coupling strongly in the solid inertia at the fluid-structure interface, as in [FMV13, Fer13]. The non-linear solid elastic term $\mathbf{a}^s(\mathbf{d}^{n-1}, \hat{\mathbf{v}})_{\hat{\Sigma}}$ can be eliminated thanks to the solid equation (4.18) at the previous time-step:

$$\mathbf{a}^s(\mathbf{d}^{n-1}, \hat{\mathbf{v}})_{\hat{\Sigma}} = -(\sigma(\mathbf{u}^{n-1}, p^{n-1}) \mathbf{n}, \mathbf{v})_{\Sigma^{n-1}} - \rho^s \epsilon (\partial_\tau \mathbf{d}^{n-1}, \hat{\mathbf{v}})_{\hat{\Sigma}}.$$

As a result, we have

$$\begin{aligned} -\langle \sigma(\mathbf{u}^n, p^n) \mathbf{n}, \mathbf{v} \rangle_{\Sigma^n} &= -\langle \sigma(\mathbf{u}^{n-1}, p^{n-1}) \mathbf{n}, \mathbf{v} \rangle_{\Sigma^n} + \frac{\rho^s \epsilon}{\tau} (\hat{\mathbf{u}}^n - (\mathbf{d}^{n-1} + \tau \partial_\tau \mathbf{d}^{n-1}), \hat{\mathbf{v}})_{\hat{\Sigma}} \\ &= -\langle \sigma(\mathbf{u}^{n-1}, p^{n-1}) \mathbf{n}, \mathbf{v} \rangle_{\Sigma^{n-1}} + \frac{\rho^s \epsilon}{\tau} \langle \hat{\mathbf{u}}^n, \hat{\mathbf{v}} \rangle_{\hat{\Sigma}} \\ &\quad - \frac{\rho^s \epsilon}{\tau} \langle 2\mathbf{d}^{n-1} + \mathbf{d}^{n-2}, \hat{\mathbf{v}} \rangle_{\hat{\Sigma}} \end{aligned} \quad (4.20)$$

for $n \geq 2$. By inserting this Robin condition into (4.19), the time semi-discrete fluid variational problem reads: Find $\mathbf{u}^n \in [H^1(\Omega^n)]^d$, $p^n \in L^2(\Omega^n)$ such that

$$\begin{aligned} &\frac{1}{\tau} (\rho^f \mathbf{u}^n, \mathbf{v})_{\Omega^n} + a_n^f[(\mathbf{u}^n, p^n), (\mathbf{v}, q)] + \frac{\rho^s \epsilon}{\tau} \langle \hat{\mathbf{u}}^n, \mathbf{v} \rangle_{\hat{\Sigma}} \\ &= \frac{1}{\tau} (\rho^f \mathbf{u}^{n-1}, \mathbf{v})_{\Omega^{n-1}} - \langle P_{\text{in}}^n \hat{\mathbf{n}}, \mathbf{v} \rangle_{\hat{\Gamma}_{\text{in}}^n} - \langle P_{\text{out}}^n \hat{\mathbf{n}}, \mathbf{v} \rangle_{\hat{\Gamma}_{\text{out}}^n} \\ &\quad + \langle \sigma(\mathbf{u}^{n-1}, p^{n-1}) \mathbf{n}, \mathbf{v} \rangle_{\Sigma^{n-1}} + \langle 2\mathbf{d}^{n-1} + \mathbf{d}^{n-2}, \mathbf{v} \rangle_{\hat{\Sigma}} \end{aligned} \quad (4.21)$$

for all $\hat{\mathbf{v}} \in \mathbf{V}$ and $\hat{q} \in Q$.

Note that as for the monolithic formulation (3.8) of the previous chapter, the left-hand side of (4.21) involves a solid contribution in the form of an inertia term. However, in (4.21) the solid elastic contributions are treated in an explicit fashion, which guarantees the loosely coupled nature of the scheme, without compromising stability and accuracy.

4.2.2.3 Space discretization using fitted meshes

Finite elements are used for both the spatial discretization of the fluid and solid subproblems (4.21) and (4.18). Let consider a quasi-uniform shape regular

tetrahedral mesh \mathcal{T}_h of the domain $\hat{\Omega}$. As triangulation \mathcal{I}_h of $\hat{\Sigma}$ we consider the faces of elements of \mathcal{T}_h that lie on $\hat{\Sigma}$. In other words, \mathcal{T}_h and \mathcal{I}_h are conforming meshes. The subscript h parametrizes the level of refinement of the mesh, typically the maximum element diameter in the mesh. The geometric quantities indexed with n dependent of the space discrete ALE mapping $\hat{\mathcal{A}}_h^n$. The shape regular mesh of Ω^n is defined from \mathcal{T}_h by applying the transformation $\hat{\mathcal{A}}_h^n$ to the nodes of \mathcal{T}_h , same for \mathcal{I}_h , while keeping the same connectivity. The meshes of Ω^n and Σ^n are denoted by \mathcal{T}_h^n and \mathcal{I}_h^n respectively.

Fluid solver. For the approximation of the fluid variational formulation (4.21), the infinite dimensional spaces for the velocity and the pressure are approximated by finite dimensional spaces $\mathbf{V}_h^n \subset H^1[(\Omega^n)]^d$ and $Q_h^n \subset L^2(\Omega^n)$, respectively. The finite element interpolation spaces \mathbf{V}_h^n and Q_h^n , for the velocity and the pressure, respectively, are built using the space of continuous piecewise linear functions on the tetrahedral mesh of Ω^n :

$$X_h^n := \{v_h \in C^0(\Omega^n), v_{h|K} \in \mathbb{P}^1, \forall K \in \mathcal{T}_h\},$$

so that

$$\mathbf{V}_h^n := [X_h^n]^d, \quad Q_h^n := X_h^n.$$

We also introduce

$$X_h = \{v_h \in C^0(\hat{\Omega}), v_{h|K} \in \mathbb{P}^1, \forall K \in \mathcal{T}_h\}$$

and $\mathbf{V}_h = [X_h]^d$ and $Q_h = X_h$.

Since the considered approximation spaces $\mathbb{P}^1 - \mathbb{P}^1$ for the velocity and the pressure do not satisfy the inf-sup condition (see [GR86]) and in order to avoid spurious velocity oscillations in the convection-dominating regime, we make use of the SUPG-PSPG stabilization (see [Tez91]), through the bilinear form s_{SP} :

$$\begin{aligned} s_{\text{SP}}((\mathbf{u}^n, p^n), (\mathbf{v}, q)) &:= \\ &\sum_{K \in \mathcal{T}_h^n} \int_K \delta_K (\rho^f(\mathbf{u}^{n-1} - \mathbf{w}^n) \cdot \nabla \mathbf{u}^n + \nabla p^{n-1}) \cdot (\rho^f(\mathbf{u}^{n-1} - \mathbf{w}^n) \cdot \nabla \mathbf{v} + \nabla q), \end{aligned}$$

with δ_K the SUPG-PSPG stabilization parameter.

The spatial approximation of (4.21) writes: Find $\mathbf{u}^n \in \mathbf{V}_h^n$, $p \in Q_h^n$

$$\begin{aligned} &\frac{1}{\tau} (\rho^f \mathbf{u}^n, \mathbf{v})_{\Omega^n} + a_n^f[(\mathbf{u}^n, p^n), (\mathbf{v}, q)] + s_{\text{SP}}[(\mathbf{u}^n, p^n), (\mathbf{v}, q)] \\ &\quad + \frac{\rho^s \epsilon}{\tau} \langle \hat{\mathbf{u}}^n, \hat{\mathbf{v}} \rangle_{\hat{\Sigma}} \\ &= l^n(\mathbf{v}) \end{aligned} \tag{4.22}$$

for all $\hat{\mathbf{v}} \in \mathbf{V}_h$, $\hat{q} \in Q_h$. The linear form l^n encodes for the right-hand side with

$$\begin{aligned} l^n(\mathbf{v}) &:= \frac{1}{\tau} (\rho^f \mathbf{u}^{n-1}, \mathbf{v})_{\Omega^{n-1}} - \langle P_{\text{in}}^n \mathbf{n}, \mathbf{v} \rangle_{\Gamma_{\text{in}}^n} - \langle P_{\text{out}}^n \mathbf{n}, \mathbf{v} \rangle_{\Gamma_{\text{out}}^n} \\ &\quad + \langle \sigma(\mathbf{u}^{n-1}, p^{n-1}) \mathbf{n}, \mathbf{v} \rangle_{\Sigma^{n-1}} + \langle 2\hat{\mathbf{d}}^{n-1} + \hat{\mathbf{d}}^{n-2}, \hat{\mathbf{v}} \rangle_{\hat{\Sigma}}. \end{aligned}$$

Remark 6

After solving the fully discrete variational formulation (4.22), the stress $\langle \sigma(\mathbf{u}^n, p^n) \mathbf{n}, \mathbf{v} \rangle_{\Sigma^n}$ is not calculated by applying a space discretization, but it is treated as a residual of the variational formulation for well-chosen test functions.

Solid. We denote by $\mathbf{W}_{0,h} \subset \mathbf{W}_0$ the approximation space for the solid displacement and velocity. The fully discrete problem reads: Find $\mathbf{d}^n \in \hat{\mathbf{W}}_{0,h}$, such that

$$\begin{cases} (\frac{\rho^s \epsilon}{\tau^2} \mathbf{d}^n, \hat{\boldsymbol{\xi}})_{\hat{\Sigma}} + \mathbf{a}^s(\mathbf{d}^n, \hat{\boldsymbol{\xi}}) = b_n^s(\hat{\boldsymbol{\xi}}) - (\sigma(\mathbf{u}^n, p^n) \mathbf{n}, \boldsymbol{\xi})_{\Sigma^n} \\ \dot{\mathbf{d}}^n = \frac{1}{\tau}(\mathbf{d}^n - \mathbf{d}^{n-1}), \end{cases} \quad \text{on } \hat{\Sigma}, \quad (4.23)$$

for all $\hat{\boldsymbol{\xi}} \in \mathbf{W}_{0,h}$, with $\boldsymbol{\xi} := \hat{\boldsymbol{\xi}} \circ (\hat{\mathcal{A}}^n)^{-1}$.

Algorithm 5 Robin-Neumann loosely coupled scheme

Require: Initial conditions:

$$\begin{cases} \mathbf{d}^0 = \mathbf{d}_0, \dot{\mathbf{d}}^0 = \dot{\mathbf{d}}_0 \text{ on } \hat{\Sigma} \\ \Omega^0 = \hat{\mathcal{A}}_h^0(\hat{\Omega}), \text{ with } \hat{\mathcal{A}}_h^0 = \mathbf{I} + \mathbf{d}_f^0, \text{ and } \mathbf{d}_f^0 = \text{Ext}(\mathbf{d}_0) \\ \mathbf{u}^0 = \mathbf{u}_0, p^0 = p_0 \text{ on } \Omega^0 \end{cases} \quad (4.24)$$

for $n = 1, \dots, N_T$ **do**

A/ Fluid solver step

1. Compute the fluid domain displacement $\mathbf{d}_f^n = \text{Ext}_h(\mathbf{d}^{n-1}) \in \mathbf{V}_h$, for Ext_h defined as the \mathbb{P}_1 finite element approximation of (4.16).
2. Update the ALE velocity \mathbf{w}^n and the fluid domain Ω^n using (4.17).
3. Forward fluid step: Find $\mathbf{u}^n \in \mathbf{V}_h^n$, $p^n \in Q_h^n$, solution of (4.22).

B/ Solid solver

1. Forward solid step: Find $\mathbf{d}^n \in \mathbf{W}_{0,h}$ solution of (4.23)

end for

The discrete FSI problem can be summarized in Algorithm 5. It starts with an explicit mesh update from the previous displacement. With the explicit coupling, the fluid solver uses the previous solid quantities and computes the velocity and pressure. The stress exerted by the fluid flow at the interface is passed to the solid in the form of a residual to compute the solid state.

4.3 UcL-Fluid state estimator (moving domain)

In this section, the FSI state estimation algorithm (Algorithm 4) for fixed (fluid) domain is extended to a partitioned resolution of FSI with moving fluid domain, as formulated for the forward problem in Section 4.2. The fluid and the solid sub-problems are solved separately and coupled by means of a Robin-Neumann explicit scheme. For the FSI state estimation, the inflow and outflow boundary conditions are assumed to be unknown, and (possibly noisy) velocity data is available in the whole computational domain. The FSI state estimation is also formulated in a partitioned fashion. The fluid solver is decomposed into 2 sub-problems:

1. A preliminary unique continuation step serves to estimate non-parametric inflow and outflow boundary conditions;
2. A Luenberger state observer step for the fluid sub-problem using the estimation provided by the continuation step and the measured and velocity data.

The unique continuation step consists in finding the fluid state which minimizes the distance to the velocity data \mathbf{u}_M and satisfies the equations of the fluid sub-problem as in 4.21, without knowledge of the inflow and outflow boundary conditions.

4.3.1 Presentation of the method

In this section, the FSI state estimation UCL-Fluid is decomposed into the fluid solver part and the solid solver part. The fluid solver part combines the Luenberger state observer with a preliminary unique continuation step to estimate the fluid state without user-defined boundary conditions. The solid problem is similar to the forward problem (4.23).

The purpose of the fluid solver of the FSI state estimator is to assimilate the velocity data \mathbf{u}_M to estimate the fluid state $(\tilde{\mathbf{u}}, \tilde{p})$ with the knowledge of the fluid forward sub-problem. One possible option is to consider a Luenberger observer, by adding a nudging term with a free-parameter $\gamma_f > 0$. At the continuous level it boils down to finding $(\tilde{\mathbf{u}}, \tilde{p})$ solution of

$$\begin{cases} \rho^f (\partial_t \tilde{\mathbf{u}}|_{\tilde{\mathcal{A}}} + (\tilde{\mathbf{u}} - \tilde{\mathbf{w}}) \cdot \nabla \tilde{\mathbf{u}}) - \operatorname{div} \boldsymbol{\sigma}(\tilde{\mathbf{u}}, \tilde{p}) + \gamma_f (\tilde{\mathbf{u}} - \mathbf{u}_M) = 0 & \text{in } \tilde{\Omega}(t), \\ \operatorname{div} \tilde{\mathbf{u}} = 0 & \text{in } \tilde{\Omega}(t). \end{cases} \quad (4.25)$$

The state estimation is denoted with a tilde ("~"). To be able to solve this problem, inflow and outflow boundary conditions are required. One could plug the velocity data directly at the boundary as a Dirichlet boundary condition. However, since noisy data may lack of regularity or of (mass conservation) compatibility, the idea proposed here consists in filtering the data through a unique continuation step.

We consider fully discrete quantities. At time $t_n = n\tau$, the following quantities have been computed from the previous iteration $n - 1$:

- the fluid domain $\tilde{\Omega}^{n-1}$ and the map $\tilde{\mathcal{A}}_h^{n-1}$;
- the fluid state estimation $(\tilde{\mathbf{u}}^{n-1}, \tilde{p}^{n-1})$ defined in $\tilde{\Omega}^{n-1}$;
- the solid state estimation, namely the displacement and the velocity $(\tilde{\mathbf{d}}^{n-1}, \tilde{\mathbf{d}}^{n-1})$ defined on $\hat{\Sigma}$.

1) Mesh update in the fluid solver. Before computing the (fluid) state estimation at time t_n , the fluid domain displacement is computed and the mesh configuration is updated using the following procedure:

$$\tilde{\mathbf{d}}_f^n = \operatorname{Ext}_h(\tilde{\mathbf{d}}^{n-1}), \quad \tilde{\mathbf{w}}^n = \partial_\tau \tilde{\mathbf{d}}_f^n, \quad \tilde{\mathcal{A}}_h^n = I + \tilde{\mathbf{d}}_f^n, \quad \tilde{\Omega}^n = \tilde{\mathcal{A}}_h^n(\hat{\Omega}) \quad (4.26)$$

where $\tilde{\mathbf{d}}_f^n$ is the fluid domain displacement, and Ext_h defined as the \mathbb{P}_1 finite element approximation of (4.16)

2) Unique continuation (UC) preliminary step. Here, the unique continuation step will consist in assimilating the measurements \mathbf{u}_M^n under the constraint of the discretized weak formulation of the Navier-Stokes equations, with the interface Robin boundary conditions coming from the FSI coupling scheme, as introduced in (4.22).

In what follows, the function spaces $\tilde{\mathbf{V}}_h^n, \tilde{Q}_h^n$ take the same definition as the space function \mathbf{V}_h^n, Q_h^n , after replacing Ω^n by $\tilde{\Omega}^n$. Let $\mathbf{V}_{h,0}$ the space of functions which vanish on the inflow and outflow boundaries

$$\mathbf{V}_{h,0} := \{\mathbf{v} \in \mathbf{V}_h, \mathbf{v}|_{\tilde{\Gamma}_{\text{in}} \cup \tilde{\Gamma}_{\text{out}}} = 0\}.$$

We define $\tilde{\Gamma}_{\text{in}}^n = \tilde{\mathcal{A}}_h^n \circ \hat{\Gamma}_{\text{in}}, \tilde{\Gamma}_{\text{out}}^n = \tilde{\mathcal{A}}_h^n \circ \hat{\Gamma}_{\text{out}}$ are the inflow and outflow boundaries in the current estimated configuration. Note that due to the Dirichlet boundary conditions for the harmonic extension (4.16), $\tilde{\Gamma}_{\text{in}}^n = \hat{\Gamma}_{\text{in}} = \Gamma_{\text{in}}^n = \hat{\Gamma}_{\text{in}}$ for all $n = 1, \dots, N_T$, same for $\tilde{\Gamma}_{\text{out}}^n$. The most important point in $\mathbf{V}_{h,0}$ is to make the test functions vanish in the part of the boundary with unknown boundary conditions.

For any $\mathbf{v} \in \tilde{\mathbf{V}}_h^n$, we introduce $\hat{\mathbf{v}} : \hat{\Omega} \rightarrow \mathbb{R}^d$ and $\mathbf{v}^k : \tilde{\Omega}^k \rightarrow \mathbb{R}^d$ defined by $\hat{\mathbf{v}} := \mathbf{v} \circ \tilde{\mathcal{A}}_h^n$ and $\mathbf{v}^k := \mathbf{v} \circ \tilde{\mathcal{A}}_h^n \circ (\tilde{\mathcal{A}}_h^k)^{-1} = \hat{\mathbf{v}} \circ (\tilde{\mathcal{A}}_h^k)^{-1}$ for $k \leq n$. The unique continuation step consists in finding the solution $(\tilde{\mathbf{u}}^n, \tilde{p}^n) \in \tilde{\mathbf{V}}_h^n \times \tilde{Q}_h^n$ of

$$\begin{aligned} \min_{\mathbf{u} \in \tilde{\mathbf{V}}_h^n} \left\{ \frac{\gamma_M}{2} \|\mathbf{u} - \mathbf{u}_M^n\|_{L^2(\tilde{\Omega}^n)} \right\}, \quad (4.27) \\ \tilde{a}_{\text{fluid/FSI}}^n[(\mathbf{u}, p), (\mathbf{v}, q)] = \tilde{l}^{n-1}(\mathbf{v}) \\ \forall (\mathbf{v}, q) \in \mathbf{V}_{h,0} \times Q_h \end{aligned}$$

where

$$\begin{aligned} \tilde{a}_{\text{fluid/FSI}}^n[(\mathbf{u}, p), (\mathbf{v}, q)] := & \frac{1}{\tau} (\rho^f \mathbf{u}, \mathbf{v})_{\tilde{\Omega}^n} \\ & - (\rho^f \operatorname{div} \tilde{\mathbf{w}}^n \mathbf{u}, \mathbf{v})_{\tilde{\Omega}^n} + (\rho^f (\tilde{\mathbf{u}}^{n-1} - \tilde{\mathbf{w}}^n) \cdot \nabla \mathbf{u}, \mathbf{v})_{\tilde{\Omega}^n} \\ & + 2\mu (\varepsilon(\mathbf{u}), \varepsilon(\mathbf{v}))_{\tilde{\Omega}^n} - (p, \operatorname{div} \mathbf{v})_{\tilde{\Omega}^n} + (q, \operatorname{div} \mathbf{u})_{\tilde{\Omega}^n} \\ & \frac{\rho^s \epsilon}{\tau} \langle \hat{\mathbf{u}}, \hat{\mathbf{v}} \rangle_{\hat{\Sigma}}, \end{aligned}$$

and

$$\tilde{l}^{n-1}(\mathbf{v}) := \frac{1}{\tau} (\rho^f \tilde{\mathbf{u}}^{n-1}, \mathbf{v})_{\tilde{\Omega}^{n-1}} + \langle \sigma(\tilde{\mathbf{u}}^{n-1}, \tilde{p}^{n-1}) \mathbf{n}, \mathbf{v} \rangle_{\tilde{\Sigma}^{n-1}} + \langle 2\tilde{\mathbf{d}}^{n-1} + \tilde{\mathbf{d}}^{n-2}, \hat{\mathbf{v}} \rangle_{\hat{\Sigma}}, \quad (4.28)$$

for all $(\mathbf{u}, p) \in \tilde{\mathbf{V}}_h^n \times \tilde{Q}_h^n, (\mathbf{v}, p) \in \mathbf{V}_h \times Q_h$.

It should be noted that the PDE constraint consists of the discrete weak formulation of the forward fluid-subproblem, with as previous state, the previous FSI estimation.

Problem (4.27) is formulated as a PDE-constrained optimization problem. Since the problem is ill-posed, regularization is required to ensure solvability and stability of the discrete problem. For $[(\mathbf{u}, p), (\mathbf{z}, y)] \in (\tilde{\mathbf{V}}_h^n \times \tilde{Q}_h^n) \times (\mathbf{V}_{0,h} \times Q_h)$ we want to find the saddle points of the discrete regularized Lagrangian associated to (4.27):

$$\begin{aligned} L_h[(\mathbf{u}, p), (\mathbf{z}, y)] := & \frac{\gamma_M}{2} \|\mathbf{u} - \mathbf{u}_M^n\|_{\tilde{\Omega}^n}^2 \\ & + \tilde{a}_{\text{fluid/FSI}}^n[(\mathbf{u}, p), (\mathbf{z}, y)] - \tilde{l}^{n-1}(\mathbf{z}) \\ & + \frac{1}{2} s[(\mathbf{u}, p), (\mathbf{u}, p)] - \frac{1}{2} s^*[(\mathbf{z}, y), (\mathbf{z}, y)]. \end{aligned}$$

where the stabilization terms s and s^* act on the primal variables and their adjoints, respectively and are defined by

$$s[(\mathbf{u}, p), (\mathbf{u}, p)] := \gamma_u \sum_{F \in \tilde{\mathcal{F}}_{int}} \int_F h \llbracket \nabla \mathbf{u} \rrbracket_F \cdot \llbracket \nabla \mathbf{v} \rrbracket_F ds + \gamma_{div} \int_{\Omega} (\operatorname{div} \mathbf{u})(\operatorname{div} \mathbf{v}) dx \quad (4.29)$$

$$+ \gamma_p \int_{\tilde{\Omega}^n} h^2 \nabla p \cdot \nabla q dx, \quad (4.30)$$

and

$$s^*[(\mathbf{z}, y), (\mathbf{z}, y)] := \gamma_u^* \int_{\tilde{\Omega}^n} \nabla \mathbf{z} : \nabla \mathbf{w} dx + \gamma_p^* \int_{\tilde{\Omega}^n} yx dx, \quad (4.31)$$

for $(\mathbf{u}, p) \in \tilde{\mathbf{V}}_h^n \times \tilde{Q}_h^n$, $(\mathbf{z}, y) \in \mathbf{V}_{0,h} \times Q_h$, and non-negative free parameters $\gamma_u, \gamma_p, \gamma_u^*, \gamma_p^*, \gamma_{div}$. $\tilde{\mathcal{F}}_{int}$ the set of interior element faces of $\tilde{\mathcal{A}}_h^n(\hat{\Omega})$. The stabilization on the velocity ensures regularity by penalizing both normal gradient jumps across internal faces and the divergence of the velocity (first two terms in (4.29)). A term similar to the Brezzi-Pitkäranta stabilization regularizes the pressure (last term in (4.29)). The stabilization on the dual variables is consistent with the fact that for exact solution, the dual variables are null. The stabilization terms s and s^* ensure both the solvability and the stability of the discrete continuation.

The saddle points $[(\tilde{\mathbf{u}}^n, \tilde{p}^n), (\mathbf{z}, y)] \in (\tilde{\mathbf{V}}_h^n \times \tilde{Q}_h^n) \times (\mathbf{V}_{0,h}^n \times Q_h)$ of L_h satisfy the following optimality conditions

$$\begin{cases} \gamma_M(\tilde{\mathbf{u}}^n, \mathbf{v})_{\tilde{\Omega}^n} + s_h[(\tilde{\mathbf{u}}^n, \tilde{p}^n), (\mathbf{v}, q)] + \tilde{a}_{\text{fluid/FSI}}^n[(\mathbf{v}, q), (\mathbf{z}, y)] = \gamma_M(\mathbf{u}_M^n, \mathbf{v})_{\tilde{\Omega}^n}, \\ \tilde{a}_{\text{fluid/FSI}}^n[(\tilde{\mathbf{u}}^n, \tilde{p}^n), (\mathbf{w}, x)] - s_h^*[(\mathbf{z}, y), (\mathbf{w}, x)] = l_h^{n-1}(\mathbf{w}), \end{cases} \quad (4.32)$$

for all $(\mathbf{v}, q) \in \tilde{\mathbf{V}}_h^n \times \tilde{Q}_h^n$ and $(\mathbf{w}, x) \in \mathbf{V}_{0,h}^n \times Q_h$.

The linear system associated to the numerical resolution of (4.32) writes as follow using a matrix-block representation:

$$\left[\begin{array}{cc|cc} M_m + S_u & 0 & A^T & B^T \\ 0 & S_p & -B & 0 \\ \hline A & -B^T & -S_u^* & 0 \\ B & 0 & 0 & -S_p^* \end{array} \right] \begin{bmatrix} U_h \\ P_h \\ Z_h \\ Y_h \end{bmatrix} = \begin{bmatrix} U_m \\ 0 \\ F \\ 0 \end{bmatrix}. \quad (4.33)$$

The expression of the matrices is detailed in Appendix A.2.

Remark 7

In the definition of the bilinear form $\tilde{a}_{\text{fluid/FSI}}^n$ associated to the forward fluid sub-problem (4.22), the SUPG stabilization has not been included, which may result in instabilities at high Reynold numbers.

3) Luenberger state observer for the fluid sub-problem After solving the unique continuation system (4.32), the estimation $(\tilde{\mathbf{u}}^n, \tilde{p}^n)$ is used as boundary condition. The fluid solver estimates the fluid state by solving the following problem:

Find $(\tilde{\mathbf{u}}^n, \tilde{p}^n) \in \tilde{\mathbf{V}}_h^n \times \tilde{Q}_h^n$ such that $\forall (\mathbf{v}, q) \in \tilde{\mathbf{V}}_h \times \tilde{Q}_h$

$$\left\{ \begin{array}{l} \frac{1}{\tau} (\rho^f \tilde{\mathbf{u}}^n, \mathbf{v})_{\tilde{\Omega}^n} + \tilde{a}_n^f[(\tilde{\mathbf{u}}^n, \tilde{p}^n), (\mathbf{v}, q)] + \tilde{s}_{\text{SP}}[(\tilde{\mathbf{u}}^n, \tilde{p}^n), (\mathbf{v}, q)] \\ \quad + \frac{\rho^s \epsilon}{\tau} \langle \tilde{\mathbf{u}}^n, \mathbf{v} \rangle_{\tilde{\Sigma}^n} + \gamma_f (\tilde{\mathbf{u}}_h^n - \mathbf{u}_M^n, \mathbf{v})_{\tilde{\Omega}^n} \\ = \tilde{l}^{n-1}(\mathbf{v}) - \langle \tilde{p}^n |_{\tilde{\Gamma}_{\text{in}}^n} \mathbf{n}, \mathbf{v} \rangle_{\tilde{\Gamma}_{\text{in}}^n} - \langle \tilde{p}^n |_{\tilde{\Gamma}_{\text{out}}^n} \mathbf{n}, \mathbf{v} \rangle_{\tilde{\Gamma}_{\text{out}}^n} \end{array} \right. \quad (4.34)$$

with

$$\begin{aligned} \tilde{s}_{\text{SP}}((\mathbf{u}^n, p^n), (\mathbf{v}, q)) &:= \\ &\sum_{K \in \tilde{\mathcal{T}}_h^n} \int_K \delta_K (\rho^f (\tilde{\mathbf{u}}^{n-1} - \mathbf{w}^n) \cdot \nabla \tilde{\mathbf{u}}^n + \nabla \tilde{p}^{n-1}) \cdot (\rho^f (\tilde{\mathbf{u}}^{n-1} - \tilde{\mathbf{w}}^n) \cdot \nabla \mathbf{v} + \nabla q), \end{aligned}$$

with for $(\mathbf{v}, q) \in \tilde{\mathbf{V}}_h \times \tilde{Q}_h$.

Remark 8

Since the continuation provides a pressure and a velocity, we could use a Dirichlet boundary condition for the fluid in the inlet/outlet as well. Here we chose Neumann boundary conditions, as in the original forward problem.

Remark 9

The fluid Luenberger observer and the unique continuation are solved on the same domain $\tilde{\Omega}^n$, with the same ALE velocity.

Algorithm 6 synthesizes the skeleton of the FSI state estimation using the extension of UeL-Fluid, assuming only fluid velocity data.

4.3.2 Numerical results

This section aims at providing numerical evidence on the behavior of the FSI state estimation reported in Algorithm 6 with synthetic data. As specified in the previous section, no boundary conditions are provided to the algorithm, only velocity measurements in the whole domain. The quality of the state estimation is assessed by means of the L^2 -norm of the relative error, with and without noisy data. Finally, we motivate the need for solid data feedback in the case of initial condition for the wall.

4.3.2.1 Synthetic data generation

The synthetic data are generated by solving the forward problem (4.3), (4.6) and (4.7), using Algorithm 5. The reference fluid domain $\hat{\Omega}$ is a cylinder of radius 0.5 cm, centered in the origin, in the plan Oxy , and extruded along the axis Oz with a length $L = 5$ cm. The shape regular mesh of $\hat{\Omega}$ is composed of 10660 vertices, 58800 tetrahedra. Figure 4.2 gives an insight of the characteristic of the tetrahedral mesh.

The following uniform pressure profile $P_{\text{in}}(t)$ is applied on the inflow boundary Γ_{in} ($z = 0$):

$$P_{\text{in}}(t) = \begin{cases} -\frac{P_{\text{max}}}{2} (1 - \cos(\frac{2\pi t}{T^*})) & \text{if } t < T^*, \\ 0 & \text{otherwise,} \end{cases} \quad (4.38)$$

Algorithm 6 FSI state estimation UCL-Fluid (moving domain)**Require:**

$$\begin{cases} \tilde{\mathbf{d}}^0 = \mathbf{d}_0 \tilde{\mathbf{d}}^0 = \mathbf{v}_0 \text{ on } \hat{\Sigma} \\ \tilde{\Omega}^0 = \tilde{\mathcal{A}}_h^0(\hat{\Omega}), \text{ with } \tilde{\mathcal{A}}_h^0 = \mathbf{I} + \mathbf{d}_f^0, \text{ and } \mathbf{d}_f^0 = \text{Ext}(\mathbf{d}_0) \\ \tilde{\mathbf{u}}^0 = \mathbf{u}_0, \tilde{p}^0 = p_0 \text{ on } \tilde{\Omega}^0 \\ \gamma_M, \gamma_f > 0 \end{cases} \quad (4.35)$$

for $n = 1, \dots, N_T$ **do**Solid solver to Fluid solver: $\tilde{\mathbf{d}}^{n-1}$ **A/ Fluid solver step**

1. Compute the fluid domain displacement \mathbf{d}_f^n , the ALE velocity $\tilde{\mathbf{w}}^n$ and the fluid computational domain $\tilde{\Omega}^n$ using the procedure (4.26)
2. Unique continuation: Find $\tilde{\mathbf{u}}^n \in \tilde{\mathbf{V}}_h^n, \tilde{p}^n \in \tilde{Q}_h^n$, solution of

$$\begin{cases} \gamma_M(\tilde{\mathbf{u}}^n, \mathbf{v})_{\tilde{\Omega}^n} + s_h[(\tilde{\mathbf{u}}^n, \tilde{p}^n), (\mathbf{v}, q)] + \tilde{a}_{\text{fluid/FSI}}^n[(\mathbf{v}, q), (\mathbf{z}, y)] = \gamma_M(\mathbf{u}_M^n, \mathbf{v})_{\tilde{\Omega}^n}, \\ \tilde{a}_{\text{fluid/FSI}}^n[(\tilde{\mathbf{u}}^n, \tilde{p}^n), (\mathbf{w}, x)] - s_h^*[(\mathbf{z}, y), (\mathbf{w}, x)] = \tilde{l}_h^{n-1}(\mathbf{w}), \end{cases} \quad (4.36)$$

for all $(\mathbf{v}, q) \in \tilde{\mathbf{V}}_h^n \times \tilde{Q}_h^n$ and $(\mathbf{w}, x) \in \tilde{\mathbf{V}}_{0,h}^n \times \tilde{Q}_h^n$

3. Luenberger observer: Find $\tilde{\mathbf{u}}^n \in \tilde{\mathbf{V}}_h^n, \tilde{p}^n \in \tilde{Q}_h^n$,

$$\begin{cases} \frac{1}{\tau}(\rho^f \tilde{\mathbf{u}}^n, \mathbf{v})_{\tilde{\Omega}^n} + \tilde{a}_n^f[(\tilde{\mathbf{u}}^n, \tilde{p}^n), (\mathbf{v}, q)] + \tilde{s}_{\text{SP}}[(\tilde{\mathbf{u}}^n, \tilde{p}^n), (\mathbf{v}, q)] \\ \quad + \frac{\rho^s \epsilon}{\tau} \langle \tilde{\mathbf{u}}^n, \mathbf{v} \rangle_{\tilde{\Sigma}^n} + \gamma_f(\tilde{\mathbf{u}}_h^n - \mathbf{u}_M^n, \mathbf{v})_{\tilde{\Omega}^n} \\ \quad = \tilde{l}_h^{n-1}(\mathbf{v}) - \langle \tilde{p}^n |_{\tilde{\Gamma}_{\text{in}}^n} \mathbf{n}, \mathbf{v} \rangle_{\tilde{\Gamma}_{\text{in}}^n} - \langle \tilde{p}^n |_{\tilde{\Gamma}_{\text{out}}^n} \mathbf{n}, \mathbf{v} \rangle_{\tilde{\Gamma}_{\text{out}}^n} \end{cases} \quad (4.37)$$

for all $(\mathbf{v}, q) \in \mathbf{V}_h \times Q$.Fluid solver to Solid solver: $\langle \sigma(\mathbf{u}^n, p^n) \mathbf{n}, \mathbf{v}^n \rangle_{\Sigma^n}$ **B/ Solid solver step**

1. Find $\tilde{\mathbf{d}}^n \in \hat{\mathbf{W}}_{0,h}$ solution of (4.18), and update $\tilde{\mathbf{d}}^n \in \hat{\mathbf{W}}_{0,h}$.

end for

with $P_{\max} = 2.0 \times 10^4$ dynes/cm², $T^* = 5.0 \times 10^{-3}$ s and an homogeneous Neumann boundary condition at Γ_{out} . The total simulation time is of $T = 1.5 \times 10^{-2}$ s. The time-step length is $\tau = 1.0 \times 10^{-4}$ s, and the physical parameters are $\rho^f = 1.0$ g/cm³, $\mu = 0.035$ P, for the fluid sub-problem and $\rho^s = 1.2$ g/cm³, $\epsilon = 0.1$ cm, $E = 3.0 \cdot 10^6$ dynes/cm², $\nu = 0.3$, for the solid sub-problem. The non-linear form \mathcal{L}^e in the solid sub-problem(4.6) is derived from non-linear Reissner-Mindlin shell model which introduces as an additional unknown, the direction vector \mathbf{a} of the mid-surface

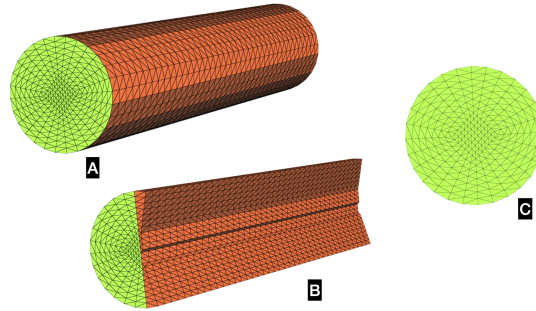


Figure 4.2: Reference geometric configuration. (A) View of the 3D cylinder, colored by surface label ($\hat{\Gamma}_{in}$ in green, $\hat{\Sigma}$ in red). (B) Plane cut visualization with tetrahedra ($y = 0$). (C) Mesh of the circular basis.

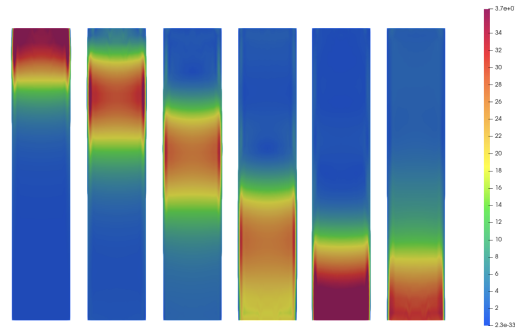


Figure 4.3: Snapshots of the velocity magnitude (reference solution) at t_{30} , t_{50} , t_{70} , t_{100} , t_{120} and t_{140} .

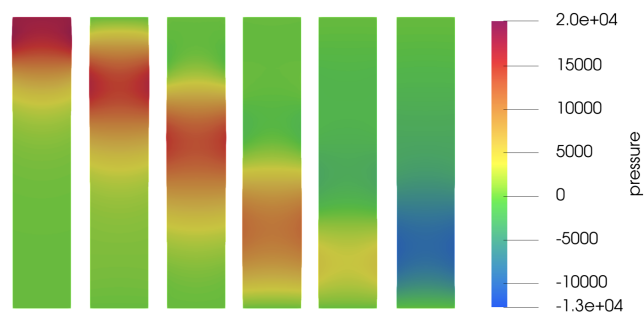


Figure 4.4: Snapshots of the pressure (reference solution) at t_{30} , t_{50} , t_{70} , t_{100} , t_{120} and t_{140} .

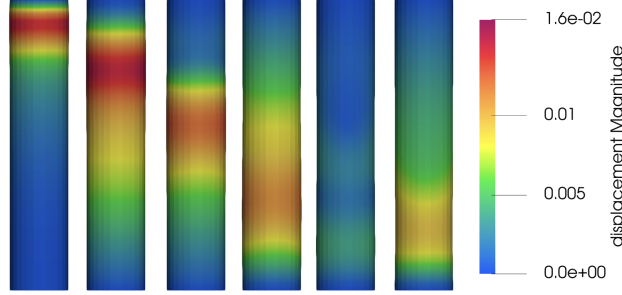


Figure 4.5: Snapshots of the wall displacement (reference solution) at t_{30} , t_{50} , t_{70} , t_{100} , t_{120} and t_{140} .

$\hat{\Sigma}$. The direction vector characterizes the alignment of material lines across the thickness of the wall. Under Reissner-Mindlin kinematic assumption, the kinematics of the wall is characterized by the displacement \mathbf{d} of the mid-surface and the field of direction vector \mathbf{a} , with the constraint that material lines orthogonal to the mid-surface must remain straight and unstretched [Rei21, CB11]. The space discretization (4.23) makes use of MITC3 shell elements.

The solution of the forward problem is a FSI state (fluid velocity and pressure, and solid displacement and velocity) with the ALE map associated to the deformation of the fluid domain. An insight of the synthetic ground truth fluid velocity in its current domain configuration is given in Figures 4.3-4.5. As expected, a pressure wave propagates across the fluid domain.

Let denote by $(\mathbf{u}^n, p^n, \mathbf{d}^n)$ the solution of the FSI forward problem as introduced in Section 4.2. The ground truth velocity field is defined on the domain $\Omega^n = \hat{\mathcal{A}}^n(\hat{\Omega})$, with $\hat{\mathcal{A}}^n$ the ALE parametrization for the ground truth fluid domain deformation.

The ground truth domain deformation does not a priori match the domain deformation obtained after FSI state estimation. If we take as synthetic data for the velocity field \mathbf{u}_M^n the ground truth velocity \mathbf{u}^n , i.e., $\mathbf{u}_M^n = \mathbf{u}^n$, we need to define the measurement \mathbf{u}_M^n in the zone of $\tilde{\Omega}^n$ not included in Ω^n , in such a way that terms of Algorithm 6 like $(\mathbf{u}_M^n, \mathbf{v})_{\tilde{\Omega}^n}$ are correctly defined. Since the ground truth state is obtained by numerical simulation with the reference mesh, the nodal values of the solution can be transported to $\tilde{\Omega}^n$ using the two ALE parametrizations $\hat{\mathcal{A}}^n$ and $\tilde{\mathcal{A}}^n$. This will be detailed in the next paragraph.

Parametrized measurements. Since the ground truth solution and the estimated FSI state share the same reference domain $\hat{\Omega}$, we propose the parametrized velocity measurement $\mathbf{u}_M^n \in \tilde{\mathbf{V}}_h^n$, $n = 1, \dots, N_T$ by transporting the values of \mathbf{u}^n from its domain configuration $\hat{\mathcal{A}}^n(\hat{\Omega})$ to the reference configuration, and from the reference configuration to $\tilde{\mathcal{A}}^n(\hat{\Omega})$, as illustrated on Figure 4.6. It reads

$$\mathbf{u}_M^n(\tilde{\mathcal{A}}^n(\hat{\mathbf{x}})) := \mathbf{u}^n(\hat{\mathcal{A}}^n(\hat{\mathbf{x}})),$$

for all $\hat{\mathbf{x}} \in \hat{\Omega}$.

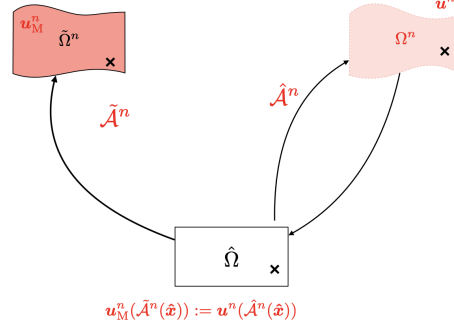


Figure 4.6: Parametrized measurements: transport of the velocity data from Ω^n to $\tilde{\Omega}^n$.

It should be noted that this approach can only be used in the case of synthetic data. In the view of clinical application using real 4D-flow MRI velocity data, we propose to extend the velocity measurements to cover a larger domain, which corresponds to an Eulerian treatment of the measurements.

Eulerian measurements (extension and interpolation). After solving the forward FSI problem in $\hat{\Omega}$, the solution is extended to a fixed domain that strictly contains all the deformed configurations of $\hat{\Omega}$, and finally interpolated on a hexahedral grid with desired resolution (which mimics the velocity data of an 4D-flow MRI exam). Let denote by \mathcal{V} , a square domain sufficiently large to strictly contain all the $\Omega^n, n = 1, \dots, N_T$. \mathcal{V} is first meshed using tetrahedral elements, with conforming nodes at $\partial\hat{\Omega}$ such that the mesh of $\hat{\Omega}$ is a sub-mesh of the mesh of \mathcal{V} , see Figure 4.7. We denote by $\hat{\Omega}_2$ the domain

$$\hat{\Omega}_2 := \mathcal{V} \setminus \hat{\Omega},$$

made of tetrahedral elements (see the rightmost subfigure in Figure 4.7).

The ground truth solution (\mathbf{u}^n, p^n) on $\hat{\mathcal{A}}^n(\hat{\Omega})$ is extended to $\mathcal{V} \setminus \hat{\mathcal{A}}^n(\hat{\Omega})$ by applying the following steps (written in strong formulation):

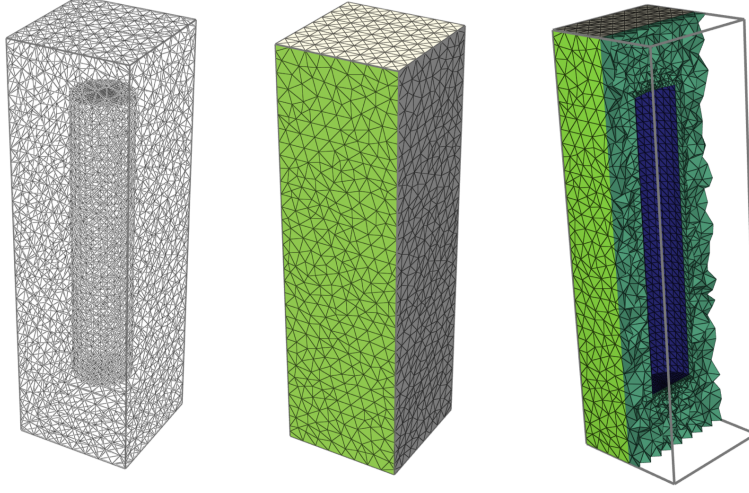
1. The displacement field $\mathbf{d}_f^n|_{\partial\hat{\Omega}}$ of the ground truth solution is extended to $\hat{\Omega}_2$ by solving the harmonic extension problem: Find $\mathbf{d}_{2,f}^n$ defined in $\hat{\Omega}_2$, solution of

$$\begin{cases} -\Delta \mathbf{d}_{2,f}^n = 0 & \text{in } \hat{\Omega}_2, \\ \mathbf{d}_{2,f}^n = \mathbf{d}_f^n & \text{on } \partial\hat{\Omega}, \\ \mathbf{d}_{2,f}^n = 0 & \text{on } \partial\hat{\Omega}_2 \setminus \partial\hat{\Omega}, \end{cases} \quad (4.39)$$

and then

$$\mathbf{w}_2^n := \partial_\tau \mathbf{d}_{2,f}^n, \quad \hat{\mathcal{A}}_2^n = I + \mathbf{d}_{2,f}^n, \quad \Omega_2^n := \hat{\mathcal{A}}_2^n(\hat{\Omega}_2). \quad (4.40)$$

2. The ground truth solution (\mathbf{u}^n, p^n) is extended to $\hat{\Omega}_2$ with continuity of the velocity at the wall interface. The problem reads: Find $(\mathbf{u}_2^n, p_2^n) \in$

Figure 4.7: Geometric configuration: $\hat{\Omega}_2$, surrounding the cylinder.

$[H^1(\Omega_2^n)]^d \times L^2(\Omega_2^n)$ such that

$$\left\{ \begin{array}{ll} \rho^f \left(\partial_\tau \mathbf{u}_2^n |_{\hat{\mathcal{A}}_2^n} + (\mathbf{u}_2^{n-1} - \mathbf{w}_2^n) \cdot \nabla \mathbf{u}_2^n \right) - \operatorname{div} \boldsymbol{\sigma}(\mathbf{u}_2^n, p_2^n) = 0 & \text{in } \Omega_2^n, \\ \operatorname{div} \mathbf{u}_2^n = 0 & \text{in } \Omega_2^n, \\ \mathbf{u}_2^n = \mathbf{u}^n & \text{on } \partial\Omega^n, \\ \boldsymbol{\sigma}(\mathbf{u}_2^n, p_2^n) \mathbf{n} = 0 & \text{on } \Gamma, \\ \mathbf{u}_2^n = 0 & \text{on } \Gamma_D, \end{array} \right. \quad (4.41)$$

where $\Gamma_D \cup \Gamma \cup \partial\Omega^n$ is a given partition of the boundary of Ω_2^n (see Figure 4.8).

Remark 10

In principle, the Stokes equations could have made a more simple and natural choice for the extension in (4.41) (no time derivative, and convective terms). The choice of the extension is arbitrary. In practice, we made use of the Navier-Stokes equations because we dispose of a ready-to-use Navier-Stokes solver.

After extension the resulting velocity field in \mathcal{V} is the combination of \mathbf{u}^n in Ω^n and of \mathbf{u}_2^n in $\Omega_2^n = \mathcal{V} \setminus \Omega^n$. It is interpolated on the nodes of an hexahedral mesh of \mathcal{V} , see Figure 4.8:C. The measured velocity \mathbf{u}_M^n is defined as the piecewise \mathbb{Q}_1 field on the hexahedral mesh with possibly the addition of noise. A sketch of the main steps of the Eulerian data generation is given by Figure 4.8. Eulerian values of \mathbf{u}_M^n are provided by linear interpolation given the values at the nodes of the structured (hexahedral) mesh.

The Eulerian data are showed in Figure 4.9 with the underlying grid resolution.

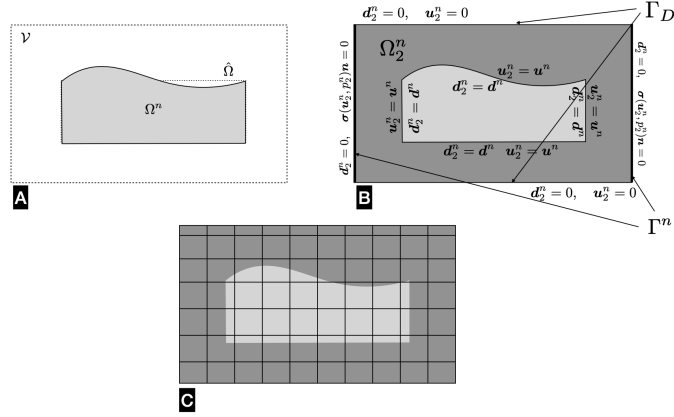


Figure 4.8: 2D sketch of the Eulerian velocity data generation. (A) Reference domains in dashed lines. (B) Extension to $\Omega_2^n := \mathcal{V} \setminus \Omega^n$. (C) Interpolation on the hexahedral grid.

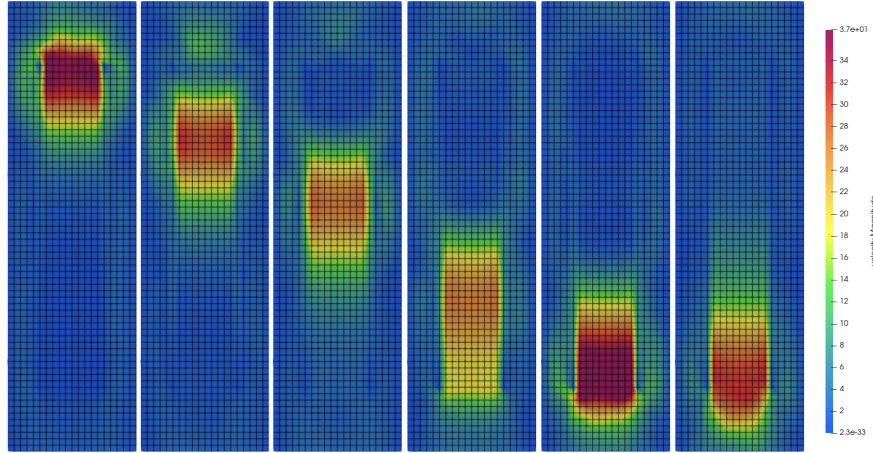


Figure 4.9: Eulerian velocity data (noise-free, grid resolution 0.1cm) at t_{30} , t_{50} , t_{70} , t_{100} , t_{120} and t_{140} .

4.3.2.2 FSI State estimation with UCL-Fluid

The FSI state estimation is performed with unknowns inflow and outflow pressure data using Algorithm 6. Zero initial displacement and velocity are imposed for the solid. We discuss both the case of parametrized and Eulerian data presented in the previous section. The capabilities of the FSI state estimator are assessed for $\gamma_M = 3 \cdot 10^3$, 10^4 , and $\gamma_f = 10^2$, 10^3 , 10^4 , in terms of relative errors for the velocity, the pressure and wall displacement in the reference configuration. Neumann inflow and outflow (pressure) from the continuation are imposed to the Luenberger state observer for the fluid sub-problem. The FSI state estimation algorithm is also tested

in the case of Dirichlet inflow and Neumann outflow boundary conditions.

Figure 4.10 reports some snapshots of the pressure estimation with Eulerian measurements obtained with Algorithm 6 for $\gamma_M = 10^4$ and $\gamma_f = 10^4$. The fluid domain displacement has been amplified by a factor 5. Qualitatively, Algorithm 6 delivers a satisfactory estimation of the fluid pressure

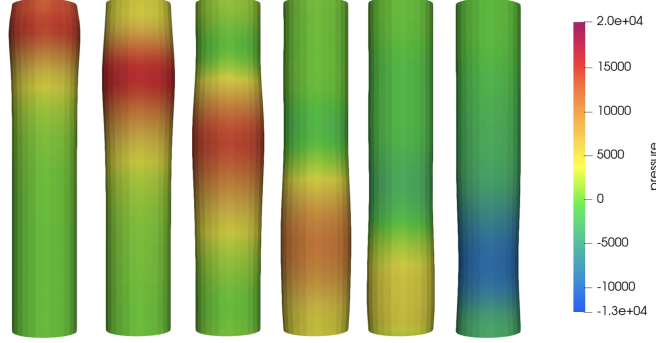


Figure 4.10: Snapshots of the pressure estimated with Algorithm 6, $\gamma_M = 10^4$, $\gamma_f = 10^4$.

In order to provide further insight on the quality of the estimation, we evaluate the relative error with respect to the ground truth solution. Because of the mismatch of the fluid domain between the ground truth and the FSI estimation, the solutions are transported in the reference configuration and the integral of the difference with the ground truth is computed on the reference domain, and normalized by the maximum value of the ground truth. For a quantity \tilde{q}^n defined on $\tilde{\Omega}^n$, the relative error is given by the formula

$$\frac{\|\tilde{q}^n \circ \tilde{\mathcal{A}}^n - q_{\text{ref}}^n \circ \hat{\mathcal{A}}^n\|_{L^2(\hat{\Omega})}}{\max_n \|q_{\text{ref}}^n\|_{L^2(\hat{\Omega})}},$$

q_{ref}^n being the reference solution defined on Ω^n .

The relative error for the velocity $\tilde{\mathbf{u}}^n$, the pressure \tilde{p}^n and the displacement field $\tilde{\mathbf{d}}_f^n$ are reported in Figure 4.11 for parametrized measurements, when inflow and outflow pressures are imposed from the unique continuation estimation. The Ucl-Fluid extended to moving domain provides a satisfactory estimation of the fluid velocity, the pressure, but also the displacement. Increasing γ_M improves the overall precision of the estimation for all γ_f . For $\gamma_f = 100$, the relative error for the displacement goes from 0.3 to less than 0.1 for the displacement, the pressure and the velocity, between $\gamma_M = 3000$ and $\gamma_M = 10000$, as shown by Figure 4.11 (lines of same color). Likewise, for a fixed γ_M , increasing γ_f improves the estimation of the velocity and of the displacement (Figure 4.11(a) and 4.11(c)). For the pressure, the accuracy is almost equivalent for $\gamma_f = 10^2, 10^3, 10^4$, one can refer to Figure 4.11(b). For Eulerian measurements, similar conclusions can be drawn for the dependence of the precision with respect to γ_M and γ_f , see Figure 4.12. Note that the accuracy of FSI state estimation with Eulerian measurements is limited by the (structured) grid resolution of the data.

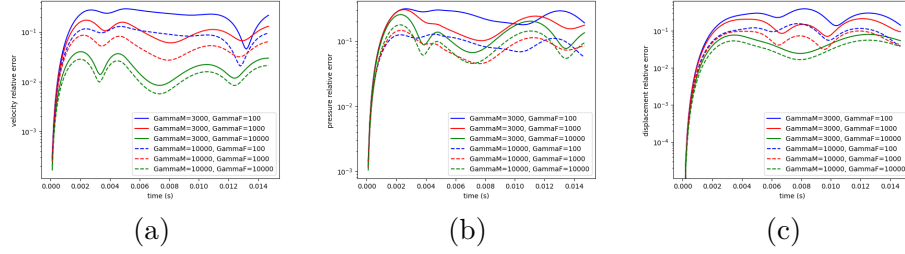


Figure 4.11: Relative errors of the estimation with Algorithm 6 using parametrized data. (a) Velocity. (b) Pressure. (c) Fluid domain displacement.

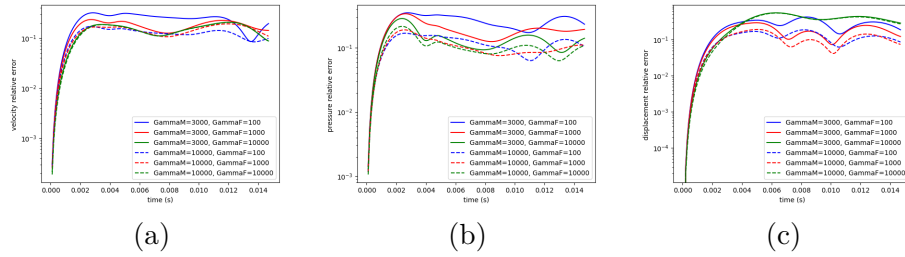


Figure 4.12: Relative errors of the estimation with Algorithm 6 using Eulerian measurements. (a) Velocity. (b) Pressure. (c) Fluid domain displacement.

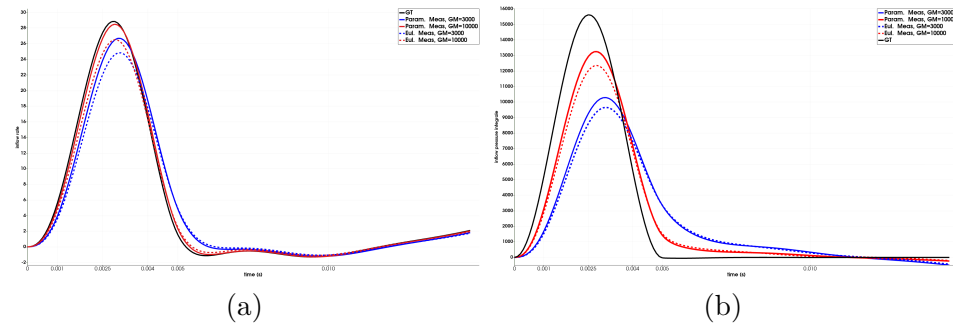


Figure 4.13: Inflow boundary data from the unique continuation. (a) Inflow rate. (b) Inflow pressure.

Another interesting feature of the algorithm is the estimation of the pressure and the boundary conditions with the solution of the unique continuation step (4.32). For $\gamma_f = 10^3$, the inflow pressure $\int_{\Gamma_{in}} \bar{p}^n$ and the inflow rate $\int_{\Gamma_{in}} \mathbf{u}^n \cdot \mathbf{n}$ estimated from the unique continuation step is compared to the ground truth for $\gamma_M = 3 \cdot 10^3$ and $\gamma_M = 10^4$ in Figure 4.13. $\gamma_M = 10^4$ provides reasonable recovery of the shape

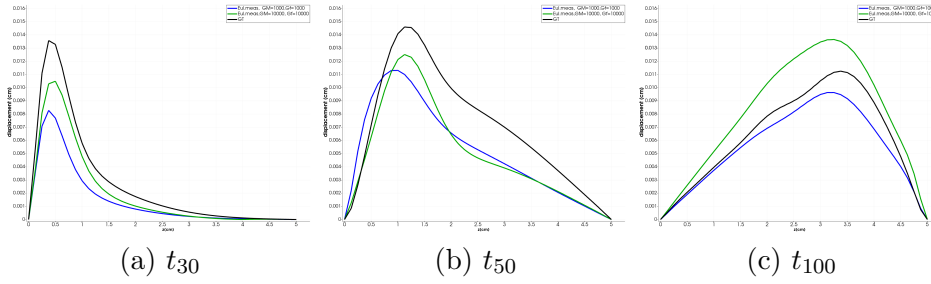


Figure 4.14: Wall displacement norm at different time instants.

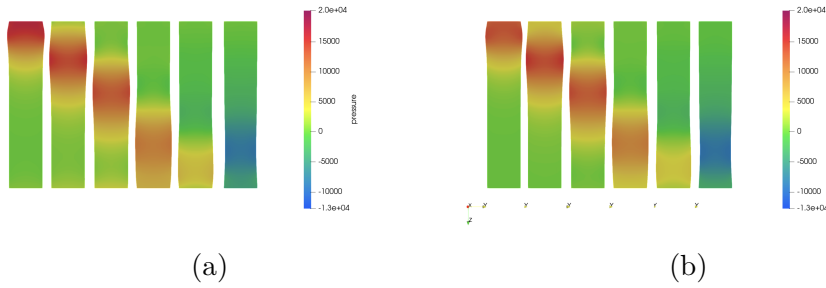


Figure 4.15: Snapshots of the pressure estimation for the two types of boundary conditions, $\gamma_M = 10^4$, $\gamma_f = 10^4$, (Eulerian velocity data). (a) Inflow Dirichlet/Outflow Neumann. (b) Inflow Neumann/Outflow Neumann.

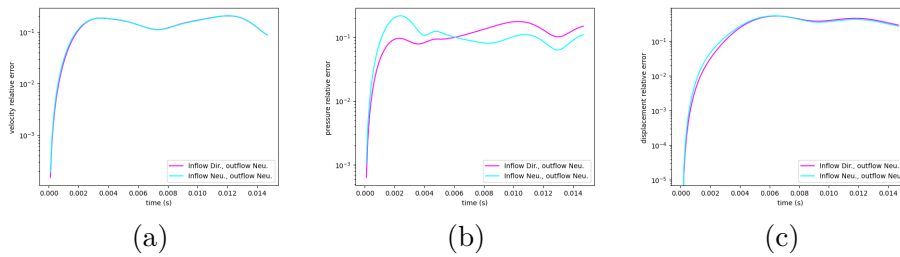


Figure 4.16: Comparison of the relative errors for two types of boundary conditions, $\gamma_M = 10^4$, $\gamma_f = 10^4$ (Eulerian velocity data). (a) Velocity. (b) Pressure. (c) Fluid domain displacement.

of the pressure profile.

Concerning the solid state estimation, the norm of the wall displacement is plotted as different time steps in Figure 4.14. for $\gamma_M = 10^4, \gamma_f = 10^4$. The maximum point-to-point displacement error is $\approx 2 \cdot 10^{-3}$, for $\gamma_M = 10^4, \gamma_f = 10^4$ (Eulerian measurements), and $\approx 1 \cdot 10^{-2}$ in norm, for $\gamma_M = 3000, \gamma_f = 10^3$. The maximum displacement of the wall in the ground truth simulation is $1.6 \cdot 10^{-2}$. The displacement

error compared to the grid resolution of the Eulerian velocity data is very small.

We now consider the case in which the FSI state estimation is performed with Dirichlet inflow boundary conditions and Neumann outflow boundary conditions in fluid Luenberger step. Figure 4.15 reports a qualitative comparison of the pressure estimation with $\gamma_M = 10^4$ and $\gamma_f = 10^4$. Similar results are obtained in the two cases of boundary conditions. This can also be inferred from Figure 4.16, which shows the relative error for the fluid velocity, pressure and domain displacement. It should be noted that the pressure estimation is a bit sensitive to the type of boundary conditions. The better accuracy of the inflow rate may suggest to impose Dirichlet (inflow) boundary conditions at the inlet rather than Neumann boundary conditions. Other numerical considerations could also orientate this choice. In clinical application, imposing inflow pressure may require backflow stabilization for aortic blood flow simulations, for instance.

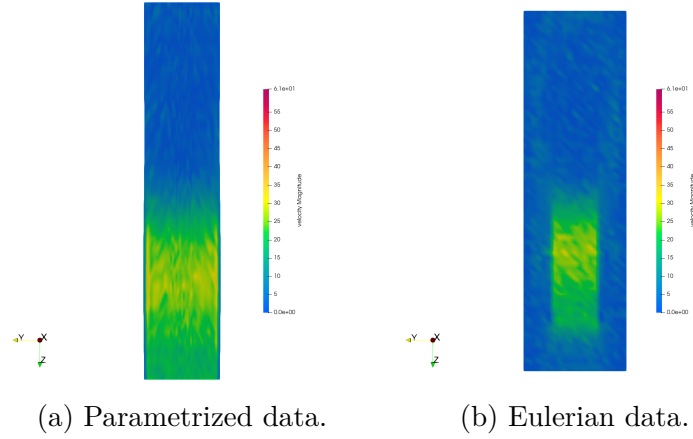


Figure 4.17: Noisy velocity data (5%), at $t_{100} = 0.01$. Note that the left figure has been rescaled.

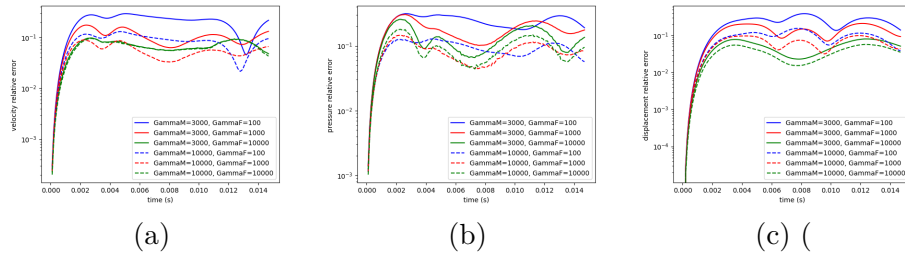


Figure 4.18: Relative errors of the estimation with Algorithm 6 using parametrized noisy data (5%). (a) Velocity. (b) Pressure. (c) Fluid domain displacement.

Finally, noisy data are also generated by adding a Gaussian noise proportional to the maximum velocity component-wise at the nodal values of \mathbf{u}_M^n . This results

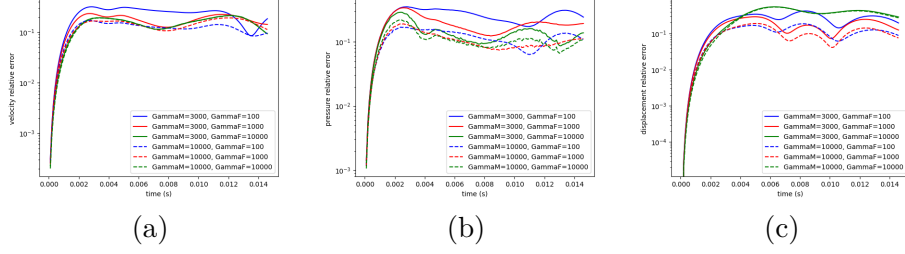


Figure 4.19: Relative errors of the estimation with Algorithm 6 using noisy Eulerian data (5%). (a) Velocity. (b) Pressure. (c) Fluid domain displacement.

in the following transformation:

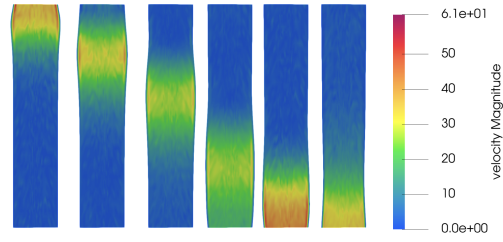
$$\mathbf{u}_M^n(\mathbf{x}_h^j) = \begin{pmatrix} \mathbf{u}_M^n(\mathbf{x}_h^j) \cdot \mathbf{e}_x \\ \mathbf{u}_M^n(\mathbf{x}_h^j) \cdot \mathbf{e}_y \\ \mathbf{u}_M^n(\mathbf{x}_h^j) \cdot \mathbf{e}_z \end{pmatrix} \rightarrow \begin{pmatrix} \mathbf{u}_M^n(\mathbf{x}_h^j) \cdot \mathbf{e}_x + \delta_{j,x} \mathbf{u}^n \\ \mathbf{u}_M^n(\mathbf{x}_h^j) \cdot \mathbf{e}_y + \delta_{j,y} \mathbf{u}^n \\ \mathbf{u}_M^n(\mathbf{x}_h^j) \cdot \mathbf{e}_z + \delta_{j,z} \mathbf{u}^n \end{pmatrix} \quad (4.42)$$

with for each component $\alpha = x, y, z$, $\delta_{j,\alpha} \mathbf{u}^n := \delta_{\text{noise}} k_j \|\mathbf{u}_M^n \cdot \mathbf{e}_d\|_\infty$, $0 \leq \delta_{\text{noise}} \leq 1$ being the level of noise, k_j a realization of a random variable with a unit normal distribution. A visualization of the noisy velocity field for the Eulerian data and the parametrized measurements is provided at one time step with $\delta_{\text{noise}} = 5\%$, in Figure 4.17(b) and Figure 4.17(a), respectively.

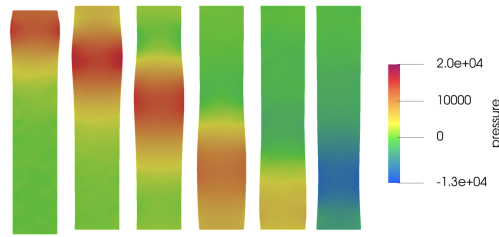
One can find in Figure 4.18, the relative error between the FSI state estimation UclFluid and the ground truth, for noisy parametrized measurements. The relative error for noisy Eulerian data is reported in Figure 4.19.

The FSI state estimation using UclFluid algorithm with noisy data yields similar results as the same test case with noise-free data. This shows a robust management of the noise in the data and give promising preliminary results. Also one can note that for $\gamma_M = 10^4$ and $\gamma_f = 10^4$, the noise in the data slightly degrades the velocity estimation whereas its effect on the pressure and displacement estimate is filtered, leading to similar results as with noise-free measurements. One can see Figure 4.20 and Figure 4.21 for snapshots of the FSI estimation. The fluid domain is deformed with the estimated displacement field that is multiplied by 5, for better visibility.

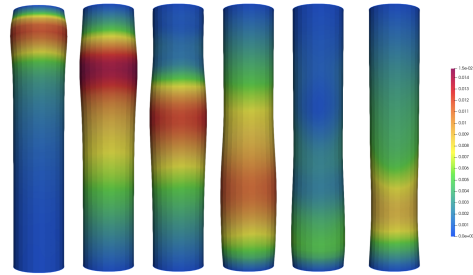
Initial condition of the wall displacement Before concluding the numerical examples, let consider the case in which arbitrary initial conditions are imposed in both the fluid and the solid sub-problems. Here we impose an initial problem on the velocity $\tilde{\mathbf{u}}^0 = 5.0 \mathbf{e}_z$ cm/s, and $\mathbf{d}^0(x, y, z) = 0.1 \left(1 - \frac{(z-L/2)^2}{(L/2)^2}\right) \mathbf{e}_z$ cm/s, for $(x, y, z) \in \hat{\Sigma}$, with represents a severely perturbed initial boundary condition. The inlet pressure defined in (4.38) for the forward problem is imposed on Γ_{in} and homogeneous Neumann boundary conditions are imposed on Γ_{out} . Those are the boundary conditions of the reference solution illustrated in Figure 4.3 to 4.5. We now estimate the FSI state using the Luenberger state observer (4.34) on the fluid with the exact boundary conditions instead of the boundary conditions obtained



(a) Velocity



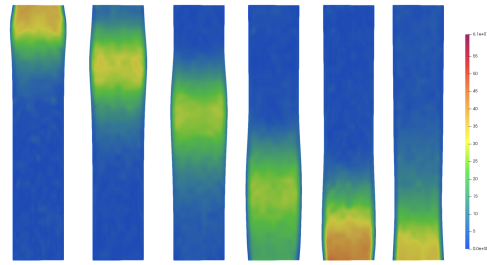
(b) Pressure



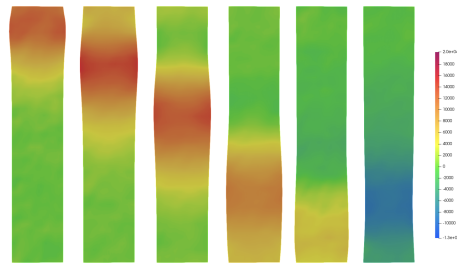
(c) Wall displacement

Figure 4.20: FSI state estimation using Algorithm 6 with (parametrized) noisy data (5%) at $t_{30}, t_{50}, t_{70}, t_{100}, t_{120}$ and t_{140} .

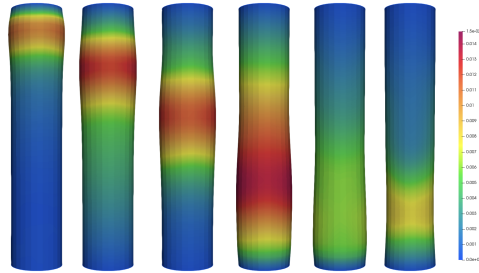
using unique continuation. The FSI state estimation with exact boundary conditions should be more accurate than a FSI state estimation with Algorithm 6. We make use of noise-free Eulerian velocity measurements in the fluid. Figures 4.22 to 4.24 provide snapshots of the FSI estimation for $\gamma_f = 1000$. Though the pressure wave propagation seems to be qualitatively well captured (see Figure 4.23), the relative errors for the fluid velocity, the pressure and the fluid domain displacement decrease at a very slow speed, as reported on Figure 4.25.



(a) Velocity



(b) Pressure



(c) Wall displacement

Figure 4.21: FSI state estimation using Algorithm 6 with (Eulerian) noisy data (5%) at $t_{30}, t_{50}, t_{70}, t_{100}, t_{120}$ and t_{140} .

4.3.3 Intermediate conclusion

The algorithm UcL-Fluid, extended to moving domain FSI, manages to estimate the FSI state of the system without any knowledge of the boundary conditions, with only velocity measurements. The accuracy of the estimation is reasonable with and without noise for a wide range of free-parameters. However, with an initial condition for the solid and with Eulerian data, the velocity data might not be sufficient to estimate the FSI state estimation. In order to address this problem, we propose to include Luenberger observers also in the solid sub-problem, which is the purpose of the next section.

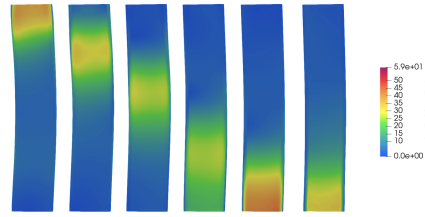


Figure 4.22: Snapshots of the estimated velocity, with initial conditions at $t_{30}, t_{50}, t_{70}, t_{100}, t_{120}$ and t_{140} .

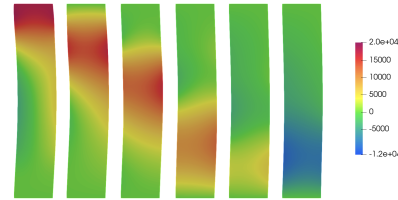


Figure 4.23: Snapshots of the estimated pressure, with initial conditions at $t_{30}, t_{50}, t_{70}, t_{100}, t_{120}$ and t_{140} .

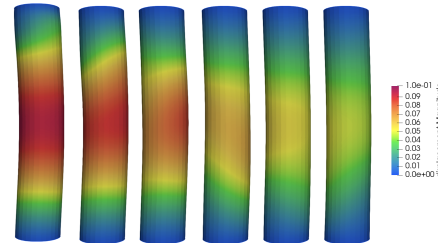


Figure 4.24: Snapshots of the estimated wall displacement, with initial conditions.

4.4 UcL-FSI estate estimator

As suggested in [BCF⁺13], Luenberger state observers can be a simple and attractive strategy for FSI state estimation, when solid measurements are available: the so-called Direct Velocity Feedback (DVF) and Schur Displacement Feedback (SDF). In this section, a FSI state estimation method from solid and fluid measurements, named UcL-FSI, is proposed. Numerical analysis of the frequency response of the wall displacement under the combined effect of the Luenberger state observer for the fluid sub-problem, the DVF and SDF for the fluid sub-problem is performed in a 2D simplified FSI problem. The goal is to provide insight on the choice of the data fidelity parameters.

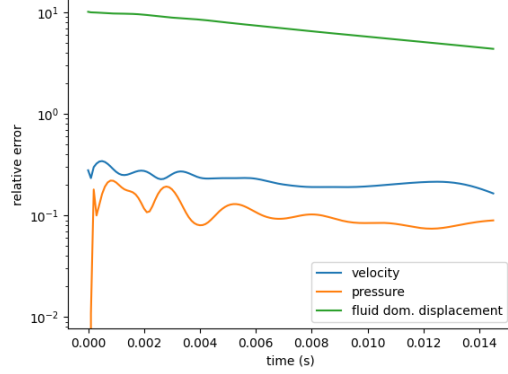


Figure 4.25: Relative errors of the estimated pressure, velocity and pressure.

Lagrangian velocity and displacement measurements of the wall could be obtained using the tracking approach introduced in Chapter 2 using 4D-flow data (grayscale images with velocity). One could however debate the use of solid data coming from a tracking algorithm whose predictions are based on a simplified dynamical model, compared to the solid sub-problem. We instead propose a more consistent alternative, which integrates directly the position observation operator presented in Section 2.2.3.2 within the SDF feedback.

4.4.1 Presentation of the algorithm

Luenberger state observer for the solid sub-problem. We assume that (Lagrangian) solid displacement and velocity measurements are available, namely $(\mathbf{d}_M^n, \dot{\mathbf{d}}_M^n)$. Application of DVF and SDF to partial differential equations has been proposed in [Moi08a], especially for elastodynamic state estimation. Those works have been followed by [BCF+13] applied to FSI state estimation, with DVF and SDF considered separately. Here, we combine the Luenberger on the velocity and on the displacement. Using DVF and SDF, the time-discrete solid weak formulation consequently reads: Find $\tilde{\mathbf{d}}^n \in \hat{\mathbf{W}}_{0,h}$, such that

$$\begin{cases} \tilde{\mathbf{d}}^n = \partial_\tau \tilde{\mathbf{d}}^n + \gamma_{\text{sdf}}(\tilde{\mathbf{d}}^n - \mathbf{d}_M^n), \\ (\rho^s \epsilon \partial_\tau \tilde{\mathbf{d}}^n, \hat{\boldsymbol{\xi}})_{\hat{\Sigma}} + \mathbf{a}^s(\tilde{\mathbf{d}}^n, \hat{\boldsymbol{\xi}}) + \gamma_{\text{dvf}}(\tilde{\mathbf{d}}^n - \dot{\mathbf{d}}_M^n, \hat{\boldsymbol{w}})_{\hat{\Sigma}} = -(\sigma(\tilde{\mathbf{u}}^n, \tilde{\mathbf{p}}^n) \mathbf{n}, \boldsymbol{\xi}^n)_{\hat{\Sigma}^n} \end{cases} \quad (4.43)$$

for all $\hat{\boldsymbol{\xi}} \in \hat{\mathbf{W}}_{0,h}$. Here, $\gamma_{\text{sdf}}, \gamma_{\text{dvf}} > 0$ stand for two free-parameters quantifying the confidence in the data. The data feedback terms add up dissipation of (4.18).

Remark 11

In practice, the discrete weak formulation (III) is not solved as it is. It is rather expressed in terms of the displacement $\tilde{\mathbf{d}}^n$. The first relation in (III), which corresponds to the perturbed displacement-velocity relation, can be rewritten as

$$\tilde{\mathbf{d}}^n = \frac{1}{\tau}(1 + \gamma_{\text{sdf}}\tau)\tilde{\mathbf{d}}^n - \frac{1}{\tau}(\tilde{\mathbf{d}}^{n-1} + \tau\gamma_{\text{sdf}}\mathbf{d}_M^n), \quad (4.44)$$

so that the second relation yields the following variational problem in terms of $\tilde{\mathbf{d}}^n$:

$$\begin{aligned} & \left(\frac{\rho^s \epsilon}{\tau^2} + \frac{\gamma_{\text{dvf}}}{\tau} \right) (1 + \tau \gamma_{\text{sdf}}) (\tilde{\mathbf{d}}^n, \hat{\boldsymbol{\xi}})_{\Sigma} + a^s(\tilde{\mathbf{d}}^n, \hat{\boldsymbol{\xi}}) = -(\sigma(\tilde{\mathbf{u}}^n, \tilde{p}^n) \mathbf{n}, \boldsymbol{\xi}^n)_{\tilde{\Sigma}^n} + \frac{\rho^s \epsilon}{\tau} (\tilde{\mathbf{d}}^{n-1}, \boldsymbol{\xi}^n)_{\Sigma} \\ & + \left(\frac{\rho^s \epsilon}{\tau^2} + \frac{\gamma_{\text{dvf}}}{\tau} \right) (\tilde{\mathbf{d}}^{n-1} + \tau \gamma_{\text{sdf}} \mathbf{d}_{\text{M}}^n, \hat{\boldsymbol{\xi}})_{\Sigma} + \gamma_{\text{dvf}} (\dot{\mathbf{d}}_{\text{M}}^n, \hat{\boldsymbol{\xi}})_{\Sigma}, \quad \forall \hat{\boldsymbol{\xi}} \in \hat{\mathbf{W}}_{0,h}. \end{aligned} \quad (4.45)$$

The UCL-FSI estimator is summarized in Algorithm 7. Compared to Algorithm 6, Algorithm 7 adds a feedback on the solid displacement and velocity, the other steps being identical.

4.4.2 Pole placement analysis

In this section, we investigate the location of the poles of FSI state estimation with fluid and solid measurements, without the unique continuation. The aim is to provide a strategy for an optimal choice of the data fidelity to dissipate low to high frequency vibrations. A simplified FSI model is used, in the spirit of [CGN05]. The placements of the poles of the error system is analyzed as performed in [Moi08a, BCF⁺13]

We consider a rectangular domain $\Omega = [0; L] \times [0; R]$ of \mathbb{R}^2 . The boundary $\partial\Omega$ is partitioned as $\partial\Omega$ between Γ_1 , Γ_2 the inflow and outflow boundary, respectively and Σ the fluid-structure interface and Γ_3 . The solid is governed by the linear elastic membrane equations. The viscous and convective effects are neglected in the fluid flow. The infinitesimal displacement of the fluid-structure interface is only vertical and we neglect the deformation of the fluid domain. The reference solution of the FSI problem is denoted by $(\mathbf{u}_{\text{ref}}, p_{\text{ref}}, d_{\text{ref}})$ and verifies:

$$\left\{ \begin{array}{ll} \rho^f \partial_t \mathbf{u}_{\text{ref}} + \nabla p_{\text{ref}} & = 0 & \text{in } (0, T) \times \Omega, \\ \operatorname{div}(\mathbf{u}_{\text{ref}}) & = 0 & \text{in } (0, T) \times \Omega, \\ p_{\text{ref}} & = \bar{p} & \text{on } (0, T) \times \Gamma_1 \cup \Gamma_2, \\ \mathbf{u}_{\text{ref}} \cdot \mathbf{n} & = 0 & \text{on } (0, T) \times \Gamma_3, \\ \mathbf{u}_{\text{ref}} \cdot \mathbf{n} & = \dot{d}_{\text{ref}} & \text{on } (0, T) \times \Sigma, \end{array} \right. \quad (4.50)$$

$$\left\{ \begin{array}{ll} \rho^s \epsilon \partial_t \dot{d}_{\text{ref}} - c^2 \partial_{xx} d_{\text{ref}} & = p_{\text{ref}} & \text{in } (0, T) \times \Sigma, \\ \dot{d}_{\text{ref}} & = \partial_t d_{\text{ref}} & \text{in } (0, T) \times \Sigma, \\ d_{\text{ref}} & = 0 & \text{on } (0, T) \times \partial\Sigma, \end{array} \right. \quad (4.51)$$

with \bar{p} the pressure profile imposed at the inflow and outflow boundary. The problem is complemented with the initial conditions: $\mathbf{u}_{\text{ref}}(0) = \mathbf{u}_0$, $d_{\text{ref}}(0) = d_0$ and $\dot{d}_{\text{ref}}(0) = v_0$.

Let consider the same system with uncertain initial conditions. The fluid sub-problem (4.50) is turned into a Luenberger observer using the fluid reference solution as measurement, and the solid problem is also enriched, using DVF and SDF with velocity and displacement measurements from the reference solution, respectively. The goal of those Luenberger observers is to stabilize the error to zero. The resulting FSI state (\mathbf{u}, p, d) is solution of:

Algorithm 7 FSI state estimation UCL-FSI (moving domain)

Require: Initial conditions:

$$\begin{cases} \tilde{\mathbf{d}}^0 = \mathbf{d}_0 \tilde{\mathbf{d}}^0 = \mathbf{v}_0 \text{ on } \hat{\Sigma} \\ \tilde{\Omega}^0 = \tilde{\mathcal{A}}_h^0(\hat{\Omega}), \text{ with } \tilde{\mathcal{A}}_h^0 = \mathbf{I} + \mathbf{d}_f^0, \text{ and } \mathbf{d}_f^0 = \text{Ext}(\mathbf{d}_0) \\ \tilde{\mathbf{u}}^0 = \mathbf{u}_0, \tilde{p}^0 = p_0 \text{ on } \tilde{\Omega}^0 \end{cases} \quad (4.46)$$

for $n = 1, \dots, N_T$ **do**
Solid solver to Fluid solver: $(\tilde{\mathbf{d}}^{n-1}, \tilde{\mathbf{d}}^{n-1})$.

A/ Fluid solver

1. Compute the fluid domain displacement \mathbf{d}_f^n , the ALE velocity $\tilde{\mathbf{w}}^n$ and the fluid computational domain $\tilde{\Omega}^n$ using the procedure (4.26)
2. Unique continuation: Find $\tilde{\mathbf{u}}^n \in \tilde{\mathbf{V}}_h^n, \tilde{p}^n \in \tilde{Q}_h^n$, solution of

$$\begin{cases} \gamma_M(\tilde{\mathbf{u}}^n, \mathbf{v})_{\tilde{\Omega}^n} + s_h[(\tilde{\mathbf{u}}^n, \tilde{p}^n), (\mathbf{v}, q)] + \tilde{a}_{\text{fluid/FSI}}^n[(\mathbf{v}, q), (\mathbf{z}, y)] = \gamma_M(\mathbf{u}_M^n, \mathbf{v})_{\tilde{\Omega}^n}, \\ \tilde{a}_{\text{fluid/FSI}}^n[(\tilde{\mathbf{u}}^n, \tilde{p}^n), (\mathbf{w}, x)] - s_h^*[(\mathbf{z}, y), (\mathbf{w}, x)] = \tilde{l}_h^{n-1}(\mathbf{w}), \end{cases} \quad (4.47)$$

 for all $(\mathbf{v}, q) \in \tilde{\mathbf{V}}_h^n \times \tilde{Q}_h^n$ and $(\mathbf{w}, x) \in \tilde{\mathbf{V}}_{0,h}^n \times \tilde{Q}_h^n$.

3. Luenberger fluid observer: Find $\tilde{\mathbf{u}}^n \in \tilde{\mathbf{V}}_h^n, \tilde{p}^n \in \tilde{Q}_h^n$,

$$\begin{cases} \frac{1}{\tau}(\rho^f \tilde{\mathbf{u}}^n, \mathbf{v})_{\tilde{\Omega}^n} + \tilde{a}_n^f[(\tilde{\mathbf{u}}^n, \tilde{p}^n), (\mathbf{v}, q)] + \tilde{s}_{\text{SP}}[(\tilde{\mathbf{u}}^n, \tilde{p}^n), (\mathbf{v}, q)] \\ \quad + \frac{\rho^s \epsilon}{\tau} \langle \tilde{\mathbf{u}}^n, \mathbf{v} \rangle_{\tilde{\Sigma}^n} + \gamma_L(\tilde{\mathbf{u}}_h^n - \mathbf{u}_M^n, \mathbf{v})_{\tilde{\Omega}^n} \\ \quad = \tilde{l}^{n-1}(\mathbf{v}) - \langle \tilde{p}^n|_{\tilde{\Gamma}_{\text{in}}^n}, \mathbf{n}, \mathbf{v} \rangle_{\tilde{\Gamma}_{\text{in}}^n} - \langle \tilde{p}^n|_{\tilde{\Gamma}_{\text{out}}^n}, \mathbf{n}, \mathbf{v} \rangle_{\tilde{\Gamma}_{\text{out}}^n} \end{cases} \quad (4.48)$$

 for all $(\mathbf{v}, q) \in \mathbf{V}_h \times Q$.

B/ Solid solver

1. Luenberger solid state estimation: Find $\tilde{\mathbf{d}}^n \in \hat{\mathbf{W}}_{0,h}$ solution of

$$(\rho^s \epsilon \partial_\tau \tilde{\mathbf{d}}^n, \hat{\boldsymbol{\xi}})_{\hat{\Sigma}} + \mathbf{a}^s(\tilde{\mathbf{d}}^n, \hat{\boldsymbol{\xi}}) + \gamma_{\text{dvf}}(\tilde{\mathbf{d}}^n - \mathbf{d}_M^n, \hat{\mathbf{w}})_{\hat{\Sigma}} = -(\sigma(\tilde{\mathbf{u}}^n, \tilde{p}^n) \mathbf{n}, \hat{\boldsymbol{\xi}}^n)_{\hat{\Sigma}^n} \quad (4.49)$$

 $\forall \hat{\boldsymbol{\xi}} \in \hat{\mathbf{W}}_{0,h}$.

2. Compute $\tilde{\mathbf{d}}^n \in \hat{\mathbf{W}}_{0,h}$ by the relation $\tilde{\mathbf{d}}^n = \frac{1}{\tau}(1 + \gamma_{\text{sdf}}\tau)\tilde{\mathbf{d}}^n - \frac{1}{\tau}(\tilde{\mathbf{d}}^{n-1} + \tau\gamma_{\text{sdf}}\mathbf{d}_M^n)$.

end for

$$\begin{cases} \rho^f \partial_t \mathbf{u} + \nabla p + \gamma_f(\mathbf{u} - \mathbf{u}_{\text{ref}}) = 0 & \text{in } (0, T) \times \Omega, \\ \text{div}(\mathbf{u}) = 0 & \text{in } (0, T) \times \Omega, \\ p = \bar{p} & \text{on } (0, T) \times \Gamma_1 \cup \Gamma_2, \\ \mathbf{u} \cdot \mathbf{n} = 0 & \text{on } (0, T) \times \Gamma_3, \\ \mathbf{u} \cdot \mathbf{n} = \dot{d} & \text{on } (0, T) \times \Sigma, \end{cases} \quad (4.52)$$

$$\begin{cases} \rho^s \epsilon \partial_t \dot{d} - c^2 \partial_{xx} d + \gamma_{\text{dvf}}(\dot{d} - \dot{d}_{\text{ref}}) = p & \text{in } (0, T) \times \Sigma, \\ \dot{d} = \partial_t d + \gamma_{\text{sdf}}(d - d_{\text{ref}}) & \text{in } (0, T) \times \Sigma, \\ d = 0 & \text{on } (0, T) \times \partial \Sigma \end{cases} \quad (4.53)$$

for $\gamma_f, \gamma_{\text{sdf}}, \gamma_{\text{dvf}} > 0$, three user-defined parameters. The initial conditions are $\mathbf{u}(0) = \mathbf{u}_0 + \delta \mathbf{u}_0$, $d(0) = d_0 + \delta d_0$ and $\dot{d}(0) = v_0 + \delta v_0$.

Let introduce \mathbf{e}_u , e_p and e_d , the errors with the data defined as follows:

$$\mathbf{e}_u := \mathbf{u}_{\text{ref}} - \mathbf{u}, \quad e_p := p_{\text{ref}} - p, \quad e_d := d_{\text{ref}} - d.$$

Theorem 1

The displacement error e_d is solution of

$$(\rho^s \epsilon \mathcal{I} + \rho^f \mathcal{M}_A) \partial_{tt} e_d \quad (4.54)$$

$$+ ((\rho^s \epsilon \gamma_{\text{sdf}} + \gamma_{\text{dvf}}) \mathcal{I} + (\rho^f \gamma_{\text{sdf}} + \gamma_f) \mathcal{M}_A) \partial_t e_d \quad (4.55)$$

$$+ (\gamma_{\text{dvf}} \gamma_{\text{sdf}} + \gamma_{\text{sdf}} \gamma_f \mathcal{M}_A) e_d - c^2 \partial_{xx} e_d = 0, \quad (4.56)$$

where the operator $\mathcal{M}_A: H^{-1/2}(\Sigma) \rightarrow H^{1/2}(\Sigma)$ denotes the added-mass operator defined by the relation

$$\mathcal{M}_A w = \mathcal{R}w|_{\Sigma},$$

for any $w \in H^{-1/2}(\Sigma)$. For $w \in H^{-1/2}(\Sigma)$, we denote by $\mathcal{R}w$ the solution of the following problem

$$\begin{cases} -\Delta \mathcal{R}w = 0 & \text{in } \Omega, \\ \mathcal{R}w = 0 & \text{on } \Gamma_1 \cup \Gamma_2, \\ \frac{\partial \mathcal{R}w}{\partial \nu} = 0 & \text{on } \Gamma_3, \\ \frac{\partial \mathcal{R}w}{\partial n} = w & \text{on } \Sigma. \end{cases} \quad (4.57)$$

Proof The dynamical equation (4.53)₁ can be expressed in terms of d using the relations (4.53)₂ and (4.51)₂, which yields

$$\partial_t \dot{d} = \partial_{tt} d + \gamma_{\text{sdf}}(\partial_t d - \dot{d}_{\text{ref}}),$$

By inserting this expression into (4.53)₁, we get

$$\rho^s \epsilon (\partial_{tt} d + \gamma_{\text{sdf}}(\partial_t d - \dot{d}_{\text{ref}})) - c^2 \partial_{xx} d + \gamma_{\text{dvf}}(\partial_t d - \dot{d}_{\text{ref}} + \gamma_{\text{sdf}}(d - d_{\text{ref}})) = p,$$

or equivalently

$$\rho^s \epsilon \partial_{tt} d + (\rho^s \epsilon \gamma_{\text{sdf}} + \gamma_{\text{dvf}})(\partial_t d - \dot{d}_{\text{ref}}) + \gamma_{\text{dvf}} \gamma_{\text{sdf}}(d - d_{\text{ref}}) - c^2 \partial_{xx} d = p.$$

Note that due to the fourth equality in (4.50), the velocity error $\partial_t d - \dot{d}_{\text{ref}}$ is also $\partial_t(d - d_{\text{ref}})$. The errors \mathbf{e}_u , e_p and e_d are thus solutions of

$$\begin{cases} \rho^f \partial_t \mathbf{e}_u + \nabla e_p + \gamma \mathbf{e}_u = 0 & \text{in } (0, T) \times \Omega, \\ \text{div}(\mathbf{e}_u) = 0 & \text{in } (0, T) \times \Omega, \\ e_p = 0 & \text{on } (0, T) \times \Gamma_1 \cup \Gamma_2, \\ \mathbf{e}_u \cdot \mathbf{n} = 0 & \text{on } (0, T) \times \Gamma_3, \\ \mathbf{e}_u \cdot \mathbf{n} = \partial_t e_d + \gamma_{\text{sdf}} e_d & \text{on } (0, T) \times \Sigma \end{cases} \quad (4.58)$$

and

$$\begin{cases} \rho^s \epsilon \partial_{tt} e_d + (\rho^s \epsilon \gamma_{\text{sdf}} + \gamma_{\text{dvf}}) \partial_t e_d + \gamma_{\text{dvf}} \gamma_{\text{sdf}} e_d - c^2 \partial_{xx} e_d = e_p & \text{in } (0, T) \times \Sigma, \\ e_d = 0 & \text{on } (0, T) \times \partial \Sigma, \end{cases} \quad (4.59)$$

We apply the divergence to (4.58) in order to eliminate the velocity unknown. It yields the following problem relating the displacement error to the pressure error:

$$\begin{cases} -\Delta e_p = 0 & \text{in } (0, T) \times \Omega, \\ e_p = 0 & \text{on } (0, T) \times \Gamma_1 \cup \Gamma_2, \\ \frac{\partial e_p}{\partial n} = 0 & \text{on } (0, T) \times \Gamma_3, \\ \frac{\partial e_p}{\partial n} = -\rho^f \partial_{tt} e_d - (\rho^f \gamma_{\text{sdf}} + \gamma_f) \partial_t e_d - \gamma_{\text{sdf}} \gamma_f e_d & \text{on } (0, T) \times \Sigma. \end{cases} \quad (4.60)$$

We introduce For any $w \in H^{-1/2}(\Sigma)$, we denote by $\mathcal{R}w$ the solution of the following problem

$$\begin{cases} -\Delta \mathcal{R}w = 0 & \text{in } \Omega, \\ \mathcal{R}w = 0 & \text{on } \Gamma_1 \cup \Gamma_2, \\ \frac{\partial \mathcal{R}w}{\partial n} = 0 & \text{on } \Gamma_3, \\ \frac{\partial \mathcal{R}w}{\partial n} = w & \text{on } \Sigma. \end{cases} \quad (4.61)$$

Due to (4.60),

$$e_p = \mathcal{R}(-\rho^f \partial_{tt} e_d - (\rho^f \gamma_{\text{sdf}} + \gamma_f) \partial_t e_d - \gamma_{\text{sdf}} \gamma_f e_d).$$

Let the operator $\mathcal{M}_A: H^{-1/2}(\Sigma) \rightarrow H^{1/2}(\Sigma)$ be defined by the relation

$$\mathcal{M}_A w = \mathcal{R}w|_{\Sigma}.$$

By definition

$$e_p|_{\Sigma} = \mathcal{M}_A(-\rho^f \partial_{tt} e_d - (\rho^f \gamma_{\text{sdf}} + \gamma_f) \partial_t e_d - \gamma_{\text{sdf}} \gamma_f e_d)$$

By using (4.59) we get (4.54), which completes the proof. \square

We look for solutions of (4.54) of the form $e^{\omega t} g$ where $\omega \in \mathbb{C}$, $g \in V$. The operator \mathcal{M}_A is compact, self-adjoint and positive on $L^2(\Sigma)$, consequently it exists a basis $(\phi_k)_k$ of $L^2(\Sigma)$, made of eigenvectors of \mathcal{M}_A . As shown, in [CGN05] the eigenfunctions and eigenvalues of (4.54) are given by:

$$\phi_k = \beta_k \sin\left(\frac{k\pi}{L} x\right), \quad \lambda_k = \frac{L}{k\pi \tanh\left(\frac{\pi R}{L}\right)}, \quad k \geq 1.$$

Consequently, we can start by looking at solution \tilde{d} of (4.54) of the form $e^{\omega_k t} \phi_k$.

Proposition 1

The complex frequencies of (4.54) are given by the roots of $P_k(\omega)$ defined by

$$\begin{aligned} P_k(\omega) := & (\rho^s \epsilon + \rho^f \lambda_k) \omega^2 + ((\rho^s \epsilon \gamma_{\text{sdf}} + \gamma_{\text{dvf}}) + (\rho^f \gamma_{\text{sdf}} + \gamma_f) \lambda_k) \omega \\ & + \gamma_{\text{dvf}} \gamma_{\text{sdf}} + \gamma_{\text{sdf}} \gamma_f \lambda_k + c^2 \left(\frac{k\pi}{L}\right)^2, \end{aligned} \quad (4.62)$$

k indexing the eigenvectors of the added-mass operator.

Proof The relation (4.54) is evaluated for $e_d = e^{\omega t} \phi_k$. A particularity of the dimension of the problem is that the eigenvector ϕ_k of \mathcal{M}_A is also an eigenvector of $-\partial_{xx}$. In fact

$$-\partial_{xx} \phi_k = -\partial_{xx} \left\{ \beta_k \sin\left(\frac{k\pi}{L} x\right) \right\} = \beta_k \left(\frac{k\pi}{L}\right)^2 \sin\left(\frac{k\pi}{L} x\right).$$

We complete the proof by injecting a displacement error in the form $e^{\omega t} \phi_k$ in (4.59). \square

The problem consists in choosing $\gamma_{\text{sdf}}, \gamma_{\text{dvf}}, \gamma_f > 0$ in such a way that they maximize the decay of the error in the displacement, or equivalently, that we minimize the real part of the eigenfrequencies. We introduce $K := \{(x_1, x_2, x_3) \in \mathbb{R}^3 : x_1 \geq 0, x_2 \geq 0, x_3 \geq 0\}$. This problem can be formulated as finding $(\gamma_{\text{sdf}}, \gamma_{\text{dvf}}, \gamma_f)^* \in K$ solution of

$$(\gamma_{\text{sdf}}, \gamma_{\text{dvf}}, \gamma_f)^* = \underset{(\gamma_{\text{sdf}}, \gamma_{\text{dvf}}, \gamma_f) \in K}{\operatorname{arg\,inf}} \sup_{k \in \mathbb{Z}^+} \{\operatorname{Re}(\omega_k)\}, \quad (4.63)$$

where ω_k is a pole of (4.62). Among all the parameters $(\gamma_{\text{sdf}}, \gamma_{\text{dvf}}, \gamma_f) \in K$, the goal is to find those which enables to place poles of (4.62) as far as possible from the imaginary axis. An insight to (4.63) is provided in Figure 4.26.

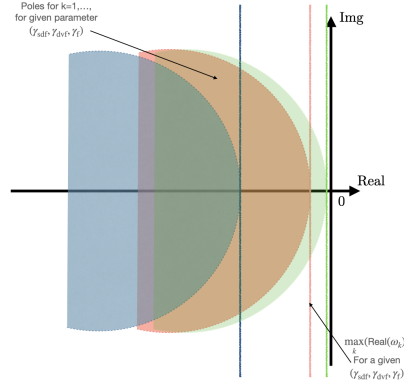


Figure 4.26: Example of placement.

Proposition 2

For a given $(\gamma_{\text{sdf}}, \gamma_{\text{dvf}}, \gamma_f) \in K$, when k sufficiently large, P_k has two complex conjugate roots $\omega_{k,1}$ and $\omega_{k,2}$ with

$$\operatorname{Re}(\omega_{k,n}) = -\frac{\alpha_k \gamma_{\text{sdf}} + \gamma_{\text{dvf}} + \gamma_f \lambda_k}{2\alpha_k} < 0, \quad n = 1, 2, \quad (4.64)$$

with $\alpha_k := \rho^s \epsilon + \rho^f \lambda_k$ and

$$\lim_{k \rightarrow \infty} \operatorname{Re}(\omega_{k,n}) = -\frac{\rho^s \epsilon \gamma_{\text{sdf}} + \gamma_{\text{dvf}}}{2\rho^s \epsilon}. \quad (4.65)$$

High frequencies decay exponentially, with a speed that is asymptotically a linear increasing function of γ_{sdf} and γ_{dvf} .

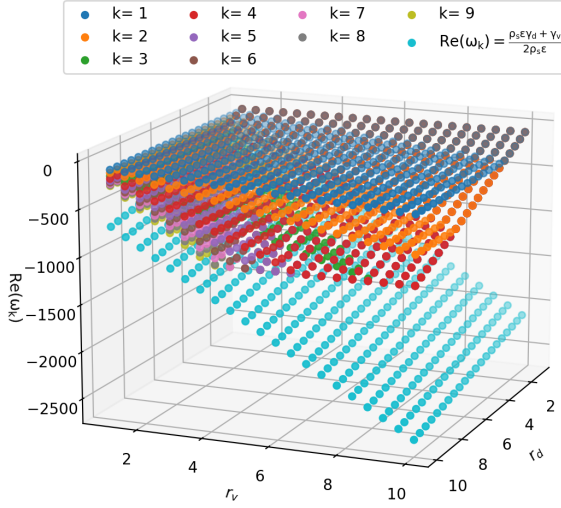


Figure 4.27: $\max_{n=1,2}\{\text{Re}(\omega_{k,n})\}$, for $\gamma_f = 100$, $R = 0.5$, $L = 5$.

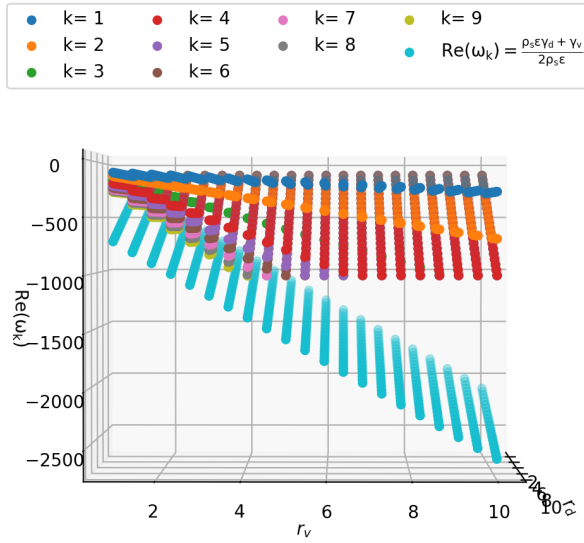


Figure 4.28: $\max_{n=1,2}\{\text{Re}(\omega_{k,n})\}$, for $\gamma_f = 100$, $R = 0.5$, $L = 5$, different view.

Proof For $k \in \mathbb{Z}^*$, the discriminant Δ_k of P_k writes:

$$\Delta_k = (\alpha_k \gamma_{\text{sdf}} + \gamma_{\text{dvf}} + \gamma \lambda_k)^2 - 4\gamma_{\text{sdf}}\alpha_k(\gamma_{\text{dvf}} + \gamma_f \lambda_k) - 4\alpha_k c^2 \left(\frac{k\pi}{L}\right)^2 \quad (4.66)$$

$$= (\alpha_k \gamma_{\text{sdf}} - \gamma_{\text{dvf}} - \gamma_f \lambda_k)^2 - 4\alpha_k c^2 \left(\frac{k\pi}{L}\right)^2. \quad (4.67)$$

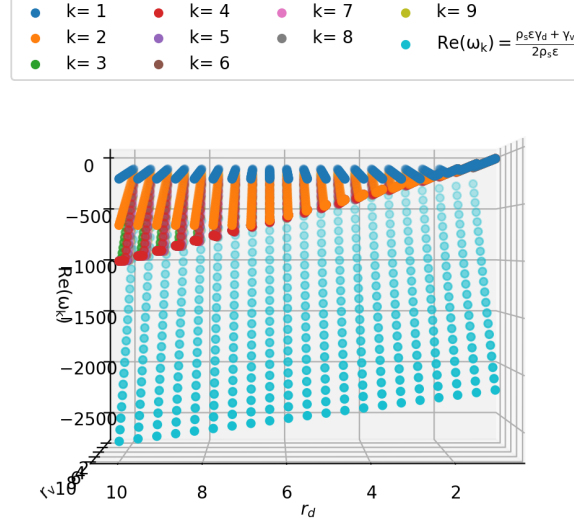


Figure 4.29: $\max_{n=1,2}\{\text{Re}(\omega_{k,n})\}$, for $\gamma_f = 100$, $R = 0.5$, $L = 5$, different view.

The function $k \mapsto \lambda_k = \frac{1}{\frac{k\pi}{L} \tanh(\frac{k\pi R}{L})}$ is monotonously decreasing, and $\lambda_k \sim (\frac{k\pi}{L})^{-1}$ when $k \rightarrow \infty$. Consequently $k \mapsto \alpha_k = \rho^s \epsilon + \rho^f \lambda_k$ is also monotonously decreasing, and $\lim_{k \rightarrow \infty} \alpha_k = \rho^s \epsilon$ when $k \rightarrow \infty$. It follows that for given $(\gamma_{\text{sdf}}, \gamma_{\text{dvf}}, \gamma_f) \in K$, when $k \gg 1$,

$$\Delta_k \sim -4\rho^s \epsilon c^2 \left(\frac{k\pi}{L}\right)^2 < 0.$$

Hence for k sufficiently large, $\Delta_k < 0$ and P_k has 2 complex conjugate roots whose real part can be expressed in terms of the coefficients of P_k , as follows

$$-\frac{(\rho^s \epsilon \gamma_{\text{sdf}} + \gamma_{\text{dvf}}) + (\rho^f \gamma_{\text{sdf}} + \gamma_f) \lambda_k}{2\rho^s \epsilon + \rho^f \lambda_k},$$

which gives (4.64) after a few manipulations. When k goes to infinity, since λ_k converges to 0 and α_k to $\rho^s \epsilon$, it yields (4.64). Which completes the proof. \square

This results shows that high frequencies are damped for all the parameters. The main difficulty relies in damping the low frequency modes. The analytical resolution of problem (4.63) is not trivial. We instead propose to investigate the numerical behavior of the real part for different values of the parameters. $\gamma_{\text{sdf}} = r_d \gamma_f$ and $\gamma_{\text{dvf}} = r_v \gamma_f$ and $\gamma_f > 0$, for $0 \leq r_d, r_v \leq 10$. For $R = 0.5$, $L = 5$, $\gamma_f = 100$, the values of $\max_{n=1,2}\{\text{Re}(\omega_{k,n})\}$ for $0 \leq r_d, r_v \leq 10$ and k going from 1 to 9, are represented on Figures 4.27–4.29. For $(\gamma_{\text{sdf}} = r_d \gamma_f, \gamma_{\text{dvf}} = r_v \gamma_f, \gamma_f)$, with $\gamma_f = 100$, P_k with $k = 1$ seems to have the rightmost real parts. The value of (r_d, r_v) that minimizes $\max_{n=1,2}\{\text{Re}(\omega_{1,n})\}$ is $(r_d \approx 2.8, r_v = 10.0)$.

4.4.2.1 FSI state estimation coupled with position observation operator (4D Flow MRI)

In this section, we assume that the data are provided in the form of 4D Flow MRI data composed of

1. time resolved image sequences $F_M^n, n = 1, \dots, N_T$ of blood flow (with visible surface wall deformation);
2. the Eulerian velocity field $\mathbf{u}_M^n, n = 1, \dots, N_T$, defined on a larger domain $\mathcal{V} \supset \hat{\Omega}$.

Using these Eulerian mixed data, measurements $(\mathbf{d}_M^n, \dot{\mathbf{d}}_M^n)$ of the Lagrangian displacement of the vessel wall are calculated sequentially in the solid sub-problem. In Chapter 2, Section 2.3.2, a procedure (Algorithm 2) to estimate the Lagrangian displacement and velocity at the vessel wall has been proposed using 4D Flow MRI data. To put it in a nutshell, at each time sample, the position observation operator takes as input the prior configuration of the interface and the image sequences $F_M^n, n = 1, \dots, N_T$, and it provides a new a priori on the localization of the interface, as described in Section 2.2.3.2 of Chapter 2. There, the position observation operator served as measurement tool for the Kalman filter (solid) state estimation. Note that one could use the tracking approach of Chapter 2 as a way of generating the displacement and velocity data for the solid Luenberger sub-problem, but this involves an inconsistency in the underlying models used for the dynamics prediction. Here, we propose to circumvent this issues by integrating directly the position observation operator of Section 2.2.3.2 in the solid Luenberger state observer of FSI estimator. As a reminder, at each time step, the previous configuration of the vessel wall is given by $\hat{\Sigma}^{n-1} = \hat{\Sigma} + \tilde{\mathbf{d}}^{n-1}(\hat{\Sigma})$ and is uniquely characterized at the discrete level by:

- the mesh nodes of $\hat{\Sigma}$;
- the nodal values of the Lagrangian displacement field $\tilde{\mathbf{d}}^{n-1}$.

Hence, the position observation operator of Section 2.2.3.2 is used to generate $(\mathbf{d}_M^n, \dot{\mathbf{d}}_M^n)$ from the 4D Flow MRI data (that is F_M^n and \mathbf{u}_M^n).

Measurement step. We denote by $\mathbf{q}_i, i = 1, \dots, N_h^\Sigma$, the position of mesh nodes of $\hat{\Sigma}$, the reference configuration. The prior configuration for the position observation operator is set to $\hat{\Sigma}^{n-1}$ whose mesh nodes position $\tilde{\mathbf{q}}_i^{n-1}$ is given

$$\tilde{\mathbf{q}}_i^{n-1} = \mathbf{q}_i + \tilde{\mathbf{d}}^{n-1}(\mathbf{q}_i),$$

for $i = 1, \dots, N_h^\Sigma$. Taking up the same notations as in Section 2.2.3.2, the nodal values of the solid displacement and the velocity measurements are given by:

$$\mathbf{d}_M^n(\mathbf{q}_i) = \mathbf{q}_{i,m}^n - \mathbf{q}_i, \quad \dot{\mathbf{d}}_M^n(\mathbf{q}_i) = \mathbf{u}_M^n(\mathbf{q}_{i,M}^n),$$

respectively.

The adaptation of Algorithm 7 to make use of 4D MRI data through the position observation operator is detailed in Algorithm 8. It should be noted that the only difference between Algorithm 7 and Algorithm 8 is the adjunction of procedure to generate the displacement and velocity measurements in the solid $(\mathbf{d}_M^n, \dot{\mathbf{d}}_M^n)$. In Algorithm 7, the measurements are generic, whereas for Algorithm 8, they are obtained by making use of position observation operator (Section 2.2.3.2).

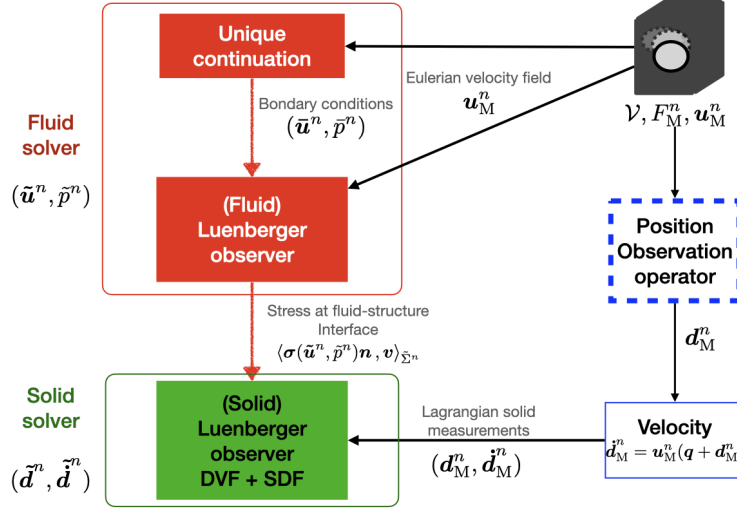


Figure 4.30: UCL-FSI using 4D MRI data

4.4.3 Numerical results

The numerical results section is organized as follow. First, the coupling between the solid Luenberger solver and the position observation operator as sequential measurement tool is validated without the FSI coupling in Section 4.4.3.1. The reference solution is the cylinder vessel at rest. An initial parabolic displacement is applied to the cylinder and with the Luenberger solid observer, a convergence to the rest state with dissipation is expected. After this preliminary step of validation, the complete UCL-FSI algorithm is tested with Eulerian measurements as for 4D Flow MRI. An initial deformation is applied to the vessel. The challenge for the FSI state estimation is to estimate the velocity, the absolute pressure and the displacement of the wall, while correcting the displacement of the wall. The accuracy of the method is evaluated by means of L^2 -relative error from the velocity, the pressure and the displacement, transported in the reference configuration and normalized by the maximum L^2 -norm in time.

4.4.3.1 Coupling between the solid Luenberger and the position observation operator

Let consider the isolated solid problem (4.6) with $\mathbf{f}_\Sigma \equiv 0$. No fluid flows in the vessel, which is initially at rest, consequently a trivial solution of the forward problem is the rest state $\mathbf{d}^n \equiv 0$, $\dot{\mathbf{d}}^n \equiv 0$, for all $n = 1, \dots, N_T$. The data are provided in the form of 4D MRI data with the image sequence F_M^n the Eulerian vector field \mathbf{u}_M^n , $n = 1, \dots, N_T$, defined on a voxel partition of a large domain $\mathcal{V} \supset \hat{\Omega}$. The position observation operator returns the sequential measured displacement and velocity of the vessel wall based on the image F_M^n , the velocity \mathbf{u}_M^n , and the previous estimated wall configuration $\hat{\Sigma}^n$, used as prior. The solid state estimation with and without the position observation operator is compared regarding the two situations:

Case 1 $(\mathbf{d}_M^n, \dot{\mathbf{d}}_M^n)$ are perfect measurements, meaning $\mathbf{d}_M^n \equiv 0$ and $\dot{\mathbf{d}}_M^n \equiv 0$,

Case 2 $(\mathbf{d}_M^n, \dot{\mathbf{d}}_M^n)$ are generated using the position observation operator, with as prior the previous state estimation.

The resolution of the voxel grid is of $0.1 \times 0.1 \times 0.1$, which is approximately 10 voxels in a cylinder diameter. The same ratio approximately holds for the exam used in the first chapter. In fact the theoretical diameter of the aorta is around 20 mm, and the resolution of the voxel grid of the 4D MRSA exam is 2 mm, in each direction. The vessel is perturbed from its initial (and reference) configuration by applying the following parabolic profile:

$$\mathbf{d}^0(x, y, z) = \begin{pmatrix} 0 \\ d_{\max} \left(1 - \frac{(z-L/2)^2}{(L/2)^2} \right) \\ 0 \end{pmatrix}, \quad (4.72)$$

where $d_{\max} > 0$ represents the maximum initial geometrical error. Note that this profile is compatible with the Dirichlet boundary conditions on $\partial\hat{\Sigma}$.

We are interested in the solution of the following problem: Find $\tilde{\mathbf{d}}^n$ such that

$$\begin{aligned} \left(\frac{\rho^s \epsilon}{\tau^2} + \frac{\gamma_{\text{dvf}}}{\tau} \right) (1 + \tau \gamma_{\text{sdf}}) (\tilde{\mathbf{d}}^n, \hat{\boldsymbol{\xi}})_{\Sigma} + a^s (\tilde{\mathbf{d}}^n, \hat{\boldsymbol{\xi}}) &= \frac{\rho^s \epsilon}{\tau} (\tilde{\mathbf{d}}^{n-1}, \boldsymbol{\xi}^n)_{\Sigma} \\ + \left(\frac{\rho^s \epsilon}{\tau^2} + \frac{\gamma_{\text{dvf}}}{\tau} \right) (\tilde{\mathbf{d}}^{n-1} + \tau \gamma_{\text{sdf}} \mathbf{d}_M^n, \hat{\boldsymbol{\xi}})_{\Sigma} + \gamma_{\text{dvf}} (\dot{\mathbf{d}}_M^n, \hat{\boldsymbol{\xi}})_{\Sigma}, & \\ \forall \hat{\boldsymbol{\xi}} \in \hat{\mathbf{W}}_{0,h}. & \quad (4.73) \end{aligned}$$

The null displacement is a trivial solution. The time discretization parameters are $\tau = 1.0 \cdot 10^{-4}$ s, $T = 1.5 \cdot 10^{-2}$ s and the physical parameters are $\rho^s = 1.1$ g/cm³, $\epsilon = 0.1$ cm, $E = 10^7$ dynes/cm² and $\nu = 0.5$. For the position observation operator, the local window search is of *1 voxel*, $\gamma = 20$ (scaling of the normalized image gradient), the regularization step uses $\kappa_{\text{obs}} \delta = 20$. One can refer to Section 2.2.3.2 for more details on the meaning of those parameters.

The decay to zero of the L2 normal of the displacement normalized by the initial L2 normal is illustrated in Figure 4.31 when measurements are exact exact (solid line), or generated with the position observation operator (dashed lines). The tests have been performed for $(\gamma_{\text{sdf}}, \gamma_{\text{dvf}}) = (100, 10), (100, 100), (300, 100), (300, 300)$.

As expected, the Schur displacement feedback (SDF) and the Direct Velocity feedback (DVF) dissipate towards zero, for exact measurements. With the position observation operator, the displacement loses 1 to 2 order of magnitude for $(\gamma_{\text{sdf}}, \gamma_{\text{dvf}}) = (300, 300)$ and $(\gamma_{\text{sdf}}, \gamma_{\text{dvf}}) = (100, 100)$. There is a plateau for the error decrease when measurements are taken from the position observation operator. This may be due to the nearest neighbor search for the minimization step in the position observation operator and the resolution of the grid.

The evolution of the deformation is reported in Figure 4.32, the solid state estimation with the exact measurement being in red, and the one with the position observation operator in blue. The displacement has been multiplied by 2 for better visibility.

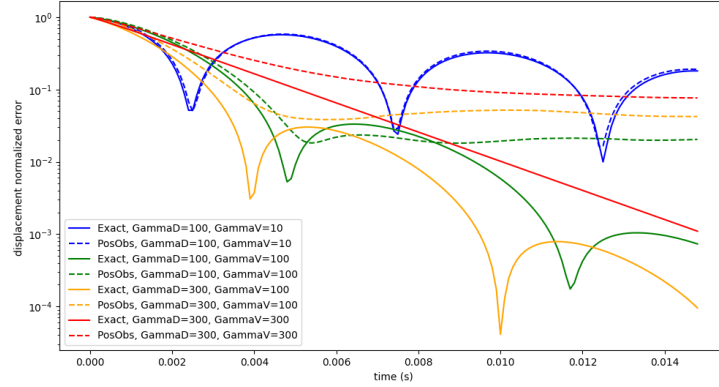
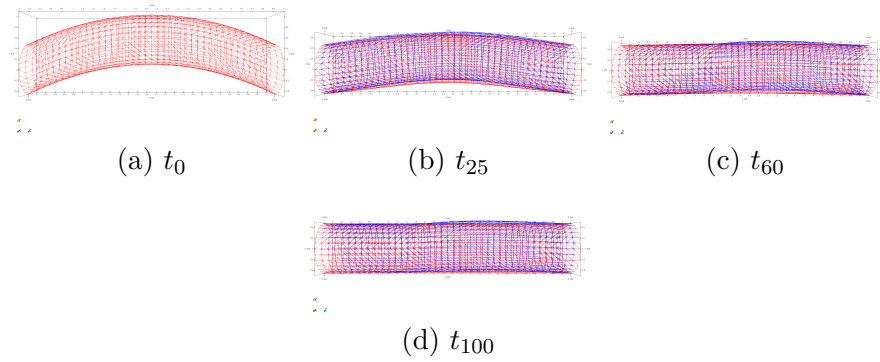
Figure 4.31: Decay of the displacement L^2 -norm

Figure 4.32: Decay of the displacement (amplified by a factor 2).

4.4.3.2 Correction of the solid geometrical error in the FSI state estimation U_cL-FSI

In this section, numerical simulations with the FSI state estimation U_cL-FSI are discussed in the case in which the vessel wall has an initial displacement profile, as in (4.72) with d_{\max} goes from 1 to 2 voxels, namely from 0.1 to 0.2. The ground truth solution is the one described in Section 4.3.2.1 with the same physical parameters. Eulerian measurements are generated with grid resolution of 0.1.

The FSI state estimation with Algorithm 8 has been performed for wide range of parameters $\gamma_f, \gamma_{\text{sdf}}, \gamma_{\text{dvf}}$, with noise-free data. It has been noted that for large values of γ_{sdf} , typically $\gamma_{\text{sdf}} > 5 \cdot 10^3$, the harmonic extension (4.16) discretized with \mathbb{P}_1 finite elements generates finite elements of negative measure, resulting in breakdown of the numerical fluid solver of the Luenberger estimator(4.34).

The estimated pressure with Algorithm 8 has been reported in Figure 4.33 for the parameters $\gamma_M = 10^5$, $\gamma_f = 50$, $\gamma_{\text{sdf}} = 2000$ and $\gamma_{\text{dvf}} = 200$. The estimated FSI state is compared with the reference solution by assessing the relative error in the velocity, pressure and displacement, that has been made available in Figure 4.34.

The difficulties in this example for the UCL-FSI estimator has to correct the initial velocity and displacement error fast enough to compute the wave propagation by means of the parameter γ_f . A naive strategy would consist in imposing large feedback on the solid. However, the correction of the displacement by the UCL-FSI estimator generates locally high pressure at the wall, and increasing γ_f increases the inertia of the combined fluid and solid system, as one may have noticed through the introduction of the added mass operator in Section 4.4.2.

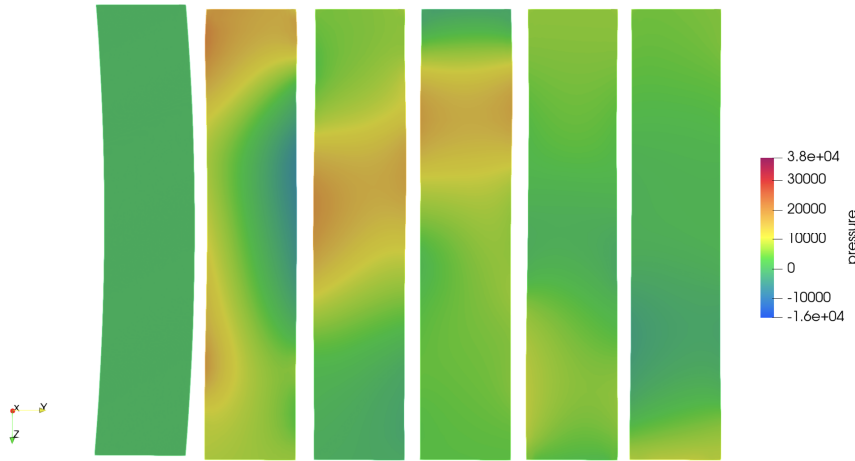


Figure 4.33: Estimated pressure with Algorithm 8 for $\gamma_M = 10^5$, $\gamma_f = 50$, $\gamma_{sdf} = 2000$ and $\gamma_{dvf} = 200$, at $t_0, t_{30}, t_{50}, t_{70}, t_{100}, t_{120}$ and t_{140} . The displacement has not been amplified

From the snapshots of the pressure estimation, the FSI state estimation with correction of the wall displacement manages to correct in a few iteration the error induced by the initial displacement.

Conclusion

This chapter presents a novel approach to estimate the full FSI state with measurements in the fluid and the solid that are derived from 4D Flow MRI (image sequences and velocity field). The FSI state estimation extends to moving fluid domain the Algorithm 4 introduced for fixed domain. The fluid sub-problem combines a unique continuation step for boundary conditions estimation with Luenberger state observer for the fluid sub-problem. The strength of the method is the ability of the unique continuation to provide an intermediate fluid state which serves to impose boundary conditions for the fluid Luenberger state estimator. The solid sub-problem assimilates displacement and velocity measurements in a Luenberger state observer. The method has been validated without solid measurement feedback in a first parts with satisfactory behavior. Then in the second part the solid feedback has been added to take into account perturbations of the initial solid condition. One can make use of the position observation operator in order to convert 4DMRI data into Lagrangian displacement et velocity measurements that are used for the

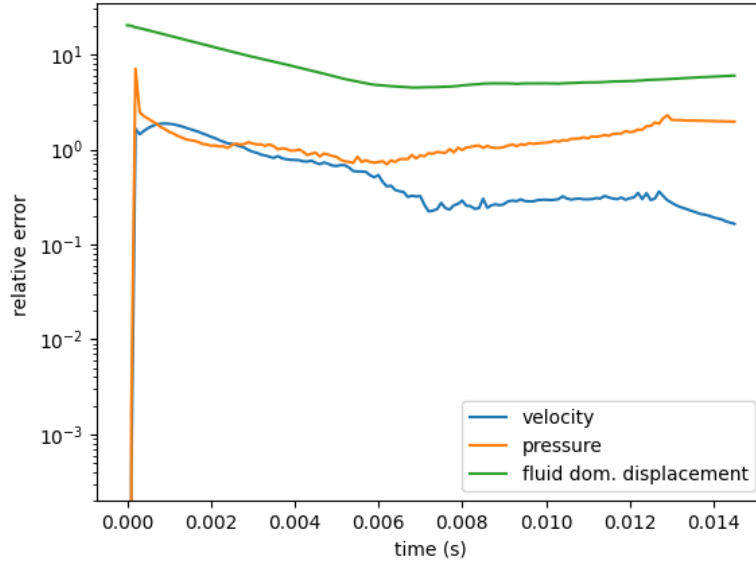


Figure 4.34: Relative error in the velocity, the pressure and the (fluid domain) displacement for $\gamma_M = 10^5$, $\gamma_f = 50$, $\gamma_{sdf} = 2000$ and $\gamma_{dvf} = 200$.

solid Luenberger state observer. The FSI state estimation algorithm 8 manages to correct the fluid velocity and the wall displacement with the full fluid velocity and solid measurements.

Algorithm 8 FSI state estimation UCL-FSI using 4D MRI data

Require: Initial conditions:

$$\begin{cases} \tilde{\mathbf{d}}^0 = \mathbf{d}_0 \tilde{\mathbf{d}}^0 = \mathbf{v}_0 \text{ on } \hat{\Sigma} \\ \tilde{\Omega}^0 = \tilde{\mathcal{A}}_h^0(\hat{\Omega}), \text{ with } \tilde{\mathcal{A}}_h^0 = \mathbf{I} + \mathbf{d}_f^0, \text{ and } \mathbf{d}_f^0 = \text{Ext}(\mathbf{d}_0) \\ \tilde{\mathbf{u}}^0 = \mathbf{u}_0, \tilde{p}^0 = p_0 \text{ on } \tilde{\Omega}^0 \\ (F_M^n, \mathbf{u}_M^n), n = 1, \dots, \\ \gamma_f, \gamma_{\text{sdf}}, \gamma_{\text{dvf}} > 0 \end{cases} \quad (4.68)$$

for $n = 1, \dots, N_T$ **do**

 Solid solver to Fluid solver: $(\tilde{\mathbf{d}}^{n-1}, \tilde{\mathbf{d}}^{n-1})$.

A/ Fluid solver

1. Compute the fluid domain displacement $\mathbf{d}_f^n = \text{Ext}_h(\tilde{\mathbf{d}}^{n-1})$ for Ext_h defined as the \mathbb{P}_1 finite element approximation of (4.16). Update the ALE velocity $\tilde{\mathbf{w}}^n$ and compute the fluid computational domain $\tilde{\Omega}^n$ using (4.26)_{2,3}.
2. Unique continuation: Find $[(\tilde{\mathbf{u}}^n, \tilde{p}^n), (\mathbf{z}, \mathbf{y})] \in (\tilde{\mathbf{V}}_h^n \times \tilde{Q}_h^n) \times (\tilde{\mathbf{V}}_{0,h}^n \times \tilde{Q}_h^n)$ solution of

$$\begin{cases} \gamma_M(\tilde{\mathbf{u}}^n, \mathbf{v})_{\tilde{\Omega}^n} + s_h[(\tilde{\mathbf{u}}^n, \tilde{p}^n), (\mathbf{v}, q)] + \tilde{a}_{\text{fluid/FSI}}^n[(\mathbf{v}, q), (\mathbf{z}, \mathbf{y})] = \gamma_M(\mathbf{u}_M^n, \mathbf{v})_{\tilde{\Omega}^n}, \\ \tilde{a}_{\text{fluid/FSI}}^n[(\tilde{\mathbf{u}}^n, \tilde{p}^n), (\mathbf{w}, x)] - s_h^*[(\mathbf{z}, \mathbf{y}), (\mathbf{w}, x)] = \tilde{l}^{n-1}(\mathbf{w}), \end{cases} \quad (4.69)$$

 for all $(\mathbf{v}, q) \in \tilde{\mathbf{V}}_h^n \times \tilde{Q}_h^n$ and $(\mathbf{w}, x) \in \tilde{\mathbf{V}}_{0,h}^n \times \tilde{Q}_h^n$.

3. Luenberger fluid state estimation: Find $\tilde{\mathbf{u}}^n \in \tilde{\mathbf{V}}_h^n, \tilde{p}^n \in \tilde{Q}_h^n$, such that $\forall (\mathbf{v}, q) \in \tilde{\mathbf{V}}_h^n \times \tilde{Q}_h^n$

$$\begin{cases} \tilde{a}_{\text{fluid/FSI}}^n[(\tilde{\mathbf{u}}^n, \tilde{p}^n), (\mathbf{v}^n, q)] + s_{\text{SUPG}}[(\tilde{\mathbf{u}}^n, \mathbf{v}^n), (\tilde{p}^n, q)] + \gamma_f(\tilde{\mathbf{u}}_h^n - \mathbf{u}_M^n, \mathbf{v}^n)_{\tilde{\Omega}^n} \\ = \tilde{l}^{n-1}(\mathbf{v}) - \langle \tilde{p}^n |_{\tilde{\Gamma}_{\text{in}}^n} \mathbf{n}, \mathbf{v}^n \rangle_{\tilde{\Gamma}_{\text{in}}^n} - \langle \tilde{p}^n |_{\tilde{\Gamma}_{\text{out}}^n} \mathbf{n}, \mathbf{v}^n \rangle_{\tilde{\Gamma}_{\text{out}}^n} \end{cases} \quad (4.70)$$

B/ Solid solver

1. Provide $(\mathbf{d}_M^n, \tilde{\mathbf{d}}_M^n)$ with the position observation operator in 2.2.3.2, using F_M^n, \mathbf{u}_M^n and the mesh nodes of $\tilde{\Sigma}^{n-1}$ as prior.
2. Luenberger solid state estimation: Find $\tilde{\mathbf{d}}^n \in \hat{\mathbf{W}}_h$ solution of

$$\begin{cases} \tilde{\mathbf{d}}^n = \partial_\tau \tilde{\mathbf{d}}^n + \gamma_{\text{sdf}}(\tilde{\mathbf{d}}^n - \mathbf{d}_M^n), \\ (\rho^s \epsilon \partial_\tau \tilde{\mathbf{d}}^n, \hat{\boldsymbol{\xi}})_{\hat{\Sigma}} + \mathbf{a}^s(\tilde{\mathbf{d}}^n, \hat{\boldsymbol{\xi}}) + \gamma_{\text{dvf}}(\tilde{\mathbf{d}}^n - \mathbf{d}_M^n, \hat{\mathbf{w}})_{\hat{\Sigma}} = -(\sigma(\tilde{\mathbf{u}}^n, \tilde{p}^n) \mathbf{n}, \hat{\boldsymbol{\xi}}^n)_{\hat{\Sigma}^n} \end{cases} \quad (4.71)$$

 for all $\hat{\boldsymbol{\xi}} \in \hat{\mathbf{W}}_{0,h}$.

end for

Part III

Conclusion

General conclusion and perspectives

In this thesis, we have focused on FSI state estimation using 4D Flow MRI (image sequences with velocity data). Compared to fixed-domain CFD simulations, patient-specific FSI require the calibration of not only the fluid state (velocity and pressure) but also the solid state (displacement of the wall), hence enabling (absolute) pressure estimation. In Chapter 2, we have proposed a new method for the reconstruction of the Lagrangian displacement and velocity of a vessel using 4D Flow MRI data exclusively. The method is formulated as Kalman filter with a specific position observation operator, which transforms the image sequences into observed configurations. The capabilities of the method have been shown using synthetic and real data, with good accuracy despite the simplified model for the prediction. The contribution of this chapter can be seen as a preliminary step for the calibration of the wall displacement with FSI.

In Chapters 3 and 4, we tackle the problem of FSI state estimation with 4D-Flow MRI on an idealized vessel geometry (straight cylinder). The FSI model involves: (i) a fluid sub-problem with the incompressible Stokes or Navier-Stokes equations; (ii) a solid sub-problem based on thin shell model; and (iii) the coupling interface conditions between the fluid and the solid. In Chapter 4, we consider fixed-domain FSI setting in which the solid displacement is expressed in terms of the fluid velocity and yields a monolithic formulation. The kinematic and dynamic coupling conditions appear as a generalized Robin boundary conditions in the fluid sub-problem. In this setting, the proposed FSI state estimation method (Algorithm 3) is based on the unique continuation method. Unique continuation does not require the knowledge of the inflow and outflow boundary conditions, which yields an ill-posed problem. This solvability problem of the unique continuation is circumvented by adding consistent stabilization and regularization at the discrete level, in the spirit of [BBFV20]. Algorithm 3 showed satisfactory accuracy for the estimation of fluid velocity, the pressure and the wall displacement. Inflow and outflow boundary quantities are also well estimated. Owing to this, unique continuation is then used to estimate the boundary conditions for a Luenberger state observer in the fluid sub-problem using fluid velocity measurements (Algorithm 4). The FSI state is estimated with good accuracy by Algorithm 4. Especially the estimated pressure and fluid domain displacement show reasonable robustness with respect to the level of noise in the data. In Chapter 4, Algorithm 4 is extended to the case of moving fluid domains and non-linear solids by leveraging the partitioned nature of a Robin-Neuman loosely coupled scheme (Algorithm 6). The FSI coupling is integrated in the continuation step through a standard Robin condition. This method provides satisfactory estimations, even with noisy data, whenever the same initial conditions for the forward (reference) problem and the FSI state estimations were considered. Nevertheless, with different initial displacement of the wall a Luenberger observer with only fluid velocity measurement is no longer sufficient. In order to circumvent this issue, a solid Luenberger observer with measurements of displacement and velocity in the solid is added to the FSI estimator (Algorithms 7). Moreover, we also considered the case in which the solid observation is based on the position

observation operator designed in Chapter 2 (Algorithm 8). First results are provided in case in which there is an error in the initial wall displacement and velocity. The FSI estimation performs a fast correction of the displacement of the structure. The conclusions are more mitigated for the fluid velocity and pressure estimation, and would require further sensitivity studies.

Several research perspectives can be foreseen after the present work.

- The tracking in Chapter 2 has been tested on a single clinical exam in Section 2.4.2, and validated with respect to the Dice metric. The Dice metric is a good indicator for the quality of the surface and the volume reconstruction. However, it does not provide information on the accuracy of the point-to-point trajectory tracking. Few imaging techniques provides direct measurements of the displacement of tissue (such as Tagged-MRI). One possible option could be to validate the estimated displacement using another image technique or another part of the body for which direct displacement measurements are available.
- In view of clinical application, more intensive validation on a cohort of patients would be required in Chapter 2.
- The PDE constraint (3.7) for unique continuation Section 4.3 Equation (4.27)(moving domain) might not be robust for high Reynolds numbers (the analysis of [BBFV20] does not cover this case). Additional stabilization might be necessary to achieve robustness in that regime.
- In Chapter 4, the numerical examples involve interfacial deflections which are relatively small (up to 10% of the vessel radius). Further numerical examples with moderate to large displacement should be considered.
- The present work did not cover the theoretical numerical analysis (stability, convergence) of the proposed FSI estimation methods. Any result in this direction will be very valuable.
- Some improvements would be needed in Algorithm 8 in order to deal with real 4D-flow MRI data. First, additional numerical sensitivity analysis with respect to the free-parameters $\gamma_f, \gamma_{sdf}, \gamma_{dvf}$ with noisy data could be performed. Then, in Algorithm 8, vanishing displacement is imposed in the inflow/outflow rings, however for large-sized vessel such as the aorta, the inflow ring (close to heart for the ascending aorta) undergoes medium to large displacement, as already illustrated in Figure 2.26. In order to circumvent this problem, the Dirichlet boundary conditions on $\partial\hat{\Omega}$ could be replaced by a data feedback term on the inflow/outflow rings. More precisely, it would consist in replacing (III) in Algorithm 8 by:

$$\begin{cases} \tilde{\mathbf{d}}^n = \partial_\tau \tilde{\mathbf{d}}^n + \gamma_{sdf}(\tilde{\mathbf{d}}^n - \mathbf{d}_M^n), \\ (\rho^s \epsilon \partial_\tau \tilde{\mathbf{d}}^n, \hat{\boldsymbol{\xi}})_{\hat{\Sigma}} + \mathbf{a}^s(\tilde{\mathbf{d}}^n, \hat{\boldsymbol{\xi}}) \\ + \gamma_{dvf}(\tilde{\mathbf{d}}^n - \mathbf{d}_M^n, \hat{\mathbf{w}})_{\hat{\Sigma}} + \gamma_{BD}(\tilde{\mathbf{d}}^n - \mathbf{d}_M^n, \hat{\boldsymbol{\xi}})_{\partial\Sigma} = -(\sigma(\tilde{\mathbf{u}}^n, \tilde{p}^n) \mathbf{n}, \boldsymbol{\xi}^n)_{\hat{\Sigma}^n} \end{cases}$$

for all $\hat{\boldsymbol{\xi}} \in \hat{\mathbf{W}}_h$, and with $\gamma_{BD} > 0$. This could also have an impact on the robustness of the harmonic lifting used to deform the fluid domain (4.26). One could instead think of an elastic harmonic extension which maintains the

inflow and outflow surfaces $\tilde{\Gamma}_{\text{in}}^n$ and $\tilde{\Gamma}_{\text{out}}^n$ relatively straight, while allowing rigid movements.

Part IV
Appendix

Unique continuation for FSI

In this section, the detail of the block-matrix terms in the linear system associated to the numerical resolution of the unique continuation estimation.

A.1 Unique continuation on fixed fluid domain

For the unique continuation applied to monolithic FSI introduced in Section 3.2.2, the saddle points $((\bar{\mathbf{u}}^n, \bar{p}^n), (\mathbf{z}, y)) \in \mathbf{V}_h \times Q_h \times \mathbf{V}_h^0 \times Q_h$ of the regularized Lagrangian L_h satisfy the following optimality conditions (3.17):

$$\begin{cases} \gamma_M(\bar{\mathbf{u}}^n, \mathbf{v})_\Omega + s_h((\bar{\mathbf{u}}^n, \bar{p}^n), (\mathbf{v}, q)) + a^{\text{fsi}}((\mathbf{v}, q), (\mathbf{z}, y)) = \gamma_M(\mathbf{u}_M^n, \mathbf{v})_\Omega, \\ a^{\text{fsi}}((\bar{\mathbf{u}}^n, \bar{p}^n), (\mathbf{w}, x)) - s_h^*((\mathbf{z}, y), (\mathbf{w}, x)) = l^n(\mathbf{w}), \end{cases} \quad (\text{A.1})$$

for all $(\mathbf{v}, q) \in \mathbf{V}_h \times Q_h$ and $(\mathbf{w}, x) \in \mathbf{V}_h^0 \times Q_h$.

The linear system associated to the numerical resolution of (3.17) writes as follow with block-matrix representation:

$$\left[\begin{array}{cc|cc} M_m + S_u & 0 & & A_{\text{fsi}}^T \\ 0 & S_p & & \\ \hline & & -S_u^* & 0 \\ A_{\text{fsi}} & & 0 & -S_p^* \end{array} \right] \begin{bmatrix} U \\ P \\ Z \\ Y \end{bmatrix} = \begin{bmatrix} U_m \\ 0 \\ L \\ 0 \end{bmatrix}. \quad (\text{A.2})$$

The block-matrix A_{fsi} can be composed block-wise:

$$A_{\text{fsi}} := \begin{pmatrix} A & -B^T \\ B & 0 \end{pmatrix}$$

We denote by $\mathcal{B}^1 := \{\chi_i\}_{i=0, \dots, N_h}$, the standard basis shape functions for the approximation space X_h^1 , N_h being the number of nodes of the shape regular mesh \mathcal{T}_h . If we assume that the first N_h^0 nodes are nodes in $\partial\Omega \setminus \{\Gamma_{\text{in}} \cap \Gamma_{\text{out}}\}$, the matrices at the left-hand side of the system (3.18) are expressed block-wise as follow:

block(0,0)

$$(M_M)_{i,j} = \gamma_M(\chi_j, \chi_i)_\Omega \mathbf{l}_2$$

$$\begin{aligned} (S_u)_{i,j} &= \gamma_{\text{div}}(\text{div } \chi_j, \text{div } \chi_i)_\Omega \mathbf{l}_2 \\ &+ \gamma_u h \sum_{F \in \mathcal{F}_{\text{int}}} (\llbracket \nabla \chi_j \rrbracket, \llbracket \nabla \chi_i \rrbracket)_F \mathbf{l}_2 \end{aligned}$$

block(0,2):

$$\begin{aligned} (A^T)_{i,j_0} &= \frac{\rho^f}{\tau} (\chi_i, \chi_{j_0})_\Omega + 2\mu(\varepsilon(\chi_i), \varepsilon(\chi_{j_0}))_\Omega \\ &\quad + \left(\frac{\rho^s \varepsilon}{\tau} \langle \chi_i^{(2)}, \chi_{j_0}^{(2)} \rangle_\Sigma + \tau a^s(\chi_i^{(2)}, \chi_{j_0}^{(2)}) \right) \mathbf{E}_{22} \\ &:= a_h(\chi_i, \chi_{j_0}) \end{aligned}$$

block(0,3):

$$B_{i,j}^T = (\chi_j, \operatorname{div} \chi_i)_\Omega,$$

block(1,1)

$$(S_p)_{i,j} = s_p(\chi_j, \chi_i) = \gamma_p h^2 (\nabla \chi_j, \nabla \chi_i)_\Omega,$$

block(1,2)

$$-B_{i,j_0} = -(\chi_i, \operatorname{div} \chi_{j_0})_\Omega,$$

block(2,0)

$$A_{i_0,j} = a_h(\chi_j, \chi_{i_0})$$

block(2,1)

$$-B_{i_0,j}^T = -(\chi_j, \operatorname{div} \chi_{i_0})_\Omega,$$

block(2,2) :

$$-(S_u^*)_{i_0,j_0} = s_u^*(\chi_{j_0}, \chi_{i_0}) = \gamma_u^* (\nabla \chi_{j_0}, \nabla \chi_{i_0})_\Omega,$$

block(3,0):

$$B_{i,j} = (\chi_i, \operatorname{div} \chi_j)_\Omega,$$

block(3,3):

$$-(S_p^*)_{i,j} = -\gamma_p^*(\chi_j, \chi_i)_\Omega,$$

for $i, j = 1, \dots, N_h$ and $i_0, j_0 = 1, \dots, N_h^0$. For the right-hand side:

- block (0):

$$(U_m)_i = \gamma_M(\mathbf{u}_M^n, \chi_i)_\Omega$$

- block (2)

$$\begin{aligned} L_{i_0} &= \sum_{j=1}^{N_h} \left[\frac{\rho^f}{\tau} \begin{pmatrix} (\chi_j^1, \chi_{i_0}^2)_\Omega & \\ & (\chi_j^2, \chi_{i_0}^2)_\Omega \end{pmatrix} U_j^{n-1} + \begin{pmatrix} 0 & \\ & \frac{\rho^s \varepsilon}{\tau} \langle \chi_j^2, \chi_{i_0}^2 \rangle_\Sigma \end{pmatrix} U_j^{n-1} \right] \\ &\quad \sum_{j=1}^{N_h} + \begin{pmatrix} 0 & \\ & -a^s(\chi_j^2, \chi_{i_0}^2) \end{pmatrix} \begin{pmatrix} 0 \\ D_j^n \end{pmatrix} \end{aligned}$$

for $i, j = 1, \dots, N_h$ and $i_0 = 1, \dots, N_h^0$. The solution of the matrix-vector system is related to the discrete solution of (3.17) by means of the following decomposition:

$$\bar{\mathbf{u}}^n = \sum_{j=1}^{N_h} \begin{pmatrix} \chi_j^1 \\ \chi_j^2 \end{pmatrix} U_j, \quad \bar{p}^n = \sum_{k=1}^{N_h} P_k \chi_k, \quad \bar{\mathbf{z}}^n = \sum_{j^0=1}^{N_h^0} \begin{pmatrix} \chi_{j^0}^1 \\ \chi_{j^0}^2 \end{pmatrix} Z_{j^0}, \quad \bar{\mathbf{y}}^n = \sum_{m=1}^{N_h} Y_m \chi_m$$

and

$$\bar{d}^n = \sum_{r=1}^{N_h} D_r^n \chi_r|_{\Sigma},$$

for $U_j, Z_{j^0} \in \mathbb{R}^2$, $P_k, Y_m \in \mathbb{R}$.

A.2 Unique continuation for moving domain

After finite element approximation, the linear system associated to the numerical resolution of (4.32) writes as follow with matrix representation:

$$\left[\begin{array}{cc|cc} M_m + S_u & 0 & A^T & B^T \\ 0 & S_p & -B & 0 \\ \hline A & -B^T & -S_u^* & 0 \\ B & 0 & 0 & -S_p^* \end{array} \right] \begin{bmatrix} U_h \\ P_h \\ Z_h \\ Y_h \end{bmatrix} = \begin{bmatrix} U_m \\ 0 \\ F \\ 0 \end{bmatrix}. \quad (\text{A.3})$$

The system is similar the one obtained with fixed domain setting. Note that the integrals on the left-hand side are performed on the current configuration $\tilde{\Omega}^n$, whereas some integrals on the right-hand side are calculated in the previous configuration.

Let denote by $(\hat{\mathbf{x}}_i)_{i=1, \dots, N_h}$ the nodes of the shape regular mesh of $\hat{\Omega}$ with the first N_h^0 nodes being the nodes on $\partial\hat{\Omega} \setminus \{\hat{\Gamma}_{\text{in}} \cup \hat{\Gamma}_{\text{out}}\}$. We introduce the standard family $\{\chi_i, i = 1, \dots, N_h\}$ of piecewise linear shape functions on the tetrahedra \mathcal{T}_h of $\hat{\Omega}$, such that for $i = 1, \dots, N_h$, $\chi_i(\hat{\mathbf{x}}_j) = \delta_{ij}$ for all $j = 1, \dots, N_h$, and $\chi_i \equiv 0$ on the elements K if $\hat{\mathbf{x}}_i$ is not a node of K . $\{\chi_i, i = 1, \dots, N_h\}$ defines a basis of X_h^1 . For $n > 0$, we associate to the basis function χ_i , the function shape χ_i^n defined on $\tilde{\Omega}^n = \tilde{\mathcal{A}}^n(\hat{\Omega})$ such that $\chi_i^n(\mathbf{x}_j^n) = \chi_i(\hat{\mathbf{x}}_j)$, for $\mathbf{x}_j^n = \tilde{\mathcal{A}}^n(\hat{\mathbf{x}}_j)$, $j = 1, \dots, N_h$. With this family of time-dependent basis functions, we ensure $\partial_\tau \chi_i|_{\tilde{\mathcal{A}}} = 0$ for the ALE map $\tilde{\mathcal{A}}^n$ at the time discrete level. For a function $v \in X_h^1$, the $v_i, i = 1, \dots, N_h$ will denote the degrees of freedom of v , such that

$$v = \sum_{j=1}^{N_h} v_j \chi_j.$$

At each time step, the solution $\bar{\mathbf{u}}^n \in \tilde{\mathbf{V}}_h^n$ is decomposed component-wise on the basis $\{\chi_i, i = 1, \dots, N_h\}$, same for the pressure $\bar{p}^n \in Q_h^n$ and the dual variables $(\bar{\mathbf{z}}^n, \bar{\mathbf{y}}^n) \in \times(\mathbf{V}_{0,h}^n \times Q_h^n)$.

$$\bar{\mathbf{u}}^n = \sum_{j=1}^{N_h} \begin{pmatrix} U_{1,j}^x \chi_j^1 \\ U_{2,j}^y \chi_j^2 \\ U_{3,j}^z \chi_j^3 \end{pmatrix}, \quad \text{with } \chi_j^1 \equiv \chi_j^2 \equiv \chi_j^3, \quad \forall j = 1, \dots, N_h,$$

$$\bar{p}^n = \sum_{m=1}^{N_h} P_m \zeta_m,$$

$$\bar{\mathbf{z}}^n = \sum_{j^0=0}^{N_h^0} \begin{pmatrix} Z_{1,j^0} \chi_{j^0}^1 \\ Z_{2,j^0} \chi_{j^0}^2 \\ Z_{3,j^0} \chi_{j^0}^3 \end{pmatrix},$$

$$\bar{y}^n = \sum_{l=1}^{N_h} Y_l \zeta_l.$$

The notation ζ will be used for test function on the pressure and its dual variable, and χ for the velocity and its dual variable.

The matrices in (A.3) can be explicitly provided blockwise. We introduce the following notations: $\boldsymbol{\chi} := (\chi^1, \chi^2, \chi^3)^T$, and

$$(\mathcal{B}\boldsymbol{\chi}_i; \mathcal{D}\boldsymbol{\chi}_j)_\Omega = \begin{pmatrix} (\mathcal{B}\chi_i^1; \mathcal{D}\chi_j^1)_\Omega & & \\ & (\mathcal{B}\chi_i^2; \mathcal{D}\chi_j^2)_\Omega & \\ & & (\mathcal{B}\chi_i^3; \mathcal{D}\chi_j^3)_\Omega \end{pmatrix},$$

with \mathcal{B}, \mathcal{D} , two differential operators.

block(0,0):

$$(M_m)_{i,j} = \gamma_M(\boldsymbol{\chi}_j^n; \boldsymbol{\chi}_i^n)_{\bar{\Omega}^n},$$

$$(S_u)_{i,j} = s_u(\boldsymbol{\chi}_j, \boldsymbol{\chi}_i) = \gamma_{div}(\operatorname{div} \boldsymbol{\chi}_j^n; \operatorname{div} \boldsymbol{\chi}_i^n)_{\bar{\Omega}^n} \\ + \gamma_u h \sum_{F \in \mathcal{F}_i} ([\nabla \boldsymbol{\chi}_j^n]; [\nabla \boldsymbol{\chi}_i^n])_F$$

block(0,2):

$$(A^T)_{i,j} = \frac{\rho^f}{\tau}(\boldsymbol{\chi}_i^n; \boldsymbol{\chi}_{j^0}^n)_{\bar{\Omega}^n} \\ + 2\mu(\varepsilon(\boldsymbol{\chi}_i^n); \varepsilon(\boldsymbol{\chi}_{j^0}^n))_{\bar{\Omega}^n} \\ - \rho^f(\operatorname{div} \tilde{\boldsymbol{w}}^n \boldsymbol{\chi}_i^n; \boldsymbol{\chi}_{j^0}^n)_{\bar{\Omega}^n} \\ + \frac{\rho^f}{2}(\operatorname{div} \tilde{\boldsymbol{u}}^{n-1} \boldsymbol{\chi}_i^n; \boldsymbol{\chi}_{j^0}^n)_{\bar{\Omega}^n} \\ + \rho^f((\tilde{\boldsymbol{u}}^{n-1} - \tilde{\boldsymbol{w}}^n) \nabla \boldsymbol{\chi}_i^n; \boldsymbol{\chi}_{j^0}^n)_{\bar{\Omega}^n} \\ + \frac{\rho^s \epsilon}{\tau}(\boldsymbol{\chi}_i^n; \boldsymbol{\chi}_{j^0}^n)_{\bar{\Sigma}^n} \quad := \tilde{a}_f^n(\boldsymbol{\chi}_i^n; \boldsymbol{\chi}_{j^0}^n)$$

block(0,3):

$$B_{i,j}^T = (\zeta_j, \operatorname{div} \boldsymbol{\chi}_i^n)_{\bar{\Omega}_h^n},$$

block(1,1):

$$(S_p)_{i,j} = s_p(\zeta_j, \zeta_i) = \gamma_p h^2(\nabla \zeta_j^n, \nabla \zeta_i^n)_{\bar{\Omega}^n},$$

block(1,2):

$$-B_{i,j} = -(\zeta_i, \operatorname{div} \boldsymbol{\chi}_{j^0}^n)_{\bar{\Omega}^n},$$

block(2,0):

$$A_{i,j} = \tilde{a}_f^n(\boldsymbol{\chi}_{j^0}^n, \boldsymbol{\chi}_i^n)$$

block(2,1):

$$-B_{i,j}^T = -(\zeta_j, \operatorname{div} \boldsymbol{\chi}_{i^0}^n)_{\bar{\Omega}^n},$$

block(2,2):

$$-(S_u^*)_{i,j} = s_u^*(\boldsymbol{\chi}_{j^0}^n, \boldsymbol{\chi}_{i^0}^n) = \gamma_u^*(\nabla \boldsymbol{\chi}_{j^0}^n, \nabla \boldsymbol{\chi}_{i^0}^n)_{\bar{\Omega}^n},$$

block(3,0):

$$B_{i,j} = (\zeta_i, \operatorname{div} \boldsymbol{\chi}_j^n)_{\tilde{\Omega}^n},$$

block(3,3):

$$-(S_p^*)_{i,j} = -\gamma_p^*(\zeta_j, \zeta_i)_{\tilde{\Omega}^n},$$

Concerning the right-hand side :

block (0):

$$(U_m)_j = \gamma_M(\mathbf{u}_M^n; \boldsymbol{\chi}_j^n)_{\tilde{\Omega}^n}$$

block (2):

$$F_i = \frac{1}{\tau} (\rho^f \tilde{\mathbf{u}}^{n-1}; \boldsymbol{\chi}^{n-1})_{\tilde{\Omega}^{n-1}} + \langle \sigma(\tilde{\mathbf{u}}^{n-1}, \tilde{p}^{n-1}) \mathbf{n}, \boldsymbol{\chi}^{n-1} \rangle_{\tilde{\Sigma}^{n-1}} + \langle 2\tilde{\mathbf{d}}^{n-1} + \tilde{\mathbf{d}}^{n-2}, \boldsymbol{\chi} \rangle_{\tilde{\Sigma}},$$

Bibliography

- [AB15] Luigi Adamo and Alan C Braverman. Surgical threshold for bicuspid aortic valve aneurysm: a case for individual decision-making. *Heart*, 101(17):1361–1367, 2015.
- [Act09] Scott T. Acton. Chapter 20 - diffusion partial differential equations for edge detection. In Al Bovik, editor, *The Essential Guide to Image Processing*, pages 525–552. Academic Press, Boston, 2009.
- [AGPT09] Matteo Astorino, Jean-Frédéric Gerbeau, Olivier Pantz, and Karim-Frédéric Traoré. Fluid–structure interaction and multi-body contact: Application to aortic valves. *Computer Methods in Applied Mechanics and Engineering*, 198(45):3603–3612, 2009. Models and Methods in Computational Vascular and Cardiovascular Mechanics.
- [ALB⁺22] Mocia Agbalessi, Alain Lalande, Olivier Bouchot, Toshiyuki Hayase, Jean-Joseph Christophe, Miguel Angel Fernández, and Damiano Lombardi. Tracking of blood vessels motion from 4D-flow MRI data. working paper or preprint, September 2022.
- [AXM⁺20] Christopher J. Arthurs, Nan Xiao, Philippe Moireau, Tobias Schaeffter, and C. Alberto Figueroa. A flexible framework for sequential estimation of model parameters in computational hemodynamics. *Advanced Modeling and Simulation in Engineering Sciences*, 7(1):48, 2020.
- [BBFV20] Muriel Boulakia, Erik Burman, Miguel A Fernández, and Colette Voisembert. Data assimilation finite element method for the linearized Navier-Stokes equations in the low Reynolds regime. *Inverse Problems*, 36:085003, 2020.
- [BCF⁺13] C. Bertoglio, D. Chapelle, M.A. Fernández, J.-F. Gerbeau, and P. Moireau. State observers of a vascular fluid–structure interaction model through measurements in the solid. *Computer Methods in Applied Mechanics and Engineering*, 256:149–168, 2013.
- [Ber12] Cristobal Bertoglio. *Forward and Inverse Problems in Fluid-Structure Interaction. Application to Hemodynamics*. Theses, Université Pierre et Marie Curie - Paris VI, November 2012.
- [BFO20] Erik Burman, Ali Feizmohammadi, and Lauri Oksanen. A finite element data assimilation method for the wave equation. *Math. Comput.*, 89:1681–1709, 2020.
- [BGCE17] Mariana Bustamante, Vikas Gupta, Carl-Johan Carlhäll, and Tino Ebbers. Improving visualization of 4d flow cardiovascular magnetic resonance with four-dimensional angiographic data: generation of a 4d phase-contrast magnetic resonance cardioangiography (4d pc-mrca). *Journal of Cardiovascular Magnetic Resonance*, 19(1):47, 2017.

- [BHL18] Erik Burman, Peter Hansbo, and Mats G. Larson. Solving ill-posed control problems by stabilized finite element methods: an alternative to Tikhonov regularization. *Inverse Problems*, 34(3):035004, 36, 2018.
- [BKFG19] Ludovic Boilevin-Kayl, Miguel Angel Fernández, and Jean-Frédéric Gerbeau. Numerical methods for immersed FSI with thin-walled structures. *Computers and Fluids*, 179:744–763, January 2019.
- [BMG12] Cristóbal Bertoglio, Philippe Moireau, and Jean-Frederic Gerbeau. Sequential parameter estimation for fluid–structure problems: Application to hemodynamics. *International Journal for Numerical Methods in Biomedical Engineering*, 28(4):434–455, 2012.
- [BNG⁺17] Cristobal Bertoglio, Rodolfo Núñez, Felipe Galarce, David Nord-sletten, and Axel Osses. Relative pressure estimation from velocity measurements in blood flows: state-of-the-art and new approaches. *International Journal for Numerical Methods in Biomedical Engineering*, September 2017.
- [BNO19] Erik Burman, Mihai Nechita, and Lauri Oksanen. Unique continuation for the helmholtz equation using stabilized finite element methods. *Journal de Mathématiques Pures et Appliquées*, 129:1–22, sep 2019.
- [BP84] F. Brezzi and J. Pitkäranta. *On the Stabilization of Finite Element Approximations of the Stokes Equations*, pages 11–19. Vieweg+Teubner Verlag, Wiesbaden, 1984.
- [BSN⁺99] Helmut Baumgartner, Thomas Stefenelli, Julia Niederberger, Heinrich Schima, and Gerald Maurer. “overestimation” of catheter gradients by doppler ultrasound in patients with aortic stenosis: a predictable manifestation of pressure recovery. *Journal of the American College of Cardiology*, 33(6):1655–1661, 1999.
- [Bur13] Erik Burman. Stabilized finite element methods for nonsymmetric, noncoercive, and ill-posed problems. part i: Elliptic equations. *SIAM Journal on Scientific Computing*, 35(6):A2752–A2780, 2013.
- [Bur16] Erik Burman. *Stabilised Finite Element Methods for Ill-Posed Problems with Conditional Stability*, pages 93–127. Springer International Publishing, Cham, 2016.
- [BvOP⁺16] Emilie Bollache, Pim van Ooij, Alex Powell, James Carr, Michael Markl, and Alex J. Barker. Comparison of 4d flow and 2d velocity-encoded phase contrast mri sequences for the evaluation of aortic hemodynamics. *The International Journal of Cardiovascular Imaging*, 32(10):1529–1541, 2016.
- [Can86] John Canny. A computational approach to edge detection. *Pattern Analysis and Machine Intelligence, IEEE Transactions on*, PAMI-8:679 – 698, 12 1986.
- [CB11] Dominique Chapelle and Klaus-Jürgen Bathe. *Shell Mathematical Models*, pages 95–134. Springer Berlin Heidelberg, Berlin, Heidelberg, 2011.

- [CCM⁺17] Alfonso Caiazzo, Federica Caforio, Gino Montecinos, Lucas O Muller, Pablo J Blanco, and Eluterio F Toro. Assessment of reduced-order unscented kalman filter for parameter identification in 1-dimensional blood flow models using experimental data. *International journal for numerical methods in biomedical engineering*, 33(8):e2843, 2017.
- [CDE⁺18] Elliot L. Chaikof, Ronald L. Dalman, Mark K. Eskandari, Benjamin M. Jackson, W. Anthony Lee, M. Ashraf Mansour, Tara M. Mastracci, Matthew Mell, M. Hassan Murad, Louis L. Nguyen, Gustavo S. Oderich, Madhukar S. Patel, Marc L. Schermerhorn, and Benjamin W. Starnes. The society for vascular surgery practice guidelines on the care of patients with an abdominal aortic aneurysm. *Journal of Vascular Surgery*, 67(1):2–77.e2, 2021/08/05 2018.
- [CGN05] P. Causin, J.F. Gerbeau, and F. Nobile. Added-mass effect in the design of partitioned algorithms for fluid–structure problems. *Computer Methods in Applied Mechanics and Engineering*, 194(42):4506–4527, 2005.
- [CL13] A. D. Caballero and S. Laín. A review on computational fluid dynamics modelling in human thoracic aorta. *Cardiovascular Engineering and Technology*, 4(2):103–130, 2013.
- [DGC⁺02] Ryan R. Davies, Lee J. Goldstein, Michael A. Coady, Shawn L. Tittle, John A. Rizzo, Gary S. Kopf, and John A. Elefteriades. Yearly rupture or dissection rates for thoracic aortic aneurysms: simple prediction based on size. *The Annals of Thoracic Surgery*, 73(1):17–28, Jan 2002.
- [Dou76] Todd Douglas, Jimand Dupont. Interior penalty procedures for elliptic and parabolic galerkin methods. In R. Glowinski and J. L. Lions, editors, *Computing Methods in Applied Sciences*, pages 207–216, Berlin, Heidelberg, 1976. Springer Berlin Heidelberg.
- [EHN96] Heinz Werner Engl, Martin Hanke, and Andreas Neubauer. *Regularization of inverse problems*, volume 375. Springer Science & Business Media, 1996.
- [Fer13] Miguel A. Fernández. Incremental displacement-correction schemes for incompressible fluid-structure interaction. *Numerische Mathematik*, 123(1):21–65, January 2013.
- [FH13] Kenichi Funamoto and Toshiyuki Hayase. Reproduction of pressure field in ultrasonic-measurement-integrated simulation of blood flow. *International Journal for Numerical Methods in Biomedical Engineering*, 29(7):726–740, 2013.
- [FMV13] Miguel A. Fernández, Jimmy Mullaert, and Marina Vidrascu. Explicit robin–neumann schemes for the coupling of incompressible fluids with thin-walled structures. *Computer Methods in Applied Mechanics and Engineering*, 267:566–593, 2013.
- [GJ⁺10] Gaël Guennebaud, Benoît Jacob, et al. Eigen v3. <http://eigen.tuxfamily.org>, 2010.

- [GR86] Vivette Girault and Pierre-Arnaud Raviart. Finite element methods for Navier-Stokes equations: Theory and algorithms. *NASA STI/Recon Technical Report A*, 87:52227, January 1986.
- [GTdM13] D. R. Koolbergen G. Tokmaji, B. J. Bouma and B. A.J.M. de Mol. *Calcific Aortic Valve Disease*. IntechOpen, Rijeka, Jun 2013.
- [HKK⁺16] Hojin Ha, Guk Bae Kim, Jihoon Kweon, Sang Joon Lee, Young-Hak Kim, Namkug Kim, and Dong Hyun Yang. The influence of the aortic valve angle on the hemodynamic features of the thoracic aorta. *Scientific Reports*, 6(1):32316, 2016.
- [HSW⁺14] Michael D. Hope, Monica Sigovan, S. Jarrett Wrenn, David Saloner, and Petter Dyverfeldt. Mri hemodynamic markers of progressive bicuspid aortic valve-related aortic disease. *Journal of Magnetic Resonance Imaging*, 40(1):140–145, 2014.
- [IGOY98] Takuji Ishikawa, Luis F R Guimaraes, Shuzo Oshima, and Ryuichiro Yamane. Effect of non-newtonian property of blood on flow through a stenosed tube. *Fluid Dynamics Research*, 22(5):251, may 1998.
- [Kál60] R. Kálmán. A new approach to linear filtering and prediction problems. *Transactions of the ASME—Journal of Basic Engineering*, 82:35–45, 1960.
- [KB61] R. Kálmán and R. Bucy. New results in linear filtering and prediction theory. *Journal of Basic Engineering*, 83:95–108, 1961.
- [KET⁺17] Andreas Kühnl, Alexander Erk, Matthias Trenner, Michael Salvermoser, Volker Schmid, and Hans-Henning Eckstein. Incidence, treatment and mortality in patients with abdominal aortic aneurysms. *Deutsches Arzteblatt international*, 114(22-23):391–398, Jun 2017.
- [KFL⁺10] Taco Kind, Theo JC Faes, Jan-Willem Lankhaar, Anton Vonk-Noordegraaf, and Michel Verhaegen. Estimation of three-and four-element windkessel parameters using subspace model identification. *IEEE Transactions on Biomedical Engineering*, 57(7):1531–1538, 2010.
- [KKB⁺15] Fabian A. Kari, Nadja Kocher, Friedhelm Beyersdorf, Anke Tscheuschler, Philipp Meffert, Bartosz Rylski, Matthias Siepe, Maximilian F. Russe, and Michael D. Hope. Four-dimensional magnetic resonance imaging-derived ascending aortic flow eccentricity and flow compression are linked to aneurysm morphology†. *Interactive Cardio-Vascular and Thoracic Surgery*, 20(5):582–588, 01 2015.
- [KPG⁺16] Benjamin Köhler, Uta Preim, Matthias Grothoff, Matthias Gutberlet, Katharina Fischbach, and Bernhard Preim. Motion-aware stroke volume quantification in 4d pc-mri data of the human aorta. *International Journal of Computer Assisted Radiology and Surgery*, 11(2):169–179, 2016.
- [KWT88] Michael Kass, Andrew Witkin, and Demetri Terzopoulos. Snakes: Active contour models. *International Journal of Computer Vision*, 1(4):321–331, 1988.

- [LCV⁺18] Hwa-Liang Leo, Federico Canè, Benedict Verhegghe, Matthieu De Beule, Philippe B. Bertrand, Rob J. Van der Geest, Patrick Segers, and Gianluca De Santis. From 4d medical images (ct, mri, and ultrasound) to 4d structured mesh models of the left ventricular endocardium for patient-specific simulations. *BioMed Research International*, 2018:7030718, 2018.
- [LF19] Alessandro Veneziani Luca Formaggia, Alfio Quarteroni. *Cardiovascular Mathematics*. Springer Milano, 2019.
- [LL15] Sang-Hoon Lee and Sanghoon Lee. Adaptive kalman snake for semi-autonomous 3d vessel tracking. *Computer Methods and Programs in Biomedicine*, 122(1):56–75, 2015.
- [LSY⁺14] Chi Wan Lim, Yi Su, Si Yong Yeo, Gillian Maria Ng, Vinh Tan Nguyen, Liang Zhong, Ru San Tan, Kian Keong Poh, and Ping Chai. Automatic 4d reconstruction of patient-specific cardiac mesh with 1-to-1 vertex correspondence from segmented contours lines. *PLOS ONE*, 9(4):1–14, 04 2014.
- [LVCF17] Mikel Landajuela, Marina Vidrascu, Dominique Chapelle, and Miguel A. Fernández. Coupling schemes for the fsi forward prediction challenge: Comparative study and validation. *International Journal for Numerical Methods in Biomedical Engineering*, 33(4):e2813, 2017. e2813 cnm.2813.
- [MBS⁺15] Lucia Mirabella, Alex J. Barker, Neelakantan Saikrishnan, Elizabeth R. Coco, Daniel J. Mangiameli, Michael Markl, and Ajit P. Yoganathan. Mri-based protocol to characterize the relationship between bicuspid aortic valve morphology and hemodynamics. *Annals of Biomedical Engineering*, 43(8):1815–1827, 2015.
- [MBX⁺12] Philippe Moireau, Cristobal Bertoglio, Nan Xiao, C. Alberto Figueroa, Charles Taylor, Dominique Chapelle, and Jean-Frédéric Gerbeau. Sequential identification of boundary support parameters in a fluid-structure vascular model using patient image data. *Biomechanics and Modeling in Mechanobiology*, 12(3):475–496, July 2012.
- [MC11] Philippe Moireau and Dominique Chapelle. Reduced-order Unscented Kalman Filtering with application to parameter identification in large-dimensional systems. *ESAIM: Control, Optimisation and Calculus of Variations*, 17(2):380–405, 2011. See also erratum DOI:10.1051/cocv/2011001.
- [MCLT08] Philippe Moireau, Dominique Chapelle, and Patrick Le Tallec. Joint state and parameter estimation for distributed mechanical systems. *Comput. Methods Appl. Mech. Engrg.*, 197(6-8):659–677, 2008.
- [MCLT09] Philippe Moireau, Dominique Chapelle, and Patrick Le Tallec. Filtering for distributed mechanical systems using position measurements: perspectives in medical imaging. *Inverse Problems*, 25(3):035010, 25, 2009.

- [MdSJK⁺16] Sen Mei, Francisco S.N. de Souza Júnior, May Y.S. Kuan, Naomi C. Green, and Daniel M. Espino. Hemodynamics through the congenitally bicuspid aortic valve: a computational fluid dynamics comparison of opening orifice area and leaflet orientation. *Perfusion*, 31(8):683–690, 2016. PMID: 27484972.
- [mEA⁺14] Authors/Task Force members, Raimund Erbel, Victor Aboyans, Catherine Boileau, Eduardo Bossone, Roberto Di Bartolomeo, Holger Eggebrecht, Arturo Evangelista, Volkmar Falk, Herbert Frank, Oliver Gaemperli, Martin Grabenwöger, Axel Haverich, Bernard Iung, Athanasios John Manolis, Folkert Meijboom, Christoph A. Nienaber, Marco Roffi, Hervé Rousseau, Udo Sechtem, Per Anton Sirnes, Regula S. von Allmen, Christiaan J.M. Vrints, ESC Committee for Practice Guidelines (CPG), Jose Luis Zamorano, Stephan Achenbach, Helmut Baumgartner, Jeroen J. Bax, Héctor Bueno, Veronica Dean, Christi Deaton, Çetin Erol, Robert Fagard, Roberto Ferrari, David Hasdai, Arno Hoes, Paulus Kirchhof, Juhani Knuuti, Philippe Kolh, Patrizio Lancellotti, Ales Linhart, Petros Nihoyannopoulos, Massimo F. Piepoli, Piotr Ponikowski, Per Anton Sirnes, Juan Luis Tamargo, Michal Tendera, Adam Torbicki, William Wijns, Stephan Windecker, Document reviewers, Petros Nihoyannopoulos, Michal Tendera, Martin Czerny, John Deanfield, Carlo Di Mario, Mauro Pepi, Maria Jesus Salvador Taboada, Marc R. van Sambeek, Charalambos Vlachopoulos, Jose Luis Zamorano, Michael Grimm, Oktay Musayev, Agnès Pasquet, Zumreta Kušljugić, Maja Cikes, Georgios P. Georghiou, Josef Stasek, Henning Molgaard, Sirje Kõvask, Ville Kytö, Guillaume Jondeau, Zviad Bakhutashvili, Yskert von Kodolitsch, Costas Tsioufis, András Temesvári, Ronen Rubinshtein, Francesco Antonini-Canterin, Olga Lunegova, Peteris Stradins, Elie Chammas, Regina Jonkaitiene, Andrew Cassar, Knut Bjørnstad, Kazimierz Widenka, Miguel Sousa Uva, Daniel Lighezan, Jovan Perunicic, Juraj Madaric, Isidre Vilacosta, Magnus Bäck, Abdallah Mahdhaoui, Recep Demirbag, and Ivan Kravchenko. 2014 ESC Guidelines on the diagnosis and treatment of aortic diseases: Document covering acute and chronic aortic diseases of the thoracic and abdominal aorta of the adult. The Task Force for the Diagnosis and Treatment of Aortic Diseases of the European Society of Cardiology (ESC). *European Heart Journal*, 35(41):2873–2926, 08 2014.
- [MFK⁺12] Michael Markl, Alex Frydrychowicz, Sebastian Kozerke, Mike Hope, and Oliver Wieben. 4d flow mri. *Journal of Magnetic Resonance Imaging*, 36(5):1015–1036, 2012.
- [Moi08a] Philippe Moireau. *Assimilation de données par filtrage pour les systèmes hyperboliques du second ordre - Applications à la mécanique cardiaque*. Theses, Ecole Polytechnique X, December 2008.
- [Moi08b] Philippe Moireau. *Filtering based data assimilation for second order hyperbolic PDEs - Applications in cardiac mechanics*. PhD thesis, Ecole Polytechnique X, Dec 2008.

- [Moi18] Philippe Moireau. A Discrete-time Optimal Filtering Approach for Non-linear Systems as a Stable Discretization of the Mortensen Observer. *ESAIM: Control, Optimisation and Calculus of Variations*, 24(4):1815 – 1847, 2018.
- [Mon99] Johan Montagnat. *Modèles déformables pour la segmentation et la modélisation d’images médicales 3D et 4D*. PhD thesis, Université de Nice Sophia-Antipolis, 1999.
- [MRB⁺19] David Marlevi, Bram Ruijsink, Maximilian Balmus, Desmond Dillon-Murphy, Daniel Fovargue, Kuberan Pushparajah, Cristóbal Bertoglio, Massimiliano Colarieti-Tosti, Matilda Larsson, Pablo Lamata, C. Alberto Figueroa, Reza Razavi, and David A. Nordsletten. Estimation of Cardiovascular Relative Pressure Using Virtual Work-Energy. *Scientific Reports*, 9(1):1375, February 2019.
- [MRM⁺20] Sara Moccia, L. Romeo, Lucia Migliorelli, E. Frontoni, and Primo Zingaretti. Supervised cnn strategies for optical image segmentation and classification in interventional medicine. 2020.
- [Nec20] Mihai Nechita. *Unique continuation problems and stabilised finite element methods*. PhD thesis, 10 2020.
- [NV08] Fabio Nobile and Christian Vergara. An effective fluid-structure interaction formulation for vascular dynamics by generalized robin conditions. *SIAM J. Scientific Computing*, 30:731–763, 01 2008.
- [Pre70] Judith M.S. Prewitt. Object enhancement and extraction. *Picture Processing and Psychopictorics*, (1):75–149, 1970.
- [PTI⁺07] Linda A. Pape, Thomas T. Tsai, Eric M. Isselbacher, Jae K. Oh, Patrick T. O’Gara, Arturo Evangelista, Rossella Fattori, Gabriel Meinhardt, Santi Trimarchi, Eduardo Bossone, Toru Suzuki, Jeanna V. Cooper, James B. Froehlich, Christoph A. Nienaber, and Kim A. Eagle. Aortic diameter ≥5.5 cm is not a good predictor of type a aortic dissection. *Circulation*, 116(10):1120–1127, 2007.
- [Pui19] Thomas Puisseux. *Numerical simulations for phase-contrast magnetic resonance imaging*. Theses, Université Montpellier, November 2019.
- [PVV11] Mauro Perego, Alessandro Veneziani, and Christian Vergara. A variational approach for estimating the compliance of the cardiovascular tissue: An inverse fluid-structure interaction problem. *SIAM Journal on Scientific Computing*, 33:1181–1211, 05 2011.
- [PYG⁺12] K. A. Patwardhan, Y. Yu, S. Gupta, A. Dentinger, and D. Mills. 4d vessel segmentation and tracking in ultrasound. In *2012 19th IEEE International Conference on Image Processing*, pages 2317–2320, 2012.
- [Rei21] Eric Reissner. The Effect of Transverse Shear Deformation on the Bending of Elastic Plates. *Journal of Applied Mechanics*, 12(2):A69–A77, 03 2021.
- [RMP⁺17] Jose Rozado, Maria Martin, Isaac Pascual, Daniel Hernandez-Vaquero, and Cesar Moris. Comparing american, european and asian practice guidelines for aortic diseases. *Journal of thoracic disease*, 9(Suppl 6):S551–S560, 05 2017.

- [SAG⁺14] Zoran Stankovic, Bradley D. Allen, Julio Garcia, Kelly B. Jarvis, and Michael Markl. 4d flow imaging with mri. *Cardiovascular diagnosis and therapy*, 4(2):173–192, Apr 2014.
- [Seu] Seungbin Ko. Improvement of hemodynamic analysis by 4d flow MRI: Reynolds resolution, partial volume effect, carotid flow. Publisher: Hanyang University.
- [SII⁺09] Y. Shimogonya, T. Ishikawa, Y. Imai, N. Matsuki, and T. Yamaguchi. A realistic simulation of saccular cerebral aneurysm formation: focussing on a novel haemodynamic index, the gradient oscillatory number. *International Journal of Computational Fluid Dynamics*, 23(8):583–593, 2009.
- [SML06] Will Schroeder, Ken Martin, and Bill Lorensen. *The Visualization Toolkit—An Object-Oriented Approach To 3D Graphics*. Kitware, Inc., fourth edition, 2006.
- [SMY15] Neelakantan Saikrishnan, Lucia Mirabella, and Ajit P. Yoganathan. Bicuspoid aortic valves are associated with increased wall and turbulence shear stress levels compared to trileaflet aortic valves. *Biomechanics and Modeling in Mechanobiology*, 14(3):577–588, 2015.
- [Sob14] Irwin Sobel. An isotropic 3x3 image gradient operator. *Presentation at Stanford A.I. Project 1968*, 02 2014.
- [Tem68] R. Temam. Une méthode d’approximation de la solution des équations de navier-stokes. *Bulletin de la Société Mathématique de France*, 96:115–152, 1968.
- [Tez91] T.E. Tezduyar. Stabilized finite element formulations for incompressible flow computations†††this research was sponsored by nasa-johnson space center (under grant nag 9-449), nsf (under grant msm-8796352), u.s. army (under contract daal03-89-c-0038), and the university of paris vi. volume 28 of *Advances in Applied Mechanics*, pages 1–44. Elsevier, 1991.
- [TGS17] J. Tiago, T. Guerra, and A. Sequeira. A velocity tracking approach for the data assimilation problem in blood flow simulations. *International Journal for Numerical Methods in Biomedical Engineering*, 33(10):e2856, 2017. e2856 cnm.2856.
- [Thi08] Marc Thiriet. *Biology and Mechanics of Blood Flows - Part II : Mechanics and Medical Aspects*, volume 2 of *CRM Series in Mathematical Physics*. Springer, 2008.
- [WMQ⁺12] Xiaoxu Wang, Viorel Mihalef, Zhen Qian, Szilard Voros, and Dimitris Metaxas. 3d cardiac motion reconstruction from ct data and tagged mri. In *2012 Annual International Conference of the IEEE Engineering in Medicine and Biology Society*, pages 4083–4086, 2012.
- [WSC⁺12] David Wendell, Margaret Samyn, Joseph Cava, Laura Ellwein-Fix, Mary Krolikowski, Kimberly Gandy, Andrew Pelech, Shawn Shadden, and John LaDisa. Including aortic valve morphology in computational fluid dynamics simulations: Initial findings and application to aortic coarctation. *Medical engineering & physics*, 35, 08 2012.

- [WSW96] Lars Wigström, Lars Sjöqvist, and Bengt Wranne. Temporally resolved 3d phase-contrast imaging. *Magnetic Resonance in Medicine*, 36(5):800–803, 1996.
- [XP98] Chenyang Xu and Jerry L. Prince. Generalized gradient vector flow external forces for active contours1a preliminary version of this paper appeared in the proceedings of the johns hopkins university 1997 conference of information sciences and systems.1. *Signal Processing*, 71(2):131–139, 1998.
- [YHMF18] Tomomi Yamada, Toshiyuki Hayase, Suguru Miyauchi, and Kenichi Funamoto. Numerical analysis of the effect of trabeculae carneae models on blood flow in a left ventricle model constructed from magnetic resonance images. *Journal of Biomechanical Science and Engineering*, 13(2), 2018. Publisher Copyright: © 2018 The Japan Society of Mechanical Engineers.
- [YSFJ16] Pouya Youssefi, Rajan Sharma, C. Alberto Figueroa, and Marjan Jahangiri. Functional assessment of thoracic aortic aneurysms – the future of risk prediction? *British Medical Bulletin*, 121(1):61–71, 12 2016.
- [ZZW+06] Fei Zhao, Honghai Zhang, Andreas Wahle, Thomas Scholz, and Milan Sonka. Automated 4d segmentation of aortic magnetic resonance images. pages 247–256. British Machine Vision Conference, 01 2006.